

On the Nature of Phase Transitions in Covalent Liquids

A numerical study of phosphorus and carbon

ACADEMISCH PROEFSCHRIFT

ter verkrijging van de graad van doctor
aan de Universiteit van Amsterdam
op gezag van de Rector Magnificus
Prof. mr. P.F. van der Heijden

ten overstaan van een door het college voor promoties ingestelde
commissie, in het openbaar te verdedigen in de Aula der Universiteit

op donderdag 19 januari 2006, te 12.00 uur

door

Luca Massimiliano Ghiringhelli

geboren te Lagos, Nigeria

Promotiecommissie:

Promotor:

- Prof. Dr. D. Frenkel

Co-promotor:

- Dr. E. J. Meijer

Overige leden:

- Prof. Dr. V. Rhyzov
- Prof. Dr. A. Fasolino
- Prof. Dr. Ir. B. Smit
- Prof. Dr. R. Krishna
- Dr. J. Carlsson

Faculteit der Natuurwetenschappen, Wiskunde en Informatica

The research reported in this thesis was carried out at the Van 't Hoff Institute for Molecular Sciences, Faculty of Science, University of Amsterdam (Nieuwe Achtergracht 166, 1018 WV, Amsterdam, The Netherlands) with financial support from the Stichting voor Fundamenteel Onderzoek der Materie (FOM)

A coloro che sanno ...

*... alta pur dianzi e tesa scorrea
la vista a scernere prode remote ...*

*... es ist etwas Willkürliches daran, dass
er hier stehen blieb, zurückblickte, sich um-
blickte, dass er hier nicht mehr tiefer grub
und den Spaten weglegte, es ist auch etwas
Misstrauisches daran.*

Contents

1	To the reader	v
2	Liquid – liquid transitions in simple fluids	1
2.1	A simple model	1
2.2	Water	8
2.3	Two simple potentials	9
3	Ab initio molecular dynamics	13
3.1	Car-Parrinello molecular dynamics	13
3.2	Density functional theory	16
3.3	Pseudopotentials	18
3.4	Constant ionic and electronic temperature in CPMD	20
3.5	Constant pressure in CPMD	21
4	Phosphorus: first principle simulation of a LLPT	24
4.1	Overview of the LLPT in phosphorus	24
4.2	Computational methods	26
4.3	Choice of density functional	27
4.4	Liquid – liquid phase transition and equation of state	28
4.5	Properties of the two liquids	31
4.5.1	Static properties	31
4.5.2	Dynamical properties	35
4.5.3	Electronic properties	36
4.6	Summary and discussion	39
4.7	Appendix. Definition of the orientation parameter	41
5	Simulating the phosphorus LLPT up to the critical point	43
5.1	Introduction	43
5.2	Method	43
5.3	Description of the transitions	44
5.4	Structural properties	52
5.5	Electronic properties	56
5.6	Discussion	60
5.7	Conclusions	62

6	Bond order potentials for covalent elements.	63
6.1	Localized orbitals model	65
6.2	Second moment approximation	69
6.3	Bond order potentials (BOPs)	71
6.4	The Tersoff potential	72
6.5	The REBO potential	73
6.6	The LCBOP	76
6.6.1	The conjugation term	78
6.6.2	The non bonded interactions	80
6.7	The LCBOP ⁺	80
6.7.1	New switching functions	80
6.7.2	Angular function	81
6.7.3	Torsional term	83
6.8	Appendix. Further details for the LCBOP and the LCBOP ⁺	85
6.8.1	Interpolation scheme of F^{conj}	85
6.8.2	Parameters for the LCBOP and the LCBOP ⁺	86
6.8.3	Binding energy curves	87
6.9	Appendix. Conjugated molecules	89
7	The phase diagram of carbon at very high pressures and temperatures	90
7.1	The history of carbon phase diagram	91
7.2	On graphite melting line	97
7.3	History of the LLPT for carbon	99
7.3.1	An analysis of experimental data	99
7.3.2	A model for a insulator-into-metal transition	100
7.3.3	A semi-empirical equation of state	100
7.3.4	Experimental suggestions from the graphite melting line	101
7.3.5	Prediction of a short range bond order potential	101
7.3.6	An ab initio confutation of the LLPT	102
8	The carbon phase diagram according to the LCBOP⁺	104
8.1	Methods	104
8.1.1	The Lennard-Jones liquid	105
8.1.2	The Einstein crystal	106
8.1.3	From the Helmholtz free energy to the chemical potential	107
8.2	Results	108
8.3	Appendix. Chemical potential as a function of density	115
9	The nature of liquid carbon: absence of a <i>first-order</i> LLPT	116
9.1	Properties of liquid carbon, according to selected BOPs	116
9.1.1	Methods	116
9.1.2	Results	118
9.2	Ruling out the LLPT in the stable liquid region	121
9.3	High pressure diamond-like liquid carbon	124
9.4	Appendix. Pressure estimation without evaluating the virial	127
9.5	Appendix. Pressure evaluation in a NVT CPMD simulation	128

10 Diamond nucleation	129
10.1 Introduction	129
10.2 Method: direct estimate of a rate constant	131
10.2.1 The forward flux sampling algorithm	131
10.2.2 The parallel optimized FFS	132
10.2.3 Definition of state \mathcal{A}	133
10.2.4 Parallelization and derived constraints	133
10.2.5 Setting the interfaces	134
10.2.6 A comment on correlations among trajectories	134
10.3 The setup for the diamond nucleation	134
10.3.1 The phase diagram	134
10.3.2 Identification of the ‘solid’ cluster	136
10.3.3 ‘Surface’ particles	141
10.3.4 Algorithm for ‘solidicity’ in summary	141
10.3.5 Choice of the box size: frozen nuclei analysis	142
10.3.6 Monte Carlo ‘time-step’	143
10.4 Results	144
10.4.1 Results at 85 GPa	144
10.5 Calculation of the free energy barrier via umbrella sampling	148
10.6 Summary and conclusions	149
10.7 Appendix. Classical nucleation theory	151
10.7.1 Free energy barrier	151
10.7.2 Equilibrium cluster distribution	153
11 The LCBOP II	155
11.1 Introduction	155
11.2 The LCBOP II	157
11.2.1 Switch functions	157
11.2.2 Short range potential	158
11.2.3 Long range potential	167
11.2.4 Middle range potential	167
11.3 Properties	169
11.3.1 Bulk equilibrium structures and elastic constants.	169
11.3.2 Diamond (111) and (001) reconstructed surfaces	170
11.3.3 Graphite to diamond transformation.	172
11.3.4 Vacancy in diamond and vacancy in graphite	173
11.3.5 The 5-77-5 defect of graphite.	174
11.4 Appendix. Detail of DF calculations	175
11.5 Appendix. Parameters for the LCBOP II	177
12 The LCBOP II: performance in the liquid	179
12.1 Introduction	179
12.2 Methods	180
12.3 Equation of state	182
12.3.1 Comparison	182
12.3.2 Predictions	183
12.4 Coordination	186

12.4.1	Comparison	186
12.4.2	Predictions	188
12.5	Radial distribution function	190
12.5.1	Comparison	190
12.5.2	Predictions	190
12.5.3	Partial radial distribution functions	193
12.6	Angular distribution function	196
12.6.1	Comparison	196
12.6.2	Predictions	197
12.7	Conclusions	201
13	Who is we?	203
14	Summary	204
15	Samenvatting	207
16	Synopsis	211
17	Acknowledgements	228

To the reader

Scope of this thesis is the study of liquid phosphorus and carbon, by means of computer experiments.

When we started working on this project, both these chemical elements were thought to exhibit a liquid – liquid phase transition at very high temperatures (i.e. thousands of kelvins) and pressures (i.e. several gigapascals). For phosphorus, it existed a strong experimental evidence of the liquid – liquid phase transition [1] at a temperature of ~ 1300 K and a pressure of ~ 1 GPa. For carbon, a full liquid – liquid phase transition coexistence line was identified in a computer experiment [2], using a semiempirical* potential [3, 4] that was known to be very reliable. The transition was found at temperatures ranging from ~ 5000 to ~ 9000 K and at pressures ranging from ~ 3 to ~ 11 GPa.

Due to the relative heterogeneity of the topics we faced and the methods we employed, each chapter starts with its own introduction, comprising all the references that were felt as relevant. The following lines should be intended as a quick reference map, about the content of this thesis.

The thesis opens (chapter 2) with a general view of the liquid – liquid phase transitions, as they are understood today. We point out that, contrary to transitions in solids that have been experimentally thoroughly investigated and theoretically well understood, liquid – liquid phase transitions are by far less studied and understood. This is due to the difficulty of their experimental investigations, for they are located at extreme pressures/temperatures, and/or are hindered by competing solidification. The model we adopt to introduce the world of liquid – liquid phase transitions is a combinations of models that have been proposed in the last forty years [5 – 10]; with this we aim to justify the different kinds of liquid – liquid phase transitions that are expected to occur in nature.

Chapters 4 (see also Ref. [11]) and 5 ([12]) are dedicated to liquid phosphorus and its transition. We studied this system with the aid of density functional based molecular dynamics, a method that has been of growing importance in these recent years. We will show that, confirming experiments, a molecular fluid[†], made exclusively of P_4 tetrahedral molecules, transforms upon increasing pressure or temperature into an atomic, network forming, liquid. These two chapters are introduced by chapter 3, in which we present the ab initio molecular dynamics scheme, worldwide known as Car-Parrinello molecular dynamics, we used for studying phosphorus (and, in part, carbon). We pay particular attention in explaining how constant temperature and constant pressure simulations are

*A semiempirical potential (see chapter 6) combines a theoretical analysis leading to its functional form, with an empirical fitting of its parameters.

[†]The system is indeed at temperatures higher than the gas/liquid critical temperature.

performed within Car-Parrinello molecular dynamics. The reader is assumed to be familiar with the (classical) molecular dynamics technique (see e.g. Ref. [13]).

The remaining chapters are devoted to carbon, in several aspects. The initial target regarding carbon was more ambitious than for phosphorus. Besides the study of the possible liquid – liquid phase transition, we wanted to shine some light into the whole phase diagram, at high temperatures and pressures, of this element. In fact, the study of the phase diagram of carbon has a long history (see chapter 7), but many of its features are far from being assessed (e.g. regarding the melting line of diamond, experiments can only predict its positive slope). Furthermore, the knowledge of the phase diagram was intended to serve as a basis knowledge for the study of nucleation of diamond from the melt. In order to fulfill all these goals, it was needed an interaction potential for carbon that could be computationally fast but still able to reproduce the flexibility of carbon bonding. Soon after the beginning of our project, a density functional based molecular dynamics study of liquid carbon [14] cast serious doubts on the possibility of the occurrence of a liquid – liquid phase transition, as described in Ref. [2]. In Ref. [14] it was shown that the semiempirical potential used in Ref. [2] was not able to properly describe the liquid phase of carbon; thus, for our purposes, we had to devise a more reliable potential. The starting point for this new potential was the one introduced by Los and Fasolino [15]. This potential, as well as the one used in Ref. [2], belongs to the class of *bond order* potentials[‡] and is called long range carbon bond order potential (LCBOPI). A small modification (see chapter 6) of this already extremely transferable[§] and accurate potential led us to the potential we called LCBOPI⁺. With the LCBOPI⁺ we a) studied the phase diagram of carbon, comprising graphite, diamond, and the liquid (chapter 8 and Ref. [16]), b) re-examined the issue of the liquid – liquid phase transition (chapter 9 and Refs. [17, 18]), and c) studied the mechanism and rate of nucleation of diamond from the melt in different state points (chapter 10 and [19]). The reader is assumed to be familiar with standard Metropolis Monte-Carlo techniques (see e.g. Ref. [13]).

The thesis ends with the description (chapter 11 and [20]) and validation in the liquid phase (chapter 12 and [21]) of a further improvement of the LCBOPI⁺. The result is called LCBOPII. Far from being a purely academical *divertissement*, the improvement was suggested by some small, and in first instance neglected, inaccuracies of the potential in the description of the liquid phase. Finding a proper way to cope with those inaccuracies, required a re-thinking of many of the characteristics of a bond order potential and the introduction of new, hopefully seminal, features.

[‡]The functional form of these potentials reproduces the strength, or *order*, of a bond, by analyzing the environment in which the bond, i.e. the pair of atom defining the bond, is found (see chapter 6).

[§]The transferability of a potential refers to its capability of yielding a good description of the energy landscape for any possible realistic atomic configuration.

Liquid – liquid transitions in simple fluids

*There are more things in Heaven and Earth, Horatio,
Than are dreamt of in your philosophy.*

In solids, phase transitions are well-known and well-understood phenomena both at normal conditions and at high pressures. The variety of transition types can be classified by thermodynamics (1st, 2nd order, λ -points) and kinetic characteristics (martensitic, diffusion). The transitions can be structural, i.e. taking place with changes in the crystalline lattice in a subsystem of atoms, spins, dipoles ... or they can be of electronic nature (a change in electronic state that does not influence the lattice symmetry). A transformation can be caused by a variation of external parameters (pressure, temperature, magnetic or electric fields) or by direct external influence (irradiation, ion implantation, plastic deformations).

In contrast to crystals, no strong, consistent theory for the liquid phase has been created, yet. Phase transitions in disordered systems, such as liquids, are not well-understood. The liquid – liquid phase transition (LLPT) is not even widely accepted as a phenomenon, due to its counterintuitive nature and to experimental difficulties in the validation: the candidate transitions either occur at extreme pressure and/or temperature or appear in metastable regions (e.g. are hidden by competing solidification).

The main part of this chapter is dedicated to the illustration of a simple and general statistical mechanics model, accounting for a first order transition between disordered phases. Subsequently we will summarize the speculated LLPT in water. At the end of the chapter we will review two simple model potentials, proposed in the last years, specifically designed for producing a LLPT: the purpose is to show which mechanisms are thought to be necessary conditions for the occurrence of a LLPT.

2.1 A simple model

A number of similar models to describe liquid – liquid phase transitions have been proposed in the past years [5, 6, 7, 8, 9, 10]. We will here sketch a model, based on the notation of the “two state model with cooperativity” of Ref. [10], that unifies all those cited. Following [10] the unifying characteristic of LLPTs is that *the formation of local structures*

(i.e. of a middle range ordering) is a universal feature in liquid. The proper understanding of a phenomenon starts with the identification of the relevant order parameters prone to describe it. In the usual picture of a liquid, only one order parameter is widely used, the density ρ that, for instance, perfectly describes the gas/liquid phase transition. From a different point of view, the interactions even in a simple liquid can always be thought as constituted by an isotropic part, that would always prefer close packing, and a directional, covalent part that would favour locally ordered structures, depending on the bonding capabilities of the material. Such a picture is supported by the observation of local ordering via diffraction experiments on covalent fluids [22]: the structure factor of covalent elements in the liquid state can depart noticeably from the “simple liquid” behaviour, especially near freezing, favouring low coordinated, non close packed, structures. While ρ easily accounts for the properties of the isotropic interactions, the covalent interactions need to be described by an order parameter that can identify local ordering. More than one of such local ordering parameters would be needed when the material has more than one bonding possibility. An example would be carbon, that can choose between a linear sp , a planar sp_2 and a tetrahedral sp_3 bonding configuration. Without losing generality, the local ordering parameters can be reduced to one, that will be labelled here on with s , without precise characterization. The model assumes that:

- there exist locally ordered structures (a property that can be called “middle range ordering”);
- such structures are cooperatively elicited in a sea of a disordered background (the normal-liquid structure).

The state characterized by normal-liquid structures is labelled with the subscript ρ , the state of locally ordered structures, is S ; the ‘pure’ ρ and S states are described by the following properties: g_S and g_ρ are the degeneracies of their energies, E_S and E_ρ ; v_S and v_ρ are their specific volumes. The ordering parameter acts as a coordinate s , labelling the continuous variation of the system from the ρ state ($s = 0$) to the S state ($s = 1$): in other words s is the concentration of locally ordered structure in the liquid.

It is assumed that there is one locally ordered structure, but many normal-liquid structures: this implies loss of entropy going from ρ to S , i.e. $\Delta\sigma = k_B \ln(g_\rho/g_S) > 0$. The entropy as a function of s , the fraction of the system in the S state, is:

$$\sigma(s) = -k_B \left[s \ln \frac{s}{g_S} + (1-s) \ln \frac{1-s}{g_\rho} \right] \quad (2.1)$$

Without cooperative effects (coupling) between the states, the total configurational energy is just a linear combination of the pure states energies:

$$U = sE_S + (1-s)E_\rho \quad (2.2)$$

The cooperation is then introduced as a frustration, i.e. as a second order upward correction to the total energy:

$$U = sE_S + (1-s)E_\rho + Js(1-s) \quad (2.3)$$

The coupling parameter J is intrinsically positive because of frustration: the neighbouring of alike structures is more favoured than the vicinity of different structures*. In the

*It can be shown [23] that this expression for the total energy comes from the assumption (called *zerth order approximation* in binary mixtures theory) that the distribution of the two kinds of molecules is

following we show that the value of J , i.e. the strength of the coupling between the two states, plays the central role in determining the possibility of a first order phase transition.

The chemical potential of the “mixture” is:

$$\begin{aligned}\mu(s) &= U - T\sigma + [sv_S + (1-s)v_\rho]P \\ &= sE_S + (1-s)E_\rho + [sv_S + (1-s)v_\rho]P + \\ &+ k_B T \left[s \ln \frac{s}{g_S} + (1-s) \ln \frac{1-s}{g_\rho} \right] + Js(1-s)\end{aligned}\quad (2.4)$$

where T is the temperature and P the pressure. This is not a true binary mixture, since s is not conserved. It is sometimes referred to as a *pseudo-binary mixture*[†]. The equilibrium value for s is given by: $\partial\mu(s)/\partial s = 0$. From Eq. 2.4:

$$\beta[-\Delta E - \Delta v P + J(1-2s)] + \ln \frac{g_\rho s}{g_S(1-s)} = 0 \quad (2.5)$$

where $\Delta E = E_\rho - E_S > 0$, $\Delta v = v_\rho - v_S$, and $\beta = 1/k_B T$. A critical point is readily devised imposing $\mu'_s(s_c) = 0$, $\mu''_s(s_c) = 0$, $\mu^{(3)}_s(s_c) = 0$ and $\mu^{(4)}_s(s_c) > 0$:

$$s_c = \frac{1}{2} \quad (2.6)$$

$$T_c = \frac{J}{2k_B} \quad (2.7)$$

$$P_c = \frac{T_c \Delta\sigma - \Delta E}{\Delta v} \quad (2.8)$$

A first order phase transition occurs at a temperature $T_t < T_c$. Defining $\Delta\mu^0$ in the spirit of the theory of mixtures, as the difference of the chemical potentials of the “pure species”, the equilibrium condition (Eq. 2.5) reads:

$$\begin{aligned}\beta\Delta\mu^0 &\doteq \beta(\mu(0) - \mu(1)) = \beta(\Delta E + P\Delta v) - \frac{\Delta\sigma}{k_B} \\ &= \beta J(1-2s) + \ln \frac{s}{1-s}\end{aligned}\quad (2.9)$$

It is instructive to study the behaviour of $\beta\Delta\mu^0$ as a function of the only order parameter s , with βJ acting as a parameter. Figure 2.1 shows the family of curves $\beta\Delta\mu^0$ at different values of βJ . At a fixed temperature, the value of $\beta\Delta\mu^0$ is governed by the pressure, since ΔE , Δv , and $\Delta\sigma$ in this model are assumed to be intrinsic properties of the system, i.e. not influenced by external parameters. The plot displays in a pictorial way what

completely random, in spite of the non-zero energy of mixing (as denounced by the non-zero coupling term J).

[†]The *pseudo-binary mixture* model is equivalent to the *two-level* model of Kittel [6]. In that model, the local ordered liquid is in the energetic ground state, while the normal liquid has an excitation energy ϵ ; the meanings of the degeneracies g_1 and g_2 are the same as the above g_S and g_ρ . The energy in the non-interacting limit is written as $U = (1-s)N\epsilon$; the energy of the system with two interacting levels, following the molecular field approximation, is corrected to $U = N((1-s)\epsilon - (1-s)^2\gamma)$, with $\gamma > 0$. The two models are equivalent when $E_S = 0$ in Eq. 2.3 and $U = N((1-s)\epsilon - (1-s)^2\gamma) = (1-s)E_\rho + Js(1-s)$.

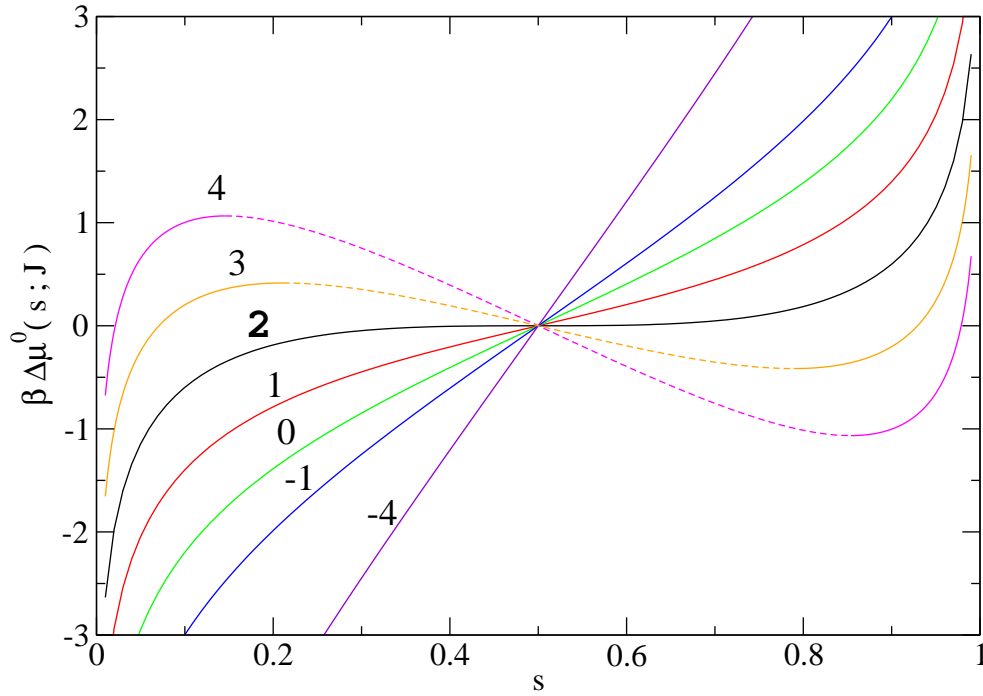


Figure 2.1: Parametric plot of $\beta\Delta\mu^0(s; J)$. The curves are labelled by the value of βJ . The value $\beta J = 2$, in bold, is the critical value for the appearance of two maxima in the curves. The dashed intervals of curves with $\beta J > 2$ are mechanically unstable (see footnote §).

is already written in Eq. 2.7: 2 is a critical value[‡] for βJ . In fact, $\beta\Delta\mu^0(s; J)$ has two maxima at $\bar{s}_{1,2} = 1/2 \pm 1/2 \sqrt{1 - 2/(\beta J)}$; they are real for $\beta J \geq 2$. When $\beta J < 2$ (i.e. for temperatures $T > T_c$), there is an equilibrium value s for any T and P . When $\beta J > 2$ (i.e. for temperatures $T < T_c$), there is an interval in P inside which the equilibrium condition is valid at two[§] different values of s : the system chooses the lowest in chemical potential $\mu(s)$. There will exist an infinitesimal interval in P in which the system will “jump” between

[‡]Eq. 2.4 for (*pseudo*)binary mixtures is valid for *regular* solutions and is referred to as Bragg-Williams approximation [23]. In its original paper, Rapoport [5] gives also the derivation of the critical value of J for a more realistic model, the Bethe-Guggenheim quasi-chemical approximation [23], finding the rather close value of 2.188. This is the model on which the analysis on Cesium [24] and Tellurium [25] was carried out (*vide infra*).

[§] A third intersection is in the negative slope part of the curve, thus in a mechanically unstable region for the liquid. This is easily proven by writing:

$$\left. \frac{\partial \Delta\mu^0(s; J)}{\partial s} \right|_T = \left. \frac{\partial \Delta\mu^0(s; J)}{\partial P} \right|_T \left. \frac{\partial P}{\partial v} \right|_T \left. \frac{\partial v}{\partial s} \right|_T$$

The first partial derivative in the chain is evaluated from Eq. 2.9, while the third can be calculated by writing: $v(s) = v_\rho + s(v_S - v_\rho) = v_\rho - s\Delta v$. Working out:

$$\left. \frac{\partial \Delta\mu^0(s; J)}{\partial s} \right|_T = (\Delta v) \frac{\partial P}{\partial v} (-\Delta v) = \frac{(\Delta v)^2}{v} K_T$$

where K_T is the isothermal bulk modulus, that, for mechanical stability, ought to be positive. Being all the quantities at the right hand side of the above equation positive, when $\partial \Delta\mu^0(s; J)/\partial s < 0$, the system is mechanically unstable.

two different values of s . In the expression of $\bar{s}_{1,2}$, we note that, upon increasing βJ , the values of $\bar{s}_{1,2}$ approach $\bar{s}_{1,2} = 0, 1$, respectively. Thus, for large values of βJ , the system is stable only in the proximity of the pure states. In contrast, for moderate values of βJ (but still larger than 2), states with a value of s significantly different from 0 and 1, are stable. Thus, the occurrence of the LLPT *does not* imply that the system transforms from a pure ρ state into a pure S state.

Note that, even when $\beta J < 2$, there exists a rather narrow interval in pressures in which s changes very quickly.

Depending on the values assumed by J , the critical temperature T_c of the LLPT can be above or below the melting line(s) of the underlying crystal(s). Furthermore, the set ΔE , Δv , and $\Delta\sigma$ can yield either a positive or a negative critical pressure P_c . Different regimes are then identified.

- $P_c < 0$. The position of T_c determines the two different regimes:
 - When T_c is higher than the melting temperature of the underlying crystal, a first order LLPT exists in the stable liquid state (see Fig. 2.2). Note that such a transition can be responsible for an abrupt change of slope in the melting line of the underlying crystal. The slope of the coexistence line of a first order phase transition (i.e. both the melting transition and the LLPT) is given by the Clausius-Clapeyron equation[¶]. The presence of a first order LLPT implies a coexistence line between the two liquids; in the LLPT model we have depicted, the coexisting liquids have two different densities. When the LLPT coexistence line meets the melting line of the crystal, two liquids with an infinitesimal difference in pressure (and temperature) and coexisting with the solid phase have two different densities; thus, the Clausius-Clapeyron equation, applied to the two segments of melting line coexisting with the two liquids, implies that the slope of the two segments are different in an infinitesimal range of pressures. Were one of the liquids denser than the solid phase, the melting line would abruptly invert its slope. The two segments of the melting line and the LLPT coexistence line meet in a triple point.
 - When T_c is lower than the melting temperature of the underlying crystal, the LLPT would be completely hidden in the solid stable state (see Fig. 2.3, left hand panel). Water is a candidate to fit into this regime (see section 2.2). The critical point and the LLPT coexistence line might be difficult or impossible to probe experimentally, but still can be evidenced by anomalous behaviour of thermodynamic quantities in the accessible region (this is exactly the case of water). A slightly different, speculative, possibility is shown in Fig. 2.4, where the LLPT coexisting line starts from a maximum in the prolongation of the (metastable) melting line of the lower pressure solid, into the region of stability of the higher density solid. This could be the case of every melting line that encounters a solid/solid/liquid triple point, before reaching a maximum (see chapter 8). The slope of the LLPT coexistence line needs not to be positive. In case it is negative, the line could re-enter the stable liquid region, thus ending

[¶]It reads: $dT/dP = \Delta v/\Delta s$, where Δs is the difference in specific entropies between the coexisting phases.

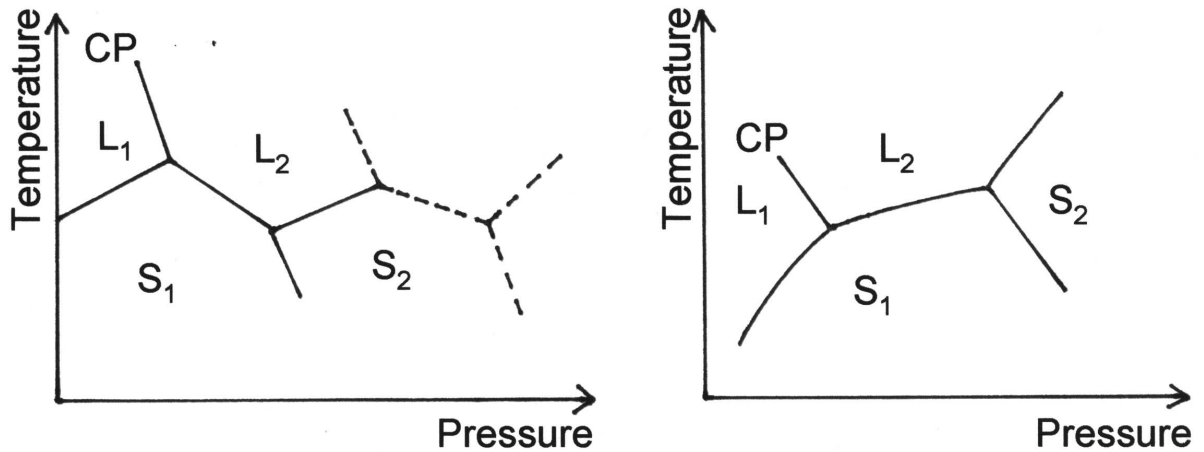


Figure 2.2: Schematic phase diagrams for LLPTs, in the case in which the critical temperature is above the melting line of the underlying solid. The symbols S_i , with integer i , label the solid states, L_i indicate the liquids, CP the critical point. In the left panel we show the case in which the triple point L_i - L_{i+1} - S_i , induces a change of slope in the melting line of S_i . Dashed in this panel is a possible further LLPT, in correspondence with a maximum in a higher pressure stable solid (also the further boundaries of the solid phase are dashed). In principle there could be a LLPT for each possible maximum in each stable solid phase of a given substance. In the right panel it is shown a situation in which the inversion in slope is not needed for a first order LLPT: a discontinuity in slope is a sufficient condition.

in a CP in this stable liquid region, and causing a discontinuity in the slope of the melting line of S_2

- $P_c < 0$. If T_c puts the critical point above the crystal melting line, a portion of the LLPT coexistence line can still be in the positive pressure region and in the stable liquid region: the LLPT coexistence line would be still experimentally accessible. Anyway, even if T_c were in the stable crystal temperature range (see Fig. 2.3, right hand panel), traces of the hidden transition could be seen at low pressures by enhanced fluctuations of the order parameter s , similarly to the case illustrated in the left panel of Fig. 2.3. This means that locally ordered structures could rapidly form and disappear, a possibility that would reflect in density fluctuations with huge correlation length. The phenomenon of an excess light scattering at wave number $q = 0$ in glassy polymers, implied by anomalously long correlation lengths, has indeed been observed originally by Debye and Bueche [26] in 1949: today it is known as ‘Fisher clusters’ [27] by the name of the researcher that systematically studied it. The appearance of transient structures accompanied by anomalously high density fluctuations, thus possibly related to a unaccessible critical point, has also been observed in protein solutions [28].

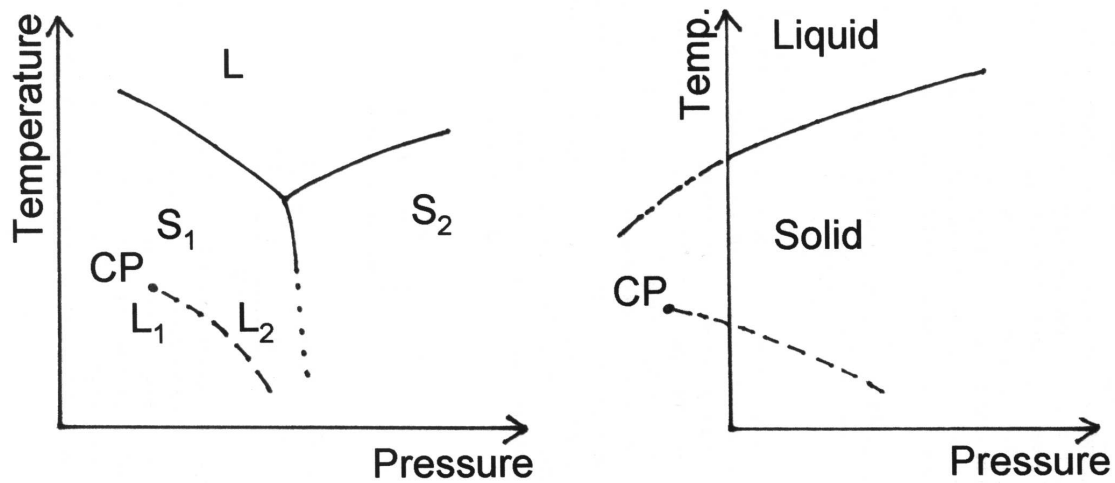


Figure 2.3: Schematic phase diagram for a LLPT in which the critical point is in the stable region of the underlying solid. The symbols S_i , with integer i , label the solid states, L_i indicate the liquids, CP the critical point.

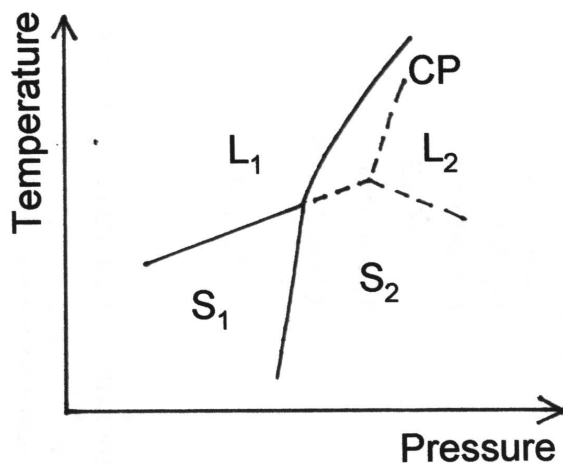


Figure 2.4: Schematic phase diagram for a LLPT in which the critical point is in the stable region of the underlying solid. The symbols S_i , with integer i , label the solid states, L_i indicate the liquids, CP the critical point. The peculiarity here depicted is that the LLPT coexistence line starts from a maximum in the prolongation of the (metastable) melting line of S_1 into the stable region of S_2 .

Application to Cesium and Tellurium

In his analysis of the liquid structure of Cesium, Rapoport [24] could estimate the value of J introducing further assumptions. Cesium is a unique material because it has two melting line maxima in its $P - T$ phase diagram at pressures below 4 GPa. In this range there are two solid phases, a bcc and an fcc crystal. A rather steep change in electrical resistivity in the liquid was experimentally observed at the temperature of 493 K and near the maximum of the melting line of the fcc crystal [29]: consistently Rapoport argues the existence of

two liquids, L' and L". Under reasonable assumptions on the electrical resistivity and the specific volume of the liquid mixture as a function of the electrical resistivities and the specific volumes of the two pure liquids and the fcc crystal, Rapoport could estimate $\beta J \cong 1.5$. This implies a critical temperature $T_c \cong 367$ K, that is in the fcc crystal stable region. In fact [24] the change in concentration of L", as a function of P , is steep but not discontinuous. Note that the concentration of L" was not measured, but calculated.

A similar analysis was carried out [25] for liquid Tellurium, finding indeed a near critical value of βJ at 737 K and 0.43 GPa. In the Tellurium melting line was indeed seen a discontinuity in the slope, but not an inversion, being also the denser liquid lighter than the underlying crystal.

Other elements and compounds

The list of substances for which a LLPT has been at least argued is quite long. We will focus in the next section on the interesting case of water: besides carbon and phosphorus, object of this thesis, we will confine all the other cases in the following list. Amongst pure substances, there have been experimental and/or computer simulation evidences of pressure induced transitions in rather narrow pressure-temperature intervals for As [30], Bi [31], Ge [32], Hg [33], S [34], Sb [35], Se [36], Si [37, 38], Sn [39], H₂ [40], I₂ [41]. Besides water, two other network forming fluids ^{||}, SiO₂ [43] and GeO₂ [44], might show a LLPT.

2.2 Water

According to Stanley *et al.* [45], water exhibits a space-filling hydrogen bonded network, as expected from continuum models. However, when focusing on the “well-bonded” molecules, it is found that water can be regarded as having certain clustering features - the clusters being not isolated icebergs in a sea of dissociated liquid, but rather patches of well-bonded molecules** embedded in a highly connected network, or “gel”. Water exhibits some mysterious properties. For example, it has been recognized as long as 300 years ago that water has a maximum density at 4° C and atmospheric pressure. Furthermore, at atmospheric pressure and temperatures of 46, and 20° C [46] water has a minimum isothermal compressibility and shear viscosity, respectively. Fig. 2.5 [47] shows a phase diagram of water, focused on the region below the melting line where, rather than the stable ices, the (mostly hypothesized) boundaries of the metastable glasses and undercooled liquids are shown. Below T_H , no matter how slowly it is cooled down, water crystallizes via homogeneous nucleation. Upon quenching at low pressure, water transforms into a low density amorphous (LDa) below T_X [48]. In 1984 it was discovered [49] also a high density amorphous (HDa) obtained by quenching at pressure above 200 MPa down below T_X . Upon heating, both amorphous phases crystallize into ice above T_X . The region comprised between $T_H(P)$ and

^{||}According to Roberts *et al.* [42] network-forming fluids are “fluids which form orientation-specific, intermolecular bonds which are strong relative to London (dispersion) forces. For the canonical network-forming fluids such as water and silica, the formation of bonds (e.g., hydrogen bonds in water) induces low-density structures in the liquid which increase in lifetime and size as the liquid is cooled”.

**Well-bonded water molecules in the water network have four bonds arranged in a tetrahedral configuration. Two bonds are the covalent O–H bonds, whereas the other two are O···H hydrogen bonds with neighbouring molecules.

$T_X(P)$ is known as “No man’s land”, since it is impossible to have there a phase other than ice, in an experiment. Soon later, Mishima *et al.* [50] proved that one can transform reversibly LDa into HDa; the transition, characterized by a 20% density change, is supposed to be first order (the coexistence line is the thick dashed line of Fig. 2.5). If the coefficient of thermal expansion, the isothermal compressibility, and the constant-pressure specific heat are extrapolated below the minimum temperature at which these properties can be measured (-38°C , see Fig. 2.5), they appear to diverge at the (unreachable) temperature of -45°C . Putting this observations together, a possible physical explanation would involve a LLPT with a coexistence line (tiny dashed line in Fig. 2.5) ending in a critical point (C_2), all hidden in the “No man’s land” region.

Molecular dynamics simulations with empirical potentials seem to support this hypothesis [51, 52, 53, 54, 55, 56]. Given the small samples and the short probing times of molecular dynamics, homogeneous nucleation is in fact rarely seen; in this way complete $P(\rho)$ isotherms in the experimentally forbidden region were calculated: they evidenced ‘kinks’ at temperatures below T_{C_2} . This finding, together with the analysis of the structure of the liquid in proximity of a kink, strongly suggests that “computer water” shows a LLPT. It is interesting to report the hypothesis that Mishima and Stanley [57] make for the existence of a second critical point (being the first, C_1 , the usual point ending the boiling line). Since the existence of a (pairwise) interaction potential with a minimum is sufficient to yield a (liquid/vapour) critical point, then a (pairwise) interaction potential with two minima might imply two critical points. In Fig. 2.7 is reported such an interaction potential; the approximation of this potential with a square-well one will be discussed in the next section. The argument is the following: when the temperature is below a critical one, the liquid is forced to ‘condense’ into one of the two sub-wells, depending on the pressure of the system (into the outer sub-well at low enough pressures and into the inner sub-well for high enough pressures). On the other hand, at high enough temperatures (i.e. above the critical one), the system should be able to sample both sub-wells. Mishima and Stanley also propose the identification of two possible clusters in the hydrogen bond network, whose (averaged) pair interactions would yield the potential with two minima. In Fig. 2.6 (taken from Ref [57]) are shown the two relative orientations of the well-bonded (tetrahedral) water clusters, that would yield a local minimum in the interaction energy.

In conclusion, the possibility of a LLPT in undercooled water appears as a well-posed and consistent hypothesis that can explain most of the anomalous behaviours, if not all, of this liquid; it is nonetheless not easy to prove, if not outright impossible, and it competes with other well-posed hypotheses [57].

2.3 Two simple potentials

Recently, two simple, isotropical, model potentials [47, 59], able to show LLPTs in a computer simulation, have been designed.

Soft-core, double-step potential

This interaction potential has been thought by Franzese *et al.* [47, 58] to model the anomalous properties of water, mentioned in the previous section. Following the hypothesis of Mishima and Stanley [57], Franzese *et al.* constructed a potential with an attractive part

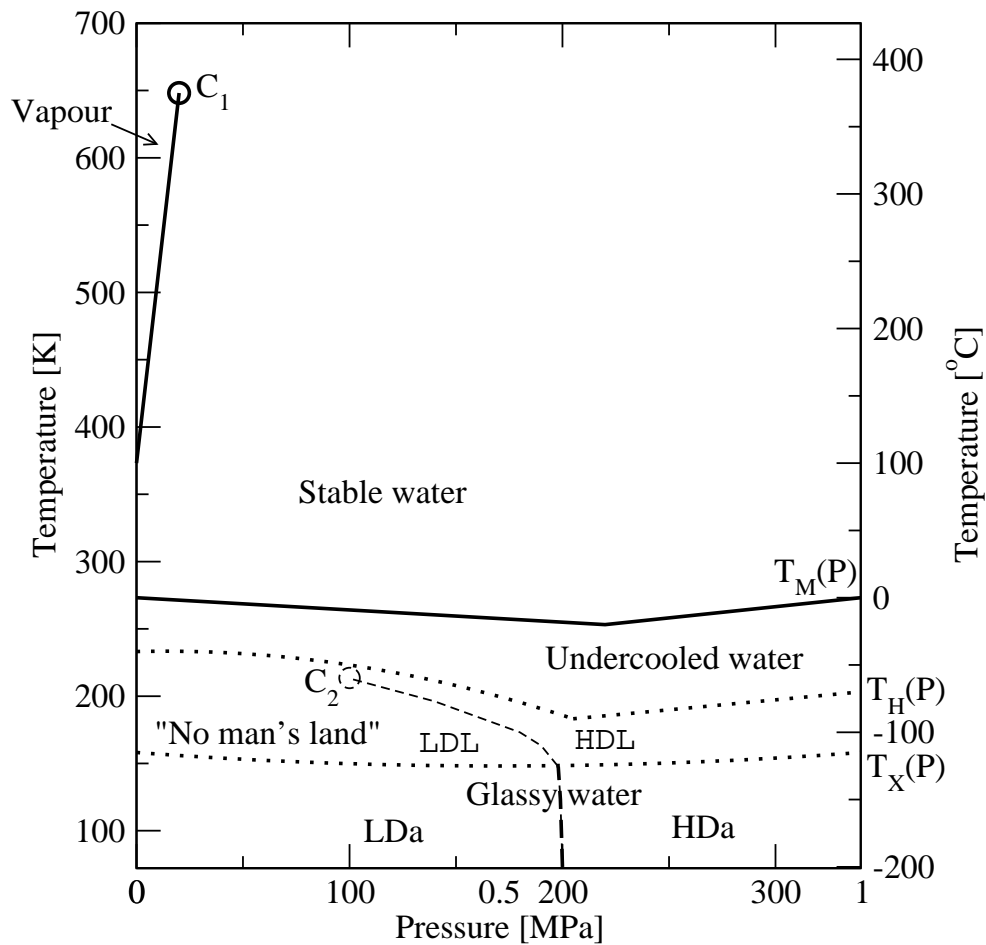
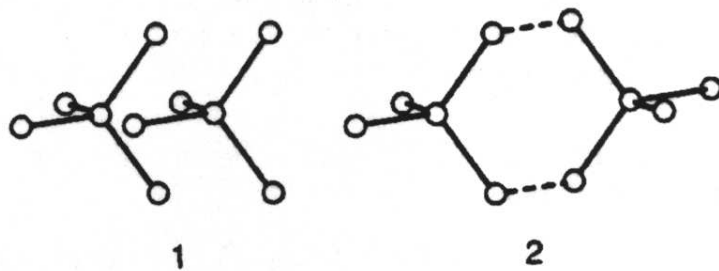


Figure 2.5: Phase diagram for water comprising the vapour, the stable liquid, the high density and low density amorphous solids, and the probable position of the low density - high density liquid (LDL and HDL) coexistence line, ending in a second critical point, C_2 . In region below the (solid) melting line, Ice-I is the stable phase (up to the pressure of the minimum in the line): thus all the phases referred in the plot are there metastable. Upon quenching below T_X glassy water is obtained, in its two forms, high density amorphous (HDa) and low density amorphous (LDa). Even at the slowest heating rate one can achieve experimentally, when heating the glass above T_X , the system rapidly crystallizes into ice. When undercooling water below T_H , homogeneous nucleation of ice rapidly occurs. The region between the two dotted lines is the so called “No man’s land”, since it cannot be reached in experiments.

Figure 2.6: The two (local) minimum energy relative orientations of water clusters, according to Mishima and Stanley [57].



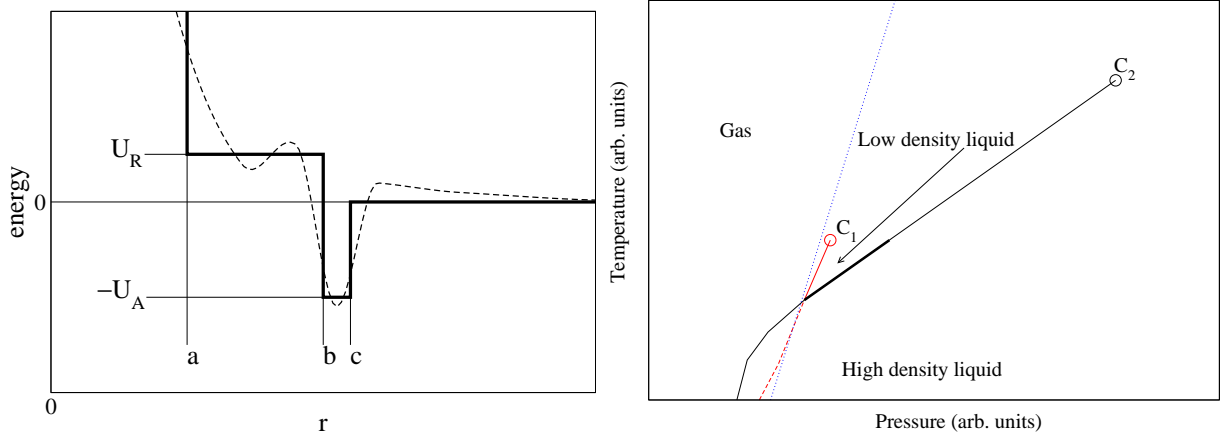
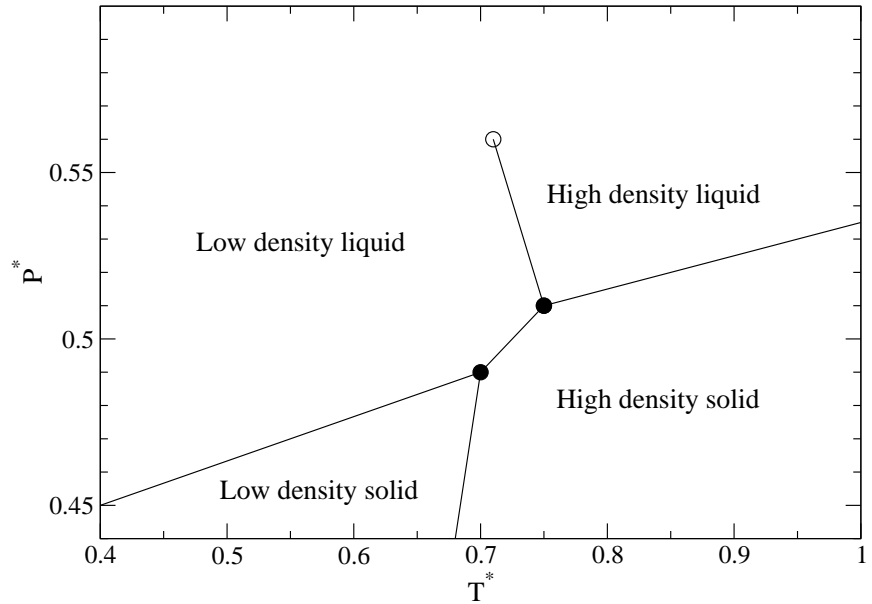


Figure 2.7: Left panel: double-square-well potential from Ref. [47, 58]. The dashed line has the shape of the (smooth) potential with two minima hypothesized by Mishima and Stanley [57]. Right panel: Pressure-Temperature phase diagram [47, 58] for the double-step potential shown in the left panel. The solid line ending in the critical point C_2 is, at low temperature, the HDL-gas coexistence; it thickens at intermediate temperatures to a liquid – liquid coexistence and then thins back at higher temperatures to a HDL-fluid coexistence. The dashed line is the (metastable) LDL-gas coexistence; it prolongs into the (solid) LDL-gas coexistence line ending in the critical point C_1 . The dotted line is the deduced melting line.

and two characteristic short-range repulsive distances, the shorter representing the hard core and the longer the soft core of the simulated species. More precisely (see Fig. 2.7), the potential consists of a hard core of radius a with a repulsive square shoulder of height $U_R > 0$ and radius $b > a$, plus an attractive component having the shape of a square well of depth $-U_A < 0$ extending from $r = b$ to $r = c$. If the hard-core radius is chosen as the length unit and the well depth as the unit of energy, there are three free parameters: b/a , c/a and U_R/U_A . With a suitable choice of the parameters ($b/a = 2.0$, $c/a = 2.2$, and $U_R/U_A = 0.5$, i.e. the situation shown in Fig. 2.7) the potential reproduces the above mentioned anomalies. In fact, according to Franzese *et al.*, at sufficiently low pressures and temperatures, nearest-neighbour pairs are separated by a soft-core distance $r \approx b$ to minimize the energy. As temperature increases, the system explores a larger portion of the configurational space in order to gain more entropy. This includes the penetration of particles into the softened core, which can cause an anomalous contraction upon heating. The resulting $P - T$ phase diagram is shown in Fig. 2.7. The solid line ending in the critical point (C_2) is, at low temperature, the HDL-gas coexistence. The dashed line is the (metastable) LDL-gas coexistence. When these two lines meet in a HDL-LDL-gas triple point, the dashed line becomes, at temperatures above the triple point, the LDL boiling line, ending in the critical point C_1 . The HDL boiling line becomes the liquid – liquid coexistence line (thick solid line), then, at temperatures above the critical point C_1 , it transforms into the HDL-fluid coexistence line. The fluid above C_1 can be thought as a dense gas containing some local structures of the LDL liquid (i. e. the structures dictated by the absolute minimum of the potential). The dotted line is the melting line of the underlying solid: it is not shown in the P-T diagram published in [47, 58], but deduced by us from the pressure-density diagrams reported there. The melting line reveals that both

Figure 2.8: Phase diagram of the Lennard-Jones liquid with spin (for $\sigma_u = 0.5\sigma_l$, see text for these symbols), as reported in Ref [59]. The reduced temperature (T^*) and pressure (P^*) are the usual reduced units for the Lennard-Jones liquid (i.e. $T^* = k_B T/\epsilon$ and $P^* = P\sigma^3/\epsilon$).



critical points (C_1 and C_2) are in the stable region of the solid.

According to Franzese *et al.*, when the attractive well width ($(c - b)/a$) exceeds 0.7, C_1 goes into the stable fluid phase. By decreasing the relative width of the attractive shoulder, b/a , or by increasing its height U_R/U_A , the temperature of C_2 , T_{C_2} , decreases until it becomes lower than T_{C_1} . When both these features occur, the resulting phase diagram would be topologically equivalent to the one hypothesized for water (Fig. 2.5). If there were a set of parameters such that $T_{C_2} > T_{C_1}$ and both were in the stable phase of the fluid, the resulting phase diagram would be topologically equivalent to the one found for phosphorus.

Lennard-Jones liquid with spin

Another ad-hoc interaction potential, proposed by Lee and Swedensen [59], defined two liquid species A and B , or “spin-up” and “spin-down”. The interactions $A - A$ and $B - B$ are described by identical 12-6 Lennard-Jones potentials, with parameters ϵ and σ_l . The interaction $A - B$ are described by the repulsive (proportional to r^{-12}) part of a Lennard-Jones potential, with parameters ϵ and σ_u . Furthermore, in connection with the “two species model”, an atom of species A can randomly flip into an atom of species B , and viceversa, according to Boltzmann statistics.

When $\sigma_u < \sigma_l$, Lee and Swedensen, performing 2D simulations, show the existence of two solid phases and two liquid phases, as reported in Fig. 2.8. The low density liquid has coordination six with preferred neighbouring of atoms of the same species (parallel spin ordering). The high density liquid has coordination three and preferred antiparallel spin ordering, so that the average first neighbour distances are smaller in this second case. Similarly, the high density solid has a perfect antiparallel ordering (with coordination three), while the low density liquid is only of one species, in an hexagonal lattice. The LLPT is strongly first order.

Ab initio molecular dynamics

We are all in the gutter, but some of us are looking at the stars.

In this chapter we will describe Density Functional based Car-Parrinello Molecular Dynamics technique. We used this technique to investigate the LLPT in phosphorus (see chapters 4 and 5). For the investigation of the LLPT in carbon the CPMD method was used in two respects: a) to validate the findings of the semi-empirical potential used for the phase diagram calculation (LCBOPI⁺, see chapter 8), b) to generate data to be fitted for the improved version of the semi-empirical potential (LCBOPII, see chapters 11 and 12).

In section 3.1 we will focus on the justification of the CPMD method from quantum mechanics considerations. In section 3.2 the density functional theory for electronic system will be introduced, in a way already targeted to its implementation into the CPMD framework.

In section 3.3 we will illustrate the two related techniques adopted in the particular implementation of the CPMD method we used [60]: the plane wave expansion of the electronic wavefunction, and the pseudo-potential method to restrict the electronic degrees of freedom to the valence (i.e. chemically “active”) states.

In section 3.4 we will discuss the implementation of thermostats into the CPMD method. These were required since all the simulations in the liquids (both carbon and phosphorus) were carried out at constant temperature. Furthermore, the high density liquid phase of phosphorus and liquid carbon were found to be metallic: this requires a special thermostat.

For the LLPT investigation in liquid phosphorus, that is accompanied by a density change at a given pressure, the use of constant pressure MD was necessary. Section 3.5 is devoted to the discussion of this method, with particular attention to its implementation in CPMD.

3.1 Car-Parrinello molecular dynamics

Classical molecular dynamics can be derived from quantum mechanics. The standard Hamiltonian can be written as a sum of the kinetic energy of the nuclei and a term comprising all the electronic contributions:

$$\mathcal{H} = T_{\text{nuclei}} + \mathcal{H}_e \tag{3.1}$$

The total wavefunction $\Phi(\{\mathbf{r}_i\},\{\mathbf{r}_I\};t)$, solution of the time-dependent (non-relativistic) Schrödinger equation

$$i\hbar\frac{\partial}{\partial t}\Phi(\{\mathbf{r}_i\},\{\mathbf{r}_I\};t) = \mathcal{H}\Phi(\{\mathbf{r}_i\},\{\mathbf{r}_I\};t) \quad (3.2)$$

where i labels the electronic and I the nuclear degrees of freedom, needs to be factorized into its electronic and nuclear part.

Treating the nuclei as classical point particles, there are two approaches that justify classical molecular dynamics. The first is the so called Ehrenfest dynamics, whose equations of motion, with the electronic wavefunction in its ground state (Ψ_0), read:

$$\begin{aligned} M_I\ddot{\mathbf{r}}_I(t) &= -\nabla_I\langle\Psi_0|\mathcal{H}_e|\Psi_0\rangle \\ i\hbar\frac{\partial}{\partial t}\Psi_0 &= \mathcal{H}_e\Psi_0 \end{aligned} \quad (3.3)$$

In this ‘‘on-the-fly’’ approach, nuclei move under forces obtained by the expectation values of an electronic hamiltonian. The electronic wavefunction, that enters the expectation value evaluations, is propagated via the time dependent Schrödinger equation of the electronic subsystem. In this way, the electronic wavefunction has to be minimized once for all at the initial step, and the propagation is intrinsically unitary (i.e. the wavefunction preserves its norm and the set of orbitals used to build the wavefunction up remain orthonormal).

The second approach is the Born-Oppenheimer (BO) dynamics; in this case, in the electronic ground state, the equations of motion are:

$$\begin{aligned} M_I\ddot{\mathbf{r}}_I(t) &= -\nabla_I\min_{\Psi_0}\{\langle\Psi_0|\mathcal{H}_e|\Psi_0\rangle\} \\ \mathcal{H}_e\Psi_0 &= E_0\Psi_0 \end{aligned} \quad (3.4)$$

This means that a static electronic structure problem, at a given position of the nuclei, gives the (expectation value of the) potential energy whose gradient yields the forces that propagate the nuclei, via classical (newtonian) dynamics. In this formulation the electronic wavefunction is always in its ground state and the time dependence of the electronic structure is a consequence of the motion of the nuclei. BO dynamics relies, for the electronic ground state calculation, on any method that is expressed through a variational formulation, as is the case for the Hartree-Fock approximation [61] and the density functional theory (see next section).

In Ehrenfest dynamics the time-scale (and thus the integration time step) is dictated by the intrinsic (fast) dynamics of the electrons. On the other hand, the time scale of the BO dynamics is dictated by the nuclear motion, since there is no electron dynamics. However, at each time step, a computationally quite expensive determination of the wavefunction minimizing $\langle\mathcal{H}_e\rangle$ has to be carried out. An improvement of both methods should allow the integration of the equation of motion on a time scale set by the nuclear motion, but nevertheless the electronic subsystem should be dynamically propagated, taking advantage of the smoothness of its time evolution. The Car-Parrinello method is indeed such an improvement [62].

Now, within a variational formulation, consider the energy of the electronic subsystem to be dependent on the nuclear positions and the electronic wavefunction Ψ_0 . If Ψ_0 is expressed by means of a set of one-electron orbitals $\{\psi_i\}$, as in Hartree-Fock or density

functional theory, then the energy of the electronic subsystem is a functional of $\{\psi_i\}$. In classical mechanics the forces governing the dynamics of the nuclei are obtained from the derivative of the Lagrangian of the system with respect to the nuclear positions. In the same way, a functional derivative of a suitable Lagrangian, with respect to the atomic orbitals interpreted as classical fields, could give the forces on the orbitals. Adding constraints (that are readily treated in the Lagrangian formalism) for the set of orbitals, Car and Parrinello [62] postulates the following Lagrangian:

$$\mathcal{L}_{CP} = \underbrace{\sum_I \frac{1}{2} M_I \dot{\mathbf{r}}_I^2 + \sum_i \frac{1}{2} \mu_i \langle \dot{\psi}_i | \dot{\psi}_i \rangle}_{\text{kinetic energy}} - \underbrace{\langle \Psi_0 | \mathcal{H}_e | \Psi_0 \rangle}_{\text{potential energy}} + \underbrace{\text{constraints}}_{\text{orthonormality}} \quad (3.5)$$

Euler-Lagrange equations yields:

$$M_I \ddot{\mathbf{r}}_I(t) = - \frac{\partial}{\partial \mathbf{r}_I} \langle \Psi_0 | \mathcal{H}_e | \Psi_0 \rangle + \frac{\partial}{\partial \mathbf{r}_I} \{ \text{constraints} \} \quad (3.6)$$

$$\mu_i \ddot{\psi}_i(t) = - \frac{\partial}{\partial \psi_i^*} \langle \Psi_0 | \mathcal{H}_e | \Psi_0 \rangle + \frac{\partial}{\partial \psi_i^*} \{ \text{constraints} \} \quad (3.7)$$

The μ_i are the (fictitious) masses of the electronic (inertia parameters) coupled to the orbital degrees of freedom, and $\psi_i^* \doteq \langle \psi_i |$. With these equations of motion, the nuclei evolve at a certain (instantaneous) temperature $\propto \sum_I M_I \dot{\mathbf{r}}_I^2$, while the orbitals evolve at the fictitious temperature $\propto \sum_i \mu_i \langle \dot{\psi}_i | \dot{\psi}_i \rangle$. The method describe a realistic dynamics as soon as the orbitals stay “cold”, i.e. the electronic subsystem remains close to the exact instantaneous minimum energy $\min_{\{\psi_i\}} \{ \langle \Psi_0 | \mathcal{H}_e | \Psi_0 \rangle \}$. Thus, as for the BO dynamics, the Car-Parrinello dynamics builds up from an electronic structure method expressed through a variational principle. The dynamics of the two subsystems can remain decoupled, in a maintained metastable condition, when the power spectra (i.e. the Fourier spectra of the statistically averaged velocity autocorrelation functions) stemming from both dynamics do not have substantial overlap, preventing energy transfer from “hot” nuclei to “cold” electrons. The crucial parameter is the fictitious electron mass μ (normally only one mass, the same for all the orbitals, is defined), that can be adjusted to avoid overlap in the power spectra. In fact, a simple harmonic analysis of the frequency spectrum of the classical fields describing the orbitals gives a dependency on the square root of the excitation gap of the lowest frequency [63]:

$$\omega_e^{\min} \propto \left(\frac{E_{\text{gap}}}{\mu} \right)^{1/2} \quad (3.8)$$

where E_{gap} is the energy difference between the lowest unoccupied and the highest occupied orbital and is a property of the system. Since also the highest phonon frequency is dictated by the system, μ should be chosen as small as possible. On the other hand also the highest electronic frequency depends on the inverse square root of μ . The highest frequency limits the largest time step for the integration of the equations of motion. It can be shown that the maximum time step is [63]:

$$\Delta t^{\max} \propto \left(\frac{\mu}{E_{\text{cut}}} \right)^{1/2} \quad (3.9)$$

The energy E_{cut} is a parameter governing the accuracy of the calculation. In the most popular Car-Parrinello Molecular Dynamics implementation [64, 60], the one used throughout this thesis work, the orbitals are expanded in a plane wave basis set: E_{cut} is the kinetic energy at which the expansion is truncated (*vide infra* in section 3.3 for details). The higher its value the more accurate the calculation, but this implies more computational costs. Typically, in a simulation one has to find the lowest E_{cut} and the optimal μ to have: 1) decoupling of the nuclear and electronic subsystem (adiabaticity), 2) low computational cost retaining the desired accuracy, 3) the largest possible integration time step. It was proved [65] that, fixing E_{cut} , μ can be automatically and iteratively optimized during short MD runs.

3.2 Density functional theory

Up to here nothing was said on the electronic structure method used to evaluate the expectation value of the electronic Hamiltonian \mathcal{H}_e . Even if this is not the only possibility, traditionally the CPMD scheme has been implemented in conjunction with Hohenberg-Kohn-Sham density functional (DF) theory [66, 67].

The total ground state energy is:

$$\min_{\Psi_0} \{ \langle \Psi_0 | \mathcal{H}_e | \Psi_0 \rangle \} = \min_{\{\phi_i\}} E^{KS}[\{\phi_i\}] \quad (3.10)$$

Thus, the expectation value of \mathcal{H}_e when the system is in its ground state, can be found by minimizing a functional, called Kohn-Sham energy (E^{KS}), with respect to a proper set of auxiliary functions $\{\phi_i(\mathbf{r})\}$. These are the Kohn-Sham orbitals, that satisfy the orthonormality condition $\langle \phi_i | \phi_j \rangle = \delta_{ij}$, and are related to the electron density $n(\mathbf{r})$ by:

$$n(\mathbf{r}) = \sum_i^{\text{occ}} f_i |\phi_i(\mathbf{r})|^2 \quad (3.11)$$

where the sum runs over all the occupied states. The minimization with respect of all the possible all-body wavefunctions Ψ is dramatically simplified into the minimization with respect to the Kohn-Sham orbitals $\{\phi_i\}$, that are one-particle functions.

The Kohn-Sham energy is:

$$E^{KS}[\{\phi_i\}] = T_s[\{\phi_i\}] + \int d\mathbf{r} V_{\text{ext}}(\mathbf{r})n(\mathbf{r}) + \frac{1}{2} \int d\mathbf{r} V_H(\mathbf{r})n(\mathbf{r}) + E_{\text{xc}}[n] \quad (3.12)$$

The equality in Eq. 3.10 holds in virtue of the theorem proved by Hohenberg and Kohn [66]. It states that *if interacting electrons move in an external potential V_{ext} , the ground-state electron density $n(\mathbf{r})$ minimizes the functional*

$$E[n] = F[n] + \int d\mathbf{r} V_{\text{ext}}(\mathbf{r})n(\mathbf{r}) \quad (3.13)$$

where $F[n]$ is a universal functional of n and the minimum value of the functional $E[n]$ is the exact ground-state electronic energy.

The term $T_s[\{\phi_i\}]$ in Eq. 3.12 is the kinetic energy of the reference non interacting system consisting of the same number of electrons exposed to the same potential as in the fully

interacting system. The term V_{ext} is the sum of the nuclei-electrons interactions, seen as an external potential acting on the single electron, and the nuclei-nuclei interactions. These are here added in view of the propagation of the nuclear positions. In the implementation of CPMD we used, core electrons are replaced by pseudopotentials (see section 3.3) and so this term has to be particularized to this case. The third term is the Hartree energy, i.e. the electrostatic energy of two charge clouds stemming from the electronic density, obtained from the Hartree potential V_{H} . The last contribution, the exchange-correlation functional $E_{\text{xc}}[n]$ is basically the remainder between the exact energy and the Kohn-Sham decomposition into the three above mentioned terms.

Kohn and Sham [67] proved that the minimum of the Kohn-Sham energy is obtained by varying the energy functional for a fixed number of electrons with respect to orbitals subjected to the orthonormality constraint. The Lagrangian formalism provides one way to solve the minimization problem. In fact, the expression

$$\min_{\{\phi_i\}} \left\{ \langle \Psi_0 | \mathcal{H}_e^{KS} | \Psi_0 \rangle \right\} \Big|_{\langle \phi_i | \phi_j \rangle = \delta_{ij}} \quad (3.14)$$

can be worked out through the Lagrangian:

$$\mathcal{L} = -\langle \Psi_0 | \mathcal{H}_e^{KS} | \Psi_0 \rangle + \sum_{i,j} \Lambda_{ij} (\langle \phi_i | \phi_j \rangle - \delta_{ij}) \quad (3.15)$$

where the Λ_{ij} are associated Lagrangian multipliers. The unconstrained minimum condition for the Lagrangian with respect to the orbitals,

$$\frac{\delta \mathcal{L}}{\delta \phi_i^*} = 0 \quad (3.16)$$

leads to:

$$\mathcal{H}_e^{KS} \phi_i(\mathbf{r}) = \sum_j \Lambda_{ij} \phi_j(\mathbf{r}) \quad (3.17)$$

The matrix Λ can be diagonalized to give:

$$\mathcal{H}_e^{KS} \phi_i(\mathbf{r}) = \epsilon_i \phi_i(\mathbf{r}) \quad (3.18)$$

The one-particle Hamiltonian \mathcal{H}_e^{KS} is expressed as:

$$\mathcal{H}_e^{KS} = \frac{1}{2} \nabla^2 + V_{\text{ext}}(\mathbf{r}) + V_{\text{H}}(\mathbf{r}) + \frac{\delta E_{\text{xc}}[n]}{\delta n(\mathbf{r})} \quad (3.19)$$

The corresponding total energy now results:

$$E^{KS} = \sum_i \epsilon_i - \frac{1}{2} \int d\mathbf{r} V_{\text{H}}(\mathbf{r}) n(\mathbf{r}) + E_{\text{xc}}[n] - \int d\mathbf{r} \frac{\delta E_{\text{xc}}[n]}{\delta n(\mathbf{r})} n(\mathbf{r}) \quad (3.20)$$

Crucial to the application of DF theory is the approximation of the unknowable exchange and correlation functional. In the simplest, but astonishingly powerful, approximation, the ‘‘Local Density Approximation’’ (LDA):

$$E_{\text{xc}}^{\text{LDA}}[n(\mathbf{r})] = \int d\mathbf{r} n(\mathbf{r}) \epsilon_{\text{xc}}^{\text{LDA}}(n(\mathbf{r})) \quad (3.21)$$

where ε^{LDA} is the exchange and correlation energy density of an interacting but homogeneous electron gas at the density given by the density $n(\mathbf{r})$ at a point \mathbf{r} in the inhomogeneous system. This energy density has been parameterized via Monte Carlo method [68]. Although the LDA is very successful for a large variety of problems, it has become clear that the description of many interesting systems in atomic physics (see e.g. [69]), quantum chemistry [70, 71] and condensed matter physics [72, 73, 74] requires nonlocal corrections to the LDA. We underline here that the success of the LDA has been shown, by quantum Monte-Carlo calculations [75, 76], to result from a real-space cancellation of errors in the LDA exchange and correlation energies.

A step forward is the so called ‘‘Generalized Gradient Approximation’’ (GGA [77, 78, 79, 80]):

$$E_{\text{xc}}^{\text{GGA}}[n(\mathbf{r})] = \int d\mathbf{r} n(\mathbf{r}) \varepsilon_{\text{xc}}^{\text{GGA}}(n(\mathbf{r}); \nabla n(\mathbf{r})) \quad (3.22)$$

in which the energy density depends also on the gradient of the density at a given point in the space. It has been demonstrated that GGAs give excellent atomic ground state energies [70, 71, 81] and significantly improve dissociation energies and bond lengths of small molecules [70, 71, 81, 82, 83]. Similarly, the cohesive properties of many solids are reproduced more accurately by GGAs [81, 84, 85, 86]. Energy differences like ionization potentials and electron affinities, on the other hand, are not always improved by GGAs [81]. GGAs neither provide a description of atomic negative ions nor are they able to deal with dispersion forces (nor does LDA). Furthermore, the differences between the results obtained with the various proposed GGAs are often almost as large as those between individual GGAs and the LDA, so that the optimum form of a GGA is not obvious. Practically one has to choose, amongst the nowadays large variety of proposed functionals, the functional yielding the best possible description of the particular system under analysis. This is the route we followed in this work: we selected two different (*correlation*) functionals for the two elements we studied (phosphorus and carbon), on the basis of comparisons with reference data of the properties calculated with a number of available functionals.

3.3 Pseudopotentials

As already mentioned, in the implementation of CPMD, the orbitals are expanded in a plane wave basis set. Plane waves are defined:

$$f_D^{\text{PW}} = \mathcal{N} \exp(-i\mathbf{D}\mathbf{r}) \quad (3.23)$$

The normalization $\mathcal{N} = 1/\sqrt{\Omega}$, where Ω is the volume of the periodically replicated cell in which the system is simulated; each plane wave is labelled by D , that is any vector of the reciprocal space that satisfies the applied periodic boundary conditions. In the expansion are retained all the terms for which it holds:

$$\frac{1}{2} |\mathbf{D}|^2 \leq E_{\text{cut}} \quad (3.24)$$

Thus, the precision of the calculation is governed by the only parameter E_{cut} . An approximate relation between the number of independent plane waves and the cut-off energy is:

$$N_{\text{PW}} \cong \frac{1}{2\pi^2} \Omega E_{\text{cut}}^{3/2} \quad (3.25)$$

with E_{cut} expressed in hartree units. The number of plane waves N_{PW} is also the number of the electronic degrees of freedom. Plane waves constitute an unbiased basis-set, in the sense that they do not “favour” certain atoms or regions over others. On the other hand, an increasingly large number of components would be needed to resolve structures in real space on decreasingly small distance scales. Unfortunately, already orbitals of the first row atoms display strong and rapid oscillations close to the nuclei (due to the Pauli principle, that imposes orthogonality of the orbitals). However, most of chemistry is ruled by the valence electrons, whereas the core electrons are essentially inert. This means that core-electron wave functions remain essentially unchanged when placed into different chemical environment; their main contribution to the chemical bonding is to enforce the valence wave functions orthogonality to the core state. The idea of substituting the true atomic potential with a *pseudopotential* that effectively reproduces the features of the core electrons dates back to Fermi [87], while its seminal development is due to Phillips and Kleinman [88]. A pseudopotential practically takes out from the explicit calculation of the electronic structure the innermost electrons, by representing them with *smooth* and *nodeless* effective potentials. Such potentials, that are seen as *external* potentials* from the valence electrons, give rise to smooth wavefunctions, suitably described by plane waves, without recurring to unpracticably large number of components (or E_{cut}). For constructing pseudopotentials used in ab initio calculations, one has to fulfill the following requirements:

- the resulting valence electron pseudo-wavefunction (pseudo since obtained from a total energy that includes a pseudopotential) should not contain nodes;
- all-electron and pseudo eigenvalues must agree;
- the (normalized) pseudo-wavefunction must be equal to the normalized all-electron wavefunction beyond a chosen cut-off radius r_{PP} from the nucleus;
- the integral from 0 to r of the pseudo and all-electron densities (the squared modulus of the pseudo and all-electron wavefunctions) must agree for $r > r_{\text{PP}}$ (the so called requirement of ‘norm-conservation’[†]).

Pseudopotentials are normally generated exactly by optimizing the electronic structure in one or more selected ‘prototype’ atomic configurations: the last two requirements are crucial for the so called *transferability* of the pseudopotential to ideally all the possible chemical environments. The constraints posed do not yield a univocal formulation of a pseudopotential. Details on pseudopotentials and their construction can be found in ref. [91]. Needless to say, properties of the system that depend on the structure of the wavefunction close to the core[‡] cannot be straightforwardly obtained in a calculation where pseudopotentials are used.

*The total energy becomes (compare to Eq. 3.12): $E_{\text{total}} = E_{\text{kin}} + E_{\text{PP}} + E_{\text{xc}} + E_{\text{ES}}$, i.e. the kinetic energy, the (external) pseudopotential, the exchange-correlation energy, and electrostatic energy.

[†]This constraint is released in the alternative approach known as “ultra-soft” pseudopotential [89, 90].

[‡]“Close” refers to distances smaller than r_{PP} . In a MD simulation particles should never approach to a distance smaller than twice r_{PP} .

3.4 Constant ionic and electronic temperature in Car-Parrinello Molecular Dynamics

In the limit of ergodic sampling, standard molecular dynamics creates the microcanonical (NVE) ensemble. In order to generate a canonical (NVT) ensemble, which is preferred for obvious physical reasons, the naive attempt to barely fix the total kinetic energy of the system is inexact. A *deterministic* algorithm achieving the purpose, in the spirit of the extended system dynamics [92] is a sort of dynamical friction, firstly introduced by Nosé [93] and later refined by Hoover [94, 95], is widely known as Nosé-Hoover thermostat. In its original formulation, the thermostat was shown [94] to not yield ergodic sampling in certain peculiar classes of Hamiltonians (such as the harmonic oscillator). The related technique of the Nosé-Hoover-chain [96] thermostat was introduced to insure ergodicity. This is obtained by attaching to the first thermostat another thermostat, which is in turn thermostatted via a chain of K similar devices. The constant temperature CPMD equations of motion for the ionic system are [97]:

$$M_I \ddot{\mathbf{r}}_I = -\nabla_I E^{KS} - M_I \dot{\xi}_1 \dot{\mathbf{r}}_I \quad (3.26)$$

$$Q_1^n \ddot{\xi}_1 = \left[\sum_I M_I \dot{\mathbf{r}}_I^2 - g k_B T \right] - Q_1^n \dot{\xi}_1 \dot{\xi}_2 \quad (3.27)$$

$$Q_k^n \ddot{\xi}_k = \left[Q_{k-1}^n \dot{\xi}_{k-1}^2 - k_B T \right] - Q_k^n \dot{\xi}_{1k} \dot{\xi}_{k+1} (1 - \delta_{kK}) \quad (3.28)$$

where $k = 2, \dots, K$, E^{KS} was introduced in Eq. 3.20, T is the target kinetic energy, and g is the number of (nuclear) degrees of freedom to which the chain is coupled. The “mass” parameters Q_k^n are chosen such that the power spectra of the thermostat coordinates (the ξ ’s) and of the thermostatted system have a maximum overlap. Masses are related to frequencies in this way:

$$Q_1^n = \frac{g k_B T}{\omega_n^2}, \quad Q_k^n = \frac{k_B T}{\omega_n^2} \quad (3.29)$$

In practice, one has to calculate the power spectrum of the not thermostatted system by Fourier transforming the velocity autocorrelation function of the nuclei. A typical frequency of the spectrum can be taken for ω_n . From Eqs. 3.26-3.28 it is clear how the thermostat works: ξ_1 is a sort of dynamical friction coefficient that casts the equations of motion into the realm of dissipative dynamics. The accelerations of the nuclei (thus the label n in apex) are damped resulting in cooling or heating of the system when the instantaneous kinetic energy of the nuclei is higher or lower than the chosen $k_B T$.

An apparently unrelated problem is solved in the same fashion in the CPMD framework. As discussed at the end of section section 3.1, the CPMD method relies on the separation of the physical and fictitious temperatures of the nuclear and electronic subsystems. The metastability of this separation of temperatures breaks down when the electronic excitation gap is comparable to the thermal energy (of the nuclei) or smaller (see Eq. 3.8): this is e.g. the case for metallic systems. For these systems, a thermostat to the electronic degrees of freedom, in the spirit of the above described equations of motion, can be introduced. This was originally proposed by Blöchl and Parrinello [98] as an *ad hoc* remedy, whose rigorous foundation was proven only recently [99]. The equations of motion of the (thermostatted)

degrees of freedom are in the same form as for the ionic system:

$$\mu\ddot{\phi}_i = \mathcal{H}_e^{KS}\phi_i + \sum_{ij} \Lambda_{ij}\phi_j - \mu\dot{\eta}_1\dot{\phi}_i \quad (3.30)$$

$$Q_1^e\ddot{\eta}_1 = 2 \left[\sum_I^{\text{occ}} \mu \langle \dot{\phi}_i | \dot{\phi}_i \rangle - T_e^0 \right] - Q_1^e\dot{\eta}_1\dot{\eta}_2 \quad (3.31)$$

$$Q_l^e\ddot{\eta}_l = \left[Q_{l-1}^e\dot{\eta}_{l-1}^2 - \frac{1}{\beta_e} \right] - Q_l^e\dot{\eta}_l\dot{\eta}_{l+1}(1 - \delta_{lL}) \quad (3.32)$$

where $l = 2, \dots, L$, \mathcal{H}_e^{KS} and Λ_{ij} were introduced in Eqs. 3.19 and 3.15, respectively. T_e^0 is the target kinetic energy; this can be calculated, following Ref. [98], as:

$$T_e^0 = 2k_B T \frac{\mu}{M} \sum_i \langle \phi_i | -\frac{1}{2}\nabla^2 | \phi_i \rangle \quad (3.33)$$

The target kinetic energy in Eq. 3.32 is: $1/\beta_e = 2T_e^0/N_{\text{PW}}$. The fictitious masses of the thermostat coordinates are related to their vibrational frequency through:

$$Q_1^e = \frac{2T_e^0}{\omega_e^2}, \quad Q_l^e = \frac{1}{\beta_e \omega_e^2} \quad (3.34)$$

ω_e needs to be within the power spectrum of the thermostatted electronic subsystem. A practical way to find the electronic power spectrum consists in Fourier transforming the velocity autocorrelation function of the electronic degrees of freedom, as obtained from a simulation with suddenly frozen nuclei.

3.5 Constant pressure in Car-Parrinello Molecular Dynamics

The constant pressure molecular dynamics was introduced, in the framework of the extended system dynamics, by Andersen [92], only for isotropic fluctuations of the volume cell. The method was extended allowing fluctuations of the box shape by Parrinello and Rahman [100]. Particularized to the CPMD method, the problem is solved treating the primitive Bravais lattice vectors \mathbf{a}_1 , \mathbf{a}_2 , and \mathbf{a}_3 of the simulation cell as added dynamical variables. Defining the matrix $\mathbf{h} = [\mathbf{a}_1, \mathbf{a}_2, \mathbf{a}_3]$, the real-space position (\mathbf{r}_I) of a particle is expressed as:

$$\mathbf{r}_I = \mathbf{h}\mathbf{s}_I \quad (3.35)$$

The equation defines \mathbf{s}_I , with I labelling the particles, that has the role of a scaled coordinate (for each component of \mathbf{s}_I : $\mathbf{s}_{I,u} \in [0,1]$, where u runs over the coordinates of \mathbf{s}_I) of a particle in the unitary volume cube. The metric tensor is readily defined: $\mathcal{G} = \mathbf{h}^t\mathbf{h}$. It converts distances measured in scaled coordinates into real distances according to:

$$(\mathbf{r}_I - \mathbf{r}_J)^2 = (\mathbf{s}_I - \mathbf{s}_J)^t \mathcal{G} (\mathbf{s}_I - \mathbf{s}_J) \quad (3.36)$$

The periodic boundary condition are enforced through:

$$\mathbf{r}_{\text{pbc}} = \mathbf{r} - \mathbf{h}[\mathbf{h}^{-1}\mathbf{r}]_{NINT} \quad (3.37)$$

where $[\dots]_{NINT}$ indicates ‘nearest integer’. In the CPMD scheme also the orbitals have to be suitably expressed in the scaled coordinates \mathbf{s} . The normalized orbitals in real-space coordinates \mathbf{r} are transformed via:

$$\phi_i(\mathbf{r}) = \frac{1}{\sqrt{\Omega}}\phi_i(\mathbf{s}) \quad (3.38)$$

where i label the state. Ω is the volume of the cell: $\Omega = \det \mathbf{h}$. In this way each of the corresponding members of the two sets of orbitals have the same normalization, if their modulus is integrated over the respective volume. In other words, for the charge density, it holds, in the unit cube:

$$n(\mathbf{r}) = \frac{1}{\Omega}n(\mathbf{s}) \quad (3.39)$$

This achieves the desired task to have the scaled fields $\phi(\mathbf{s})$ (and their charge density) *independent* of the dynamical variables associated to the cell degrees of freedom. On the other hand, the real-space fields $\phi(\mathbf{s})$ *do depend* on \mathbf{h} through the normalization by the cell volume Ω .

All is set to write the variable-cell extended Lagrangian for CPMD:

$$\begin{aligned} \mathcal{L} &= \sum_i \mu \langle \dot{\phi}_i(\mathbf{s}) | \dot{\phi}_i(\mathbf{s}) \rangle - E^{KS}[\{\phi_i\}, \{\mathbf{h}_I\}] \\ &+ \sum_{ij} \Lambda_{ij} (\langle \phi_i(\mathbf{s}) | \phi_j(\mathbf{s}) \rangle - \delta_{ij}) \\ &+ \sum_I \frac{1}{2} M_I (\dot{\mathbf{s}}_I^t \mathcal{G}_I \dot{\mathbf{s}}_I) + \frac{1}{2} W \text{Tr} \dot{\mathbf{h}}^t \dot{\mathbf{h}} - P\Omega \end{aligned} \quad (3.40)$$

This constant pressure (P) Lagrangian reduces to the usual CPMD Lagrangian (that was given only in a schematic form in Eq. 3.5) when $\dot{\mathbf{h}} \rightarrow 0$ (apart from the constant $P\Omega$). W is the fictitious mass (or inertia parameter) that controls the time-scale of the motion of the cell. The resulting equations of motion are:

$$M_I \ddot{\mathbf{s}}_{I,u} = - \sum_{v=1}^3 \frac{\partial E^{KS}}{\partial \mathbf{r}_{I,v}} (\mathbf{h}^t)^{-1}_{vu} - M_I \sum_{v=1}^3 \sum_{s=1}^3 \mathcal{G}_{uv}^{-1} \dot{\mathcal{G}}_{vs} \dot{\mathbf{s}}_{I,s} \quad (3.41)$$

$$\mu \ddot{\phi}_i(\mathbf{s}) = - \frac{\delta E^{KS}}{\delta \phi_i^*(\mathbf{s})} + \sum_j \Lambda_{ij} \phi_j(\mathbf{s}) \quad (3.42)$$

$$W \ddot{\mathbf{h}}_{uv} = \Omega \sum_{s=1}^3 (\Pi_{us}^{\text{tot}} - p \delta_{us}) (\mathbf{h}^t)^{-1}_{sv} \quad (3.43)$$

The total internal stress tensor is[§]:

$$\Pi_{us}^{\text{tot}} = \frac{1}{\Omega} \left(\sum_I M_I (\dot{\mathbf{s}}_I^t \mathcal{G}_I \dot{\mathbf{s}}_I) - \sum_v \frac{\partial E_{\text{total}}}{\partial \mathbf{h}_{uv}^t} \mathbf{h}_{vs}^t \right) \quad (3.44)$$

The barostat acts as a frictional feedback mechanism. It leads the average internal pressure ($P^{\text{int}} = \langle (1/3) \text{Tr} \Pi^{\text{tot}} \rangle$) to be equal to the external applied pressure P with a frictional coefficient $\propto \dot{\mathcal{G}}$. Following Andersen [92], W should be chosen in order to obtain a relaxation

[§]The expression is in the familiar form: $P = \rho k_B T - dE_{\text{total}}/d\Omega$.

time of the cell of the order of $\tau = L/c$, being L the linear dimension of the simulation box and c the sound velocity inside the system. It is also possible [101] to estimate the characteristic frequency of the system $1/\tau$ by linearizing Eq. 3.43, so that $W = 3 \sum_i M_i / (4\pi)$. Ergodic trajectories are obtained integrating Eqs. 3.41–3.43.

The actual implementation of the constant pressure dynamics involves a subtlety. There is a problem arising from a straightforward implementation of the above equations of motion, due to the use of a finite basis set: this is known as Pulay stress [102][¶]. When a finite basis set is used, in presence of volume fluctuations, one can either fix the number of plane waves (N_{PW}) or the energy cut-off E_{cut} . A constant N_{PW} does not lead to any Pulay stress, but it implies a systematic decreasing of the precision in case of volume increase (from Eq. 3.25, $E_{\text{cut}}^{3/2}$ would effectively decrease). One can imagine the (real space) grid of the plane wave expansion being stretched with the volume, so that details are systematically lost. On the other hand, constant E_{cut} would have better convergence properties towards the infinite-basis-set limit [102]. Unfortunately N_{PW} is an integer while the box would change continuously: when an extra term is added to the plane-wave expansion, the total energy (and thus the equation of state) changes discontinuously. Furthermore, due to the fact that dealing with a variable number of degrees of freedom is highly undesirable in Molecular Dynamics, the CPMD implementation [60] requires a fixed N_{PW} . One can recover reasonable dynamics, without going to computationally prohibitively high E_{cut} with a practical remedy consisting in modifying the electronic kinetic energy term (E_{kin}), that normally reads^{||}:

$$E_{\text{kin}} = \sum_i f_i \sum_{\mathbf{q}} \frac{1}{2} |\mathbf{D}|^2 |c_i(\mathbf{q})|^2 \quad (3.45)$$

The employed modification [103, 101] is:

$$\tilde{E}_{\text{kin}} = \sum_i f_i \sum_{\mathbf{q}} \frac{1}{2} \left| \tilde{\mathbf{D}}(A, \sigma, E_{\text{cut}}^{\text{eff}}) \right|^2 |c_i(\mathbf{q})|^2 \quad (3.46)$$

$$\left| \tilde{\mathbf{D}}(A, \sigma, E_{\text{cut}}^{\text{eff}}) \right|^2 = |\mathbf{D}|^2 + A \left\{ 1 + \text{erf} \left[\frac{\frac{1}{2} |\mathbf{D}|^2 - E_{\text{cut}}^{\text{eff}}}{\sigma} \right] \right\} \quad (3.47)$$

where A , σ , and $E_{\text{cut}}^{\text{eff}}$ are positive parameters to be adjusted. The constant N_{PW} result is recovered in the limit of vanishing smoothing ($A \rightarrow 0$, $\sigma \rightarrow \infty$). In the opposite situation of sharp step function, ($A \rightarrow \infty$, $\sigma \rightarrow 0$), all the plane wave for which $1/2 |\mathbf{D}|^2 \gg E_{\text{cut}}^{\text{eff}}$ have negligible weight in \tilde{E}_{kin} and so drop out from the ground state wave function: this would mimic a constant cut-off (at $E_{\text{cut}}^{\text{eff}}$) dynamics. Therefore, for this trick to work, it must be: $E_{\text{cut}} \gg E_{\text{cut}}^{\text{eff}}$. When $A > 0$, the stress tensor has an extra term, that can be identified with the Pulay stress. This parameter should be high enough to be close to the constant cut-off (while a reasonable value of σ prevents discontinuities). On the other hand, it has to be kept as small as possible, due to an increase of the highest frequency of the electronic power spectrum ($\propto A/E_{\text{cut}}$), that would limit the maximum allowed molecular dynamics integration time step (see Eq. 3.9).

[¶]The Pulay stress is the difference between the stress tensor ($\partial E / \partial \mathbf{h}$), calculated with the finite basis-set adopted, and the fully-converged-basis value.

^{||}In this expression we implicitly considered only the $\mathbf{k} = 0$ (Γ) point.

Phosphorus: first principle simulation of a liquid – liquid phase transition

On a long enough timeline, the survival rate for everyone drops to zero.

In this chapter we will report on a Car-Parrinello molecular dynamics study of the liquid – liquid phase transition in phosphorus. The report will be opened with a short review of the up to date ideas in the field of phosphorus LLPT. Subsequently we present the results of DF-MD simulations to demonstrate and analyze the presence of a LLPT in liquid phosphorus, followed by a careful analysis of the structure of both phases. In contrast to earlier DF-MD studies we employ a gradient-corrected functional that provides a significant improvement over LDA in the description of the interatomic interactions, as we will show. Moreover we take care to simulate the transition by a gradual increase of the pressure. Section 4.2 describes the computational methods, section 4.3 discusses the choice of the density functional, and in section 4.4 we present results for the equation of state at 1500 K for both liquids, together with a phenomenological analysis of the observed phase transitions. Section 4.5 is devoted to the analysis of structural and dynamical properties of both liquids. We conclude with a discussion.

4.1 Overview of the liquid – liquid phase transition in phosphorus

Recently, the first direct experimental observation of a LLPT has been reported. Using X-ray diffraction techniques Katayama and co-workers [1] obtained strong evidence for a pressure-induced transformation between two distinct forms of liquid phosphorus. Further analysis [107] of the data suggested that the low-pressure phase is a molecular liquid consisting of tetrahedral P_4 molecules, whereas the high-pressure phase is an atomic liquid with a polymeric network structure. The LLPT was found at a pressure (P) of the order of 1 GPa and a temperature (T) of around 1300 K (open circles in Fig. 4.1) and shows a significant density change. Recently, Monaco *et al.* [108] extended the X-ray study of LLPT study of Katayama and co-workers up to a temperature of 2500 K. They found

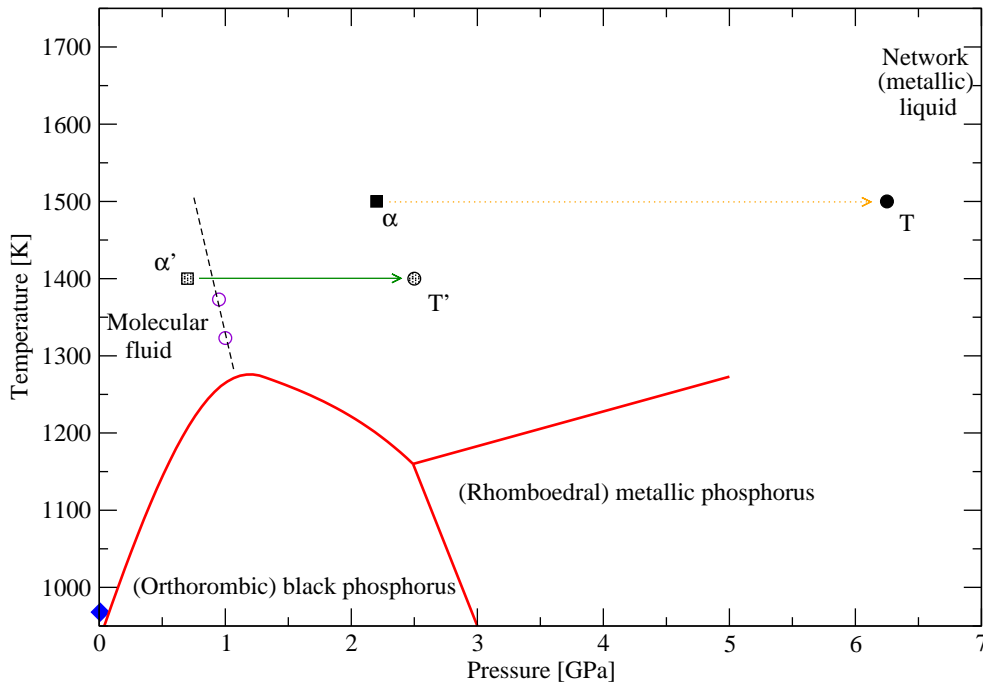


Figure 4.1: Pressure-Temperature phase diagram of phosphorus in the relevant region for the LLPT. The open circles are experimental points (Katayama et al. [1]). The solid/liquid and solid/solid (solid lines) boundaries are taken from [104] and references therein. The full diamond at the bottom left of the plot is the critical point ending the (low density) gas/liquid line [105]. We started our simulation from the point α and increased the pressure with small steps, along the dotted arrow, up to the point T , where we obtained the LLPT. In the simulation reported in [106] the sample was brought from the state point α' to the point T' in one step. At this last point the system instantaneously exhibited the LLPT.

the (dP/dT) slope of the coexistence line to be negative, and suggested the LLPT critical temperature to be not lower than 2500 K: these data are shown in the next chapter, in Fig. 5.2. In Fig. 4.1 we show the stable phases in the relevant region for the LLPT: liquid phosphorus freezes into an insulating, orthorhombic solid phase (black phosphorus) for pressures up to 2.6 GPa, and into a metal with rhombohedral structure for pressures beyond 2.6 GPa. On basis of the experimental data, the LLPT coexistence line is proposed to start from the melting line at $P \sim 1$ GPa and $T \sim 1250$ K, where it shows a maximum in the $P - T$ plane of the phase diagram. The tetrahedral P_4 molecule appearing in the low-density liquid phase is the principal component of the gas phase of phosphorus [109]. P_4 is also the basic unit of white phosphorus [110], i.e. the metastable solid phase obtained by vapour condensation at ambient conditions. White phosphorus melts into the molecular liquid at 317.4 K at atmospheric pressure. It has also to be noted that the critical point at the end of the P_4 liquid/vapor transition line (solid diamond in Fig. 4.1) is calculated to be 8.2 MPa and 968 K [105]. Thus the P_4 liquid is supercritical all along the predicted LLPT line [108] and should be rather referred to as molecular *fluid*.

The experimental studies revealing a possible existence of a LLPT in phosphorus had been preceded by a pioneering paper by Hohl and Jones [111], reporting the study of liquid phosphorus by density-functional theory based molecular dynamics (DF-MD) simulation employing the local density functional (LDA). By heating up a molecular P_4 liquid, they

observed a transition into a polymeric-like phase. In a recent DF-MD study using LDA, Morishita [106] observed the LLPT from the molecular into the network phase, by imposing an instant pressure change of 1.8 GPa on the system (i.e. from the shaded square to the shaded circle, connected with an arrow in Fig. 4.1). Employing the same computational approach (LDA DF-MD) Senda *et al.* [112] addressed both the structural and the electronic properties of the two liquid phases, finding that the molecular liquid is an insulator while the network liquid is metallic.

4.2 Computational methods

We performed DF-MD simulations using the Car-Parrinello [62] method as implemented in the CPMD package [60]. The electronic structure was calculated using the Kohn-Sham formulation of density functional theory employing a gradient-corrected functional. The calculations were performed using a periodic fcc cell. The Kohn-Sham state are expanded in a plane-wave basis set sampled at the Γ point in the Brillouin zone, and truncated at a kinetic energy (E_{cut}) of 25 Ry. This value ensures convergence of the binding energy of small P clusters (vide infra for details) within 5 kJ/mol per bond. Semi-local norm-conserving Martins-Troullier pseudopotentials [113] are used to restrict the number of electronic states to those of the valence electrons. The pseudopotential was constructed with an excited positively charged valence-electron configuration $s^{1.75}p^{2.25}d^{0.50}$, using core-radii of 1.5, 1.7, and 1.9 a.u. for the $l = s, p,$ and d terms, respectively. The pseudopotential was transformed into the Kleinman-Bylander form [114] with $l = d$ as the local term. The incorporation of a d -potential is required to achieve an accurate description of the contribution of d -orbitals to the bonding. The mass associated with the fictitious degree-of-freedom was taken 1000 a.u. This allowed for a time step of 5 a.u. (0.12 fs) in the velocity Verlet integration of the equations of motion. The ionic temperature was controlled via a Nosé-Hoover thermostat chain of length 4 (coupled to the frequency of 300 cm^{-1}). The network liquid is expected to be metallic [109, 111, 112]. For metallic systems the Car-Parrinello method requires the electronic degrees of freedom to be coupled to a thermostat. Here we coupled a Nosé-Hoover chain thermostat to the electronic degrees of freedom with a target energy of 0.035 eV and a coupling frequency of 15000 cm^{-1} . The target energy was estimated using the procedure proposed by Blöchl and Parrinello [98]. The coupling frequency of 15000 cm^{-1} was chosen to be in the range of dominant frequencies of the wavefunctions, determined from a CPMD simulation with fixed ion positions. Imposing thermostats breaks the conservation of the linear momentum, may lead to a significant drift of the center of mass of the system. This collective motion can absorb part of the kinetic energy of the ions, yielding a decrease of the ionic temperature. We monitored the magnitude of this drift, and found it to be negligible, thus making a periodic reset of the velocity of the center of mass unnecessary.

The implementation of the constant pressure (NPT) simulations was done following the methodology explained in section 3.5. Referring to the symbols introduced there, we chose $E_{\text{cut}}^{\text{eff}} = 25 \text{ Ry}$: this required use of a real plane-wave basis set truncated at $E_{\text{cut}} = 35 \text{ Ry}$. The height and the width of the smoothing function, A and σ in Eq. 3.47 were set to 40 and 6 Ry, respectively.

		Exp. [110]	LDA	B-LYP	BP
P ₂	atomization energy	490.1	551	499	502
P ₂	bond length	1.89	1.93	1.90	1.90
D _∞ P ₃	atomization energy	617.4	788	633	654
D _∞ P ₃	bond lengths	1.95	1.94	1.97	1.96
C _{2v} P ₃	atomization energy	748.6	910	734	768
C _{2v} P ₃	short bonds	2.07	2.06	2.09	2.08
C _{2v} P ₃	long (basis) bond	2.25	2.23	2.27	2.26
C _{2v} P ₃	basis angles	57.2	57.3	57.1	57.2
C _{2v} P ₃	vertex angle	65.6	65.4	65.8	65.6
T _d P ₄	atomization energy	1200.1	1492	1170	1248
T _d P ₄	bond lengths	2.22	2.18	2.22	2.21

Table 4.1: Comparison of energies and geometries of the smallest P cluster among different functionals and experiments. Energies are in kJ/mol, distances in Å, and angles in degree.

4.3 Choice of density functional

To validate the choice of the density functional we determined the binding energy and equilibrium geometry of small P clusters, ranging from the dimer to the P₄ tetrahedron for three functionals: the LDA functional [115] and two gradient corrected functionals, B-LYP [79, 80] and BP [79, 78]. Table 4.1 lists the calculated geometries and energies together with experimental data. It shows that the LDA significantly overestimates the binding energies, a well-known feature of this functional. In contrast the B-LYP and BP functionals show much better agreement with the experimental data. The geometries are of comparable accuracy for all functionals, with B-LYP slightly better than BP. We therefore chose to use B-LYP in the DF-MD simulations of liquid phosphorus.

The structure of the molecular liquid is determined by the interactions among P₄ molecules. The attractive part of this interaction is dominated by dispersion. However, dispersion forces are not accounted for by local (LDA) or semilocal (BP and B-LYP) functionals as it is a non-local long-range correlation effect [116, 117, 118]. To assess the performance of LDA and B-LYP for the intermolecular P₄ interaction we determined the potential energy function of the P₄ dimer. As there is no data available we compared the results to the non-bonded Lennard-Jones part of an empirical force field, the Unified Force Field [119] (UFF). We realize that this is an approximate description of the dispersion. However, as the UFF Lennard-Jones parameters has been especially fitted for P₄ molecules, we believe it provides a reasonable description. Fig. 4.2 shows the effective potentials between two tetrahedra as function of center of mass (CoM) distance. The LDA and B-LYP results were obtained by averaging, for each CoM distance, 50 configurations with random orientations of the two tetrahedra. For the UFF calculations, 5000 configurations were used. The error due to the limited number of orientations is smaller than the symbol size. B-LYP shows only repulsive forces between molecules, while the effective radius of the molecules, considering an average thermal energy of 12.1 kJ/mol at 1500 K, is in agreement with UFF. On the

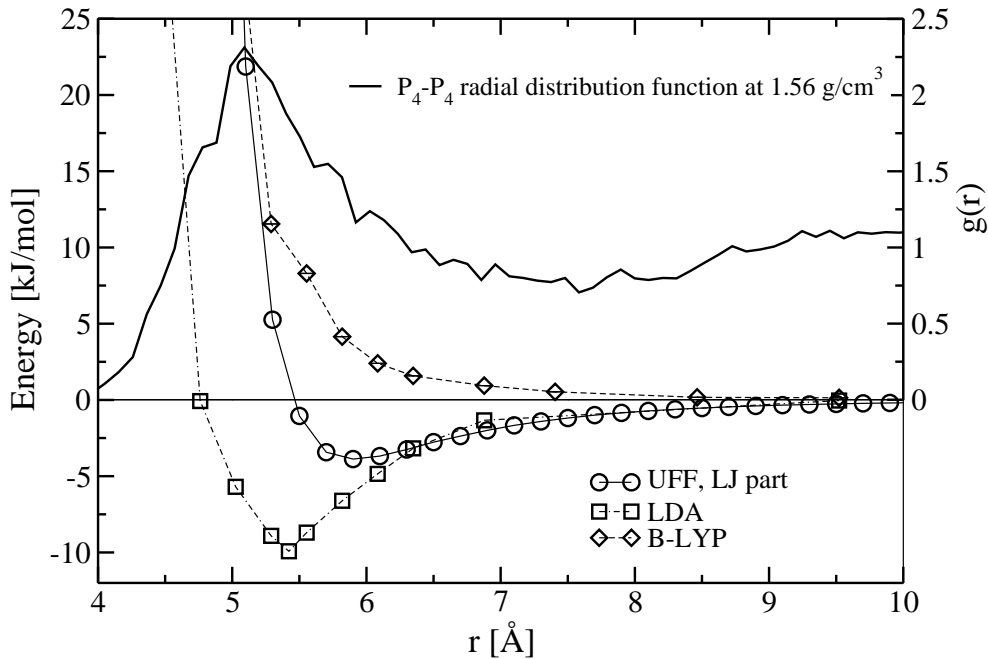


Figure 4.2: Calculated interactions between P_4 molecules for the B-LYP functional, the LDA functional, and the intermolecular Lennard-Jones term of the UFF empirical force field. The energy scale is on the left vertical axis. Superimposed is the radial distribution function $g(r)$ for the P_4 centers of mass. The scale is on the vertical axis at the right side.

other hand, LDA predicts a much smaller effective radius and a spurious strong attraction at the distance corresponding to the effective radius of UFF. The observed behavior of LDA and B-LYP for dispersive intermolecular interactions is also seen for noble gases [116] and benzene [118]. It has its origin in the approximate nature of the functionals for reasons that are not yet fully understood. On the basis of this analysis, it is questionable whether the LDA functional can accurately describe the molecular liquid. This might also implicate an inaccurate description of the liquid – liquid phase transition.

4.4 Liquid – liquid phase transition and equation of state

We studied the liquid – liquid phase transition by examining the $T=1500$ K isotherm for a range of pressures. The thermodynamic phase transition is at a pressure at which the molecular and network phases have equal Gibbs free energy. Techniques for locating phase transitions by free-energy calculations are by now well developed (see e.g. the thermodynamic integration in Frenkel and Smit [13]). For the present system an obvious route would be thermodynamic integration along transition-free paths to a state point above the critical temperature. However, we did not employ such methods in the present study due to prohibitive computational costs. The reason for this is that an accurate implementation would require convergence of the absolute electronic energy. This requires the simulations to be performed at a much larger plane-wave cutoff energy, implying an order of magnitude increase in computational cost. We therefore limited our present study of the phase

transition in phosphorus to the direct observation of the transition, leaving more accurate free-energy based studies for the future.

The initial molecular liquid configuration was obtained by melting a configuration of 16 randomly oriented tetrahedra with the CoM's in a diamond structure in a 5 ps constant volume (NVT) simulation at density of 1.56 g/cm^3 . This is near the experimental coexistence density at $T \sim 1300 \text{ K}$ [120]. This state point was expected to be located in the molecular phase region, not too far from the transition line. Its temperature is significantly below the experimental estimate for the lower bound of the critical temperature of around 2500 K [108]. Isotropic cell fluctuations were then allowed, starting from an imposed pressure of 2.2 GPa , equal to the one calculated in the constant density run at 1.56 g/cm^3 (this state point is labelled as α in Fig. 4.1). Subsequent molecular liquid simulations of various state points along the isotherm were performed by successive small step-wise changes of the pressure. Simulations of the network liquid state points were performed in two ways. For higher pressures this was done by starting from the molecular liquid that spontaneously evolved into a network liquid. For lower pressures we started from one of the high-pressure network liquid simulations and performed subsequent simulations by successively decreasing the pressure by small steps. For all state point simulations consisted of an equilibration of a few ps, and a production run of at least 4 ps. The equilibration period was chosen large enough to ensure that the amplitude of the oscillatory variation of the simulation box volume induced by the instantaneously imposed pressure change had been damped out. Note that we limited the imposed pressure changes to be relatively small ($\leq 0.5 \text{ GPa}$) in order to prevent too large initial volume oscillations and to ensure damping of these oscillations within 1 ps.

Fig. 4.3 reports the calculated equation of state. Upon compression of the molecular phase from 2.2 GPa up to 6.2 GPa we found that no lasting structural changes appeared, with the P_4 molecules remaining intact for most of the time. However, with increasing pressure the temporary break up of the molecules was observed with increasing frequency. In this process one of the six bonds breaks and the molecule opens up and flattens in a ‘butterfly’ shape [111]. This usually happens for two neighbouring P_4 molecules simultaneously, where two undercoordinated atoms from different molecules temporarily link. Chains of this ‘butterfly’ molecules were first suggested by Pauling and Simonetta [121] as a possible mechanism for the breakup of tetrahedral molecules.

Whereas during the 8 ps simulation at 6.2 GPa no lasting global structural change appeared, a phase transition occurred after 2.4 ps in the subsequent simulation at a marginally higher pressure of 6.25 GPa (point T in Fig. 4.1). Note that, at that moment, the volume oscillations due to the imposed pressure change of 0.05 GPa were already damped out. The phase transition appears as an abrupt decrease of the simulation cell size, accompanied by a breaking up of all the tetrahedral molecules. In a second simulation at 6.25 GPa , starting from a different initial molecular liquid configuration, we observed the transition to occur in a similar fashion. Closer inspection of the trajectories just before the transition revealed a possible picture of the microscopic mechanism of the phase transition: the transition occurred whenever a chain of ‘butterfly’ molecules spanning the whole simulation box was formed: only after this event the breaking of tetrahedra propagated through the whole system. In Fig. 4.12, central panel, the chain of ‘butterfly’ molecules is highlighted. Obviously, this process is expected to be dependent on the system size, as the chain of ‘butterfly’ molecules spanned the simulation box, effectively making an infinite chain in

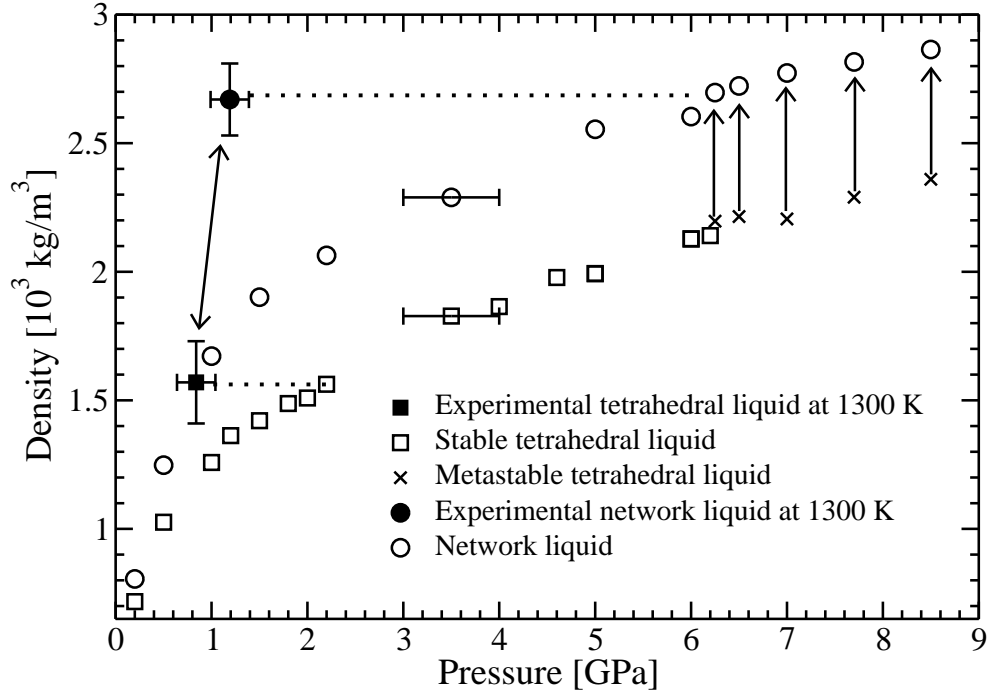


Figure 4.3: Equations of state of liquid phosphorus at 1500 K. Open triangles (Δ) and open circles (\circ) indicate calculated points of the molecular and network phase, respectively. Crosses (\times) and associated arrows indicate simulations manifesting transitions from the molecular to the network phase. The error bars of the two points at 3.5 GPa indicate the estimated inaccuracy in the imposed pressure and holds for all the simulated points. The solid symbols indicate two experimental points near the transition at $T \sim 1300$ K. The dotted lines indicate the difference between experimental and calculated pressures.

the periodic system. For a larger system the formation of a system-spanning chain of ‘butterfly’ molecules could be less probable, and possibly only appearing at a larger pressure or not at all. Still, our observation constitutes an interesting possible mechanism that is consistent with the infinite chain mechanism [121]. In the simulations starting with a network configuration no phase transition to the molecular liquid was observed. For pressures below 5.0 GPa occasionally one or two tetrahedra were observed to form. However, they break apart after a short time. An exception to this was observed during the lowest pressure simulation: in the 1.0 GPa network liquid simulation three tetrahedra formed and remained, but the molecular phase was never completely reformed.

On the basis of these observations, we cannot rule out the possibility that the phase transition is second order, with the density pressure curves crossing at a pressure below the lowest pressure considered in our calculation. Still, given the fact that the structures of both phase are so different and the fact that over the range of pressures considered both phases have different densities our results strongly suggest that the transition is first order.

Obviously, given the small system size and the limited timespan of the simulations, the observed transition from the molecular liquid to the network liquid is expected to be above the thermodynamic coexistence pressure. Indeed, both the density (2.30 g/cm³) and pressure (6.25 GPa) of the molecular liquid are significantly above the experimental values ($P \sim 0.8$ GPa [108]). These limitations can bias the results, and the observed structural

changes should be interpreted as qualitative.

Experimental data for the equation of state of liquid phosphorus in this region of the phase diagram is limited to two state points along the $T \sim 1300$ K isotherm [120]: $\rho = 1.57 \pm 0.16$ g/cm³ at $P = 0.84 \pm 0.2$ GPa for the molecular liquid, and $\rho = 2.67 \pm 0.14$ g/cm³ at $P = 1.19 \pm 0.2$ GPa for the network liquid, and indicated in Fig. 4.3. The figure shows that the calculated pressures at the experimental densities are significantly higher than the experimental values. The overestimate is approximately 1 and 5 GPa for the molecular and network liquid, respectively. For the molecular liquid this discrepancy could be related to the absence of attractive dispersion forces among the P₄ molecules when using the B-LYP functional as shown in Fig. 4.2. An estimate of the dispersion contribution to the pressure can be obtained by taking the dispersion term of the UFF force field [119]. This yields a downward pressure shift of around 0.5 GPa at the density of the experimental state point, bringing the calculated state point towards the experimental result. For the network liquid the discrepancy between the experimental and calculated pressure could be attributed to two factors. Firstly, as for the molecular phase, the absence of the dispersion forces in B-LYP will give rise to an overestimate of the pressure. Note, that this shift is larger than for the molecular liquid as it depends quadratically on the density. A second erroneous enhancement of the pressure could originate from an overestimate of the range of the repulsion in the interatomic interactions in the network phase. An indication for this is the slightly too long bond lengths in B-LYP calculations of small P clusters (Tab. 4.1). We did not attempt to quantify these effects as an estimate would be rather inaccurate. However, the arguments indicate that the effect is larger for the network liquid than for the molecular liquid, consistent with the observed discrepancies between the experimental and calculate pressures.

Overall, our B-LYP DF-MD results for the phase transition and the equation of state are significantly off the experimental results. This is in sharp contrast to the results of the LDA DF-MD simulation of Ref. [106] where the phase transition from the molecular phase to the network phase appeared at the experimental conditions. However, we think the seemingly accurate LDA result should be considered fortuitous. First of all, given the first-order nature of the transition and the small simulation system a significant hysteresis effects is to be expected giving yielding a transition pressure beyond the thermodynamic coexistence point. Secondly, both the description of the intermolecular and the interatomic interactions is rather poor in LDA. In the molecular phase LDA provides an erroneous attraction among P₄ molecules (Fig. 4.2) partly compensating for the absence of dispersion in local functionals. For small P clusters LDA gives a slightly too short bond length and a far too large binding energy (Tab. 4.1). These factors contribute to an underestimate of the pressure and an overestimate of the stability in the network phase.

4.5 Properties of the two liquids

4.5.1 Static properties

To quantify the local structure of the liquid we calculated the radial distribution function $g(r)$, the atomic coordination, and the molecular orientational correlation in the molecular phase. Fig. 4.4 shows the calculated $g(r)$ of the molecular liquid at the experimental coexistence density ($P = 2.2$ GPa, $\rho = 1.56$ g/cm³) and at a density just below the calculated

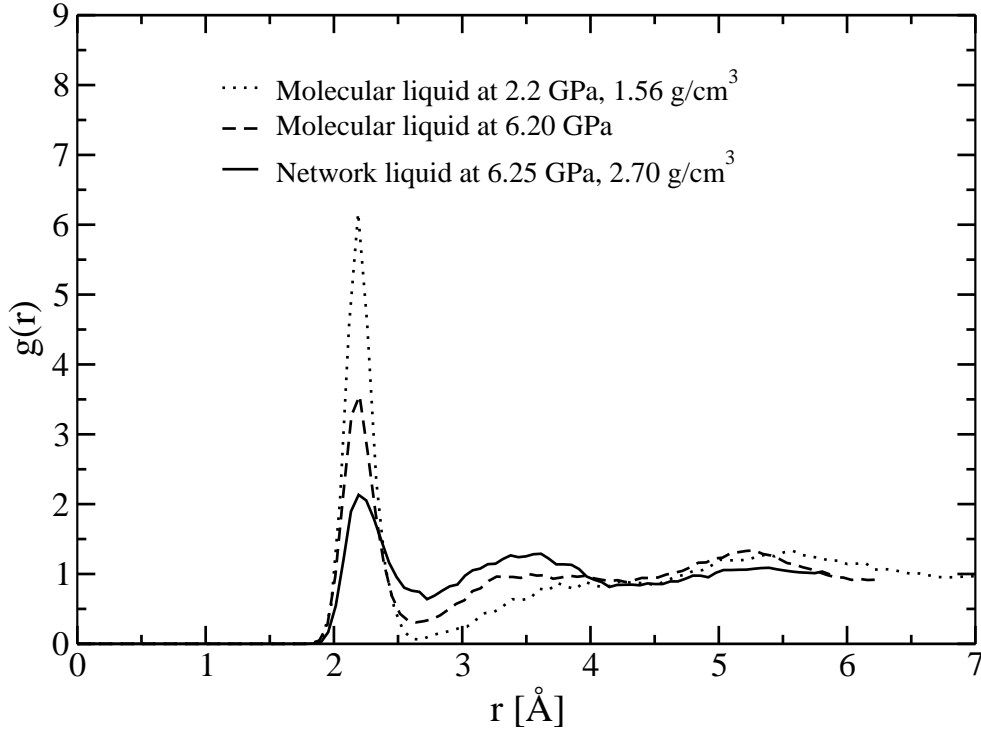


Figure 4.4: Comparison of the radial distribution functions at 2.2 GPa and 1.56 g/cm^3 , i.e. the experimental density near the coexistence (dotted line), at 6.20 GPa (dashed line), and at 6.25 GPa (solid line), just below and above the molecular to network transition. The network liquid density (2.70 g/cm^3) equals the experimental density near coexistence.

phase transition ($P = 6.20 \text{ GPa}$, $\rho = 2.20 \text{ g/cm}^3$). It also shows the calculated $g(r)$ of the network phase at a density just above the calculated phase transition ($P = 6.25 \text{ GPa}$, $\rho = 2.70 \text{ g/cm}^3$). First we will discuss the local structure of the molecular phase. The result should be considered qualitative, as a system of 16 P_4 molecules is too small to provide an accurate description of the local structure, providing just enough molecules for a complete shell of nearest neighbours. The shape of the $g(r)$ is typical for a molecular liquid. The first peak near 2.2 \AA coming from the intermolecular P-P bond is followed directly by a rather pronounced minimum after which a broad second peak centered at around 5 \AA appears. The second peak originates from neighbouring P_4 molecules. Note that the minimum becomes less pronounced with increasing density. This indicates more frequent near approaches and larger deformations of the P_4 molecules. This is confirmed by the atomic coordination. Near the phase transition, nearly 50 % of the atoms in the molecular liquid are four-fold coordinated, meaning that many apexes of the tetrahedral molecules have an apex of another molecule in the first shell, i.e. at a distance close to the intramolecular P-P bond length. The life time of this proximity is very short. In order to improve upon the description of the structure of the molecular liquid, we performed a NVT simulation of a larger system consisting of 54 P_4 molecules at the experimental coexistence density of 1.56 g/cm^3 . This system was prepared by cutting out a suitable fcc cell of 8 replicas of an equilibrated 16 P_4 molecule configuration. After a short equilibration of 0.25 ps, the large system was sampled for 0.75 ps. The calculated pressure of this sample was, within the error margin, the same as for the 16 tetrahedra sample at the same density.

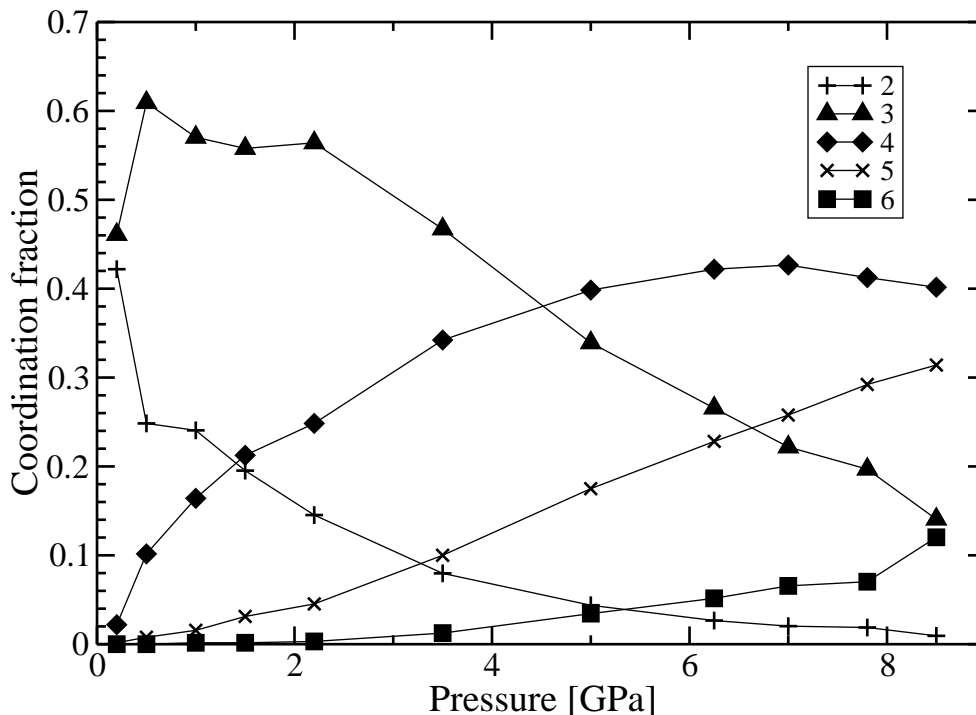


Figure 4.5: Coordination fractions for the network liquid at all the simulated state points.

The $g(r)$ of the molecular CoM's is also plotted in Fig. 4.2. Integrating the radial distribution for the large system up to the minimum at 7.5 Å yields a value of 12 for the average number of nearest neighbours.

For the large system we also analyzed the orientational correlation between neighbouring P_4 molecules using a careful analysis outlined in the appendix 4.7. Low temperature ($T=323$ K) neutron diffraction studies of molecular liquid phosphorus [122], showed strong angular correlations between the tetrahedra that extended over a range larger than in any other known molecular liquid. The DF-MD calculations of Hohl and Jones [111] at 500 K provided some indication of a long range orientational ordering. In our simulation at 1500 K we did not find any indication of orientational correlation. From this we conclude that, around this temperature, the P_4 molecules in the molecular liquid can be effectively considered spherical objects.

We now turn to the structure of the network liquid. The $g(r)$ plotted in Fig. 4.4 is typical for the simulated network liquid state points above 6 GPa. It shows a pronounced first peak, a clear second peak and a weak third peak at close distance from the first peak. The minima are clearly present, but only of moderate depth. Fig. 4.5 shows the coordination fractions for the network liquid state point. The distribution of coordination numbers was determined by counting for all atoms the number of atoms within the radius of the first minimum of the $g(r)$. As typical for a covalently bonded liquid, the dominant coordination increases with the density. For lower densities the coordination is mainly three-fold, whereas for the higher densities the four-fold coordinations dominate. Note that in the density region where the molecular liquid is experimentally found to be stable ($\rho < 2.5$ g/cm³), the dominant coordination is three-fold. This might be a manifestation of the liquid arranging itself into a proper local structure for the conversion into a molecular liquid. Obviously, this is prohibited in our simulations by hysteresis.

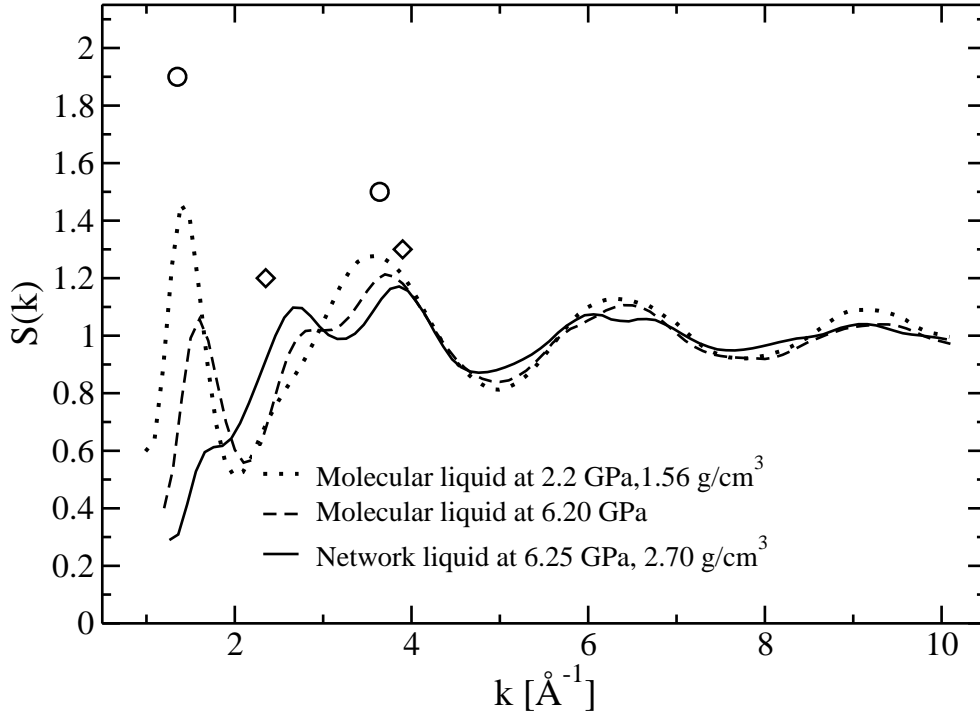


Figure 4.6: Comparison of the structure factors at the same state point as in Fig. 4.4. The circles (\circ) are the first two peaks of the structure factor for the molecular phase, as found in experiments [1, 107]. The diamonds (\diamond) are the first two experimental peaks for the network phase. The error margins for the experimental points are around 0.2.

To be able to directly compare to the experiments [1], we also calculated the structure factor $S(k)$. Fig. 4.6 shows the structure factors corresponding to the radial distribution functions of Fig. 4.4. The structure factor for the molecular liquid state shows a peak at $\sim 1.5 \text{ \AA}^{-1}$, related to the correlation between the CoM's of tetrahedral molecules, and is typical for liquids of tetrahedral molecules [123]. With increasing density, the position of this peak shifts slightly to the right indicating that the CoM's approach. The position of the first peak, together with the location of the second one (3.6 \AA^{-1}), related to the intramolecular correlations and the occurrence of a shoulder (around 2.9 \AA^{-1}), is in perfect agreement with the experimental data, whereas also the relative intensities of the peaks are well reproduced. Upon transformation from the molecular to the network liquid at 6.25 GPa, the peak below 2.0 \AA^{-1} disappears and the shoulder at 3.0 \AA^{-1} becomes a peak at 2.6 \AA^{-1} . At larger wavevectors the shape of the structure factor for both liquids is rather similar, indicating that the nearby interatomic correlations are comparable. With decreasing pressure the structure factor of the network phase (not shown) develops features typical for the molecular liquid. The peak at around 1.5 \AA^{-1} reappears, albeit with a lower height, and the second peak around 3.0 \AA^{-1} changes to become a shoulder of the peak at around 3.7 \AA^{-1} . The peak at around 1.5 \AA^{-1} cannot be related to correlations among tetrahedra, since at most a few P_4 molecules are present. Instead, it could indicate to the presence of local structures in the network liquid that are a precursor of the transition to the molecular liquid.

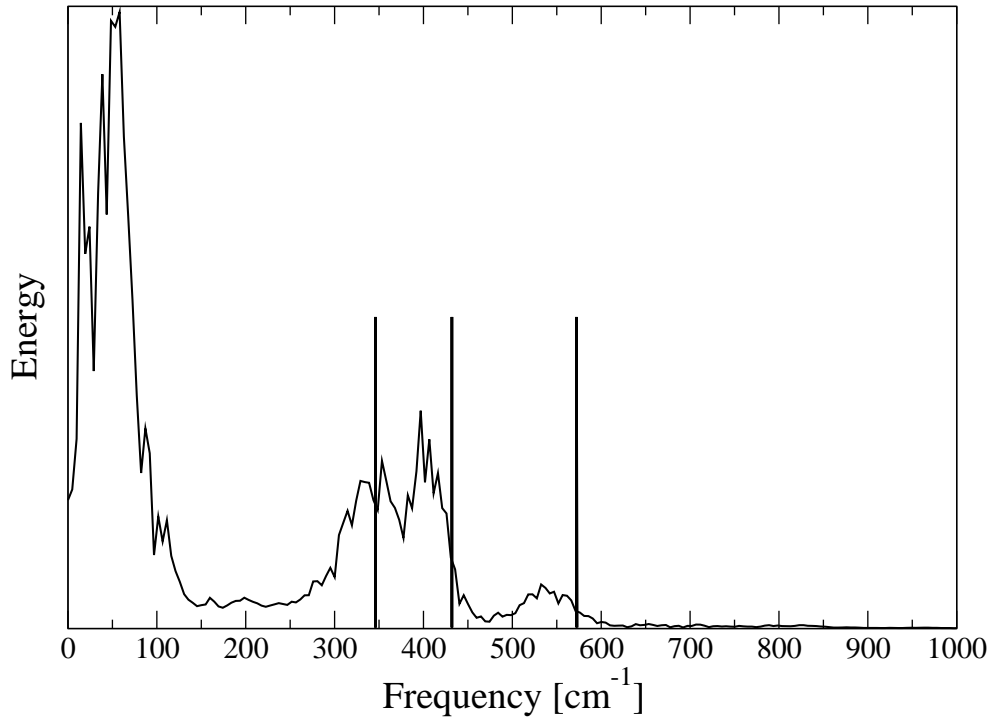


Figure 4.7: *Vibrational spectrum of the low density liquid, at $P = 2.2$ GPa. The vertical lines represent the three harmonic frequencies in the gas phase.*

4.5.2 Dynamical properties

From the mean-square displacement of the atoms we estimated the autodiffusion coefficient using

$$D = \frac{1}{6} \lim_{t \rightarrow \infty} \frac{d\langle r^2(t) \rangle}{dt}.$$

Here $r^2(t)$ denotes the normalized mean square displacement of all atoms and the brackets $\langle \dots \rangle$ indicate the time average. The derivative is evaluated from the slope of a linear fit of the calculated mean square displacement. The calculated autodiffusion coefficient is around 10^{-4} cm²/s for the molecular phase, while it is an order of magnitude smaller for the network phase, with a value of around 10^{-5} cm²/s. The network phase shows liquid-like behavior as the mean square displacement is a continuous increasing function with time.

We also determined the velocity autocorrelation function. From the lowest to the highest density, the decay time ranged from 0.2 to 0.5 ps for the molecular liquid, and from 0.5 to 0.1 ps for the network phase. The vibrational spectrum (Fig. 4.7) was obtained by Fourier transforming the velocity autocorrelation function. In the molecular phase the spectrum shows three broad peaks near the three (harmonic) vibrational frequencies of the gas phase P_4 . The peak centers are slightly red shifted with respect to the (harmonic) vibrational frequencies of the gas phase P_4 molecule. In the gas-phase the six vibrational modes consist of the two degenerate bending modes, three asymmetrical stretching modes, and one symmetric stretching mode. The harmonic frequencies for B-LYP are 346, 432 and 572 cm⁻¹, that are ~ 10 % lower than the experimental ones [124].

The vibrational spectrum of the network phase shows two broad bands around 150 and 350 cm⁻¹, and is rather different from that of the molecular liquid. For the molecular phase

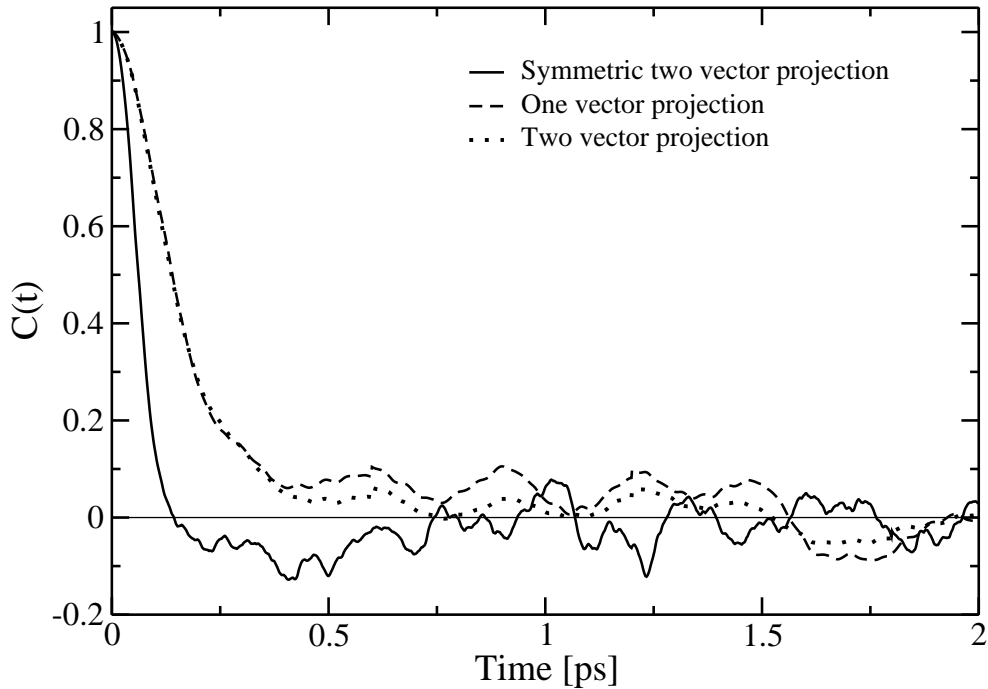


Figure 4.8: *Oriental time autocorrelation functions of the P_4 molecules from the 54 tetrahedra simulation of the molecular phase at $P = 2.2$ GPa. The three curves correspond to different definitions of the orientation (see text).*

we determined the relaxation of the rotational motion by calculating the orientational time autocorrelation of the P_4 tetrahedra. The symmetry of the tetrahedra requires some care in the assignment of the molecular orientation. We used a few (intuitive) criteria to define the orientation of the molecules: *a*) the projection of only one unit vector from the CoM of each molecule to one of the four molecules randomly chosen at each t_0 ; *b*) the sum of two projections of two unit vectors chosen as in *a*), and *c*) the sum of the projections of two unit vectors, as in *b*), but this time to the closest of the 12 equivalent orientations of the molecule at t_0 , to look for symmetry related correlations. The last criterion is expected to be relevant only in presence of a directional force between the molecules or an external field. Fig. 4.8 shows the results of the application of these three methods. The decay time obtained by method *a*) and *b*) is similar, implying isotropicity in the orientation of the instantaneous axis of rotation (if a tetrahedron would spin around the initial axis the criterion *a*) could give correlation 1). The decay time obtained from method *c*) is shorter since the ‘farthest’ configuration* is much ‘closer’ than in *a*) and *b*) to be reached.

4.5.3 Electronic properties

The molecular and network phases have distinct electronic properties. They have been characterized within the LDA approximation by Senda *et al.* [112]. Our results, obtained using the more accurate B-LYP functional, provide a similar picture. Figs. 4.9 and 4.10 shows the electronic density of states (DoS) averaged over 10 configurations for each liquid, both at 5 GPa. The DoS was obtained calculating the Kohn-Sham energies for 160 occupied

*The dual one, with new vertexes on the normal to the center of the faces of the initial configuration.

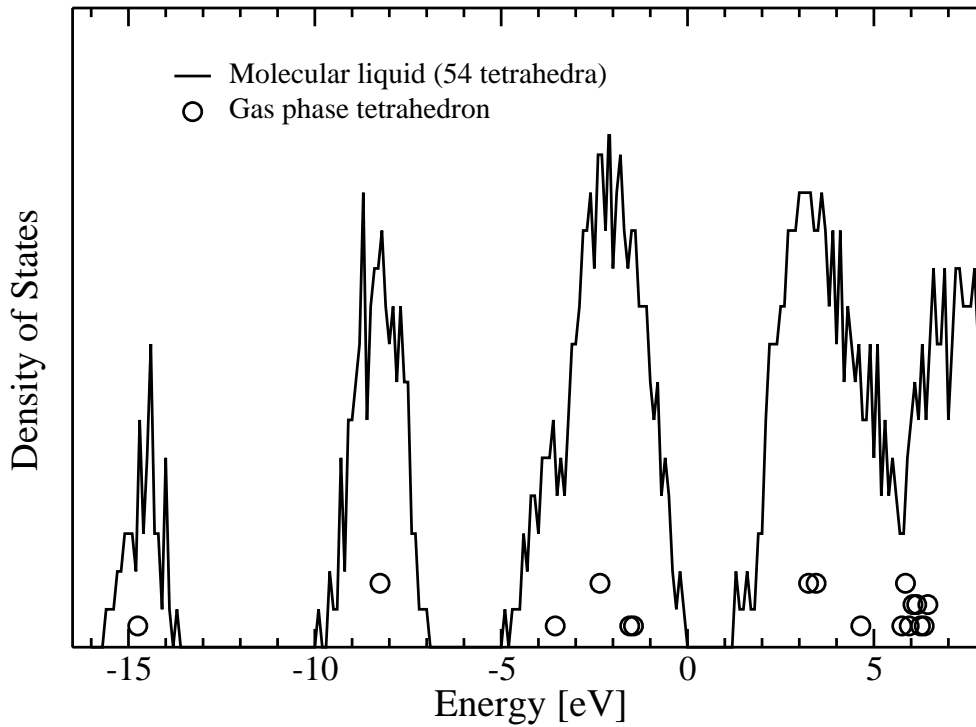


Figure 4.9: *Electronic DoS for the molecular liquid at $P = 2.2$ GPa. Gas phase P_4 molecule energy levels are plotted for reference; the height is proportional to the multiplicity of the level.*

and 160 non-occupied levels. For comparison we have also plotted the Kohn-Sham levels of the isolated tetrahedron and the isolated phosphorus atom. For both liquid phases no appreciable difference were found for samples at different pressures. For the network phase, which is expected to be metallic, the restriction of the k -point sampling to the Γ point could be insufficient. To assess this we also determined the DoS for a larger system of 256 atoms.

The DoS of the molecular liquid shown in Fig. 4.9 shows three broad bands below the Fermi energy that are spread around energy levels of the gas-phase P_4 molecule. There is a significant gap around the Fermi level indicating the non-metallic nature of the molecular liquid. The DoS of the network liquid deviates substantially from that of the molecular phase. Both the results for the 256-atom system, shown in Fig. 4.10, and the 64-atoms system (not shown) show a stepped profile with the first step spread around the -11 eV P-atom s-orbital level, and the second step spread around the -2.5 eV P-atom p-orbital level. Around the Fermi level there is some discrepancy between the large and small system. The 256-atom system shows a flat DoS profile, whereas for the 64-atom system there appears a small dip. This indicates that, for the small system, a Γ -point sampling of the Brillouin zone is not entirely sufficient. The absence of a gap around the Fermi level indicates that the network liquid is metallic. Fig. 4.11 shows the time evolution of the HOMO-LUMO gap of a simulation at 8.4 GPa during which a molecular to network phase transition occurs. It demonstrates that the structural transition is accompanied by an insulator-metal transition, with the density change and simultaneous breaking up of the P_4 tetrahedra is accompanied by a closing of the HOMO-LUMO gap.

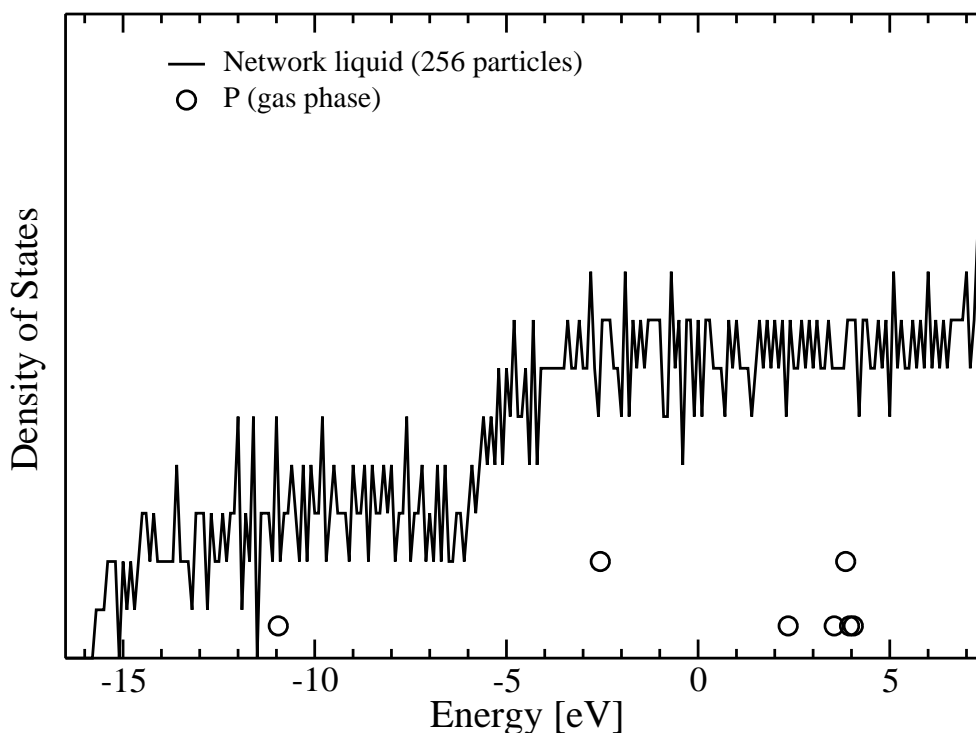


Figure 4.10: *Electronic DoS for the network liquid at $P = 6.25$ GPa. Gas phase P atom energy levels are plotted for reference; the height is proportional to the multiplicity of the levels.*

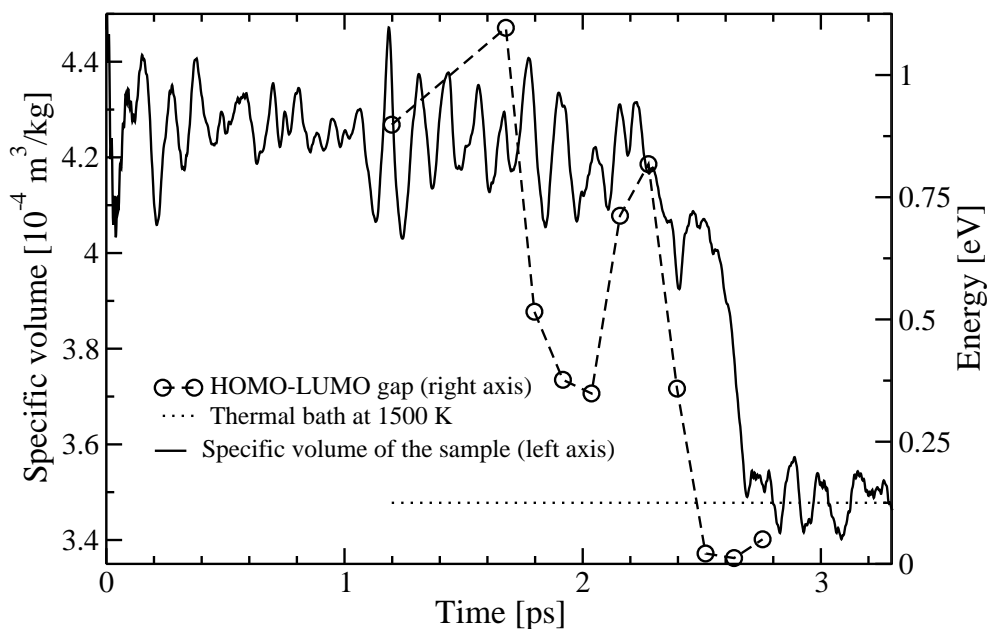


Figure 4.11: *Superposition of the time evolution of the specific volume (solid line; left axis) and the HOMO-LUMO gap (circles; right axis) for a 64-atom simulation at 8.5 GPa in which a molecular to network phase transition occurs. The dotted line gives the level of the average kinetic energy of the ions at 1500 K, and is plotted for reference.*

4.6 Summary and discussion

In summary, we reported a density-functional theory based atomistic simulation of the liquid – liquid phase transition of elemental phosphorus from a molecular to a network phase. We studied the transition along the $T=1500$ K isotherm by the constant-pressure Car-Parrinello molecular dynamics using a gradient-corrected functional (B-LYP) to describe the electronic structure.

The simulations of the molecular phase showed a liquid of P_4 molecules, whereas the network phase appeared clearly as an atomic liquid with coordinations ranging from mainly two and three-fold at lower densities to mainly four- and five-fold at higher densities. The structure was consistent with experimental diffraction data and results from LDA-based Car-Parrinello simulations. Orientational order of the P_4 molecules was absent. For both phase we observed a finite diffusion indicating the liquid nature of the systems.

At the experimental coexistence density the calculated pressure for the molecular phase is in reasonable agreement with the experimental value. However for the network phase we obtained a significantly higher pressure. This discrepancy should be attributed to the approximate nature of the B-LYP functional. Here it should be noted that the pressure is very sensitive to small changes in the interatomic forces. We observed a transition from the molecular to the network phase at a pressure of around 6 GPa, which is significantly above the experimentally value of around 0.8 GPa ($T=1500$ K). This discrepancy should be mainly attributed to hysteresis effects, that are expected to be significant for the small periodic system of the present simulations. The presence of hysteresis prevented the occurrence of the reverse network to molecular phase transition. Analysis of the electronic states showed that the density and structural change during the molecular to network phase transition is accompanied by an insulator to metal transition.

Analysis of the structural changes during the phase transition revealed that a chain of linked opened up (‘butterfly’) P_4 molecules is crucial for triggering the transition of the molecular phase to the network phase. The appearance of ‘butterfly’ P_4 molecules is also reflected in the electronic structure: the spike in the time-evolution of the HOMO-LUMO gap around 2 ps in Fig. 4.11 can be related to the formation of two couples of ‘butterfly’ molecules (as visually observed in the trajectory). The identification of such structures is important for the understanding of the kinetics of the phase transition, that requires identification of local structures, that act as a seed for the phase transition. The ‘butterfly’ chain could serve as such a structure. Obviously, these observations could be biased by the relatively small system size. A more conclusive study would require simulations with larger system sizes. In our future work we aim to achieve this by employing empirical force fields that are obtained from accurate ab initio simulations.

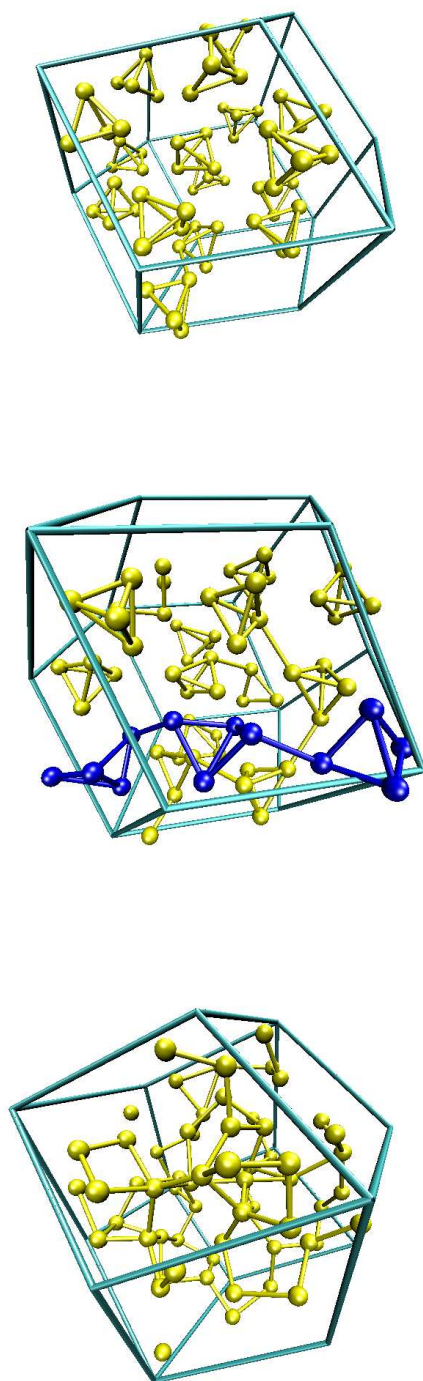


Figure 4.12: Three snapshots across the LLPT at 6.25 GPa. The top panel is representative of the molecular phase, the bottom panel shows a typical configuration of the network phase. In the center panel we have highlighted the chain of three ‘butterfly’ molecules that initiates the transition.

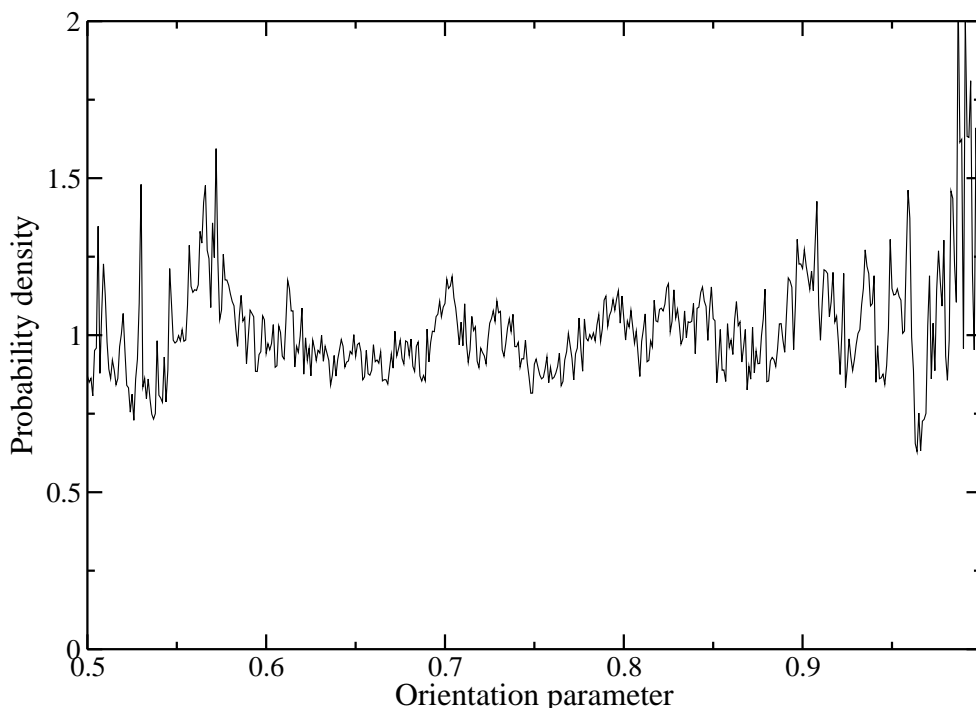


Figure 4.13: Ratio between the distribution of orientations of the tetrahedra in the molecular liquid and the distribution of randomly oriented tetrahedra. The reciprocal orientation is sampled between molecules whose centers of mass are closer than 6.5 \AA , value taken observing the $g(r)$ in Fig. 4.2. The sample is at 1.56 g/cm^3 .

4.7 Appendix. Definition of the orientation parameter

A complete analysis of the spatial correlations should be carried out expanding the total pair distribution $g(\mathbf{R}_1, \mathbf{R}_2)$ in a series of spherical harmonics, as a function of the 6 needed variables while taking in account the peculiar symmetry of the P_4 molecule. This series is known to be slowly convergent [125] even for linear molecules, and the tetrahedral symmetry imposes null contribution for many of the lower order harmonics. Furthermore, in order to give meaning at the $g(\mathbf{R}_1, \mathbf{R}_2)$, one needs to observe the behaviour of the function for only one variable, while keeping all the other fixed and eventually parametrically changing them. Practically, for such a liquid, one needs to know whether some peculiar reciprocal orientations between two molecules are preferred, such as ‘face to face’ rather than a ‘apex to apex’ or a ‘face to apex’.

This result can be achieved exploiting the geometrical features of the tetrahedral shape. One can define for each of two selected tetrahedra a set of four unit vectors from the CoM’s pointing to the four vertexes ($\hat{\alpha}_i$ for a tetrahedron A and $\hat{\beta}_i$ for a tetrahedron B), In the same way one can define four unit vectors from the CoM’s to the outward perpendicular directions to the four faces (\hat{a}_i for A and \hat{b}_i for B). For a perfect tetrahedron it is not needed to define the two sets of vectors, being possible to pass from one to the other with an inversion of coordinates; even though the P_4 molecules are found to be always ‘close’ to an ideal tetrahedron, we preferred to release this constraint and use the two independent set of four

unit vectors. To look for particular reciprocal orientation is now crucial to project these unit vectors on the (oriented) unit vector joining the CoM's of two molecules A and B (\hat{r}_{AB}). Looking for the 'face to face' configuration, for instance, one has to consider the maximum projection of a unit vector normal to the faces of tetrahedron A ($\max_i(\hat{a}_i \cdot \hat{r}_{12})$) and the minimum projection of a unit vector normal to the faces of tetrahedron B ($\min_j(\hat{b}_j \cdot \hat{r}_{12})$). If the 'face to face' configuration is preferred, the joint distribution of these two quantities, sampled on the liquid, would show more points close to the values (1;-1) than in a random distribution of orientations. Alternatively, to have a more clear function of one variable, one can safely consider the quantity $[\max_i(\hat{a}_i \cdot \hat{r}_{12}) - \min_j(\hat{b}_j \cdot \hat{r}_{12})]/2$, bounded between 1/3 and 1. Fig. 4.13 shows the probability for two neighbour molecules (defined as molecules closer than 6.5 Å, consistently with the molecular $g(r)$, Fig. 4.2) to be found 'face to face', normalized on the random distribution of two unrelated tetrahedra: no particular departure from the random distribution in the area near the value 1 can be appreciated. The same result, once defined the suitable quantities, is found for 'apex to apex' or 'apex to face' reciprocal orientation. Even arbitrarily looking at molecules whose CoM are closer than 5 Å we can not see any correlation between the orientation, the same is valid at the higher densities observed [†].

[†]The correlation at other densities were sampled on the small 16 tetrahedra system.

Simulating the phosphorus liquid – liquid phase transition up to the critical point

Ich sage euch: man muss noch Chaos in sich haben, um einen tanzenden Stern gebren zu können.

Ich sage euch: ihr habt noch Chaos in euch.

I tell you all: one must have chaos left in oneself, to be able to give birth to a dancing star. I tell you all: you do have chaos left in yourselves.

5.1 Introduction

In this chapter we report on a DF-MD study of the phosphorus LLPT at various temperatures. In the previous chapter we focused on the LLPT along the 1500 K isotherm. Here, we aim to determine the pressure-temperature dependence of the LLPT and, more interestingly, to find and characterize the critical point that ends the LLPT coexistence line.

Monaco *et al.* [108] reported on a experimental study of the LLPT of phosphorus for temperatures up to ~ 2500 K. They found that the transition pressure decreases with increasing temperature and that, as already observed in [1, 106], the transition can be obtained both by increasing the pressure at constant temperature and increasing temperature at constant pressure, yielding the same values for the coexistence state points. Furthermore, the authors note that the magnitude of the slope of the coexistence line, that is negative, is decreasing with increasing temperature towards zero slope. They suggest that this indicates the approach of the critical point. However, at the highest temperature probed in [108] (~ 2500 K), no signs of criticality were found. We studied the LLPT also at temperatures beyond 2500 K.

5.2 Method

For the DF-MD part, we used the same set up as for the previous chapter. We employed the B-LYP gradient-corrected functional with a plane-wave basis set, sampled at the Γ point,

truncated at a kinetic energy (E_{cut}) of 25 Ry. We used semi-local norm-conserving Martins-Troullier pseudopotential [113] constructed with an excited positively charged valence-electron configuration $s^{1.75}p^{2.25}d^{0.50}$, using core-radii of 1.5, 1.7, and 1.9 a.u. for the $l = s, p,$ and d terms, respectively. The pseudopotential was transformed into the Kleinman-Bylander form [114] with $l = d$ as the local term. The fictitious mass of the electronic degrees of freedom was set to 1000 a.u and the time step for the integration of the equations of motion to 5 a.u. (0.12 fs). The ionic temperature was controlled via a Nosé-Hoover chain thermostat of length 4 (coupled to the frequency of 300 cm^{-1}). The Nosé-Hoover chain thermostat of length 4 for the electronic degrees of freedom was targeted to an energy of 0.035 eV, with a coupling frequency of 15000 cm^{-1} . For the barostat, we chose $E_{\text{cut}}^{\text{eff}} = 25 \text{ Ry}$, $E_{\text{cut}} = 35 \text{ Ry}$, $A = 40 \text{ Ry}$ and $\sigma = 6 \text{ Ry}$ (see Eq. 3.47 for the meaning of the symbols). The simulations were performed using a periodic fcc cell.

5.3 Description of the transitions

Fig. 5.1 shows the calculated temperature-density phase diagram for the phosphorus LLPT. We show the transitions we determined (solid arrows or ellipses labelled with numbers), together with a selection of the state points visited in our simulations. The dotted arrows indicate the paths through the points, i.e. the history of the samples. We started from a 16 tetrahedra (64 atoms) sample equilibrated at 1 GPa and 1500 K (a); this state point was visited during the equation of state calculation at 1500 K, reported in the previous chapter. The figure also shows the state point at 2.2 GPa and 1500 K (α) that was the initial sample of the calculation we performed at 1500 K. Therefore we have also connected point α to transition ‘0’, i.e. the same reported in the previous chapter, and the arrow connecting α to point a . The paths are either at constant temperature or at constant pressure. In the plot we show the measured rather than the imposed temperature*, so that points at the same imposed temperature are not on the same vertical line. However, the variation in temperature for the different state points is within the error margin of $\sim 50 \text{ K}$, so that the points can be considered at the same temperature. Typically, the target temperature was increased by steps of 100 K, by velocity scaling at each MD step over typically several hundreds steps. The pressure was typically increased by steps of 0.2 GPa. Most of the state points were simulated for at least 4 ps[†]. Note that typical decay times of the velocity autocorrelation functions were around 0.5 ps.

A straight dashed line in Fig. 5.1 connects the LDF state points of the simulations at $T=1500 \text{ K}$ and $T=3500 \text{ K}$ that showed a LDF to HDL transition. A similar line connects the HDL state points of these two simulations. We note that the other state points, before and after the transitions, lay fairly close to these dashed lines. Since the LDF state points along the (bottom) line are at the mechanical stability limit for the LDF, they can be interpreted as one of the spinodal lines for the LLPT.

In the following list we give the detail of each transition shown in the Figs. 5.1. In contrast to the plot, here we indicate the imposed rather than the measured temperatures. The measured values of temperatures, pressures and densities are given in Table 5.1.

*In detail, the temperature was estimated by calculating the average of the kinetic energy of the nuclei.

†All the state points reported in Table 5.1 were simulated for at least 4 ps. All the other, not reported state points, were at least simulated for 1 ps.

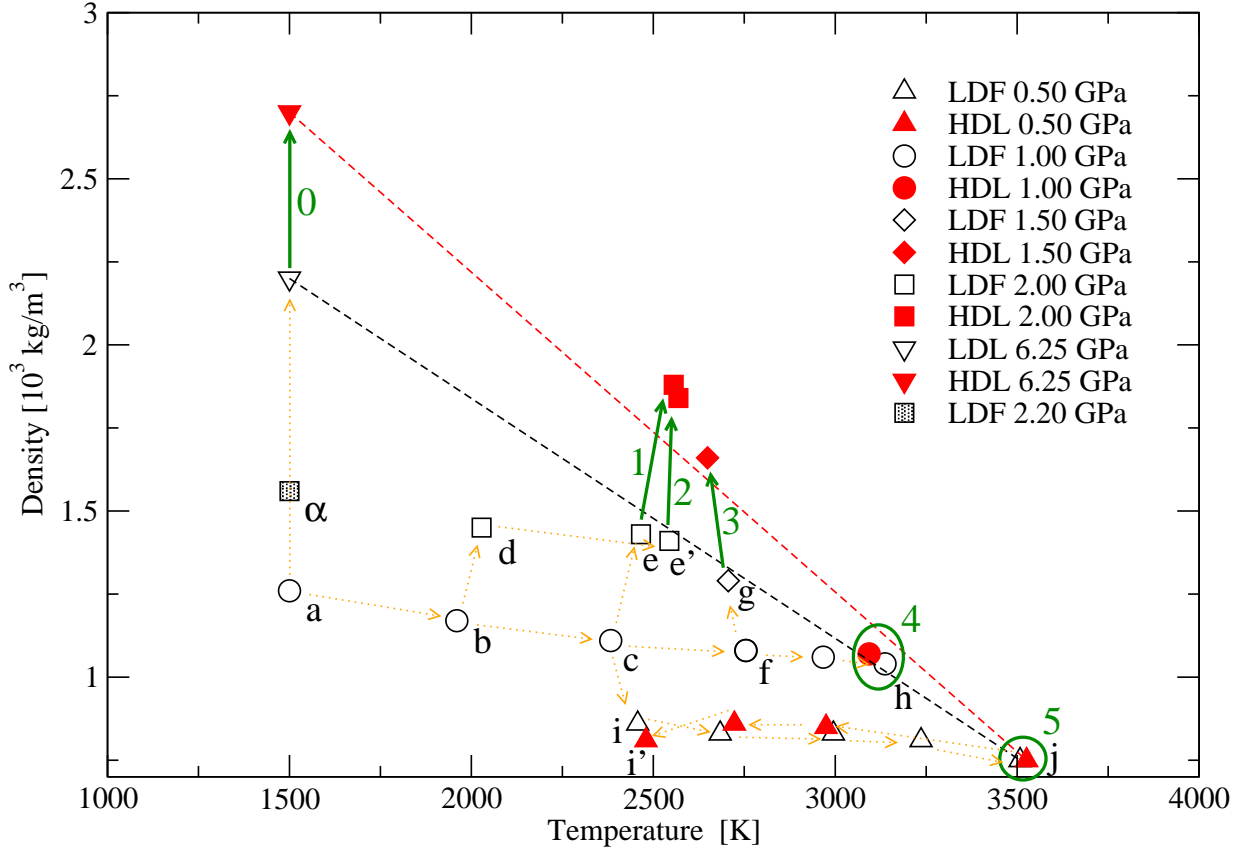


Figure 5.1: Temperature-Density phase diagram for the phosphorus LLPT. The transitions are shown either with numbered solid arrows connecting the point in LDF to the point in the HDL, or with (numbered) ellipses surrounding such points. The symbols represent a selection of the state points visited to reach the transition points; the dotted arrows describe paths followed. The two dashed lines connect the two LDLs and the two HDLs of the two extreme transitions (i.e. at $T=1500$ and $T=3500$ K).

1. At constant pressure (1.0 GPa), from 1500 K (*a*) to 2500 K (*c*). Then, at constant temperature (2500 K) from 1.0 to 2.0 GPa (*e*). The transition initiated after 2.4 ps and lasted[‡] for 3 ps.
2. At constant pressure (1.0 GPa), from 1500 K (*a*) to 2000 K (*b*). Then at constant temperature (2000 K) from 1.0 to 2.0 GPa (*d*). Then at constant pressure (2.0 GPa) from 2000 K up to 2500 K (*e'*). The transition initiated after 3 ps and lasted for 1.1 ps.
3. At constant pressure (1.0 GPa), from 1500 K (*a*) to 2700 K (*f*). Then at constant temperature (2700 K) from 1.0 up to 1.5 GPa (*g*). The transition was obtained twice: from the run at 1.4 GPa and 2700 K we extracted two initial configurations for the subsequent runs at 1.5 GPa and 2700 K. The two transitions had rather different histories : one initiated after 3 ps and then lasted 0.7 ps, the other initiated after

[‡]We say that the transition “initiates” when the first tetrahedron break irreversibly, and “lasts” until the last of the *initial* tetrahedra breaks. Tetrahedra, that form and break during and after the transition, comprising a different set of four atoms compared to any of the initial tetrahedra, are not considered.

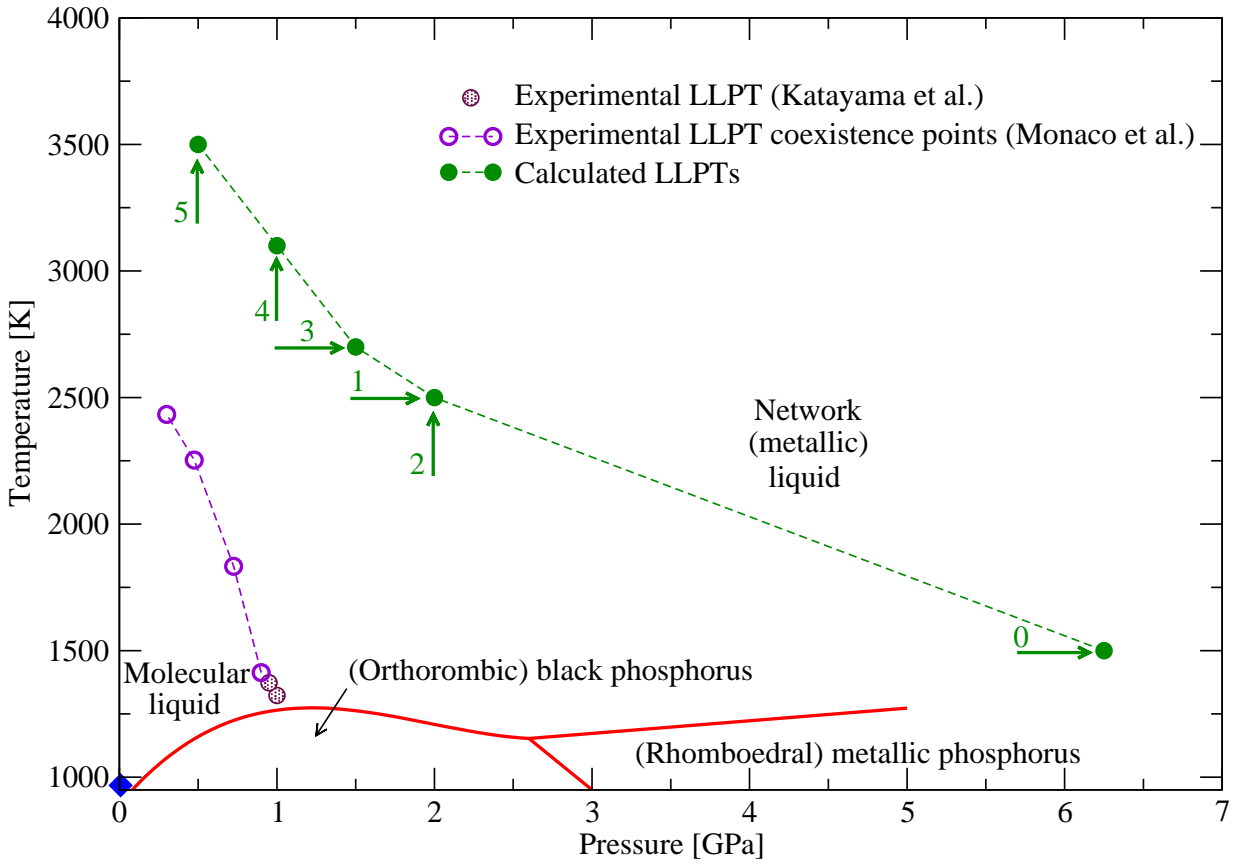


Figure 5.2: Pressure-Temperature phase diagram for the phosphorus LLPT. Our data (full circles) are state points of the occurred transitions. The arrows indicate whether the transition occurred along a constant temperature (vertical arrow) or a constant pressure (horizontal arrow) path. The numbers agrees with the labelling in Fig. 5.1. The shaded circles are experimental transition points (Katayama et al. [1]). The open circles (Monaco et al. [108]) are experimental coexistence points. The solid/liquid and solid/solid (solid lines) boundaries are taken from [104] and references therein. The full diamond at the bottom left of the plot is the critical point ending the (low density) liquid boiling line [105].

only 0.4 ps and lasted 1.5 ps; on the other hand, the two transitions started and ended in almost overlapping state points. This given, only one of these two transitions is shown in the plot.

4. At constant pressure (1.0 GPa), from 1500 K (a) to 3100 K (h). The transition initiated after 1.2 ps and lasted for 3 ps.
5. At constant pressure (1.0 GPa), from 1500 K (a) to 2500 K (c). Then at constant temperature (2500 K) from 1.0 to 0.5 GPa (i). Then at constant pressure (0.5 GPa) from 2500 up to 3500 K (j). Above 3000 K the step in temperature was changed to 250 K. The transition initiated after 1 ps and lasted for 5.5 ps. After the LLPT, the liquid was cooled in steps of 250 K down to 2500 K.

Obtaining a transition at a certain state point was not sufficient to report it on the

Low density fluid								
P [GPa]	Target T [K]	T [K]			ρ [10^3 kg/m 3]			
0.50	(2500)	2457	\pm	77	0.86	\pm	0.03	(i)
0.50	(2700)	2684	\pm	104	0.83	\pm	0.02	
0.50	(3000)	2995	\pm	56	0.83	\pm	0.02	
0.50	(3250)	3236	\pm	47	0.81	\pm	0.01	
0.50	(3500)	3508	\pm	59	0.75	\pm	0.01	(j)
1.00	(1500)	1505	\pm	14	1.26	\pm	0.01	(a)
1.00	(2000)	1960	\pm	58	1.17	\pm	0.02	(b)
1.00	(2500)	2383	\pm	107	1.11	\pm	0.01	(c)
1.00	(2700)	2754	\pm	61	1.08	\pm	0.02	(f)
1.00	(3000)	2983	\pm	94	1.05	\pm	0.02	
1.00	(3000)	2991	\pm	46	1.03	\pm	0.02	(h)
1.00	(3100)	3137	\pm	50	1.04	\pm	0.01	
1.50	(2500)	2450	\pm	50	1.28	\pm	0.02	
1.50	(2700)	2694	\pm	90	1.25	\pm	0.01	(g)
2.00	(2000)	2028	\pm	27	1.45	\pm	0.01	(d)
2.00	(2500)	2466	\pm	33	1.43	\pm	0.01	(e)
2.00	(2500)	2544	\pm	50	1.41	\pm	0.02	(e')
2.00	(2700)	2687	\pm	24	1.42	\pm	0.01	
2.20	(1500)	1512	\pm	20	1.56	\pm	0.01	α

High density liquid (and fluid)								
P [GPa]	Target T [K]	T [K]			ρ [10^3 kg/m 3]			
0.5	(2500)	2480	\pm	15	0.81	\pm	0.03	(i')
0.5	(2750)	2723	\pm	14	0.85	\pm	0.04	
0.5	(3000)	2975	\pm	19	0.85	\pm	0.04	
0.5	(3500)	3526	\pm	60	0.75	\pm	0.01	
1.0	(2500)	2456	\pm	14	1.28	\pm	0.03	
1.0	(3100)	3093	\pm	48	1.07	\pm	0.01	
1.5	(2500)	2549	\pm	49	1.66	\pm	0.01	
1.5	(2700)	2682	\pm	50	1.58	\pm	0.02	
2.0	(2500)	2556	\pm	23	1.88	\pm	0.02	
2.0	(2500)	2569	\pm	91	1.84	\pm	0.02	
2.0	(2700)	2789	\pm	28	1.81	\pm	0.02	

Table 5.1: Values of pressure, target and measured temperature, and measured density, for selected state points. The last column reports the label used to indicate the same state point in Fig. 5.1.

plot. The state point sampled just before the state point in which a transition occurred was simulated longer; to do that, we ran from the final sample, the same that served as initial sample of the run in which we obtained the transition, continuing with the final set of coordinates and velocity (both of the nuclei and the electronic degree of freedom) for 3-4 ps more. If a transition was obtained, the procedure was repeated until no transition

was obtained in the time span set. For example, the (pressure induced) transition at 2500 K ('1') firstly occurred at 3 GPa; subsequent runs, revealed it occurred also at 2.4 and 2.0 GPa, while it did not at 1.8 GPa for 4 ps. Thus, the state point at 2500 K and 2.0 was considered as the lower limit for the (spontaneous) transition at 2500 K to occur. Also at 2700 K (transition '3') we incurred in a similar situation: the transition was firstly found at 2.0 GPa and then assessed at 1.5 GPa. For transition '2', we did not obtain any transition at 2.0 GPa and 2400 K. Regarding transition '4', we did not find a transition at 3000 K and 1.0 GPa. Concerning transition '5', no signs of transition were seen at 3250 K and 0.5 GPa. Needless to say, the relatively small size of the sample, together with the relatively short time of the runs, could hinder a transition that could have occurred at lower temperatures and/or pressures.

In Table 5.1 we show the pressure, the target and measured temperature, and the measured density of a larger set of points than plotted in Fig. 5.1. Still, these are not all the points sampled, but only those that were simulated for at least 4 ps. The measured pressure always corresponded to the target one, within 0.01 GPa. The averages were determined after a brief relaxation time (typically 0.5 ps) from data collected for at least 3.5 ps. The rather short relaxation time is a-priori justified a) by the small perturbation (0.2 GPa or 100 K) imposed to the system on moving from a state points to the next, and, a posteriori, b) by the fact that the velocity autocorrelation functions decay in times not longer than 0.5 ps.

In Fig. 5.2 we show the calculated pressure-temperature phase diagram of phosphorus compared with experimental data, in the region relevant for the LLPT. The experimental knowledge of the (stable) solid phases is reported through their boundaries (solid lines, from Ref. [104] and references therein). The full diamond at the bottom left of the plot is the critical point ending the (low density) liquid/gas transition line. The position of that critical point implies that the LDF is indeed a supercritical fluid. The shaded circles are experimental *transition* points (Katayama et al. [1]). With 'transition point' we mean state points in which the system was prepared in the LDF phase and that rapidly transformed into the HDL phase. From these shaded points, upon a 0.02 GPa decrease of the pressure, the system transformed back into the LDF phase. The open circles (Monaco et al. [108]) are experimental *coexistence* points: the X-ray diffraction pattern measured at these points suggested indeed a coexistence of the LDF and HDL phase. Our data (full circles) refer to transitions occurred in our 64-atoms sample at the state points shown. The arrows indicate whether the transition occurred along a constant temperature (vertical arrow) or a constant pressure (horizontal arrow) path. The numbers are consistent with the labelling in Fig. 5.1. In paragraph 5.6 we will further discuss the comparison between the calculated and experimental LLPT line.

In Figs. 5.5, 5.3, and 5.6 we show the evolution of the density of simulations that showed a LLPT (we chose transitions labelled with '1', '4', and '5' in Figs. 5.1 and 5.2). In all these figures we indicate the moment the transition sets in and the moment the transition ends. Note that, the actual simulation lasted longer than what is shown, both before and after: average densities were obtained from collecting data also from outside the interval we display.

In Fig 5.5 (T=2500 K) we note that the rise of the density, that characterizes the transition, starts markedly after the first breaking. The transition, i.e. the overall breaking of the tetrahedra, took 3 ps. The two circles enclose short time spans in which two

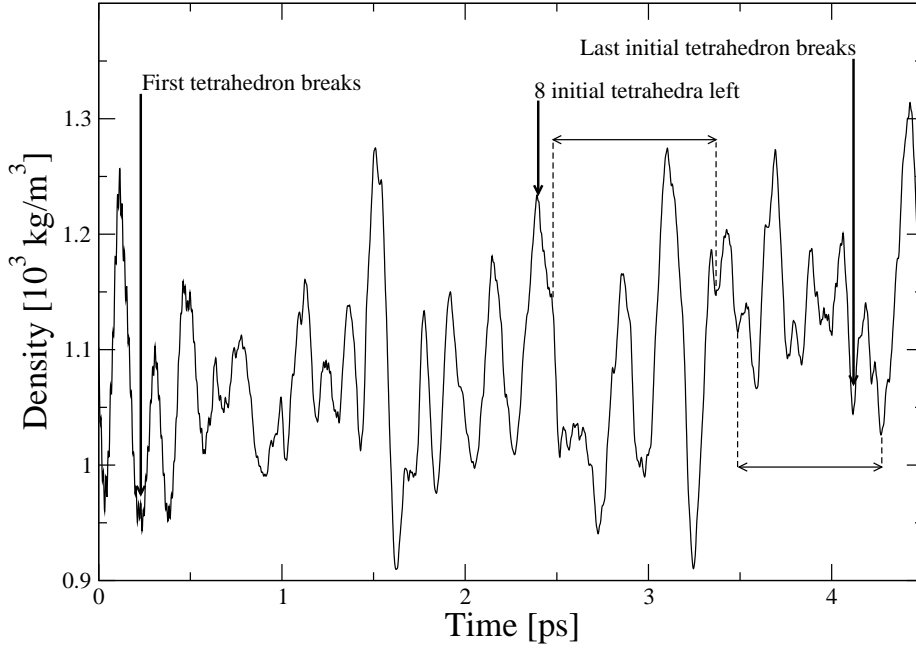


Figure 5.3: Evolution of the density during the simulation regarding the transition at 3100 K and 1.0 GPa (transition ‘4’). We indicate the initial and final point of the transition. Here the living time interval of two newly formed tetrahedra are marked by the double arrows. This state point was actually simulated longer than the window here shown and the average densities, before and after the transition, are sampled outside from this time interval.

tetrahedra ‘newly formed’ and quickly broke up, when the sample was in the HDL phase. The newly formed tetrahedron consisted of atoms that did not previously form a single tetrahedron. Looking at the snapshots of the trajectories, a ‘newly formed’ tetrahedron is recognized when four atoms topologically arrange in a tetrahedron[§] and none of them has any other bonds with the surrounding atoms.

The density evolution for the transition at $T=3100$ K, reported in Fig. 5.3, shows a change of only $\sim 3\%$, so that the change is hardly visible in the plot, given the large fluctuations. In the time intervals marked by the double arrows, two newly formed tetrahedra survive for a time of the order of 1 ps.

In Fig. 5.4 we show three representative snapshots taken from the simulation at 1.0 GPa and 3100 K, across transition ‘4’. From top to bottom, these snapshots are taken at a time $t \simeq 1, 3, 4.4$ ps, respectively, where the time scale agrees with that of Fig. 5.3. We have highlighted four atoms that at $t \simeq 3$ ps belong to a ‘newly formed’ tetrahedron, whereas at $t \simeq 1$ ps they belong to different tetrahedra. At $t \simeq 4.4$ ps three of them still belong to a triangular cluster and the fourth was taken away into a dimer after a collision of the tetrahedron with a triangular cluster. The apparently single, non bonded atoms that can be seen especially in the bottom snapshot are an artefact: these atoms are actually connected to other atoms, via periodic boundary conditions.

In Fig. 5.6 we show the density evolution for the transition at $T=3500$ K; we found

[§]This means that each of them is bonded, i.e. is closer than 2.8 \AA , to the other three atoms, without any other requirement on bond lengths and angles.

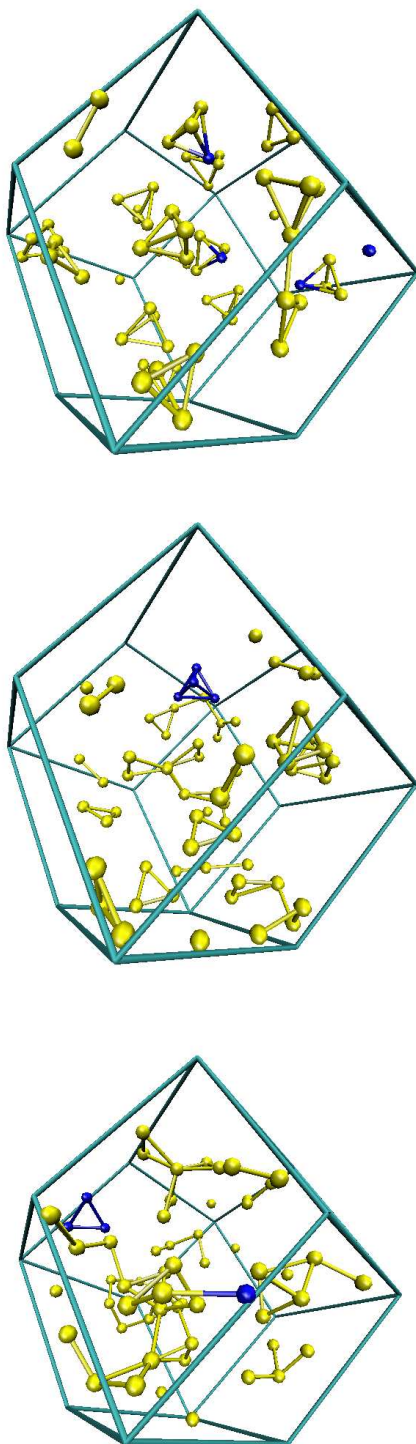


Figure 5.4: Representative snapshots of the transition at 1.0 GPa and 3100 K, with the fcc box explicitly shown. In all the snapshots we highlight the same four atoms that in the center snapshot belong to a ‘newly formed’ tetrahedron, while in the top and bottom belong to different structures.

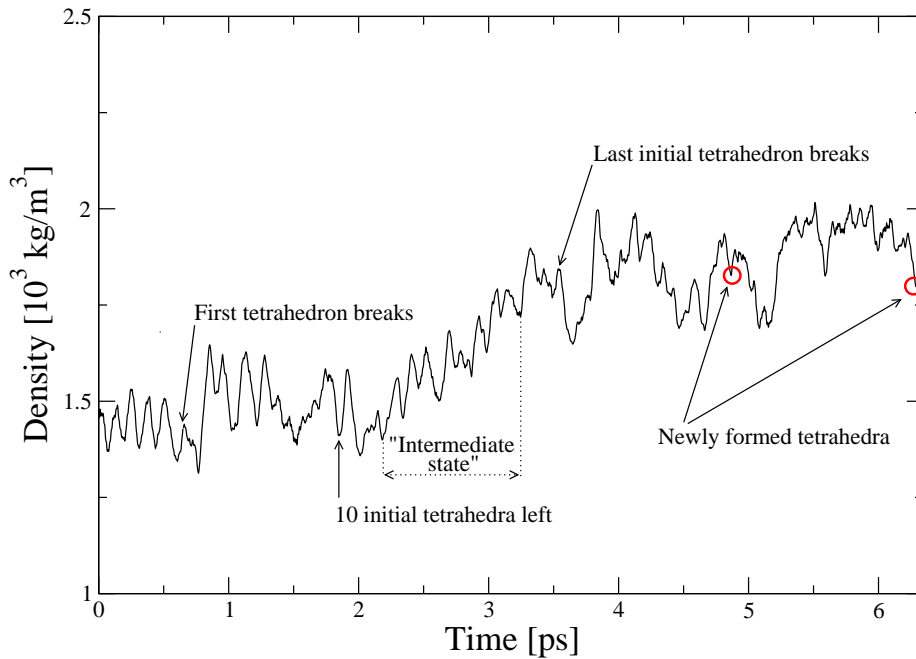


Figure 5.5: Evolution of the density during the simulation regarding the transition at 2500 K and 2.0 GPa (transition ‘1’). We indicate the initial and final point of the transition. The two circles enclose short time spans in which two tetrahedra ‘newly formed’ and quickly decayed. Within interval labelled as ‘Intermediate state’ were selected points to calculate the structure factor shown with a dashed line in Fig. 5.8. This state point was actually simulated longer than the window here shown and the average densities, before and after the transition, are sampled outside from this time interval.

that the average densities before (the LDF) and after (the HDL) the transition were the same, within the error margin of $0.01 \cdot 10^3 \text{ kg/m}^3$. This common density is marked with a dotted line.

Visual inspection of the trajectories for all the transitions revealed some characterization of the transition mechanism. At the two lower temperatures (2500 and 2700 K), all the four transitions we could observe were initiated by the formation of a chain of three ‘butterfly’ molecules[¶]: this led to the disruption into smaller clusters of the three P_4 molecules involved. In both cases we also observed several collisions between two tetrahedra, leading only to a temporary breaking of one of two bonds of the two molecules involved. The broken bonds soon reformed, without any exchange of atoms. A similar mechanism is also observed for the transition at 1500 K. The only difference we noticed at this higher temperatures was in that single tetrahedra could fluctuate into the a ‘butterfly’ shape without any correlation with the neighbours. In contrast, at 1500 K the opening of one bond only occurred when a neighbouring tetrahedron simultaneously did the same, so that the two molecules temporarily linked. After on or two of those chain of three ‘butterfly’ molecules formed, rather complicated clusters of many atoms formed. After this description we can specify that the “first initial tetrahedron breaking” referred to in Fig. 5.5, is actually a

[¶]A ‘butterfly’ molecule, introduced by Pauling and Simonetta [121], and already referred to in the previous chapter, is a tetrahedral P_4 where one of the six bonds is opened, so that the molecule assumes a flattened shape.

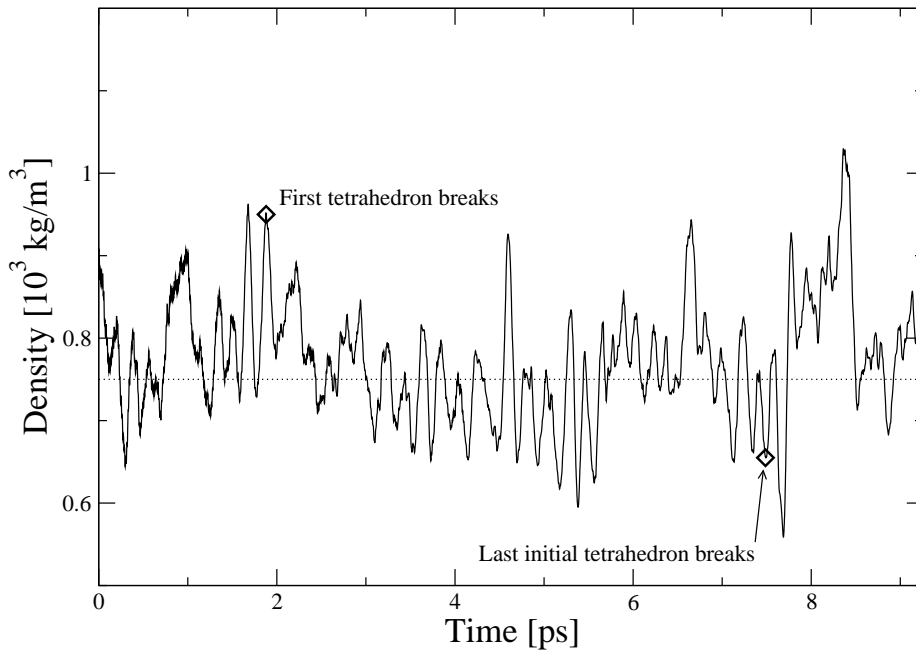


Figure 5.6: Evolution of the density during the simulation regarding the transition at 3500 K and 0.5 GPa (transition ‘5’). We indicate the initial and final point of the transition. This state point was actually simulated longer than the window here shown and the average densities are sampled outside from this time interval. Here the average densities, before and after the transition, coincide: this common average density is marked by the dotted line.

simultaneous breaking of three tetrahedra.

At the two higher temperatures (3100 and 3500 K) a collision between two tetrahedra could already irreversibly yield smaller molecules, whose subsequent collisions with remaining tetrahedra propagated the transition. For the transition to set in it was needed that from both colliding tetrahedra an atom detached: in fact both observed transitions were initiated by the collision of two tetrahedra, yielding two triangular clusters and a dimer. We observed some typical paths for the breaking of the tetrahedra: 1) a collision of a tetrahedron with a triangular cluster, yielding 2 dimers and a triangular cluster, that was never the original one; 2) a collision of a tetrahedron with a dimer yielding two triangular clusters. We did not observe the direct dissociation of a tetrahedron into two dimers. In these cases the “first initial tetrahedron breaking” comprises two simultaneous breakings.

5.4 Structural properties

Fig. 5.7 shows the radial distribution functions (rdf’s) obtained from the simulations that showed a transition. The LDF-side state points for the two transitions at 2500 K (i.e. ‘1’, at increasing pressure and ‘2’, at increasing temperature) were almost identical. This also holds for the HDL-side points. Therefore, the rdf’s at 2500 K were reported only for transition ‘1’. The same holds for the two transitions at 2700 K.

The figures show that the rdf’s of the LDF’s at different temperatures are rather similar. The local structure of the P_4 molecules dominates, with the first peak indicating the atoms

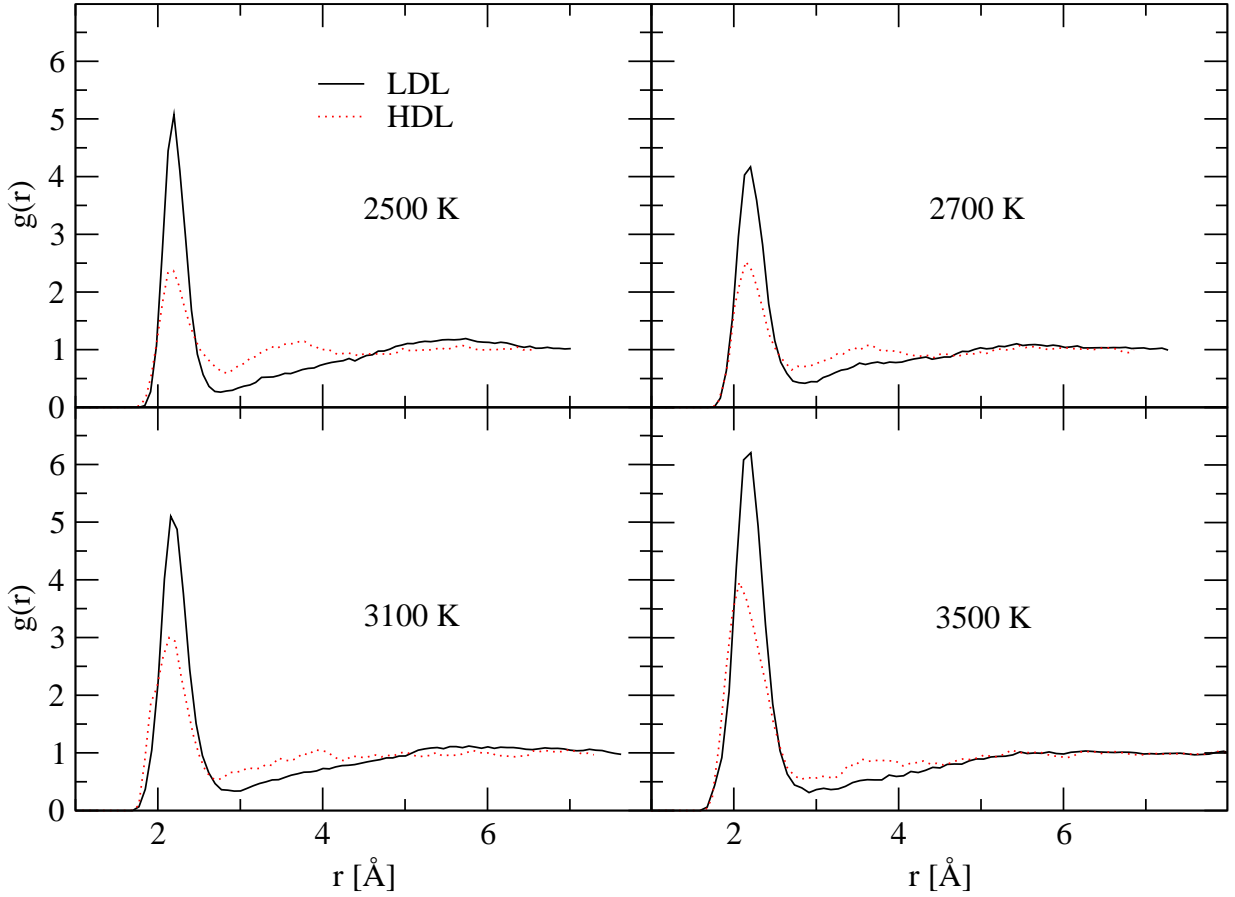


Figure 5.7: Radial distribution functions (rdf's) before and after all the considered transitions. Top left panel: LDF and (solid line) and HDL (dotted line) at 2500 K and 2.0 GPa (transition ‘1’ and ‘2’). Top right panel: LDF and (solid line) and HDL (dotted line) at 2700 K and 1.5 GPa (transition ‘3’). Bottom left panel: LDF and (solid line) and HDL (dotted line) at 3100 K and 1.0 GPa (transition ‘4’). Bottom right panel: LDF and (solid line) and HDL (dotted line) at 3500 K and 0.5 GPa (transition ‘5’).

within one molecule that are at a typical mutual distance of around 2.2 Å. Beyond the first peak the rdf's are structure-less, signature of the super-critical nature of the low density *fluid*. In contrast, the rdf's of the HDL's change markedly with state point. This holds in particular for the behavior of the second peak that indicates the presence of two regimes. At the lower temperatures (2500 and 2700 K) a second peak around 3.5 Å is clearly present. It is rather broad but comparable to the one found for the HDL at 1500 K (see Fig. 4.4). At higher temperatures (3100 and 3500 K), the second peak has disappeared, with the rdf's indicating a rather structure-less liquid beyond the first, pronounced, peak. The intensity of the first peak of the HDL's increases with temperature (note that the pressure is decreasing in the meanwhile). At these higher temperatures, the presence of covalent interactions still determines a strongly structured first coordination shell, while, beyond it, any trace of order seems to be lost. When comparing the rdf's of the LDF and HDL we note that, with increasing temperature the rdf of the LDF and the HDL before and after the transition become more similar.

Upon visual inspection, at 2500 and 2700 K the HDL appears as an all-connected

network of atoms with few isolated dimers and triangular clusters. Rare spontaneously formed tetrahedra occur after a collision of a triangular cluster and a singly bonded atom at the end of a branch of the network, and are short lived. At 3100 and 3500 K, the HDL is a mixture of dimers, triangular clusters, and clusters formed by triangular rings (rarely four or five membered rings) connected by one bond. The rings were never connected via one or more bridging atoms. Furthermore, at 0.5 GPa ($T=3500$ K) the HDL always counts 2 – 4 ‘newly formed’ tetrahedra, whose lifetimes range from 1.5 to 4 ps.

In Table 5.2 we list the average coordination numbers for the HDL. For the temperatures range from 2500 K to 3100 K a marked trend can be seen. Considering the one-fold coordinated atoms we see that they are almost absent at lower temperatures, but are significantly present at 3100 K. A one-fold coordinated atom is obviously either a part of a dimer or the end of a larger cluster. The sudden appearance of the one-fold marks the change in structure we visually observed and that we reported in the previous paragraph. The sudden increase of the one-fold atoms is accompanied by a slow increase of the two-fold, by a mild decrease of the four-fold, and balanced by a fast decrease of the fraction of four-fold and the five-fold coordinated atoms. In the high-temperature range from 3100 to 3500 K the coordination fractions are almost identical (considering also an error bar of size 0.01).

We calculated the structure factor for the state points corresponding to transition ‘1’ and ‘5’. In Fig. 5.8 we show the structure factors at 2500 K and 2.0 GPa (transition ‘1’). The solid line is for the LDF, the dotted line for the HDL. These structure factors were obtained from 10 configurations taken from a 4 ps interval of the trajectory. The dashed line is an average over 10 configurations in the central ps of the transition (see Fig. 5.5). Even if the system is there not in equilibrium, we consider this time interval as an ‘intermediate state’ between the LDL and the HDL. The LDF structure factor is characterized by the usual two peaks at ~ 1.5 and ~ 3.6 \AA^{-1} , that are related [123] to the intermolecular and intramolecular correlations, respectively. This shape of the structure factor was also observed in our study at 1500 K (Fig. 4.6 and [11]), as well as in the simulations at 1400 K by Senda *et al.* [112] and in the experiments at ~ 1350 K of Katayama *et al.* [1]. In Ref. [108] it is pointed out that the structure factor of the HDL changes shape, when going from ~ 1400 to ~ 1900 K. At lower temperature it shows two peaks, at ~ 2.9 and ~ 4 \AA^{-1} , plus a shoulder at ~ 1.5 \AA^{-1} . This is also reported in Ref. [1, 112, 11] (see also Fig. 4.6). According to Monaco *et al.* [108], when increasing the temperature to ~ 1900 K ($P \sim 0.7$ GPa), the two peaks at ~ 2.9 and ~ 4 \AA^{-1} merge into a broad peak, and the shoulder at ~ 1.5 \AA^{-1} disappears. The HDL structure factor we find at 2500 K ($P = 2.0$ GPa) has indeed only one well-defined peak at ~ 4 \AA^{-1} , in contrast to the two peaks present at 1500 K. On the other hand, at 2500 K we find a shoulder at 2.5 \AA^{-1} , and at 1.5 \AA^{-1} a rather pronounced peak is still present. The presence of more structure

P [GPa]	T [K]	1-fold	2-fold	3-fold	4-fold	5-fold
2.0	2500	0.02	0.22	0.47	0.25	0.04
1.5	2700	0.03	0.28	0.41	0.22	0.06
1.0	3100	0.18	0.33	0.37	0.11	0.01
0.5	3500	0.20	0.34	0.39	0.06	0.01

Table 5.2: Coordination fractions for the HDL along the LLPT line.

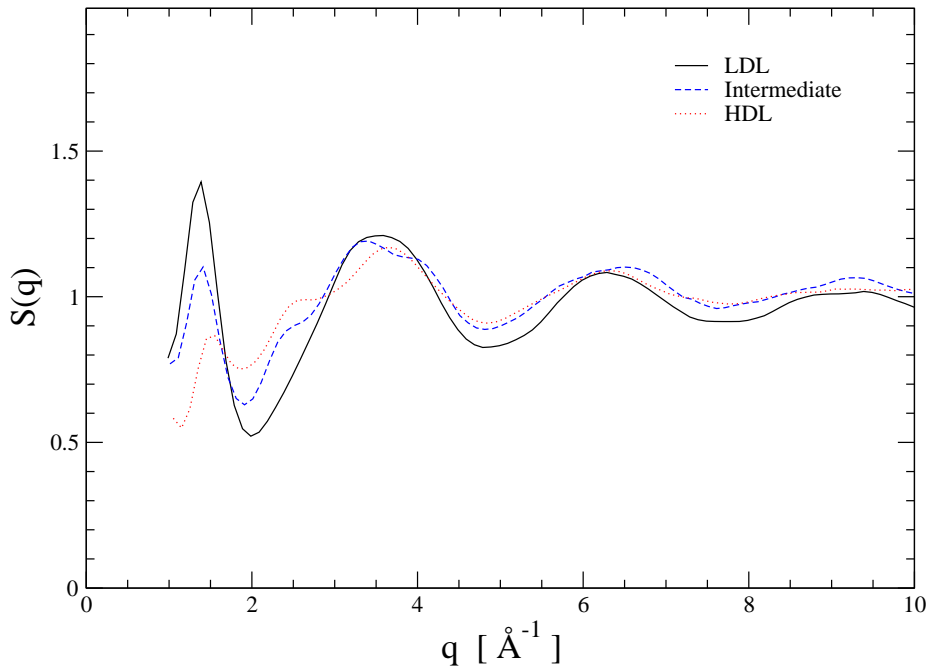


Figure 5.8: Structure factor at 2500 K and 2.0 GPa (transition ‘1’). The solid line is for the LDF, the dotted line for the HDL.

in our HDL can be justified by considering that our pressure (and possibly our density) is somewhat higher than in the experiment (the experimental densities are not known at these high temperatures). In fact, a careful analysis of the HDL experimental structure factors at several state points, published by Monaco *et al.* [108], suggests that the two peaks at around 2.5 and 4 \AA^{-1} , as well a shoulder at 1.5 \AA^{-1} reappear when increasing pressure. For example, they are present at slightly higher pressure (i.e. at $P = 0.9$ GPa), at ~ 1850 K. We therefore argue that the one-peak-shape is a feature of the *low pressure* HDL. With increasing pressure (and density), we predict that the shoulder (at ~ 2.5 \AA^{-1}) and the peak (at ~ 1.5 \AA^{-1}) reappear, as a signature of longer range correlations between atoms. At 2500 K, the ‘intermediate state’ structure factor (Fig. 5.8) seems to interpolate between the two stable states at small wave vectors, whereas almost overlapping the HDL structure factor large wave vectors. This would suggest that the shorter range correlation are already settled while the longer range correlations are more slowly changing when the system is transforming from one phase into the other.

In Fig. 5.9 we show the structure factors at 3500 K and 0.5 GPa (transition ‘5’). The LDF structure factor (solid line), still shows the ‘intramolecular’ peak at ~ 3.6 \AA^{-1} . Compared to the lower temperature structure factors, the positions of the first peak shifts to the left, from 1.5 to 1.0 \AA^{-1} . If the attribution to intermolecular correlations of this peak still holds, this shift implies that the correlation lengths between the P_4 molecules moves to larger values. The similarity of the structure factors of the LDF and HDL is even more pronounced than the similarity of the associated rdf’s.

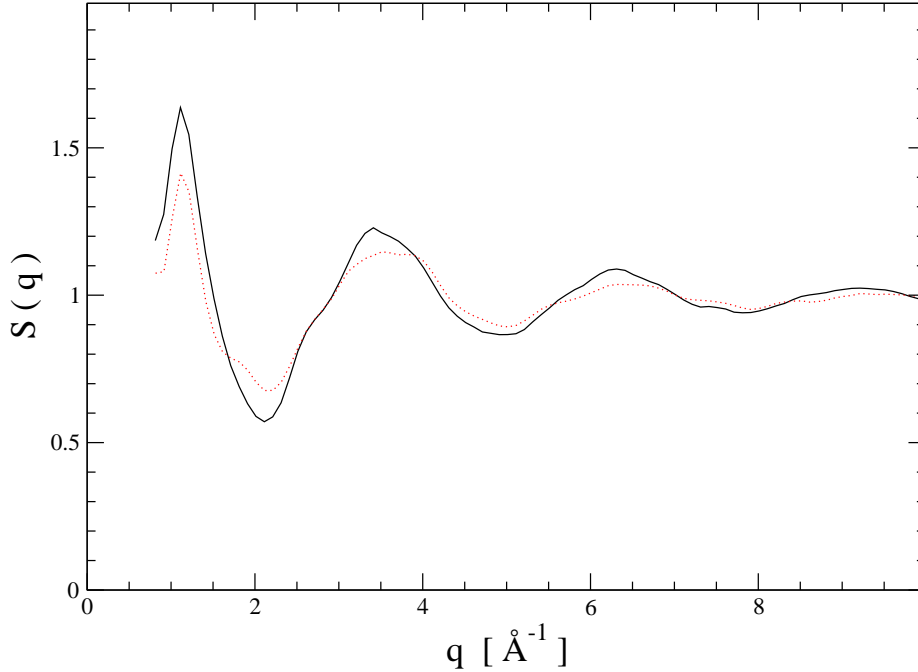


Figure 5.9: Structure factor at 3500 K and 0.5 GPa (transition ‘5’). The solid line is for the LDF, the dotted line for the HDL.

5.5 Electronic properties

We have calculated the electronic density of states (DoS) for configurations across three selected LLPT’s. The DoS were obtained calculating the Kohn-Sham energies for 160 occupied and 100 non-occupied levels. In Figs. 5.10, 5.11, and 5.12 we show the results for transition ‘1’ ($T = 2500$ K and $P = 2.0$ GPa), ‘4’ ($T = 3100$ K and $P = 1.0$ GPa), and ‘5’ ($T = 3500$ K and $P = 0.5$ GPa), respectively. The DoS in each panel is an average over three configurations, that were selected close to each other in the trajectory around the time declared in the panel.

In Fig. 5.10 we see initially (at 0.5 ps, top left panel) three pronounced and well separated bands in the valence region (below the Fermi level) and a fourth band in the conducting region; the gap around the Fermi level is small in energy, but still indicating the non metallic nature of the molecular fluid. The evolution of the DoS then proceeds with a) the closing of the gap at the Fermi level followed by the disappearance of the dip between the valence and conducting bands and b) the merging of the two valence bands at lower energies, with the disappearance of the band gap at ~ -13 eV. Until the end of the trajectory there remains a dip around -7 eV, that separates the density of states into two bands. The closure of the gap at the Fermi level indicates the transition of the non-metallic, molecular fluid into a metallic liquid.

In Fig. 5.11, the evolution of the density of states is similar to the previous case, i.e. from four sharp to two broad bands, with the noticeable difference that the gap at the Fermi level is already closed at the initial step, even if a deep dip keeps valence and conducting bands rather separate. This means that at this state points already the molecular fluid shows some metallic features.

In Fig. 5.12, the evolution follows the usual non-metal-to-metal path, with two peculiar

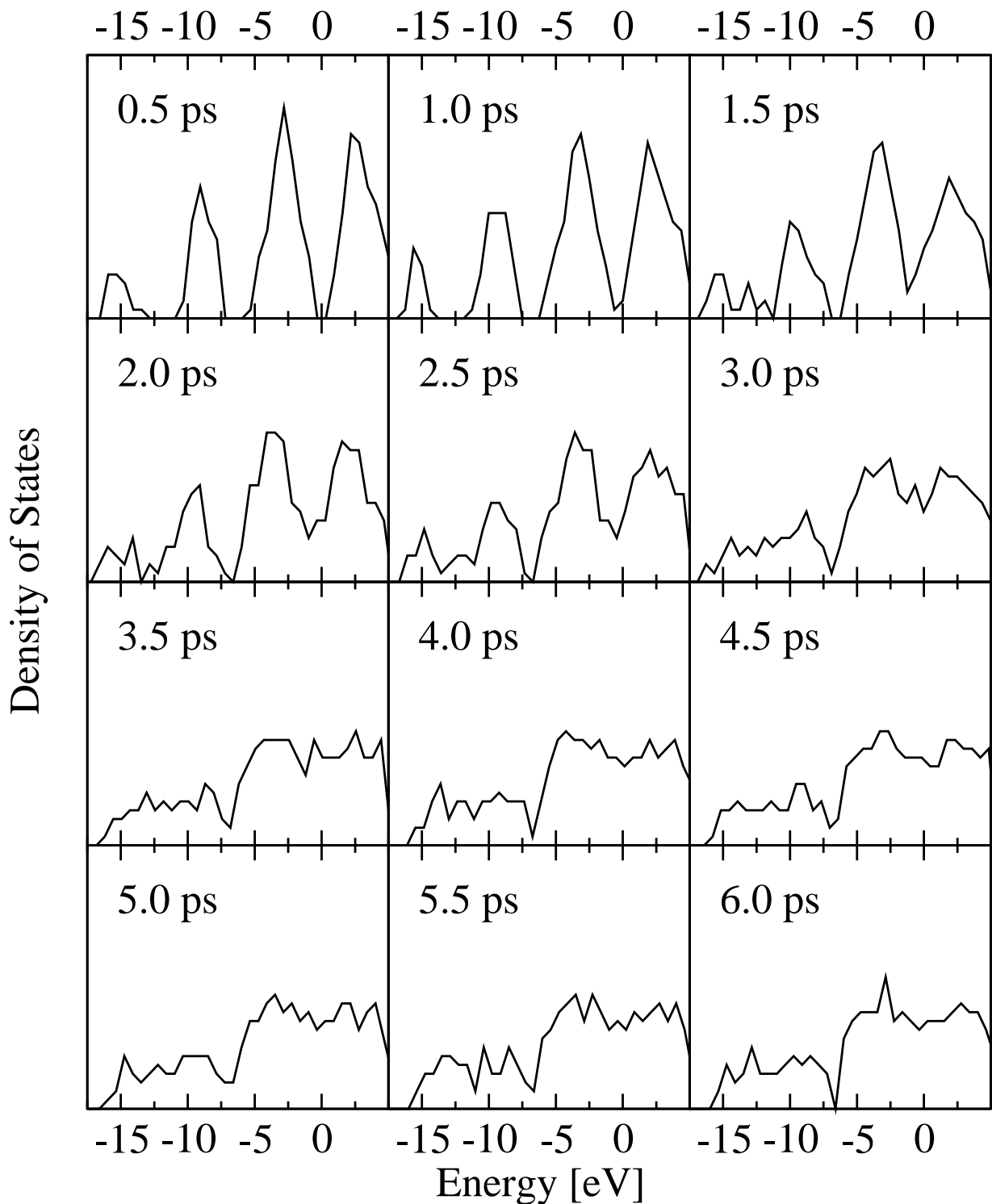


Figure 5.10: Evolution of the density of states (distribution of the Kohn-Sham levels) across transition ‘1’ at 2500 K and 2.0 GPa. The time scale agree with that of Fig. 5.5.

features. Initially (at 0.75 ps, top left panel), the DoS falls to zero at the Fermi level, but the gap is vanishingly small. More strikingly, the DoS maintains until the end of the trajectory a defined splitting into four bands, even if the gaps between them close and

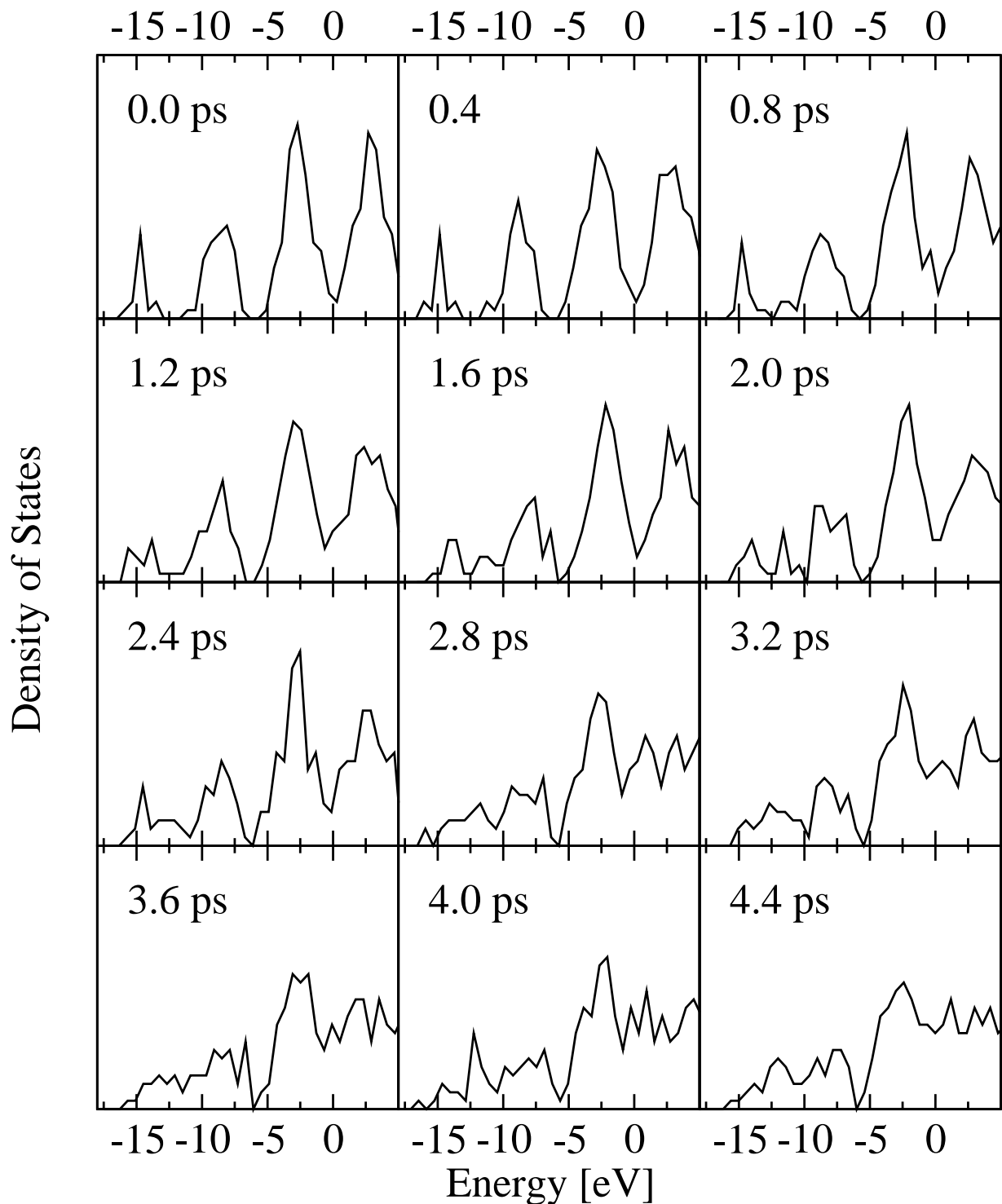


Figure 5.11: Evolution of the density of states (distribution of the Kohn-Sham levels) across transition ‘4’ at 3100 K and 1.0 GPa. The time scale agree with that of Fig. 5.3.

the bands become rather broad. From approximately $t = 6$ ps on, the density of states appears as a superposition of a density of states peculiar to the molecular fluid (see the first row in Fig. 5.10, but also Fig. 4.9, taken at 1500 K) and one typical of the metallic liquid (see the last row in Fig. 5.10, but also Fig. 4.10, taken at 1500 K).

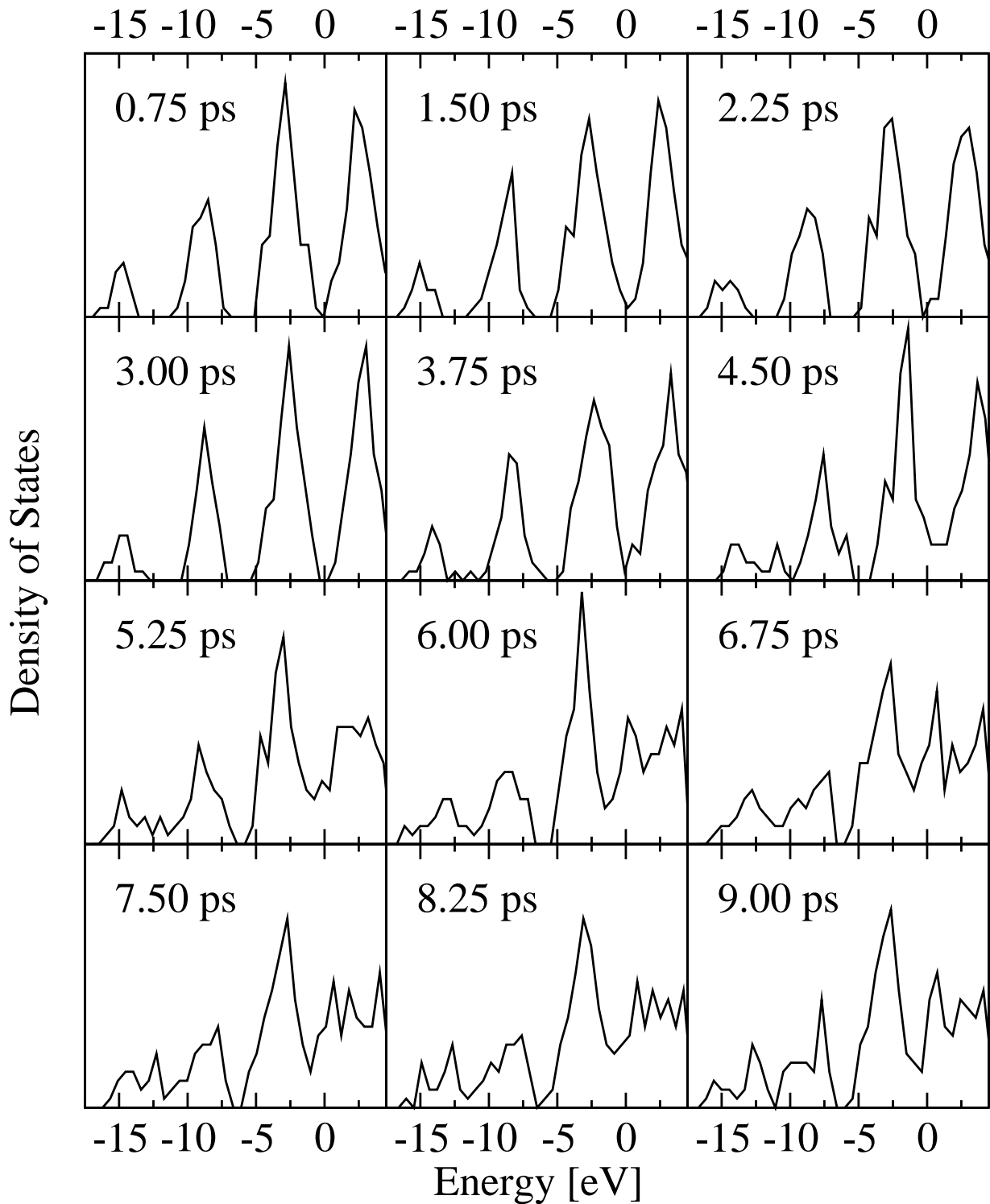


Figure 5.12: Evolution of the density of states (distribution of the Kohn-Sham levels) across transition ‘5’ at 3500 K and 0.5 GPa. The time scale agree with that of Fig. 5.6.

We have performed the calculation of the DoS also for the LDF and the HDL, both at 0.5 GPa and 2500 K. These state points are labelled as *i* and *i*’ in Fig. 5.1. We remind that the HDL at state point *i*’ was obtained by cooling the liquid equilibrated after the

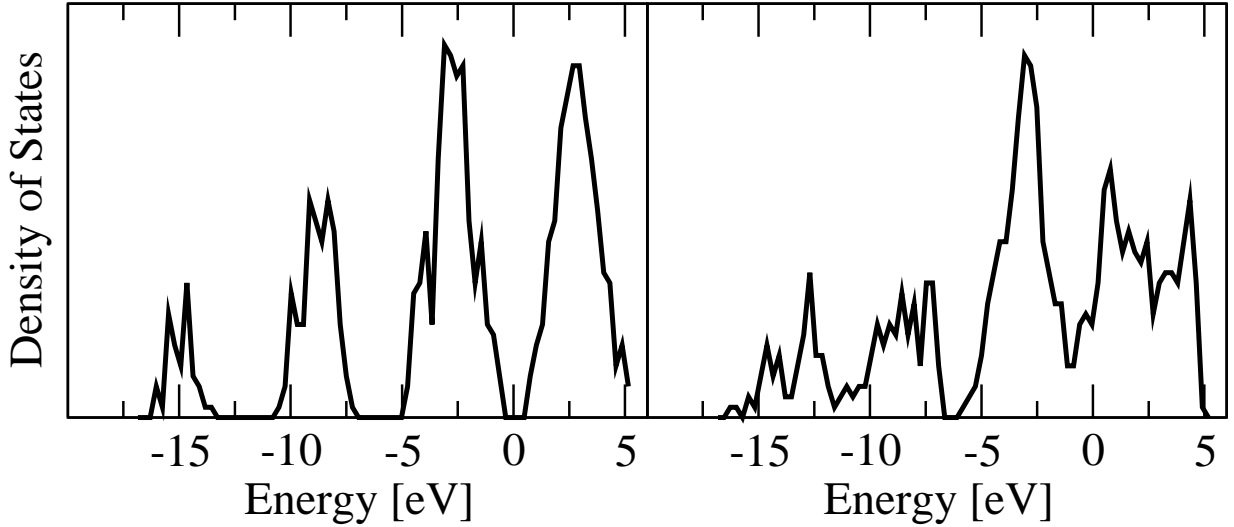


Figure 5.13: *Density of states (distribution of the Kohn-Sham levels) for the 0.5 GPa and 2500 K for both the LDF and HDL, i.e. points i and i' of Fig. 5.1.*

transition at 0.5 GPa and 3500 K. Both distributions were obtained averaging over six uncorrelated configurations. At these temperature the DoS of the molecular fluid has a large gap at the Fermi level; the DoS network liquid, on the other hand, is now clearly split into the same four bands as the molecular fluid, with the difference that the gaps among bands are closed and the bands are broader. We note that visual inspection of the trajectory of the simulation at 2500 K and 0.5 GPa for the network liquid, reveals that 2-4 tetrahedra are always present in the sample.

5.6 Discussion

Consistently with recent experimental observations [108], we have found that, upon increasing temperature, the pressure at which the low density fluid transforms into the high density liquid decreases. The transition state point proved to be independent of the history of the sample. Namely, transition ‘3’, at 2700 K and 1.5 GPa was obtained twice, starting from two different initial configurations at the state point the transition occurred; the transitions ‘1’ and ‘2’ occurred at the same state point, 2500 K and 2.0 GPa, the first upon increasing pressure at constant temperature, the second upon increasing temperature at constant pressure.

However, it is difficult to relate the transition pressures we obtain from our system to the experimental pressures. As already pointed out in the previous chapter, there are three sources of inaccuracies in the pressure calculations we cannot cope with. One is the known size-dependent hysteresis; this is always present when in a simulated system of a relatively small number of atoms, a transition is expected to overcome a free energy barrier, in order to occur. In the case of phosphorus LLPT, the free energy barrier might be given by the difficulty in breaking the tetrahedral clusters, whereas a ‘transition state’ can be found in alternative bonding configurations of the phosphorus atoms, with a free energy not too far from the tetrahedral arrangement. We suggest that the mechanism that initiates the transition becomes more probable to occur at higher temperature. Namely, at lower tem-

peratures a rather rare correlation between three tetrahedral molecules seems to be needed for the LLPT to initiate; at higher temperatures a much more probable to occur disruptive pair collision appears to be sufficient. The other two effects lead overestimation of the pressure at a given density, if compared to experimental values. This is due a) to the lack of dispersion attractions, that cannot be described by the density functionals, even at the gradient corrected level, and b) to small inaccuracies in the predicted interatomic interactions, that are magnified in the pressure calculation. We cannot quantify this last effect; in contrast, the pressure overestimation due to dispersion forces is known to be quadratically dependent on density, thus expected to decrease at low densities. In our simulations the state points in which we found LLPTs approach the experimental coexistence points: this might be due to a) a smaller hysteresis at higher temperatures, since the phase space is more efficiently sampled and the transition state seems to be more probable to occur, and b) the decreasing density that lower the contribution of the dispersion forces we neglect.

Even if the absolute pressure cannot directly be compared to experiment, for the reasons above mentioned, we note that the slope of the line connecting $P - T$ state points (see Fig. 5.2) in which our LLPTs occurred is negative as well as in experiments. In other words, consistently with Monaco *et al.* [108], with increasing temperature the transition pressure decreases. However, the curvature of the line connecting LLPT state points has opposite curvature if compared to experiments. Again, this could be due to the hysteresis effects.

Given this serious limitation, we claim that we have obtained a near critical transition at 3100 K (transition ‘4’ in Fig. 5.1 and Fig. 5.2) and a supercritical transition at 3500 K (transition ‘5’). In the following we summarize our arguments.

By comparing Figs. 4.11, 5.5, 5.3, and 5.6, we note that the fluctuations in density increase noticeably with the temperature, passing from $\sim 7\%$ at 1500 K, through $\sim 20\%$ at 2500 K and $\sim 40\%$ at 3100 K, to $\sim 50\%$ at 3500 K^{||}.

In Fig. 5.1, the slope of the two dashed line highlights the decreasing of the change in density across the LLPTs upon increasing pressure. At 3100 K the change in density is almost vanished, and it is vanished, within the error bars, at 3500 K.

The radial distribution functions of the network and molecular liquids at this two higher temperatures (Fig. 5.7, bottom panels) and the structure factors (Fig. 5.9 for transition ‘5’, while transition ‘4’ is not shown) are rather similar.

Upon cooling the network liquid obtained after transition ‘5’ (it is not any more a ‘high density liquid’!) along the isobar at 0.5 GPa, we find that its equation of state overlap the equation of state of the molecular fluid.

The network liquid at 1.0 GPa (at 3100 K) and 0.5 GPa (i.e. at all temperatures from 3500 K to 2500 K along the 0.5 GPa isobar) exhibits a great number of ‘newly formed’ tetrahedra, suggesting that the network structure and the molecular arrangement are thermodynamically of comparable stability.

The electronic density of states after the LLPT at 0.5 GPa and 3500 K (see Fig. 5.12, bottom row) appears as a superposition of a DoS peculiar to the molecular fluid and a DoS typical of the network liquid, when both phases are sampled at lower temperatures (see e.g. Figs. 4.9 and 4.10, with DoS taken at 1500 K). This feature is more pronounced when both phases are equilibrated at the same low pressure ($P = 0.5$ GPa), but at a lower

^{||}The distribution of the densities were fitted with gaussian functions with parameters (x_0, σ) and the figures reported are $2\sigma/x_0$.

temperature ($T = 2500$ K), as shown in Fig. 5.13.

5.7 Conclusions

In conclusion, we have investigated the phosphorus liquid – liquid phase transition in the range of temperatures from 2500 to 3500 K, by means of density functional based molecular dynamics (DF-MD). We have identified five different transitions at different temperatures that occurred at constant temperature and pressure in our 64-atoms (16 initial tetrahedra) system.

Visual inspection of the transition runs suggested that, upon increasing temperature, the transition mechanism changed from a three-molecule-correlation building a transient chain of ‘butterfly’ molecules to a two-molecule-collision with immediate disruption of the molecules into smaller clusters.

Our calculations suggest that the transitions at higher temperature are near-critical (at $T = 3100$ K) or super-critical (at $T = 3500$ K).

Further advance in the understanding of the liquid – liquid phase transition in phosphorus by atomistic simulation requires the parametrization of an accurate (semi)empirical potential. This would allow to extend the present DF-MD simulation timescale by at least one order of magnitude, and could provide a more detailed picture of the liquid – liquid phase transition, including its free energy characterization.

Bond order potentials for covalent elements.

Entia non sunt multiplicanda praeter necessitatem.

This chapter will be dedicated to a short history of the so called “bond order” potentials [126, 127, 128, 129, 3, 130, 15] (BOPs), that represent an interesting class of the rather scattered family of analytic potentials.

Analytic interatomic potentials (sometimes referred to as empirical, semi-empirical or classical potentials) are used for a variety of purposes, ranging from the estimation of minimum energy structures for surface reconstruction, grain boundaries or related defects, to the description of the liquid structure. All analytic potentials are defined through a functional form of the interatomic interactions, whose parameters are fitted to a selected database. According to Brenner [131], an analytic potential needs to be:

- *Flexible*: the function should be flexible enough to accommodate the inclusion of a relatively wide range of structures in a fitting database.
- *Accurate*: the potential function must be able to accurately reproduce quantities such energies, bond lengths, elastic constant, and related properties entering a fitting database.
- *Transferable*: the functional form of the potential should be able to reproduce related properties that are *not* included in the fitting database. In practise the potential should be able to give a good description of the energy landscape for any possible realistic configuration characterized by the set of atomic positions $\{\mathbf{r}_i\}$.
- *Computationally efficient*: the function should be of such a form that it is tractable for a desired calculation, given the available computing resources.

We note that one of the paradigms that has led science through its development, i.e. the Occam razor (“Entities should not be multiplied beyond necessity”), is not mentioned here. This is intentional: as it will become clearer through the chapter, even if bond order potentials are based on the beauty and simplicity of ab initio theories, they achieve computational efficiency and transferability paying the fee of a proliferation of somewhat ad-hoc adjustments, any of them implying propter-hoc parameters. In other words, on one hand

bond order potentials increase transferability, with respect to simple two-body potentials, increasing the number of parameters. On the other hand, they increase computational efficiency, with respect to ab initio calculations, at the same price of adding parameters. It has to be noted that the focus of bond order potentials is put on their performance, i.e. on the fact that they work. Thus, thinking at the Occam razor, bond order potentials give to “necessity” a meaning that is different from the traditional one. It is indeed *necessary* to introduce new entities (viz. parameters), for fulfilling the four requirements stated above.

BOPs are all expressed by giving the binding energy of a system as a sum over all pairs:

$$E_b = \frac{1}{2} \sum_i \sum_{j \neq i} [V^R(r_{ij}) - b_{ij} V^A(r_{ij})] \quad (6.1)$$

where $V^R(r_{ij})$ and $V^A(r_{ij})$ are pair-additive interactions representing all interatomic repulsions and all those attractions coming from valence electrons, respectively; r_{ij} is the distance between atoms i and j and the (scalar) quantity b_{ij} is a function of the local environment of atoms i and j , called “bond order”.

With a meaning indeed close to that used for up-to-date bond-order potentials, the term “bond order” was introduced in 1939 by Coulson [132] in treating the strength of π -bonds in polyenes and aromatic molecules. Following this author, if a given molecular orbital of a molecule ($\Psi^{(n)}$) is expressed as a linear combination of atomic orbitals ($\phi_i^{(n)}$) of the individual π -electrons: $\Psi^{(n)} = \sum_i a_i^{(n)} \phi_i^{(n)}$, with a^i a complex number, then the *partial mobile* bond order ($b_{ij}^{(n)}$) of a π -bond between atoms i and j is defined as $b_{ij}^{(n)} = \frac{1}{2} [a_i^{(n)} a_j^{(n)*} + a_i^{(n)*} a_j^{(n)}]$. The *total mobile* bond order (b_{ij}) of the π -bond, between atom i and j , is the sum of the *partial* bond orders over all the molecular orbitals involved: $b_{ij} = \sum_{(n)} b_{ij}^{(n)}$. The bond order is the *total mobile* bond order plus one, to account for the σ bond. With this definition, a bond order of value 1 or 2, would correspond to the intuitive concepts of single and double bonds, respectively. In a benzene molecule the *total mobile* bond order of each bond is $2/3$, and the bond order is $5/3$, closer to a double than to a single bond.

The form of Eq. 6.1 can be justified on the basis of the Local Orbital approach (LO) that Abell [133] developed in the framework of Chemical Pseudopotential (CPP) theory [134, 135, 136]. This theory in turn relies on the Hückel Molecular-Orbital (HMO) theory [137]. The derivation of Abell is rather instructive: a series of non trivial assumptions lead to two important results. The first is a motivation of the unexpected likeness [138] of the shape of the binding energy curves in rather different environments, ranging from pure covalent to metallic bonds; the relevant parameter that identifies the type of bonding of a reference atom is the number of its first neighbours Z . The second is a justification of the initial guess on the functional form of the term b_{ij} as used in successful BOPs: $b = Z^{-1/2}$. In the following section we will give a brief exposition of the derivation of Eq. 6.1 from LO.

The subsequent section (6.2) will suggest an alternative and much more intuitive argument to derive 6.1, based on the moments theorem [139].

In the remainder of the chapter (sections 6.4 and 6.5), a brief overview of BOPs will be given. Focus will be put on those features of the BOPs that are recurrent in all the formulations, underlining analogies and differences. Thus, we will often skip the details and we will never give the values of the fitted parameters. We will provide a full description of a BOP for the Long range Carbon Bond Order Potential (LCBOP) [15] in section 6.6.

The full description is necessary, since an improvement of this potential has been one of the early targets of the present thesis work: this modification is illustrated in section 6.7.

6.1 Localized orbitals model

Abell [133], following Anderson [134, 135, 136], writes the Hamiltonian for a system of atoms as:

$$H = K + \sum_a V_a \quad (6.2)$$

where K is the total kinetic-energy operator and V_a is the *effective potential due to the presence of atom a in the system* and the sum extends over all the atoms. The crucial hypothesis of this approach is that the V_a 's are short ranged and strongly localized about the corresponding atoms. It is also assumed that only one atomic species is involved. Molecular orbitals (ψ_i) and their energies (ε_i) are the eigenfunctions and eigenvalues of the SCF Hamiltonian:

$$H | \psi_i \rangle = \varepsilon_i | \psi_i \rangle \quad (6.3)$$

Abell shows that it is possible to find a suitable basis set, that spans the molecular-orbital subspace of $\{\psi_i\}$, and whose elements are atomic-like orbitals, that allows to write the Hamiltonian as a sum of (environment dependent) pairwise interaction terms. Calling φ_m the elements of this searched basis, the Hamiltonian can be rewritten:

$$\begin{aligned} H &= \sum_m [\varepsilon_0 + \sum_{k \neq m} V_R(r_{km})] | \varphi_m \rangle \langle \varphi_m | + \\ &+ \sum_m \sum_{k \neq m} V_A(r_{km}) | \varphi_m \rangle \langle \varphi_k | \end{aligned} \quad (6.4)$$

and

$$\psi_i = \sum_m C_{mi} \varphi_m \quad (6.5)$$

where the index m runs all over the atoms.

The explicit expressions for V_R and V_A , coming from the CPP theory [136], need the introduction of \tilde{V}_m – as the SCF one-electron atomic potential of atom m (including exchange and correlation) appropriated to the isolated atom – and of \tilde{V}_k – as the difference from the atomic potential \tilde{V}_m due to the presence of atom k . Introducing the unperturbed atomic orbitals ϕ_m^0 , the energy ε_0 of the isolated atom is easily written:

$$\varepsilon_0 = \langle \phi_m^0 | (T + \tilde{V}_m) | \phi_m^0 \rangle \quad (6.6)$$

and

$$\begin{aligned} V_A(r_{km}) &= \langle \phi_k^0 | \tilde{V}_k | \phi_m^0 \rangle \\ V_R(r_{km}) &= \langle \phi_m^0 | \tilde{V}_k | \phi_m^0 \rangle - S_{km}^0 \langle \phi_k^0 | \tilde{V}_k | \phi_m^0 \rangle \end{aligned} \quad (6.7)$$

with $S_{km}^0 = \langle \phi_k^0 | \phi_m^0 \rangle$. In the above expressions for V_A and V_R , the crucial approximation of using the unperturbed atomic orbitals ϕ_m^0 has been adopted. The Hamiltonian in Eq. 6.4 is therefore approximated by the introduction of these V_A and V_R .

The binding energy E_b of the system is defined as the total energy, expressed as the sum of the energies ε_i of the occupied orbitals, minus the sum of the energies ϵ_0 of the isolated atoms*:

$$E_b = \sum_i n_i (\varepsilon_i - \epsilon_0) \quad (6.8)$$

where $n_i = 0,1$ is the occupancy of the molecular orbital ψ_i . Defining

$$q_m \doteq \sum_i n_i |C_{mi}|^2 \quad (6.9)$$

$$b_{km} \doteq \sum_i n_i C_{ki}^* C_{mi} \quad (6.10)$$

and using Eqs. 6.4 and 6.5, yields

$$E_b = \sum_m [q_m \sum_{k \neq m} V_R(r_{km}) + \sum_{k \neq m} b_{km} V_A(r_{km})] \quad (6.11)$$

Note that the definition of b_{km} explicitly resembles the definition of bond order as given by Coulson [132]. The term q_m represents the net electron density on site m .

Eq. 6.11 can be particularized for regular structures (in which each atom ‘sees’ the same environment):

$$\mathcal{E}_b = \frac{E_b}{N} = \sum_k Z_k (q V_{Rk} + b_k V_{Ak}) \quad (6.12)$$

where \mathcal{E}_b is the bond energy per atom, Z_k is the number of atoms in the k -th shell, b_k is the bond order between the reference atom and the atoms in the k -th shell, and q is the number of (valence) electrons per atom.

Under the assumption that the $V_A(r)$ is so short ranged, that one may reasonably ignore all but V_{A1} in the HMO secular equation, only the first neighbour bond order b_1 is present in Eq. 6.12:

$$\mathcal{E}_b \cong Z_1 (q V_{R1} + b_1 V_{A1}) \quad (6.13)$$

Here, V_R has also been limited to V_{R1} , since the core-core repulsion (due to the Pauli exclusion principle) and the screened electrostatic repulsion between nuclei always fall off much faster than $V_A(r)$. There are indeed systems (for instance simple metals) for which the interatomic matrix elements extend well beyond the first shell: for these cases Abell provides a numerical proof that the sum $\sum_k Z_k b_k V_{Ak}/V_{A1}$ can be fairly approximated by the product $Z_1 b_1$ when the occupancy $q \cong 1$. Note that for regular lattices, the terms b_k can be exactly calculated with a recursion method [140]. From here on it will be: $Z \doteq Z_1$ and $b \doteq b_1$. It is thus possible to write:

$$\mathcal{E}_b(\mathcal{G}, q; r) \cong Z(\mathcal{G}) [q V_R(r) + b(\mathcal{G}, q) V_A(r)] \quad (6.14)$$

The shell subscript is suppressed under the understanding that all the quantities (apart from q) refer to the first shell; the symbol \mathcal{G} symbolizes the *primary interaction topology*.

*A term called U_{es} , present in the original formulation, has been here omitted. This term would account for ion-ion repulsion and interatomic repulsion due to the superposition of free electron densities. In the original paper this term, in any case constituted by pairwise and localized terms, is later absorbed into V_R .

It is only after all these approximations, that one can describe the map of first neighbours interactions with the intuitive name of “bonds”.

Abell makes the choice of parameterizing V_R and V_A with exponential functions:

$$\begin{aligned} V_R &= Ae^{-\theta r} \\ V_A &= -Be^{-\lambda r} \end{aligned} \quad (6.15)$$

Where A, B, θ , and λ are parameters specific of the atom species. The choice is motivated partly by convenience and tradition and partly by the physical grounds that atomic orbitals indeed decay exponentially. In principle the coefficients A and B can be smoothly depending on r on the range of interest without changing the following analysis.

The remains of Abell analysis demonstrate the likeness of the *shape* of the binding energy curves for structures of rather different coordination, ranging from the dimer ($Z = 1$), with a covalent bond, to an fcc structure ($Z = 12$), with metallic bonds. Thereafter, Abell argues that the value of the bond order b can be fairly approximated by $Z^{-1/2}$ over different values of the coordination Z and the occupancy q .

After substituting Eqs. 6.15 into Eq. 6.12

$$\mathcal{E}_b = Z [Aqe^{-\theta r} - Bbe^{-\lambda r}] \quad (6.16)$$

the equilibrium interatomic separation r_e is readily found from $d\mathcal{E}_b/dr = 0$:

$$\theta Aqe^{-\theta r_e} = \lambda Bbe^{-\lambda r_e} \quad (6.17)$$

Defining

$$S = \frac{\theta}{\lambda} \quad (6.18)$$

it follows:

$$r_e = \frac{1}{\theta - \lambda} \ln \frac{ASq}{Bb} \quad (6.19)$$

and the cohesive energy at equilibrium $D_e = -\mathcal{E}_b(r_e)$:

$$D_e = ZAq(S - 1)e^{-\theta r_e} = ZBb \frac{S - 1}{S} e^{-\lambda r_e} \quad (6.20)$$

The two formulations of D_e are clearly equivalent, being obtained substituting Eq. 6.19 into either the left or right hand side of Eq. 6.17. Note the logarithmic dependence of the equilibrium radius on the bond order b : this is identical to an early empirical expression of Pauling [141].

The binding energy can be scaled on the cohesive energy and the equilibrium distance: $\mathcal{E}_b^*(x) = \mathcal{E}_b(r)/D_e$, with $x \doteq (r - r_e)/l$, and where $l \doteq D_e/(d^2\mathcal{E}_b/dr^2)_{r=r_e} = 1/\sqrt{\lambda\theta}$:

$$\mathcal{E}_b^*(x; S) = \frac{e^{-\sqrt{S}x} - Se^{-x/\sqrt{S}}}{S - 1} \quad (6.21)$$

Note that the curves are invariant under the transformation $S \rightarrow 1/S$, i.e. under the swap of the effective interaction length (λ and θ) of V_A and V_B .

A plot of $\mathcal{E}_b^*(x; S)$ (Fig 6.1) displays the soft dependence of the binding energy on S . In particular, for $|x| \lesssim 1$, $\mathcal{E}_b^*(x; S)$ is nearly independent of S . This observation justifies

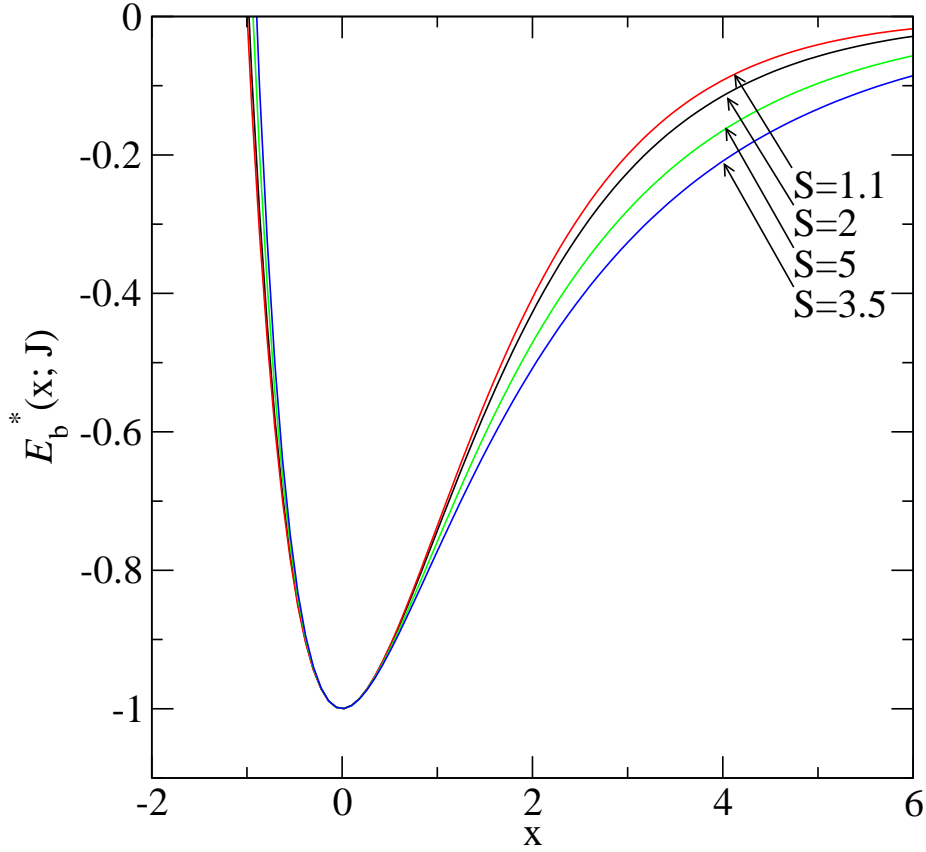


Figure 6.1: Plot of the scaled binding energy (Eq. 6.21) for some representative values of $S = \theta/\lambda$.

the empirical finding of a generalizable *shape* of the binding energy curves, pointed out in Ref. [138, 142].

A different rescaling on the dimer cohesive energy, spots the Z dependence of the cohesive energy in all the coordination situations. Putting $Z = q = b = 1$ into Eq. 6.20 the dimer cohesive energy (D_{e2}) is readily obtained. In this way the differently scaled binding energy is defined: $\mathcal{E}_b^{\mathbf{x}}(x) = \mathcal{E}_b(r)/D_{e2}$. Algebraical manipulations would give, for the reduced cohesive energy ($D_e^{\mathbf{x}}$):

$$D_e^{\mathbf{x}} = Z \left(\frac{b}{q} \right)^{\frac{S}{S-1}} \quad (6.22)$$

Note that for $S = 2$ (the case of the so called Morse potential), this reduced cohesive energy is independent of Z if $b \propto Z^{-1/2}$.

As justified above by Eq. 6.14, the bond order parameter depends on the local topology \mathcal{G} . In particular, the local topology is characterized by a) the number of nearest neighbours, b) the size of primitive loops[†]. To get rid of the influence of loops, b can be estimated for an

[†]A loop is a closed path, covered hopping from neighbour to neighbour, comprising the reference atom; a primitive loop is a loop that cannot be decomposed into shorter loops.

There is also a third dependence: on N , the number of particles in the system, for finite systems. It can be disregarded thinking to infinite or periodically replicated systems, as far as the length of the period is much longer than the typical distance of first neighbours.

(ideal) structure without loops: this is called Bethe lattice, whose topology is completely defined by Z [‡]. For this lattice, and for large Z , it is indeed

$$b_{Z \rightarrow \infty} \rightarrow \alpha(q)Z^{-1/2}. \quad (6.23)$$

For small Z , b , can still be written as $b = b_{Z \rightarrow \infty} + \Delta b$: Abell shows numerical evidence that Δb is always positive and indeed small (less than 10% of $b_{Z \rightarrow \infty}$). Going back to Eq. 6.22, for $S \gg 2$, $D_e^{\text{st}} \propto \sqrt{Z}$. This case is verified when the effective range of the repulsive part is much shorter than that of the attractive part. In this hard core limit the higher the coordination, the higher the cohesive energy, so the close packing is preferred. For $S < 2$, $D_e^{\text{st}} \propto Z^{-\delta}$, with $\delta > 0$. In this case the effective lengths of attractive and repulsive part of the potential are comparable. In this covalent regime, the diatomic species is preferred.

In summary, the analysis of Abell reported in this section, justifies the general expression of the interatomic potential of a system of particles *in a regular lattice* as a sum over all the particles of a binding energy per particle, that is a (relatively short ranged) pair interaction with a single neighbour, multiplied by the number of neighbours. Abell's suggestion is that the pair potential is split into two parts, an attractive and a repulsive part; the attractive part is to be weighted by a factor, called “bond order”, which, in first approximation, is equal to the inverse square root of the number of first neighbours of a given atom.

For non regular structures, such as a liquid, one can rely on a description of a liquid as a system with a certain short range structure. It can be argued that the LO model holds as a first approximation: to the purpose it would be better defined a binding energy *per bond*: $\mathcal{E}_b = 1/2 \mathcal{E}_b(r)/Z$. This newly defined quantity needs not to be the same for every bond of a given particle and the coordination Z can be different for every particle (it will be Z_i , then). The factor 1/2 in the definition of \mathcal{E}_b permits to write the total binding energy as a sum over all the bonds of the binding energy per bond[§], thus fully recovering Eq. 6.1.

To conclude, it is interesting to see the dependence on Z of r_e and the cohesive energy. Substituting $Z^{-1/2}$ for b into Eq. 6.19, one finds that

$$r_e \propto \ln Z \quad (6.24)$$

Defining the cohesive energy *per bond* as $D_e^{\text{bond}} = D_e/(2Z)$, and substituting into Eq. 6.20 the value $Z^{-1/2}$ for b , it holds:

$$D_e^{\text{bond}} \propto Z^{-\frac{1}{2(S-1)}} \quad (6.25)$$

Eliminating Z from the above two equations, the locus of the minima is readily found:

$$D_e^{\text{bond}} \propto e^{-\frac{r_e}{2(S-1)}} \quad (6.26)$$

6.2 Second moment approximation

Following Brenner *et al.* [131], an intuitive way of explaining the chemical bond is thinking it as arising from the broadening of electronic energies as atoms are brought together. Let

[‡]It can be visualized as an infinite tree in which each branch splits into additional branches, whose number is the coordination number Z . It does not contain loops counting more than two atoms.

[§]It is implied that the same binding energy is ascribed to a bond by both particles involved, thus the contribution can be split equally between the two.

us consider a system of N carbon atoms arranged in a greatly expanded lattice such as the atoms can be thought as non interacting. All the atomic orbitals will have the same energy. As the atoms are brought closer, the initial perfect degeneracy of the p orbitals is lost, and molecular orbitals of energies above and below the atomic orbitals are formed. Following Hund's rule, electrons fill in pair orbitals beginning from the lowest energy. The total energy is the sum of the energies of occupied orbitals. Since the p atomic orbitals are not completely filled, more orbitals below than orbitals above the level of the atomic orbitals will be occupied. Here only the overlapping of valence orbitals is taken into account and the repulsive interactions between core orbital is disregarded for sake of clarity. Thus, all this intuitive argument accounts only for the attractive part of the binding energy. Under this specification, the packing thus causes an overall lowering of the total energy and the formation of a chemical bond. The orbital energies e assumes a specific distribution: $D(e) = \sum_k \delta(e - \epsilon_k)$, where δ is the delta function and the sum extends all over the occupied and unoccupied states ϵ_k . As any distribution, it can be described by its momenta; in this case it can be written as the sum of the momenta about the unperturbed atomic orbital energy (ϵ^{atomic}): $M^n \doteq \sum_k (e - \epsilon^{\text{atomic}})^n D(e)$. Invoking (local) charge neutrality, the first momentum is identically zero. In Ref. [131] it is shown that, for the considered carbon system, the binding energy (taken as the difference of the total energy of the system and N times the energy of the atomic orbital) is fairly depicted as linearly dependent (only) on the *square root* of the second moment of the energy distribution[¶]. A powerful theorem of Quantum Mechanics states that the n -th moment of the local density of states on an atom i is determined by the sum of all *paths* of order n started from atom i . Here a path, also called "hopping integral" [143], of order n is a function depending on the positions and the topology of atoms belonging to a closed loop of length n comprising atom i . If the second moment alone is necessary to describe the energy distribution, then only identical loops of length two, thus comprising only atom i and each of its first neighbours j in turn, are involved: in this respect this argument is called *second moment approximation*. Second order hopping integrals are typically parameterized [143] as exponential functions of the interatomic distance r_{ij} . Hence, the (attractive) bond energy relative to atom i will be proportional to the *square root* of the sum over all neighbours of hopping integrals.

$$E_i^{\text{attractive}} \propto \sqrt{\sum_j e^{-\beta r_{ij}}} \quad (6.27)$$

Adding a repulsive term due to core-core interactions, the binding energy for the system is:

$$E_b = \frac{1}{2} \sum_i \left[\sum_{j \neq i} A e^{-\alpha r_{ij}} - B \sqrt{\sum_{j \neq i} e^{-\beta r_{ij}}} \right] \quad (6.28)$$

The sum over j runs over all the first neighbours of atom i . This last form is known as the Finnis-Sinclair empirical N -body potential, successfully employed for transition metals [144].

[¶]The binding energy is calculated by means of the tight binding model. The simple dependence of the energy on the square root of the second moment of the energy distribution is inherent to the tight binding model. In Ref. [131] it is shown that a genealogy can be traced from density functional theory through Harris functional to tight binding. In this sense a bond order potential, based on the second moment approximation, can be thought as being justified by density functional theory, as stated in Ref. [131].

A bit of algebraical manipulations of Eq. 6.27, can lead closer to the expression of Eq. 6.1:

$$\begin{aligned}
 E_i^{\text{attractive}} &= -B \sqrt{\sum_{j \neq i} e^{-\beta r_{ij}}} = \\
 &= - \sum_{j \neq i} \left[B e^{-\beta r_{ij}/2} \left(1 + \sum_{k \neq i, j} e^{-\beta(r_{ij} - r_{ik})} \right)^{-1/2} \right] \doteq \\
 &\doteq - \sum_{j \neq i} B e^{-\beta r_{ij}/2} b_{ij}
 \end{aligned} \tag{6.29}$$

The last equality defines b_{ij} and the sums extend over first neighbours. Thus, the total binding energy can again be expressed as a sum of pairwise additive terms, depending only on the distance r_{ij} , where the attractive part is weighted by a term depending on the local coordination of atom i :

$$E_b = \frac{1}{2} \sum_i \sum_{j \neq i} A e^{-\alpha r_{ij}} - b_{ij} B e^{-\beta r_{ij}/2} \tag{6.30}$$

In a regular structure, with all the neighbours of a given atom i at the same distance, the term b_{ij} would be proportional to the inverse square root of the number of first neighbours Z : $b_{ij} \propto Z^{-1/2}$. This makes explicit the connection between the LO and second moment approximation results. Note that the higher the coordination, the smaller the bond order b_{ij} , the weaker the binding energy *per bond*.

6.3 Bond order potentials (BOPs)

The LO model suggests a *shape* of the binding energy curves that is a good first approximation for every element. BOPs have been developed originally for IV group elements [126, 127, 128, 129], first candidates for the success of the model given the single occupancy of their unperturbed atomic orbitals.

If the theoretical approach justifies the form of Eq. 6.1, the actual form of the terms b_{ij} employed in BOPs needed adjustments whose parametrization was a (self consistent) combination of chemical intuition and empirical verification. For this reason, the BOPs are also referred to as semi-empirical potentials, a class that is actually wider than BOPs: it notably comprises, among the others, the Stillinger-Weber potential for silicon [145], and the environment dependent interaction potential (EDIP) for silicon [146] and carbon [147], whose functional form is built up from the so called many body expansion.

The overview will start with the first successful BOP, the Tersoff potential [126], that was originally parameterized for silicon. Then the focus will move exclusively to carbon: the construction of an analytical potential for this element involves a number of subtleties. First it necessary to consider the so called “conjugation of the π -bond”: this is a coupling between the free orbitals of unsaturated^{||} neighbouring atoms, leading to complicated hybridization situations. The effect is strongly present only for carbon amongst the IV

^{||}Unsaturated carbon atoms are those with less than four first neighbours, or bonds. See also appendix 6.9 for a definition of conjugated systems.

group elements, since it is the smallest atom of the group (the first neighbour distance in their diamond lattice are ~ 0.15 , ~ 0.24 , ~ 0.25 nm for carbon, silicon, germanium, respectively). In order to tackle the conjugation effects, even the simplest approximation requires an approach that goes beyond the first neighbour shell.

In second place, LO accounts only for covalent (and metallic) bonds; since graphite sheets interact via weak coupling of the π -orbitals, a “long” range, non bonded part of the potential (the interplanar distance in graphite is ~ 0.34 nm, whereas first and second neighbours are at ~ 0.14 and ~ 0.25 nm) would be needed to stabilize this solid phase. In the following we will propose, step by step, the solutions to these problems.

In the actual formulation of BOPs, attention is always posed to have functions that are continuous and smooth with respect to any of their arguments: this is both for mathematical elegance and for the practical purpose of dealing with continuous forces in a molecular dynamics simulation.

6.4 The Tersoff potential

Tersoff [126] was the first who provided a BOP, based on the theoretical ideas we discussed above, that successfully applied to a covalent element, i.e. silicon. Plotting the energy calculated by means of density functional theory [148, 149, 150] (at the LDA level) of crystalline silicon as a function of the coordination Z , Tersoff pointed out the slow variation of the binding energy per atom as Z increases (with values around -4 eV/atom). On the other hand, the cohesive energy per atom for the dimer $Z = 1$ was found to be much smaller (~ 1.6 eV/atom) than for solid state coordinations ($Z \geq 3$).

A formulation of b_{ij} that could capture the essential features of silicon bonding needed to be proportional to $1/\sqrt{Z}$ only for large values of Z . Tersoff proposed:

$$b_{ij} = (1 + a^n \zeta_{ij}^n)^{-n/2} \quad (6.31)$$

$$\zeta_{ij} = \sum_{k \neq i, j} f_c(r_{ik}) \quad (6.32)$$

$$(6.33)$$

where a and n are fitting parameters. The smooth cut-off function $f_c(r_{ik})$ is 1 for r_{ik} smaller than a certain given radius R_1 , 0 for r_{ik} larger than a given radius R_2 (obviously $R_2 > R_1$) and interpolates between 1 and 0 for r_{ik} intermediate between R_1 and R_2 . Since R_1 and R_2 fall in the region between the first and the second coordination shell, Z_{ij} gives the number of neighbours of atom i , other than j : this means that also “fractional neighbours”, and fractional coordinations, are allowed.

This formulation ensures the correct dependence of the binding energy per atom on the coordination, but carries some pathologies. For instance, any regular lattice of four-fold coordinated atoms would have the same energy: a diamond lattice and a planar square lattice would be equivalent; the shear modulus of a diamond lattice would be zero, a clearly nonphysical prediction. These observations suggest that there should be some angular dependence in the term ζ_{ij} that penalizes structures that are far from the ideal angular correlations in a perfect lattice. Plotting the LDA calculated binding energy per bond, rather than per atom, one can observe its monotonic increase with increasing coordination. If two atoms, j and k , are neighbours of an atom i , they are competing to form a bond

with this atom. Both bonds will be weakened with respect to the dimer ($Z = 1$) case. It is reasonable to assume that, if one of the two neighbours, say k , is further than the other (j) from i , the weakening of the binding energy due to its presence would be lower than in the case where the distances are the same. Thus a dependence of ζ_{ij} on the difference in distances between the neighbours is required. A reasonable (second) guess for ζ_{ij} , is then:

$$\zeta'_{ij} = \sum_{k \neq i, j} f_c(r_{ik}) g(\theta_{jik}) e^{\beta(r_{ij} - r_{ik})^3} \quad (6.34)$$

where $g(\theta_{jik})$ is a not yet specified function of the angles between j and k , as seen from i . Note that a dependence of the bond order b_{ij} on an exponential term, as in the above equation, is already explicit in the *second moment approximation* argument (Eq. 6.29), but not in the LO derivation. The angular function $g(\theta_{jik})$ is chosen to be minimized by an optimal bond angle (the lower g , the smaller ζ'_{ij} , the larger b_{ij} , the stronger the binding energy). Rather than assuming an a-priori optimal angle, its value was left as a parameter to fit for the overall optimization of the potential. This is a seminal break-through. Several empirical potentials assumed, in their parametrization, an optimal angle for bonds around a reference atom (for example the tetrahedral angle of ~ 109.5 for the diamond structure), while here a certain *penalty* is associated to a particular bond angle: its preferability is connected to the other bond angles relative to the same reference atom. This feature will become more clear in presenting the REBO potential [130] in the next section. When ζ'_{ij} is introduced into the bond order (Eq. 6.31), it is evident that it can be: $b_{ij} \neq b_{ji}$. This is a result of the somewhat arbitrary division of the binding energy into a sum on the sites. Tersoff suggests that, if aesthetic reasons require a symmetric form of the bond order, the sum over pairs can be replaced by a sum over bonds (i.e. the sum over j in Eq. 6.1 runs over only those $j > i$) and the bond order is replaced by: $\bar{b}_{ij} = 1/2(b_{ij} + b_{ji})$.

The formulation of ζ'_{ij} is rather ad-hoc: anyway, it was seminal in generalizing the concept of bond order as depending not only on the number of first neighbours Z of the reference atom, but also in how these neighbours arrange. This is achieved using a weighting function in counting neighbours: if a neighbour assumes an unfavourable position with respect to the others, it is counted as more than one neighbour, thus explicitly weakening the binding energy.

This potential showed an overall good transferability in dealing with different environments, it gave reasonable values for elastic constants and phonon frequencies, but it presented several shortcomings especially in the accuracy of some of the predicted properties. Tersoff itself indicated that the shortcomings could be ascribed to 1) the rather arbitrary choice of the cut-off radii of the function f_c and 2) the somewhat excessive softness of the strain energies given by the bond-angle forces, as they are included in ζ'_{ij} . In total, the BOP for silicon, requires the specification of 13 parameters.

Later on, the potential was parameterized by Tersoff [129] also for carbon, but with a rather limited success: it became evident [3] that considering correlations beyond the first neighbour shell was necessary. This was the main contribution of Brenner [3, 4, 130]

6.5 The REBO potential

In 1990 Brenner [3] presented a successful BOP for hydrocarbon systems, thus comprising carbon and hydrogen. Subsequently, he proposed several refinement of his BOP [4, 130].

The part concerning hydrogen will be here completely disregarded and the analysis will be carried on the latest version of this BOP: the so called Reactive Empirical Bond Order (REBO) potential [130].

Brenner introduced new features in the bond order b_{ij} :

- a revised angular function, that constitutes an interesting development of the original idea of Tersoff;
- two terms that account for inaccuracies present when dealing with π -bonded carbon systems; these two new terms are the “conjugation term” (C_{ij}^π , see appendix 6.9 for the definition of “conjugation”) and the “torsional term” (T_{ij}^π); they include contributions to the binding energy from atoms beyond the first neighbour shell of the reference atom.

The description of the REBO potential will be quite discursive because many of its characteristics will be also part of the LCBOP potential that will be fully described in the next section. In the REBO potential an exponential modulated by a factor $\propto 1/r_{ij}$ is added to the familiar definition of V_R : this is required in order to properly model core-core interactions in case of energetic atomic collisions. The attractive potential V_A is now a sum of three exponentials: this provides more flexibility in fitting binding energies and distances in different lattice and molecular environments.

Following Brenner [130], the (symmetrized) bond order \bar{b}_{ij} is:

$$\bar{b}_{ij} = \frac{1}{2}[b_{ij}^{\sigma-\pi} + b_{ji}^{\sigma-\pi}] + C_{ij}^\pi + T_{ij}^\pi \quad (6.35)$$

The term valid for both σ and π bonds is similar to the term proposed by Tersoff:

$$b_{ij}^{\sigma-\pi} = [1 + \sum_{k \neq i,j} f_c(r_{ik})G(\cos \theta_{kij})]^{-1/2} \quad (6.36)$$

In this formulation, a function of the difference between the bond distances r_{ij} and r_{ik} is not present. **

The function G is constructed with the information coming from the crystalline phases. Its value at 5 properly selected points is calculated exactly via the following procedure. Graphite and diamond lattices display only one angle for first neighbours: 120 and ~ 109.5 degrees, respectively: the function G at these two angles ($G(-1/2)$ and $G(-1/3)$) is set in such a way that the binding energy is the known one, at the equilibrium distances. The strain energy to bend the linear C_3 molecule (i.e. the ‘monomer’ of the infinite *linear* chain) to the 120 degrees bent configuration (a value known from density functional calculations) is used to fix the value of $G(-1)$. The simple cubic lattice contains only angles at 180 and 90 degrees: the value of $G(0)$ is then fixed, being the only new unknown. The fcc lattice contains angles of 180, 120, 90, and 60 degrees, yielding the value of $G(1/2)$. The function in the intermediate values of the argument is estimated through an interpolating cubic spline. Encouragingly, the value of G at this 5 points is monotonically increasing with the argument $\cos \theta_{kij}$ (the shape of this G is similar to the angular function for the LCBOP,

**Comparing Eq. 6.36 with the expression proposed by Brenner, we have omitted in the square brackets a factor modulating the angular function G and an additive (corrective) term, both intervening only in presence of hydrogen atoms.

that can be seen in Fig. 6.3): consistently with the standard concept using to rationalize the shapes of small molecules, this behaviour can be ascribed to the repulsions of electron pairs in the valence shell. In other words, the atoms minimize the strain energy of their bonds at a given coordination by arranging them as open as possible: this yields angles of 180, 120, 109.5, 90, and 60 for 2, 3, 4, 6, 12 neighbours, respectively.

This definition of the angular function was not sufficient: the function G penalizes small angles at any coordination, but small carbon ring clusters are stable with quite small bond angles. For this reason, a second angular function $\gamma(\theta_{jik})$ was introduced. It was fitted to stabilize those clusters, that operates for two-fold and three-fold coordinated carbon atoms and giving a much smaller penalty for angles lower than the tetrahedral one. For four-fold and higher-fold coordinated atoms, the angular function is G .

The need for the “conjugation term” comes from the following argument. Consider a carbon atom i with three first neighbours bonded to a carbon atom j with four first neighbours (in the neighbour counting of i is included j and viceversa). The bond order according to Tersoff would give a binding energy intermediate between a single bond (i.e. both atoms with four neighbours) and a double bond (i.e. both atoms with three neighbours). The formation of the π -bond of the double bond results from the overlap of two singly occupied p atomic orbitals. Since the atom with four neighbours does not have a free p orbital, no overlap can occur. Thus the bonding situation is better described with a single bond plus a radical orbital, with a binding energy lower than a single bond configuration. Note that the situation depicted above occurs in the vacancy formation in the diamond lattice: the bonds of the first neighbours to the vacancy with their neighbours, need to be weakened by the vacancy formation. To achieve this, the term C_{ij}^π in this case needs to lower \bar{b}_{ij} : C_{ij}^π has to consider the coordination of first neighbours of i and j , thus it depends on second shell correlations. It is implemented as a function of a) the number of neighbours of atom i besides j (i.e. the term ζ_{ij} in Eq. 6.32), b) the number of neighbours of atom j besides i (ζ_{ji}), and c) a term, Z_{ij}^{conj} , that is defined as follows: it is 1 plus the square of the number of unsaturated first neighbours of i (not counting j), plus the square of the number of unsaturated first neighbours of j (i not included). For integer values of its argument, C_{ij}^π is a three dimensional matrix with entries fitted from model situations: for example each atom in a graphite lattice would give entries 2,2,9 to C_{ij}^π . Fractional entries are treated via a cubic spline.

The introduction of the “torsional” term is natural for double bonded hydrocarbons. Thinking to ethene ($\text{CH}_2=\text{CH}_2$) and imagining the two planes described by the two CH_2 groups, the bond order needs a term that could prefer the co-planar to the orthogonal arrangement of these two planes. This term is necessary even in carbon networks in which double bonds are present: it is different from zero only for bonds between three-fold coordinated atoms i and j . On a chain of four atoms, labelled k, i, j , and l , the dihedral angle ω_{kijl} is here defined, as traditionally done, with the dot product of unit vectors in the direction of the cross products $R_{ij} \times R_{ik}$ and $R_{ji} \times R_{jl}$, where $R_{\alpha\beta}$ is the vector connecting atom α to atom β . The “torsional” term T_{ij}^π is proportional to the sum of $\sin^2 \omega_{kijl}$ (thus 0 and 1 for the co-planar and orthogonal configurations described above, respectively) over all the dihedral angles that can be defined with the bond $i-j$. The proportionality factor has the same entries of C_{ij}^π . For pure double bonds (i.e. for a situation where all the neighbours of i and j are saturated atoms) the factor has its highest value. As a template for pure conjugated systems, it was used an hypothetical lattice structure, theoretically studied in

Ref. [151], with all three-fold atoms like for graphite, but with all dihedral at 90 degrees. With this choice, the torsional term carries always the same proportionality to $\sin^2 \omega_{kijl}$ and the fit of the its pre-factor yields a value ~ 10 times smaller in the full conjugated case than in the pure double bond case.

In total, the REBO potential requires the specification of more than 100 parameters, but it describes quite well bond lengths, energies, force constants (related to the curvatures of the binding energy curves in their minima), strain energies, and interstitial energies for all the solid structures and molecules reported in Ref. [130]. This BOP had two precursors developed by the same author [3]. Compared to the REBO potential, these two potentials, that will be referred to as BrennerI and BrennerII, used: 1) attractive and repulsive pair potentials directly taken from the LO model, 2) the definition of a simpler coordination independent angular function, 3) a factor multiplying the angular function depending on the difference between distances of first neighbours from the reference atom (similar to the exponential term of Eq. 6.34), and 4) a conjugation term with a slightly different definition and less parameters. The difference between BrennerI and BrennerII lied in the two parameter sets: BrennerI yielded better bond lengths and BrennerII better force constants. Furthermore, the original formulation [3] did not contain any torsional interactions, that were added for both BrennerI and BrennerII in a later publication [4] in essentially the same form as for the REBO potential, with the important difference that the barrier of the conjugated bond in these cases was around one half of the pure double bond configuration [14]. The BrennerI and BrennerII potentials differ only in the values of the parameters; BrennerI yields good bond lengths and energies, but very poor force constants; BrennerII gives good force constants, but only fair bond lengths and energies. These two potentials were the first BOPs to describe reasonably well diamond, graphite, and liquid carbon (together with many hydrocarbons).

6.6 The LCBOP I

The REBO (as well as BrennerI and Brenner II) potentials already considered correlations that went further than the first coordination shell. Anyway, these potentials describe (strong) covalent interactions: to accurately describe carbon for an extended part of the phase diagram, they required further improvement. For example a term describing the interplanar stacking in solid graphite was missing. This structure is stabilized by much weaker interactions, at least a hundred times smaller, than the covalent bonds. At the same time, upon approaching due to compression, the repulsion of graphite sheets can become an order of magnitude stronger than the attraction at equilibrium. There have been attempts to add non-bonded interactions to the short range REBO potential without perturbing its nicely fitted properties. The idea is to add interactions, e.g. of a Lennard-Jones type, that are (smoothly) switched-off for “too close” atoms. This was achieved using distance as the relevant parameter [152, 153] or neighbour connectivity [154] or both [155]. However, the distance cut-off introduces loss of accuracy if connected to an unperturbed short range potential, while the connectivity criterion (excluding from the long range interactions atoms that are first, second, or third neighbours of the reference atom) has no good physical basis.

In Ref. [15], Los and Fasolino introduced the long range potential, LCBOP I, in which the (isotropic) non-bonded interactions are regulated by a distance criterion, but the short range was completely refit to match the reference data in the distance interval in which

both contributions, bonded and non-bonded, are present. Furthermore, in the LCBOPI were introduced: 1) a scheme that accounts for conjugation effects, alternative and more transparent than for the REBO potential, and 2) a correction factor to the angular function, depending on the difference in the distances between neighbours and the reference atom, to fine tune the description of certain solid state properties. This implies that also the bonded part of the potential constitutes a novelty: in Ref. [15] it is thus proposed a different set of fitted parameters for a short range version of the LCBOPI, called CBOP, dropping the initial ‘L’ for ‘Long range’.

The binding energy is expressed as:

$$E_b = \frac{1}{2} \sum_{i,j}^N (f_{c,ij} V_{ij}^{SR} + (1 - f_{c,ij}) V_{ij}^{LR}) \quad (6.37)$$

The cut-off functions $f_{c,ij}$ have the familiar meaning, V_{ij}^{SR} is the short range, bonded, part and V_{ij}^{LR} is the long range, non-bonded, term.

The short range is written as usual:

$$V_{ij}^{SR} = V_R(r_{ij}) - \bar{b}_{ij} V_A(r_{ij}) \quad (6.38)$$

where

$$\begin{aligned} V_R(r) &= A e^{-\alpha r} \\ V_A(r) &= B_1 e^{-\beta_1 r} + B_2 e^{-\beta_2 r} \end{aligned} \quad (6.39)$$

It can be noted that this expression of the attractive part of the potential is not strictly the one proposed by Abell (see Eqs. 6.7): this implies that the analysis on the dependence of the equilibrium distance and cohesive energy does not apply any more; actually, it is not possible to calculate in a closed forms the equilibrium parameters. For this reason, in appendix 6.8.3 we will give a pictorial representation of the dependence of the binding energy on the bond order b_{ij} for the regular lattice situations.

The cut-off functions are expressed:

$$f_{c,ij}(x) = \Theta(-x) + \Theta(x)\Theta(1-x)e^{\frac{\gamma x^3}{x^3-1}} \quad (6.40)$$

where $\Theta(x)$ is the heavyside step function; $x = (r - r_1)/(r_2 - r_1)$, so that r_1 is the cut-off lower bound, i.e. the distance below which atoms are counted as integer neighbours, while r_2 is the cut-off higher bound, i.e. the distance above which atoms have only non-bonded interactions.

The bond order is split into:

$$\bar{b}_{ij} = \frac{1}{2} [b_{ij} + b_{ji} + F_{ij}^{conj}(Z_{ij}, Z_{ji}, Z_{ij}^{conj})] \quad (6.41)$$

where

$$b_{ij} = \left(1 + \sum_{k \neq i,j} f_{c,ik}(r_{ik}) G_I(\cos \theta_{jik}) H(\delta r_{jik}) \right)^{-1/2} \quad (6.42)$$

and the conjugation term $F_{ij}^{conj}(Z_{ij}, Z_{ji}, Z_{ij}^{conj})$ is defined with its arguments in section 6.6.1. The function G_I is defined, as in the REBO potential, as a spline connecting points calculated from reference data (not only the value of G_I , but also the first and second derivative at the same selected angles, can be retrieved from reference data and imposed to the spline). The function $H(\delta r_{jik})$, where $\delta r_{jik} = r_{ij} - r_{ik}$ is^{††}:

$$H(x) = \begin{cases} H_1(x) = L \left(1 + \kappa(x+d) \left(\frac{1}{1 + [\kappa(x+d)]^{10}} \right)^{1/10} \right) & x < -d \\ H_2(x) = 1 + C_1 x + \frac{1}{2} C_1^2 x^2 + C_4 x^4 + C_6 x^6 & -d \leq x \leq d \\ H_3(x) = R_0 + R_1(x-d) & x > d \end{cases} \quad (6.43)$$

The function $H(\delta r_{jik})$ is introduced to optimize elastic and surface properties. Besides, it is essential to properly describe the diamond to graphite energy barrier at 0 K, as calculated via LDA in Ref. [156].

6.6.1 The conjugation term

The coordination of an atom i is:

$$Z_i = \sum_k f_{c,ik} \quad (6.44)$$

where the sum extends over all atoms (except for i). For the conjugation scheme, it is needed to define coordinations as if j is always an integer neighbour of i , so it is introduced the quantity:

$$Z_{ij} = \min \left(3, \sum_{k \neq j} f_{c,ik} \right) = \min(3, Z_i - f_{c,ij}) \quad (6.45)$$

The binary operator $\min(x, y)$ gives the minimum of x and y . The third argument of F^{conj} , Z_{ij}^{conj} is a number in the interval [0,1], defined by:

$$Z_{ij}^{conj} = \frac{(Z_{ij} + 1)(Z_{ji} + 1)(Z_{ij}^{el} + Z_{ji}^{el}) - 4(Z_{ij} + Z_{ji} + 2)}{Z_{ij}(3 - Z_{ij})(Z_{ji} + 1) + Z_{ji}(3 - Z_{ji})(Z_{ij} + 1) + \epsilon} \quad (6.46)$$

where ϵ is a very small, positive number, added to prevent vanishing of the denominator. Z_{ij}^{el} is the (fractional) number of electrons given from i to the bond ij :

$$Z_{ij}^{el} = \frac{4 - M_{ij}}{(Z_{ij} + 1) - M_{ij}} \quad (6.47)$$

^{††}It is justified assuming exponential dependence at small $x = \delta r_{jik}$: this accounts for the first three terms in H_2 ; a certain (symmetric) ‘‘non-parabolicity’’ is required by the analysis of certain surface reconstructions, hence the x^4 term. Outside $[-d, d]$ a basically linear behaviour is assumed in order to reproduce the diamond to graphite energy barrier, as calculate by means of the LDA. Note that only three parameters, i.e. d , C_1 , and C_4 are fit, the other five, i.e. L , κ , C_6 , R_0 , and R_1 , coming from the continuity of H at $x = \pm d$, up to the second derivative. By construction $d^2 H_1/dx^2|_{x=-d} = d^2 H_3/dx^2|_{x=d} = 0$, so that C_6 follows directly from $d^2 H_2/dx^2|_{x=d} = d^2 H_2/dx^2|_{x=-d} = 0$. Furthermore, L and R_0 follow from continuity of H in $x = -d$ and $x = d$ respectively, leaving R_1 and κ to be found from continuity of the first derivative of H at $x = \pm d$.

where

$$M_{ij} = \min(3, \tilde{M}_{ij}) \quad (6.48)$$

and

$$\tilde{M}_{ij} = \sum_{k \neq i, j} f_{c,ik} X(x_{ik}) \quad (6.49)$$

Here $x_{ik} = Z_k - f_{c,ik}$, and $X(x_{ik})$ is given by:

$$X(x_{ik}) = \Theta(x_{ik} - 3) + \frac{1}{2} (1 - \cos[\pi(x_{ik} - 2)]) \Theta(x_{ik} - 2) \Theta(3 - x_{ik}) \quad (6.50)$$

Thus, \tilde{M}_{ij} counts the number of unsaturated neighbours of atom i , different from atom j . The form of Z_{ij}^{conj} comes from the following argument. In a carbon system in which all the atoms are not over-coordinated (no atom has more than four neighbours - or bonds), M_{ij} represents the number of electrons of atom i involved in single bonds (not counting the bond $i - j$), and Z_{ij}^{el} is the (fractional) number of electrons left to atom i to form π -bonds with all its unsaturated neighbours. Thereafter, it is defined as the ratio between the left electrons ($4 - M_{ij}$) and the number of unsaturated neighbours ($(Z_{ij} + 1) - M_{ij}$): the neighbour j is here part of the set, being counted always as integer. In a configuration in which both i and j are three-fold ($Z_{ij}, Z_{ji} = (3, 3)$), if the two neighbours of i and the two neighbours of j are three-fold (as in graphite), then $Z_{ij}^{el} = Z_{ji}^{el} = 4/3$, i.e. the fourth electron of atom i (and j) is proposed to be equally distributed among the three neighbours (bonds)^{‡‡}. If the two neighbours of i and the two neighbours of j were, in contrast, four-fold, $Z_{ij}^{el} = Z_{ji}^{el} = 2$, i.e. atom i would give two electron to bond j , and the same would do j to i , thus forming a double bond. For asymmetric situations ($Z_{ij}^{el} \neq Z_{ji}^{el}$), the average of the two quantities ($\bar{Z}_{ij}^{el} = (Z_{ij}^{el} + Z_{ji}^{el})/2$) is thought as the number of electrons put in the bond $i - j$ by both i and j . For a given pair (Z_{ij}, Z_{ji}), the value \bar{Z}_{ij}^{el} ranges from a minimum to a maximum value, $\min(\bar{Z}_{ij}^{el})$ and $\max(\bar{Z}_{ij}^{el})$. For ($Z_{ij}, Z_{ji} = (3, 3)$), \bar{Z}_{ij}^{el} clearly ranges from $4/3$ to 2 . This interval is linearly mapped into the interval $[0, 1]$ to give Z_{ij}^{conj} :

$$Z_{ij}^{conj} = \frac{\bar{Z}_{ij}^{el} - \min(\bar{Z}_{ij}^{el})}{\max(\bar{Z}_{ij}^{el}) - \min(\bar{Z}_{ij}^{el})} \quad (6.51)$$

Some algebraic manipulations show the equivalence of Eqs. 6.51 and 6.46. Values of the binding energies for the two limiting cases can be inferred from reference data, so that one can reasonably define $F_{ij}^{conj}(Z_{ij}, Z_{ji}, 0)$ and $F_{ij}^{conj}(Z_{ij}, Z_{ji}, 1)$. In the intermediate situations, at integer (Z_{ij}, Z_{ji}), linear interpolation holds:

$$\begin{aligned} F^{conj}(Z_{ij}, Z_{ji}, Z_{ij}^{conj}) &= (1 - Z_{ij}^{conj}) F^{conj}(Z_{ij}, Z_{ji}, 0) \\ &+ Z_{ij}^{conj} F^{conj}(Z_{ij}, Z_{ji}, 1) \end{aligned} \quad (6.52)$$

At fractional values of (Z_{ij}, Z_{ji}), the interpolation scheme 6.8 is given in the appendix 6.8.

^{‡‡}It is only “proposed”: if all the atoms “propose” the same, as in a regular lattice, the proposal is accepted, but for non symmetrical configurations, this model argues the average of the two proposals as the accepted choice.

6.6.2 The non bonded interactions

The non bonded interactions, V_{ij}^{LR} are constructed by making a best fit to LDA data for the interplanar energies in graphite [15] as a function of the interplanar spacing beyond 0.2 nm. The non bonded interactions are smoothed off to zero beyond 0.6 nm:

$$f_{c,ij}^{LR}(r) = \Theta(r_2^{LR} - r) + \frac{1}{2}(1 + \cos[2\pi(r - r_1^{LR})]) \Theta(r - r_1^{LR})\Theta(r_2^{LR} - r)$$

The functional form for V_{ij}^{LR} interactions is:

$$\begin{aligned} V^{LR}(r) &= \Theta(r_0 - r)V_1^M(r) + \Theta(r - r_0)V_2^M(r) \\ V_i^M(r) &= \epsilon_i (e^{-2\lambda_i(r-r_0)} - 2e^{-\lambda_i(r-r_0)}) + v_i \end{aligned}$$

The two Morse potentials (V_i^M), matched at their minimum value r_0 , give the flexibility of tuning independently the steepness of the left and right side of the curve. The exponential dependence of the Morse potential was preferred to the popular Lennard-Jones parametrization of non-bonded interactions, since this latter, when tested, gave unreasonably high values of the interplanar repulsion at short (~ 0.2 nm) distances. With the optimal set of parameters for the LCBOP, the value of the non bonded interactions, from the minimum (at r_0) at -0.025 eV, rises up to 0.284 eV at 0.22 nm, i.e. r_2 , when the bonded attractions are switched on. Typically, the binding energy E_b (Eq. 6.37) continues to rise up to ~ 0.3 eV at ~ 0.2 nm before the attractive part becomes predominant. This means that any atom approaching the first neighbour shell from outside, has to overcome such an energy barrier to enter the shell. The parameters of the LCBOP are given in the appendix 6.8.

With the help of ~ 70 independent parameters, the LCBOP gives an impressive recovering of the fitted database for solid state structures. Besides reasonable description of some subtle surface effects, it gives a perfect transformation of a thin diamond 111-slab into layered graphite. This transformation is not very well reproduced by the REBO potential with connectivity based non-bonded interactions [15]

6.7 The LCBOP⁺

The LCBOP⁺ is an improvement of the LCBOP, made necessary for a correct description of the liquid phase, whose investigation is one of the main topics of the present thesis. To this purpose we introduced two features into the bonded part of the LCBOP: 1) a softening of angular correlations for unsaturated atoms at low angles (in the spirit of the REBO potential) and 2) the addition of torsional interactions. Furthermore, a more flexible family of switching functions in place of $f_{c,ij}$ was introduced. These modifications are described in this section.

6.7.1 New switching functions

A family of switch functions $S^{down}(x)$ is introduced. They are defined as:

$$S^{down}(x) = \Theta(-x) + \Theta(x)\Theta(1-x)(1+2x+px^2)(1-x)^2 \quad (6.53)$$

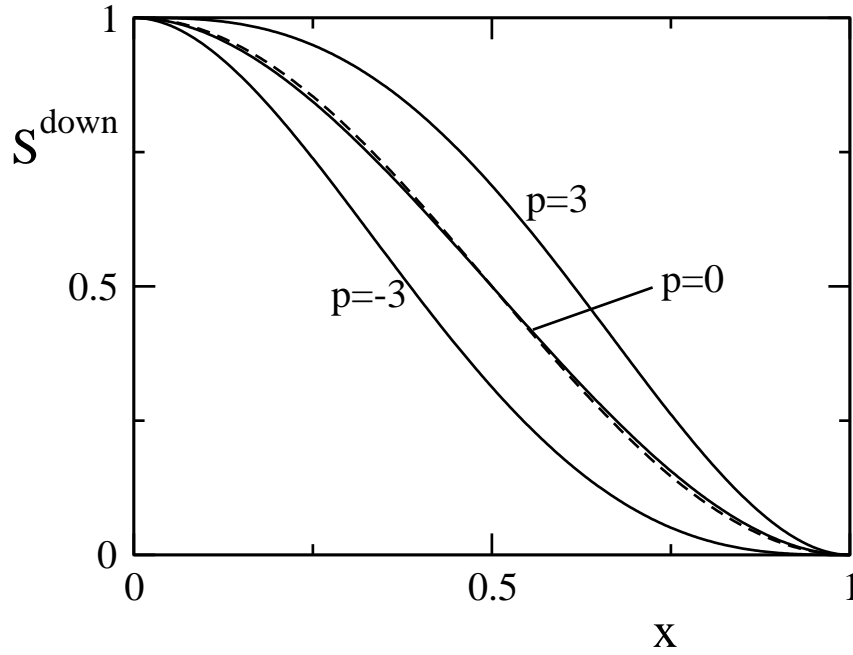


Figure 6.2: Switch function $S^{\text{down}}(x)$ for $p = -3, 0, 3$ (solid lines) compared to the Brenner's cut-off function $f_{ij} = 1/2(1 + \cos(\pi x))$ Refs. [3, 130] (dashed line).

As shown in Fig. 6.2, the parameter $p \in [-3, 3]$, offers a certain freedom in the choice of the shape of the switch function, while staying monotonic within $x \in [0, 1]$. To realize a switch as a function of a given quantity q (e.g. distance or coordination) within a desired interval $[q_{\min}, q_{\max}]$, the dimensionless argument x is defined as:

$$x = x(q) = \frac{q - q_{\min}}{q_{\max} - q_{\min}} \quad (6.54)$$

For the LCBOP⁺:

1. the switch function $f_{c,ij}$ of the LCBOP⁺ was replaced by $S_{p=3}^{\text{down}}$, in Eqs. 6.37 and 6.42. Also $f_{c,ij}^{LR}(r)$ of Eq. 6.53 was replaced by $S_{p=3}^{\text{down}}$ (here: $q_{\min} = r_1 = 0.17$ nm, and $q_{\max} = r_2 = 0.22$ nm).
2. the switch function in the definition of the coordination related quantities (Eqs. 6.44, 6.45, and 6.49) was replaced by $S_{p=-3}^{\text{down}}$ (also here: $q_{\min} = r_1 = 0.17$ nm, and $q_{\max} = r_2 = 0.22$ nm);
3. the switch function in the definition of unsaturated atoms (Eq. 6.50) has been replaced by $S_{p=0}^{\text{down}}$ (obviously, in this case, $q_{\min} = 2$, and $q_{\max} = 3$), this latter modification being negligible with respect to the LCBOP⁺ (see Fig. 6.2).

6.7.2 Angular function

The angular function of the LCBOP⁺ is written (similarly to the REBO potential [130]):

$$G_{I^+}(y, z) = \Theta(y_0 - y)G_I(y) + \Theta(y - y_0)\tilde{G}_{I^+}(y, z) \quad (6.55)$$

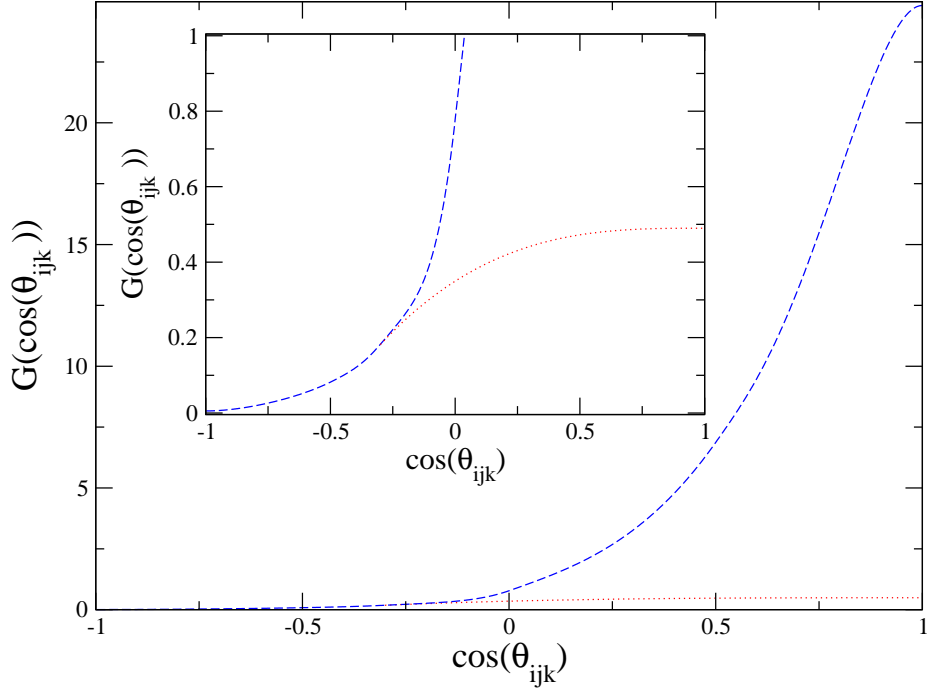


Figure 6.3: $G_I(\cos\theta_{ijk})$, dashed line, and $\Gamma(\cos\theta_{ijk})$, dotted line. The inset magnifies lower y-axis values to show the shape of Γ .

where G_I is the angular function of the LCBOP (see Eq. 6.42), $y = \cos\theta_{ijk}$, $y_0 = -1/3$ is a constant boundary value, and $z = z_{ij} = Z_i - S_{p=-3}^{down}$. The function \tilde{G}_{I+} reads:

$$\tilde{G}_{I+}(y, z) = G_I(y) + S_{p=0}^{down}(z - 2)[\Gamma(y) - G_I(y)], \quad (6.56)$$

with $\Gamma(y)$:

$$\Gamma(y) = \gamma_0(y - 1)^3 + \gamma_1 \quad (6.57)$$

The parameters γ_0 and γ_1 , given in table 6.3 in appendix 6.8, are fit to the geometries and energies (Table 6.1) of a planar rhombic cluster (C_4 , symmetry D_{2h} , Ref. [157]), with 2 angles around 60° , and a cubic cluster (C_8 , Ref. [158]), with all 24 angles at 90° . Figure 6.3 shows G_I and Γ .

Molecule		LCBOPI ⁺	Reference
C_4	E_b [kJ/mol]	1736	1669 [157]
C_4	d [nm]	0.150	0.143 [157]
C_8	E_b [kJ/mol]	4052	3888 [158]
C_8	d [nm]	0.155	0.148 [158]

Table 6.1: Comparison of total energy E_b and bond length d for the model clusters used to fit $\Gamma(y)$.

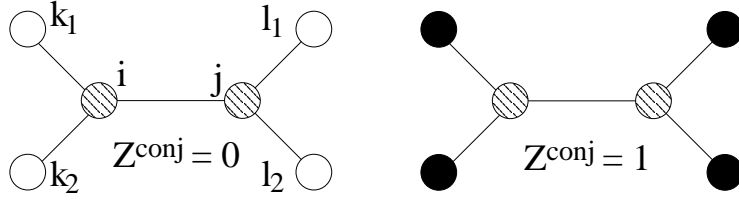


Figure 6.4: Schematic view of the molecules representing a conjugated (left) and a double (right) bond. The shaded circles represent the atoms bonded by either the conjugated or the double bond. White circles are three-fold atoms (i.e. they have other two bonds not shown in figure). Black circles are four-fold atoms. Only the number and not the nature of the bonds that the k 's (or l 's) atoms make with atoms other than i (or j) is relevant for the definition of Z_{ij}^{conj} .

6.7.3 Torsional term

The torsional term acts only for a bond between two sp_2 hybridized atoms: in Fig. 6.4 a schematic view of the relevant configurations is shown. For the LCBOP⁺, the torsion is fitted to the data of Ref. [14]. The torsion term T_{ij} is:

$$T_{ij} = D_{ij}(Z_{ij}, Z_{ji}) \sum_{k \neq i, j} \sum_{l \neq i, j} t_{ij}(\tilde{y}, Z_{ij}^{conj}) S_{p=3}^{down}(r_{ik}) S_{p=3}^{down}(r_{jl}) \quad (6.58)$$

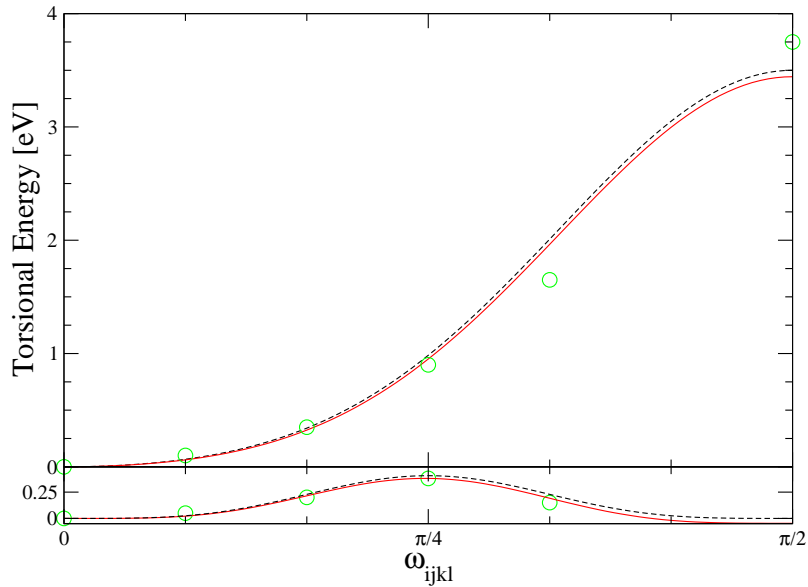


Figure 6.5: Torsional energies for the two limiting cases at the equilibrium DF bond length between atom i and j . Top: $Z_{ij}^{conj} = 1$, double bond. Bottom: $Z_{ij}^{conj} = 0$, conjugated bond. Dashed lines are the values $T_{ij} \cdot V_A(r_{ij})$. The solid lines are the same with added the difference in long range interactions coming from all the atoms of the molecule, with respect to the flat molecule: note that this gives a natural asymmetry in the conjugated configuration. DF data (circles) are from [14].

where \tilde{y} is defined as:

$$\tilde{y} \equiv \cos \omega_{ijkl} = \mathbf{e}_{ijk} \cdot \mathbf{e}_{jil} = \frac{\mathbf{r}_{ij} \times \mathbf{r}_{ik}}{|\mathbf{r}_{ij} \times \mathbf{r}_{ik}|} \cdot \frac{\mathbf{r}_{ji} \times \mathbf{r}_{jl}}{|\mathbf{r}_{ji} \times \mathbf{r}_{jl}|}$$

$D_{ij}(Z_{ij}, Z_{ji})$ is a two dimensional switch, defined for $Z_{ij}, Z_{ji} \in [1, 3]$, given by:

$$D_{ij}(x, y) = (1 - x)^4 (1 - y)^4 (1 + 4x)(1 + 4y) \Theta(x + 1) \Theta(1 - x) \Theta(y + 1) \Theta(1 - y) \quad (6.59)$$

with $x = |Z_{ij} - 2|$ and $y = |Z_{ji} - 2|$. This definition yields a) $D_{ij}(Z_{ij}, Z_{ji}) = D_{ij}(2, 2) = 1.0$, b) $D_{ij}(n, m) = 0$ when at least one of the arguments n and m is 1 or 3, and c) vanishing partial derivatives for all nine integer pairs (n, m) .

In contrast to Refs. [4] and [130], where the dependence on the Z_{ij}^{conj} is limited to the pre-factor D_{ij} , for the LCBOPI⁺ the Z_{ij}^{conj} -dependence is included in the function t_{ij} , which reads[†]:

$$t_{ij}(\tilde{y}, Z_{ij}^{conj}) = \tau_0(\tilde{y}) + \tilde{S}(Z_{ij}^{conj})(\tau_1(\tilde{y}) - \tau_0(\tilde{y})) \quad (6.60)$$

where:

$$\tau_0(\tilde{y}) = T_0 (\tilde{y}^2 (1 - \tilde{y}^2))^2 \quad (6.61)$$

$$\tau_1(\tilde{y}) = T_1 (1 - \tilde{y}^2)(2 - \tilde{y}^2)^2 \quad (6.62)$$

describe the torsional barriers for $Z_{ij}^{conj} = 0$ (Fig. 6.4, left panel) and $Z_{ij}^{conj} = 1$ (Fig. 6.4, right panel) respectively, and where the switch function $\tilde{S}(Z_{ij}^{conj})$ is given by:

$$\Lambda(Z_{ij}^{conj}) = (3(Z_{ij}^{conj})^2 - 2(Z_{ij}^{conj})^3)^6 \quad (6.63)$$

It quickly decays from $Z_{ij}^{conj} = 1.0$, in order to associate the full barrier only to configurations very close to the double bonded ones. The functions τ_0 and τ_1 are shown in Fig. 6.5. Values for T_0 and T_1 are in table 6.3 in appendix 6.8.

[†] In Refs. [4] and [130], the barrier as a function of the dihedral angle ω_{ijkl} is always described by $\sin^2(\omega_{ijkl})$ and differs only by a scale factor between these two bonding situations. The data of Ref. [14] shows the this assumption is not justified: for a completely conjugated bond the torsional energy is almost zero at $\pi/2$, but around 0.3 eV at $\pi/4$: this behaviour cannot be described by a curve $\propto \sin^2(\omega_{ijkl})$.

6.8 Appendix. Further details for the LCBOP1 and the LCBOP1⁺

6.8.1 Interpolation scheme of F^{conj}

The interpolation scheme is based on the values and derivatives on the grid of integer (Z_{ij}, Z_{ji}) . The values are given as fitting parameter. Due to symmetry arguments the derivatives has to fulfill, defining $F_{Z_{ij}^{conj}}^{conj}(Z_{ij}, Z_{ji}) \doteq F^{conj}(Z_{ij}, Z_{ji}, Z_{ij}^{conj})$ when Z_{ij}^{conj} is integer (i.e. = 0,1):

$$\left. \frac{\partial F_{Z_{ij}^{conj}}^{conj}}{\partial Z_{ij}} \right|_{0,m} = \left. \frac{\partial F_{Z_{ij}^{conj}}^{conj}}{\partial Z_{ji}} \right|_{n,m} = 0 \quad (6.64)$$

At the boundaries:

$$\left. \frac{\partial F_{Z_{ij}^{conj}}^{conj}}{\partial Z_{ij}} \right|_{n,m} = \frac{F_{Z_{ij}^{conj}}^{conj}(n+1, m) - F_{Z_{ij}^{conj}}^{conj}(n-1, m)}{2} \quad (6.65)$$

In order to avoid spurious oscillation, it has to be:

$$\left. \frac{\partial F_{Z_{ij}^{conj}}^{conj}}{\partial Z_{ij}} \right|_{2,0} = -0.088188 \quad (6.66)$$

The value of $F_{Z_{ij}^{conj}}^{conj}$ for non-integer (Z_{ij}, Z_{ji}) is given by the interpolation within the grid square (Z_{ij}, Z_{ji}) belongs to. The interpolation within the square is denoted $f^{conj}(x, y)$ (the subscript $Z_{ij}^{conj} = 0,1$ is dropped for convenience), with $x \doteq Z_{ij} - \text{Int}(Z_{ij})$ and $y \doteq Z_{ji} - \text{Int}(Z_{ji})$, so that $(x, y) \in [0,1] \times [0,1]$.

$$\begin{aligned} f^{conj}(x, y) &= (1-y)(1-x)[f_{00}^{conj} + x^2 \tilde{f}_{x,10} + y^2 \tilde{f}_{y,01}] + \\ &+ (1-y)x[f_{10}^{conj} + (1-x)^2 \tilde{f}_{x,00} + y^2 \tilde{f}_{y,11}] + \\ &+ y(1-x)[f_{01}^{conj} + x^2 \tilde{f}_{x,11} + (1-y)^2 \tilde{f}_{y,00}] + \\ &+ yx[f_{11}^{conj} + (1-x)^2 \tilde{f}_{x,01} + (1-y)^2 \tilde{f}_{y,10}] \end{aligned} \quad (6.67)$$

with

$$\tilde{f}_{x,kl} = (-1)^k \left(\left. \frac{\partial f^{conj}}{\partial x} \right|_{kl} - f_{1l}^{conj} + f_{0l}^{conj} \right) \quad (6.68)$$

$$\tilde{f}_{y,kl} = (-1)^l \left(\left. \frac{\partial f^{conj}}{\partial x} \right|_{kl} - f_{k1}^{conj} + f_{k0}^{conj} \right) \quad (6.69)$$

$$(6.70)$$

where $k, l = 0,1$, $f_{kl}^{conj} \doteq f^{conj}(k, l)$, and $\partial f^{conj} / \partial \alpha|_{kl}$ ($\alpha = x, y$) are the derivatives of F_{ij}^{conj} in the corners (k, l) .

6.8.2 Parameters for the LCBOP and the LCBOP⁺

		Short range potential V^{sr}							
	r_1	=	1.7	r_2	=	2.2	γ	=	1.5
V_R	A	=	35652.94452	α	=	6.26781252			
V_A	B_1	=	18614.83652	β_1	=	5.83045680			
	B_2	=	32.01993977	β_2	=	1.16864228			
H	d	=	0.14	C_1	=	3.335			
	C_4	=	220.0	For $C_6, L, \kappa, R_0,$ and R_1 see text.					

$\cos\theta$	G	G'	G''
-1	0.00548948	0.00	-
-1/2	0.08188859	0.30	1.13
-1/3	0.15709129	0.68633951	3.55887225
0	0.772	5.91323569	-
1/2	6.780	23.6184500	-
1	24.40	0.00	-

$F_{ij,0}^{conj}$				
	$Z_{ji} = 0$	$Z_{ji} = 1$	$Z_{ji} = 2$	$Z_{ji} = 3$
$Z_{ij} = 0$	0.000000	0.034993	-0.009085	-0.229403
$Z_{ij} = 1$	0.034993	0.000000	-0.058546	-0.147667
$Z_{ij} = 2$	-0.009085	-0.058546	0.000000	-0.083991
$Z_{ij} = 3$	-0.229403	-0.147667	-0.083991	0.000000

$F_{ij,1}^{conj}$				
	$Z_{ji} = 0$	$Z_{ji} = 1$	$Z_{ji} = 2$	$Z_{ji} = 3$
$Z_{ij} = 0$	0.000000	0.100921	0.072525	-0.229403
$Z_{ij} = 1$	0.100921	0.239564	0.010324	-0.147667
$Z_{ij} = 2$	0.071525	0.010324	0.161180	-0.083991
$Z_{ij} = 3$	-0.229403	-0.147667	-0.083991	0.000000

Long range potential V^{lr}								
r_0	=	3.716163	r_1^{LR}	=	5.5	r_2^{LR}	=	6.0
ϵ_2	=	2.617755	λ_1	=	1.359381	λ_2	=	2.073944
ϵ_1	=	$\epsilon_2\lambda_2^2/\lambda_1^2$	v_1	=	$\epsilon_1 - \epsilon_2$	v_2	=	0.0

Table 6.2: Parameters of the LCBOP. $A, B_1,$ and B_2 are in eV; $v_1, \epsilon_1,$ and ϵ_2 are in meV; $r_1, r_2, d, r_0, r_1^{LR},$ and r_2^{LR} are in Å; $\alpha, \beta_1, \beta_2, C_1, \lambda_1,$ and λ_2 are in Å⁻¹; C_4 is in Å⁻⁴; all the other parameters are dimensionless.

G_{I^+}	$y_0 =$	$-1/3$	$\gamma_1 =$	0.462131068
	$\gamma_0 =$	0.128688658		
T_{ij}	$T_0 =$	-0.182177564	$T_1 =$	-0.0147711739

Table 6.3: Parameters for the LCBOP1⁺ (all dimensionless).

6.8.3 Binding energy curves

In this appendix we show selected binding energies (V_{ij}^{SR} of Eq. 6.38) as a function of the interatomic distance r_{ij} alone, and parametrically depending on the bond order \bar{b}_{ij} as defined in Eq. 6.41. Only few situations can be meaningfully described in this way: in fact, the idea is to have structures in which \bar{b}_{ij} does not change while changing the interatomic distances. To fulfill the requirement we need:

- a regular lattice, i.e. a structure in which all the first neighbours distances are always the same, otherwise the term $H(\delta r_{jik})$ of Eq. 6.42, equal to 1 in a regular lattice, would change upon stretching the structure.
- to limit the analysis up to 0.17 nm, i.e. r_1 , the cut-off lower bound: beyond this distance, not only V_R and V_A are cut-off via $f_{c,ij}$ (see Eq. 6.40), but also \bar{b}_{ij} starts depending on r_{ij} via the cut-off $f_{c,ij}$ itself (see Eq. 6.42).
- to use the short range version of the potential (CBOP), since in the long range version the bond energy of each atom depends on all the positions of the atoms within the long range cutoff distances.

We thus limit ourselves to the chain structure, graphite, and diamond, representing coordination $Z = 2, 3, 4$ [‡]. Fig. 6.6 shows the repulsive potential $V_R(r_{ij})$ (top curve) and the attractive potential $V_A(r_{ij})$ weighted by the proper \bar{b}_{ij} . Fig. 6.7 shows the sum of the (weighted) attractive and repulsive terms yielding the binding energy *per bond* of the considered structures. The binding energy *per atom* for the chain would be the same curve; for graphite one has to multiply the curve by 3/2, while for diamond a factor 4/2 is needed. The line passing through the minima is still expressed in the form of Eq. 6.26: $\mathcal{E}_b = -D_e^{bond} = \kappa * \exp(-r_e/(2(S-1)))$, with κ calculated to yield the exact value for the case $Z = 1$ (not shown), and the effective $S = 1.22$, i.e. in the covalent regime according to Abell's analysis. These dependence of the cohesive energy on the equilibrium distance suggests that all the extra features added to the bond order b_{ij} in the actual implementation of the BOPs, do not lead excessively far from the original Abell's model.

[‡]In these three cases $\bar{b}_{ij} \cong 0.99, 0.93, 0.83$, respectively. The case $Z = 1$ (yielding $\bar{b}_{ij} = 1$), the dimer, would be almost undistinguishable from the case $Z = 2$.

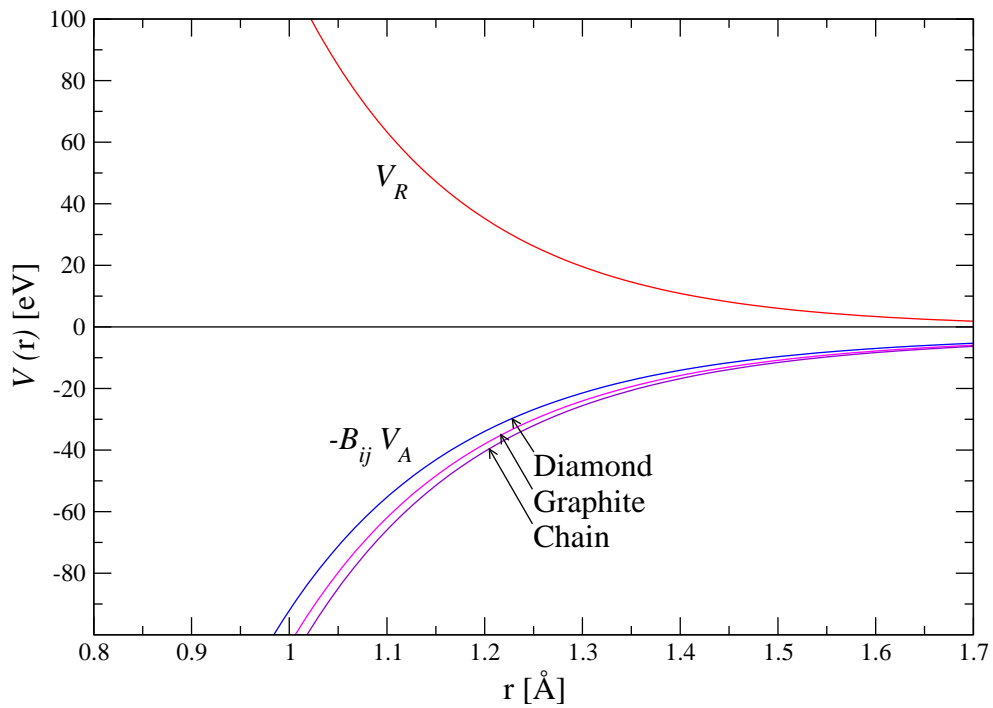


Figure 6.6: Repulsive potential (top, all positive, curve) and \bar{b}_{ij} weighted attractive potentials for the chain, graphite, and diamond.

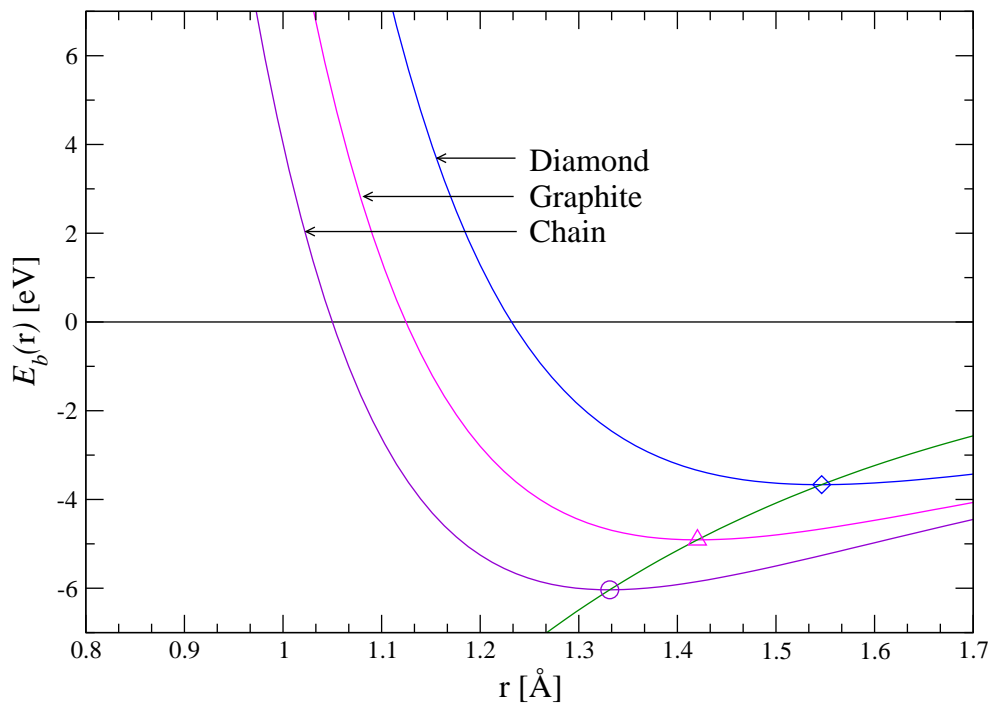


Figure 6.7: Binding energies per bond for the chain, graphite, and diamond. The curve through the minima is: $\mathcal{E}_b = -132.48 * \exp(-2.32 r)$

6.9 Appendix. Conjugated molecules

In this appendix we give a rapid overview of the distinctive features of the conjugated systems.

Conjugated molecules are [159] planar molecules, constituted of sp_2 hybridized carbon atoms, which are conventionally described as consisting of alternate double and single bonds.

These molecules have particular chemical properties, such as high reactivity, red shifted and enhanced ultraviolet absorption if compared to non conjugated systems, large magnetic susceptibilities, and easy propagation from one part to the other of the molecule of electrical influences. Especially the last feature suggests a sort of coupling between all the atoms of the conjugated molecule. The origin of this coupling can be understood thinking to the way the valence electrons of carbon hybridize in the formation of conjugated molecules. In these molecules it is given for granted that, in order to obtain maximum bonding, the valence atomic orbitals are three trigonal sp_2 hybrids pointing in the direction of the three neighbouring atoms in the plane, and a lone $2p_z$ orbital with its axis perpendicular to the molecular plane. Three of the four valence electrons of carbon enter the sp_2 orbitals and pair off, each with an electron from the corresponding neighbouring atom[§]. These electrons are called σ electrons. The remaining electron, dwelling in the $2p_z$ atomic orbital, is called a π electron, as it posses one unit of angular momentum about the carbon-carbon bond, and its molecular orbital is a π orbital. The essential distinction between the sp_z orbital and the sp_2 hybridized orbitals is that, whereas the latter overlap with only one neighbouring orbital, the $2p_z$ overlaps with a similar orbital *on either side*. Hence, whereas the σ electrons can be assigned by pairs to individual bonds, the π cannot be said belonging to any particular bond between a pair of atoms. They are in fact *delocalized* over all the sp_2 hybridized carbon atoms: this electron delocalization is the characteristic of conjugated molecules.

[§]In a all carbon system as the ones studied in this work, it will be another sp_2 hybridized carbon, in the more general case of hydrocarbons, the sp_2 orbital can pair with a $1s$ atomic orbital of a hydrogen atom.

The phase diagram of carbon at very high pressures and temperatures

Muchos años después, frente al pelotón de fusilamiento, el coronel Aureliano Buendía había de recordar aquella tarde remota en que su padre lo llevó a conocer el hielo [...].

El mundo era tan reciente, que muchas cosas carecían de nombre, y para mencionarlas había que señalarlas con el dedo.

Many years later, in front of the firing squad, colonel Aureliano Buendía would have remembered of that distant day when his father brought him to know the ice [...].

The world was so young, that many things lacked for a name, so that they were mentioned just pointing the finger at them.

The purpose of this chapter is to give an extensive review of experimental and theoretical works aimed at determining the phase behaviour of carbon at high temperatures and pressure. It provides terms of comparisons for the results presented in this thesis. We will follow a “historical” approach, starting from the beginning of the twentieth century, up to the most recent results coming from experiments and computer simulations. A historical approach may give a better understanding on why certain issues have been, and in some case still are, controversial. After setting the stage, we will focus on reviewing the long debated issue of the liquid – liquid phase transition (LLPT) in carbon, whose existence we have been able to definitely rule out. The binding energy between atoms of carbon is very large: for example, the cohesive energy of diamond is 717 kJ/mol (i.e. 7.4 eV/atom) and it melts at temperatures above 5000 K. Besides, phase transitions between carbon phases require a high activation energy. The solid state of carbon comprises the two well known crystalline phases, diamond and graphite, amorphous phases, such as glassy carbon and carbon black, and possibly metastable solid phases that are referred to as carbynes (the

existence of these phases is anyway still controversial). In addition to the bulk phases, there are the recently discovered fullerenes, C_{60} and C_{70} [160], and nanotubes [161].

From a chemical point of view, carbon exhibits three different possibilities for covalent bond formation: sp_3 , appearing in diamond, sp_2 , present, among the others, in graphite, fullerenes and nanotubes, and sp for the hypothetical carbynes.

Because of their high cohesive and activation energies, carbon polymorphs often exist in metastable form well inside pressure-temperature regions where another solid form is thermodynamically stable. For example, it is well known that diamonds survive at normal P-T conditions, where graphite would be the thermodynamically stable phase. Conversely, graphite tends to persist at very high pressures, deep into the diamond stability region of the phase diagram.

According to what is nowadays established, the boundary between the stable regions of graphite and diamond runs from 1.7 GPa at 0 K to the graphite/diamond/liquid triple point, which is located around 12 GPa and 5000 K. The graphite/liquid/vapor triple point is around 11 MPa and 5000 K. All available experimental data agree in finding a maximum at around 5-6 GPa in the graphite melting line. Anyway, the development of most sophisticated instrumentation has lowered the temperature of the maximum from 1200 K above the triple point, measured in early experiments, to 200 K above the triple point, according to the most recent data.

Starting from the mid-1980s evidences have been collected both from theory and experiments, supporting the hypothesis of a diamond melting line with positive slope. This distinguishes carbon from the heavier Group IV elements, Si and Ge. These elements display solids with a diamond structure, which melt into metallic liquids with higher densities than the solid: this property requires dT/dP to be negative along the melting line.

The nature of the liquid phase of carbon is still controversial and will be treated separately at the end of the chapter.

7.1 The history of carbon phase diagram

One of the earliest phase diagrams of carbon appeared at the beginning of the twentieth century, and is due to B. Roozeboom [162], who estimated the phase behavior of carbon on thermodynamic basis. His proposed phase diagram is sketched in Fig. 7.1. Of the two solid phases, diamond was recognized to have a slightly greater vapor pressure at a given temperature. The temperature of the graphite/liquid/vapor triple was believed to be around 3000 K. In 1909 Tamman [163] postulated the existence of a region where graphite and diamond are in pseudo-equilibrium. The existence of this pseudo-equilibrium region was at the basis of the method of synthesizing diamond starting from carbon saturated solutions of molten iron, silver, or silicates. In 1938, Rossini and Jessup [164] of the U.S. Bureau of Standards calculated, by using accurate thermodynamic data, that at 0 K the lowest pressure at which diamond would be stable against graphite is around 1.3 GPa, and around 2 GPa at 500 K. These are the first points that set the behavior of the graphite/diamond coexistence line. In 1939 Leipunskii [165] published in Russia a thorough review of the problem of diamond synthesis. On the basis of thermodynamic data, he suggested that the melting line of graphite might be at about 4000 K, with possibly some increase with pressure. This value for the melting line of graphite was rather well verified the same year by Basset [166], who established the graphite/liquid/vapor triple point to

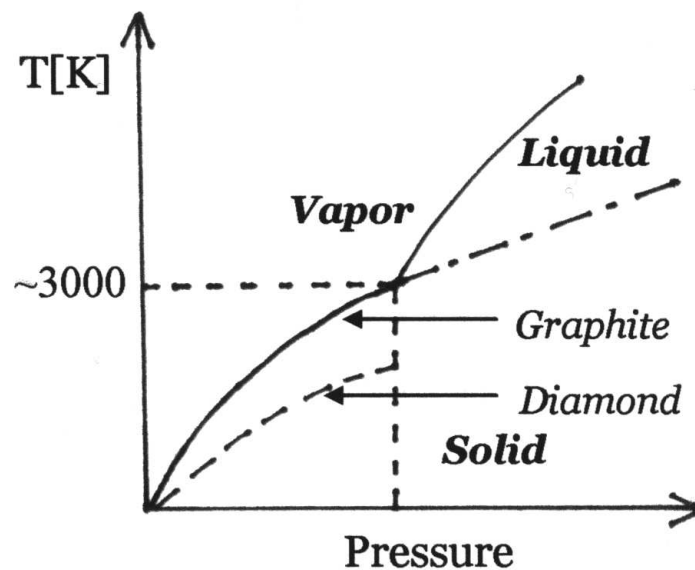


Figure 7.1: The carbon phase diagram as proposed by Roozeboom at the beginning of the twentieth century.

be at about 11 MPa and 4000 K. In that same publication, Basset reported on a rather pressure independent melting temperature of graphite at ~ 4000 K, from atmospheric pressure up to 0.1 GPa. In 1947 Bridgman [167] addressed the problem of extrapolating the graphite/diamond coexistence line beyond the region where it can be estimated from known physical properties (4 GPa/1200 K). He concluded that there was a possibility that at higher temperatures the rate of increase of P with T along the line would decrease. This hypothesis was later supported by Liljeblad [168] in 1955, while Berman and Simon [169] in the same year came to the conclusion that the best extrapolation would be a straight line. Experiments that could single out the best hypothesis were started by Bundy and coworkers in 1954, when they accomplished diamond synthesis by activating the graphite-to-diamond reaction with the use of different solvent-catalyst metals. The detailed data were published much later [170, 171], and are compatible with the Berman-Simon straight line extrapolation.

Bundy and his group made also extensive experiments on graphite melting at pressures much higher than the graphite/liquid/vapor triple point. The determination of the graphite melting line is a hard experimental challenge for many reasons. First of all, the achievement of pressures as high as 10 GPa requires the specimen to be in direct contact with a solid containing material and, because the melting temperature are so high, this material must be as refractory and inert as possible (Bundy choose boron nitride, pyrophyllite, MgO and diamond powder). Besides, the heating and observations must be carried out very rapidly, before the wall material could melt and react with the carbon sample. The experiment was performed by discharging an electric capacitor through the sample (this procedure is known as flash heating), and by monitoring the current through, and the voltage across it by means

of a two-beam oscilloscope. The discharge circuit was designed to have energy insertion in the sample within a few milliseconds. From the oscillograms, graphs of the electrical power and resistance versus time could be derived. The power curve could be integrated to obtain a curve of inserted energy versus time. From this, the instantaneous temperature can be calculated, once the heat capacity of the sample is known. The resistance of the sample is monitored in order to detect signals of phase transitions. The onset of melting was indicated by an abrupt drop in electrical resistance. This sounded quite strange, since previous experiments by Jones [172] at much lower pressures observed a sharp increase of the electrical resistance simultaneous to melting. Anyway, cross sections of the sample were inspected by a microscope, and evidences of the presence of a molten graphite core were detected. Critical points for the conversion of the data into a melting temperature-versus-pressure curve are the specimen heat capacity and the evaluation of the effective pressure inside it. The dependence of graphite (constant pressure) specific heat C_P on pressure was not taken into account, since supposed weak, and was – in any case – unknown. The dependence of C_P on temperature was measured by Hove [173]. He found that C_P increases linearly with T between 1800 K and 3200 K, while a sharp increase was detected at higher temperature. This increase was recognized as a spurious effect, and Bundy finally used a linear extrapolation of Hove's results for the calculation of the specimens' temperatures. The question of the pressure rise in the sample due to quick rise of temperature has been also carefully considered. Bundy observed that the heating is not carried on at constant volume, since the graphite specimen is surrounded by materials with about equal modulus and density. Besides, the built up of any significant shock or dynamic pressure can be ruled out, since the heat-up time is orders of magnitude greater than the time of transit of a shock wave inside the sample. Thus the pressure behavior of the specimen must have been close to that of a statically heated one in the same kind of apparatus. In this case, pressure variations due to heating are within 10 %. With these assumptions, Bundy's experiments gave a graphite melting line as shown in Fig. 7.2. A maximum melting temperature of about 4600 K is detected in the region of 6 GPa to 7 GPa. The presence of region with a negative dT/dP along the melting line indicates that, at those pressures, the density of the liquid at the melting temperature is greater than that of the solid.

During the experiments on graphite melting, Bundy and his group also investigated the graphitization of diamond by flash-heating under pressure. Small diamond crystals were embedded in the graphite sample, pressurized and then flash-heated. Experiments indicated that there is a sharp temperature threshold at which the diamond crystals completely graphitized. This threshold is a few hundreds degrees lower than the graphite melting line.

Attempts to obtain direct (i.e. without resorting to a catalyst material) conversion of graphite into diamond by the application of high pressure date back to the beginning of the twentieth century. The first success came only in 1961, when De Carli and Jamieson [174] reported the formation and retrieval of very small black diamonds when samples of low-density polycrystalline graphite were shock compressed to pressures of about 30 GPa. Later in 1961 Alder and Christian [175] reported results of the shock compression of graphite which are in substantial agreement with those of De Carli and Jamieson.

Bundy [176] achieved direct conversion of graphite into diamond by flash-heating graphite sample in a static pressure apparatus, at pressures above the graphite/diamond/liquid triple point. The threshold temperature of the transformation was found several hundred degrees below the melting temperature of the graphite, and decreases at higher pressures.

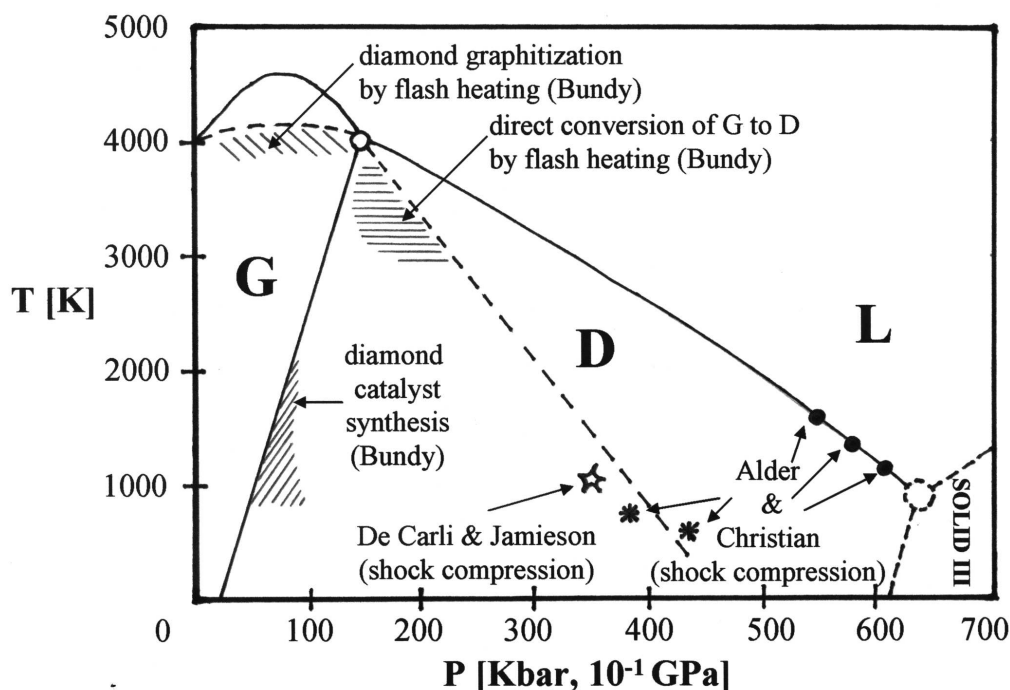


Figure 7.2: The phase diagram of carbon at high pressures proposed by Bundy in 1963 [176].

The phase transition was revealed by a sharp drop in the electrical conductivity of the samples, which were finally retrieved as pieces of finely polycrystalline black diamond. Bundy [176] pointed out that the shock compression data should stay on the graphite melting line prolonged into the diamond region. That is because, in order to convert into diamond so quickly, graphite has to virtually melt before. When the reaction time is orders of magnitude longer, as it was in his own experiments, the temperatures of conversion are shifted to values lower than the graphite melting line. The temperature boundary for the conversion of graphite to diamond under static pressure should then be, more or less, parallel to the graphite melting line approaching the graphite/diamond/liquid triple point. The same observation holds for the graphitization of metastable diamond. Then the position of the boundary for the conversion of diamond into graphite would give information about the behavior of the diamond melting line beyond the graphite/diamond/liquid triple point. The behavior of the diamond melting line was at that time essentially unexplored.

By linking his results with older ones coming both from experiments and theory, which we have quickly summarized so far, Bundy [176] proposed in February 1963 a phase diagram of carbon at high pressures as illustrated in Fig. 7.2. The diamond melting line was believed to have negative slope by analogy with the other Group IV elements, and from some evidences collected during the experiments of Alder and Christian [175].

In 1968 El Goresy and Donnay [177] identified in the products of shock-heated graphite a brand new allotropic form of carbon, with crystallographic properties rather different from graphite. After a number of independent experiments supporting the existence of this form, called “carbyne”, in 1978 Whittaker [178] proposed its structure and mechanism

of formation. Carbyne was argued to be a solid constituted of chains of carbon atoms in alternated single and triple bonds (i.e. a polymer of the monomer: $-\text{C}\equiv\text{C}-$). In a high temperature graphite sheet, alternate single bonds break and shift an electron into each of the adjacent double bonds, so that triple bonds are formed. The zigzag chains of so formed alternate triple-single bonds stretch in linear chains. The resulting solid is an hexagonal array of these linear chains, kept together by dispersive interactions, similar to graphite interplanar interactions. Carbyne was indeed identified by the appearance of a typical resonance due to the triple bond stretching vibrational frequency in the infrared spectrum. Interestingly, on the basis of his own experimental results and on those by Kasatochin [179], Whittaker proposed that graphite becomes unstable towards carbyne at 2600 K: this temperature is more or less pressure independent, so that the graphite-carbyne coexistence line would meet the diamond coexistence line in a triple point (graphite/carbyne/diamond) at ~ 6 GPa and ~ 2600 K. Upon increasing temperature, carbyne would show a number (maybe 6) of polytypes, with a similar crystallographic arrangement but with very different mechanical properties (ranging from “very soft” to “very hard”). Carbyne is expected to melt at ~ 3800 K at atmospheric pressure, with T_m mildly increasing with pressure*. The existence of a carbyne form was questioned by Smith and Buseck [180], claiming that all the experimental evidences could also be explained by the presence of sheet silicates. The dispute continued between these authors: today the existence of carbyne is still debated.

In 1973 Van Vechten [181] predicted the phase diagram of carbon by rescaling the behavior of other Group IV elements that are experimentally more accessible, using the electronegativity as a scale parameter. In 1979 Grover [182] calculated a phase diagram by using a phenomenological equation of state for the description of various solid and liquid phases of carbon. He used reasonable models for the free energies of the various phases, with parameters adjusted to match the available data on the equations of state. He found that, at all pressures, diamond transforms, before melting, into a solid metallic phase.

In more recent years, efforts have been addressed towards the collection of reliable data at even higher pressures, and towards the investigation of the properties of the different phases of carbon at high temperature and pressure. This challenging task has been faced both with experiments and theory. On the experimental side, the development of the diamond anvil cell [29] for high pressure physics has raised the necessity of investigating the stability of diamond structure under extreme conditions. The availability of high energy pulsed laser sources lead to new tools for heating up samples at very high temperatures (above the graphite melting line) [183], which were immediately addressed to the determination of the properties of liquid carbon (i.e. whether it is a conducting metallic liquid or an insulator). Unfortunately, due to the difficulties in interpreting the results of the experiments, the nature of the liquid state of carbon is nowadays not yet fully experimentally established.

On the theoretical side, the appearance of computers and the increasing of computational power, considerably helped to infer the properties of matter by using density functional theory (see section 3.2) for the description of the electronic degrees of freedom [66, 67]. This approach has been shown to yield accurate estimates of the structural properties of solids, and was later implemented in a quanta-mechanical (or *ab initio*) molecular dynamics algorithm for the calculation of thermodynamic quantities [62] (see section 3.1).

*It has to be noted that these data and relative speculations are referred to relatively low pressures, i.e. pressures not higher than 0.1 GPa.

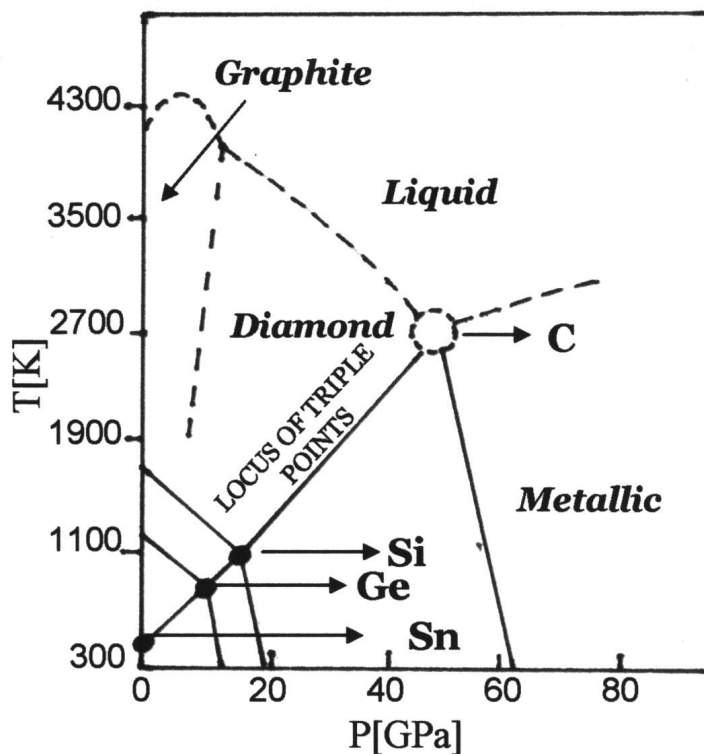


Figure 7.3: *Diamond/liquid/metal triple point for carbon extrapolated from the triple points of the other ‘Group IV’ elements, according to the “Jamieson criterion” [185]. The extrapolation is proposed by Bundy in his 1969 review [186].*

The first and most impressive application of these methods was establishing the nature of the melting line of the diamond phase [184] (*vide infra*). Prior to about 1980 the diamond melting line was believed to have negative slope, on the basis of early experimental [175, 176] and theoretical [181] work, and on a simple analogy with the known phase diagrams of Si and Ge (see Fig. 7.3). In more recent years evidences have been collected through computer simulations that the diamond melting line has positive slope. In 1983 Yin and Cohen [187] studied the total energy versus volume and the free energies versus pressure for the six possible lattices of carbon (fcc, bcc, hcp, simple cubic, β -tin, diamond). The study was carried out by using *ab initio* pseudopotential theory (this permits the investigation of the properties of the atomic system at 0 K). They found out that the calculated zero pressure volume for diamond is either close to or even smaller than those of the other five phases. This is different from what is observed for the other group IV elements, Si and Ge, and defies the common notion that diamond is an open structure and should have higher specific volume than the close packed solid structures. This at first surprising fact that diamond is effectively close packed, inhibits phase transformations at high hydrostatic pressures which are observed for heavier group IV elements. Besides, it may also suggest a revision of the other common notion that the diamond melting line should have negative slope, due to a liquid denser than the coexisting solid. Yin and Cohen also found that, at a pressure around 2300 GPa, diamond converts to a simple cubic (sc) phase. This work

was later extended [188, 189, 190] to consider also complex tetrahedral structures. It was found that a distorted diamond structure called BC-8 was stable versus diamonds at pressures above 1000 GPa (see Fig. 7.4).

In 1984 Shaner and coworkers [191] shock compressed graphite and measured the sound velocity in the material at shock pressures ranging from 80 to 140 GPa, and corresponding shock temperatures ranging from 1500 to 5500 K. They measured velocities close to those of an elastic longitudinal wave in solid diamond, which are much higher than the velocities of a bulk wave in a carbon melt. Since no melt was detected at pressures and temperatures much higher than the graphite/diamond/liquid triple point, the diamond melting line should have, according to these results, positive slope. In 1990 Togaya [192] reported experiments in which specimens of boron-doped semiconducting diamond were melted by flash-heating at pressures between 6 and 18 GPa: there were clear indications that the T_m of diamond increases with pressures.

In the same year ab initio molecular dynamics studies [184] conclusively showed that, upon melting, the pressure of the system increases. This means that the slope of the diamond melting line is positive. The shape of the diamond melting line has important consequences for the theory of planets interiors. The above explained conclusions, together with available data about temperatures and pressures in the interior of the outer planets Neptune and Uranus, as well as in the Earth mantle, would imply that inside these planets most of the free carbon should be found in the solid diamond phase [193]. In 1996 Grumbach and Martin [194] made a systematic investigation of the solid and liquid phases of carbon in a wide range of pressures and temperatures by using ab initio molecular dynamics. They studied the melting of the simple cubic and BC-8 solid phases, and investigated structural changes in the liquid in the range 400-1000 GPa. They found that the coordination of the liquid changes continuously from about four-fold to about six-fold in this range.

In 2004 Bradley *et al.* [195] reported on laser induced shock compression of diamond up to 3000 GPa. Through optical reflectivity measurements, they found for the first time direct evidences of diamond melting, at an estimated pressure of $P = 1000 \pm 200$ GPa, and temperature $T = 12000 \pm 4000$ K.

At this point, the proposed phase diagram for carbon, including regions at very high pressures and temperatures for which thermodynamics data are not available, can be roughly sketched as in Fig. 7.4. Questions such as the already treated existence of carbyne phases, the exact location of the graphite melting line, together with the triple point vapor/liquid/graphite, and the nature of the liquid are still open. The last two points will be discussed in more detail in the two following sections.

7.2 On graphite melting line: a possible heating time dependence of T_m

Asinovskii *et al.* [196] pointed out the non negligible dependence of the melting temperature (T_m) of graphite on the heating rate of the sample. Namely, heating times of the order of 10^{-5} s gave [197, 198] $T_m \sim 4800 - 5000$ K; heating times of the order of 10^{-3} s gave [199, 200] $T_m \sim 4500 - 4600$ K; finally heating times of the order of the second gave [166, 201] $T_m \sim 3800 - 4000$ K. After a thorough discussion on the experimental

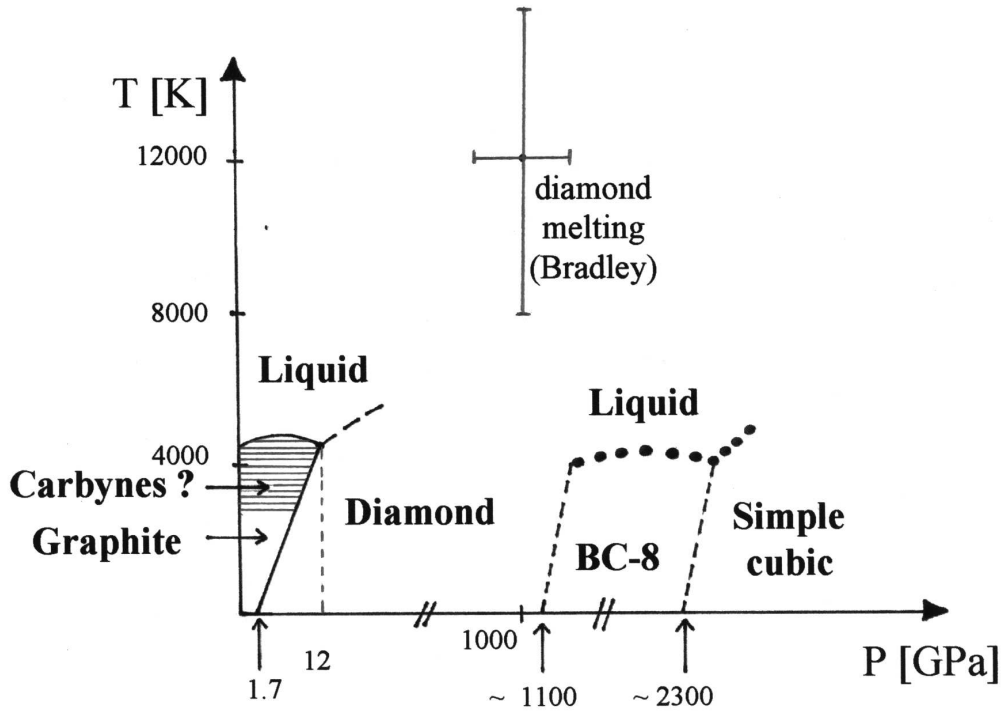


Figure 7.4: The phase diagram of carbon at high pressures as it has been developed in more recent years (excluded the results that will be illustrated in this thesis). Full lines correspond to phase boundaries for which thermodynamic data are available.

methods, the authors recommended that only data coming from experiments with heating time of the order of the second, at least, should be accepted. If so, most of the available data on graphite melting should be carefully reconsidered: the position and the shape of the melting line would be far from being established.

The following list of experiments should evidence how both the position of the melting line and the nature of the liquid upon melting are still uncertain. In 1925 [202], T_m for graphite at atmospheric pressure was detected at 3760 ± 65 K, on the basis of a slow (about half an hour) ohmic heating of the sample. On the basis of ohmic heating experiments of unspecified heating rate, in Ref. [203] of 1968, the vapor/liquid/graphite triple point was found at 10.3 MPa and $T \sim 4200$ K. The melting temperature was found to increase linearly from ~ 4200 to ~ 4300 K from 10.3 MPa to 0.1 GPa. In 1988, in Ref. [204], a $T_m = 4450 \pm 110$ K at atmospheric pressure was found, on the basis of μs electrical pulse heating. The author found a metallic liquid upon melting. In 1997 Togaya [200] presented an evaluation of the whole graphite melting line, measured by means of millisecond shock heating via capacitor discharge of graphite rods, at 6 pressures from 1.4 to 9.4 GPa. The melting line shows a maximum temperature at 5.6 GPa; the melting temperature increases from ~ 4651 to ~ 4786 K and then decreases to ~ 4640 K, so that the temperature span of the melting line is ~ 150 K (which is much lower than that measured by Bundy in earlier experiments [171]). As noted above, in 1997 Asinovskii and coworkers pointed out how, in order to correctly determine the melting line, a sufficiently slow heating of graphite

was needed. On the basis of a series of laser induced slow heating experiments [196] (i.e. heating times of the order of the second), these authors proposed the triple point vapor/liquid/graphite at ~ 4000 K and 0.1 MPa (i.e. atmospheric pressure), in open contrast with the commonly accepted values [205] of ~ 5000 K and 10 MPa. The next year the same authors [206] published results concerning the position of the graphite melting line. With an ohmic heating of graphite samples at heating rates of about 100 K/minute, they found $T_m = 3700$ K at 0.25 MPa (typically, samples melted after one hour of steady heating). Finally in 1998, on the basis of millisecond laser pulse heating [207] it was found a rather constant $T_m = 4800 \pm 150$ K from 0.03 to 0.25 GPa. The authors found a non-conducting liquid upon melting at those pressures.

7.3 History of the liquid – liquid phase transition for carbon

7.3.1 An analysis of experimental data

The possibility of a liquid – liquid phase transition (LLPT) in liquid carbon has been firstly investigated by Korsunskaya *et al.* [8], analyzing data on the graphite melting line proposed by Bundy [171], (those data showed a maximum melting temperature at 6.5 GPa). By fitting the data from Bundy into the original two levels model of Kittel [6][†] and postulating the existence of two liquids, Korsunskaya *et al.* found the critical temperature T_c of the LLPT. The model is fitted with three points on the graphite melting line, with the respective derivatives, and with the heat of melting at a selected pressure. The authors assume that:

1. liquid and solid have different compressibilities;
2. the nature of liquid carbon is described univocally by the relative fraction of the two liquids, i.e. the parameter s , as defined in section 2.1;
3. each of the two liquids presents a volume change on melting, heat of melting and entropy of melting, that are independent of T , P , and the fraction s : the volume change upon melting for the liquid is a linear combination of the volume changes of the pure species (i.e. for $s = 0,1$), while heat and entropy of melting combine according to the regular solution rules;
4. the overall entropy jump on melting is independent of T (that is equivalent to assuming the same heat capacity in the liquid and the solid).

The fitting procedure gives an estimate for the critical pressure[‡] of ~ 6.5 GPa and for the critical temperature of the searched transition at 3770 K, i.e. below the melting temperature. The fitted value for the entropy of melting is the same for the two liquids, thus implying a vertical slope (dT/dP) of the coexistence line (in the metastable liquid region just below the critical temperature)

[†]This model is one of the many flavours of the model we presented in section 2.1.

[‡]This value is not explicitly mentioned in the article [8], but can be derived from the given ΔE , $\Delta\sigma$, and Δv , using Eq. 2.8.

On the basis of these results, the authors were able to calculate also the diamond melting line: they predicted it to have a negative slope, in accordance with the commonly accepted interpretation of the experiment of Alder and Christian [175]. Note that the slope of the *graphite* melting line, and the slope of the diamond/graphite coexistence, as extracted from Bundy's data [176, 171], together with the densities of the phases obtained by fitting to the two levels model *implied* (via Clausius-Clapeyron equation) a negative slope of the diamond melting line. Different values of the slopes of the graphite boundary lines, and of the densities of the phases can yield rather different slope of the diamond melting line, as we will show in chapter 8.

Consistently with the slope of the fitted graphite melting line, the low density liquid (LDL, $s = 0$) is less heavy, and the high density liquid (HDL, $s = 1$) is heavier than the coexisting graphite. The nature of the two liquids is predicted as follows: at low pressure graphite melts into a liquid of neutral particles, which interact predominantly through dispersion (London) forces. Upon increasing pressure[§] the liquid metallizes into a close packed liquid. No assumption is made on the local structure.

7.3.2 A model for a insulator-into-metal transition

While commonly cited to support the idea of a LLPT in correspondence of the maximum in the graphite melting line, the work of Ferraz and March [208] is concerned with an insulator-into-metal transition at low pressure in the melt. Using a Landau expansion in the free energy of the liquid phase in proximity of the melting line, with an order parameter derived from the gap between the valence and conduction bands of the system, the authors predict a coexistence line between two liquids, branching off from the melting line at ~ 0.4 GPa and with a negative slope. The insulator liquid is argued to have two-fold preferred coordination, while the metallic would have a preferred open, three-fold, coordination. Ferraz and March speculate, without elaborating the model, the further transformation into a preferred four-fold liquid in correspondence with the maximum in the melting line of graphite.

7.3.3 A semi-empirical equation of state

The modern discussion on the LLPT for carbon, starts with the elaboration of a semi-empirical equation of state for carbon, valid also at high P and T , by van Thiel and Ree [209, 210]. The equation of state is constructed on the basis of experimental data and electronic structure calculations. It is postulated the existence, in the graphite melt, of a mixture of an sp_3 and an sp_4 liquid. The model of *pseudo-binary mixture* is assumed to describe the mixing of the two liquids (see Eq. 2.4); recasting the original equation reported in Ref. [210] into the formalism of section 2.1, the mixing energy J of the two liquids is written as:

$$\beta J = \frac{A_0}{1 + (P/P_0)^{3/2}} s(1 - s) \quad (7.1)$$

where A_0 and P_0 are fitting parameter. As it is clear from section 2.1, the value of these fitting parameters is essential to determine the possibility of the occurrence of a first order

[§]The transition in the stable liquid region is supercritical, thus continuous, but taking place in a short range of pressures around 6.5 GPa.

transition. Van Thiel and Ree show that fitting A_0 in order to obtain the graphite melting points of Bundy [171], the slope of the graphite melting line predicted by their model inverts its sign discontinuously in correspondence of the maximum, so that a first order LLPT arises. On the other hand, if they fit to the data from Ref. [211], the value of A_0 decreases so that the T_c of the LLPT drops below the melting line and the transition between the two liquids becomes continuous in the stable liquid region. As pointed out by Ponyatovsky [212] the expression for βJ proposed by van Thiel and Ree involves two ambiguities. Firstly, extrapolating the coexistence line between the two liquids at atmospheric pressure, the coexistence temperature would be $T \sim 3700$ K: this would imply that the sp_3 liquid (and the glass) would be more stable than the sp_2 at room pressure up to very high temperatures, which is in contrast to the experimental data. Furthermore, J is proposed to have a linear dependence on T , so that, when $T \rightarrow 0$, also the mixing energy would tend to zero, i.e. at zero temperature the regular solution would become an ideal solution. This is extremely unusual.

7.3.4 Experimental suggestions from the graphite melting line

As already mentioned in section 7.2, Togaya [200] found a maximum in the melting line at $P_{max} = 5.6$ GPa. The author fitted the six experimental points with two straight lines: with positive slope at pressures lower than P_{max} , with negative slope at pressures higher than P_{max} . The discontinuous derivative of the melting curve at the maximum would imply there a triple point graphite/LDL/HDL, as a starting point of a LLPT coexistence line.

7.3.5 Prediction of a short range bond order potential

In Ref. [2] Glosli and Ree reported a complete study of a LLPT simulated with the Brenner bond order potential [3] in its version with torsional interactions [4] (i.e. the potential defined as ‘BrennerI’ at the end of section 6.5). The authors simulated in the canonical (NVT) ensemble several samples at increasing densities at eight different temperatures. By measuring the pressure, they show the familiar van der Waals loop denouncing mechanical instabilities at certain imposed densities. Using the Maxwell equal-area construction, the authors calculated the LLPT coexistence line, ending in a critical point at $T = 8802$ K and $P = 10.56$ GPa. The lowest temperature coexistence point was calculated at $T = 5500$ K and $P = 2.696$ GPa. The LDL/HDL coexistence line should meet the graphite melting line at its maximum, but unfortunately the BrennerI potential does not contain non bonded interactions, thus it cannot describe neither bulk graphite nor its melting line. To overcome this deficiency, the authors devised an ingenious perturbation method. Assuming constant slope of the negative sloped branch of the graphite melting line[¶] and fixing the graphite/diamond/HDL triple point at a value taken from the experimental literature, they give an estimate of the graphite/LDL/HDL triple point, at $T = 5133$ K and $P = 1.88$ GPa. The LDL was found to be mainly two-fold (sp) coordinated with a polymeric-like structure, while the HDL was found to be a network forming, mainly four-fold, (sp_3) liquid. Following the predictions of this bond order potential, the sp_2

[¶]The authors adopted the graphite melting line measured by Togaya [200], see sections 7.3.4 and 7.2. This melting line is reported in Fig. 8.4, together with our results. According to Glosli and Ree, from the maximum of that melting line would branch off the LLPT coexistence line.

coordinated atoms would be completely avoided in the liquid. The authors identified the reason in the presence of torsional interactions. In fact, the increase in density demands an increase in structures with higher coordination than the sp , which is entropically favoured at low densities. The single bonds of the sp_3 structures can freely evolve around the bond axis, while bonds between sp_2 sites are constrained in a (almost) planar geometry by the torsional interactions: this implies a low entropy for a liquid dominated by sp_2 sites. This low entropy would eventually destabilize the sp_2 sites towards the sp_3 . To prove this conjecture, the authors calculated two relevant isotherms in the original version of the potential, without torsional interactions, finding no sign of a LLPT. Since some torsional interactions are definitely needed to mimic the double bond reluctance to twist, the authors concluded that the LLPT predicted by the Brenner bond order potential with torsion is more realistic than its absence when torsional interactions are switched off.

Tight binding calculations [213] showed no evidence of van der Waals loops at some of the temperatures analyzed in Ref. [2]. As Glosli and Ree note, the tight binding model used in [213] is strictly two-center, thus the torsional interactions *cannot* be described.

7.3.6 An ab initio confutation of the LLPT

In Ref. [14], Wu *et al.* reported on a series of NVT-CPMD simulations at 6000 K from density 1.27 to $3.02 \cdot 10^3 \text{ kg/m}^3$, in a range where the BrennerI potential showed the first order LLPT at the same T . No sign of a van der Waals loop was found: in contrast to the BrennerI results of the previous paragraph, two approaching series starting from the lowest and the highest density, were found to meet smoothly at intermediate densities. Looking for the reasons of the failure of the BrennerI potential, the authors calculated, with the same density functional (DF) used in the CPMD simulations, the torsional energy of two model molecules. One, $(\text{CH}_3)_2\text{CC}(\text{CH}_3)_2$ (see Fig. 6.4, right panel, for a schematic representation), was chosen so that the bond between the two central atoms represents a double bond in a carbon network: two sp_2 sites are bonded each to two sp_3 sites; the peripheral hydrogens are needed to saturate the sp_3 atoms and are intended to have no effect on the central bond. The second molecule, $(\text{CH}_2)_2\text{CC}(\text{CH}_2)_2$ (see Fig. 6.4, left panel, for a schematic representation) is a portion of a completely sp_2 coordinated network: in the bond order language, the central bond is conjugated. The two molecules were geometrically optimized in their planar configurations and then twisted around the central bond axis in steps of $\pi/12$. In each configuration the electronic wave function was optimized, without further relaxations, to give the total energy, that was compared to the planar configuration total energy. The difference is the torsional energy. The DF calculations found a surprising picture (see Fig. 6.5): while the double bond torsional energy was only slightly overestimated by the BrennerI potential at intermediate angles, the DF torsional energy for the conjugated bond showed a completely different scenario compared to the classical prediction. It shows a maximum at $\pi/4$, while the planar and orthogonal configuration have basically the same energy. For the BrennerI potential, the torsional energy in this conjugated configuration is monotonically increasing with the torsion angle, just as for the double bond configuration^{||}. On average, considering that the conjugated configuration would be characteristic of a mainly sp_2 coordinated liquid, the torsional interactions are

^{||}See section 6.5 and footnote (†) in section 6.7.3. We also compared the BrennerI potential to other bond order potentials in section 9.1.2.

enormously overestimated by the classical potential. As a further proof, the authors tried to lower torsional energy of the conjugated bond in the classical potential, by tuning the proper parameter, and found a much less pronounced LLPT. Note that, as pointed out in section 6.7.3, the functional form of the torsional interactions for the BrennerI potential *cannot* reproduce the DF data here mentioned. Wu *et al.* concluded: “Brenner potential significantly overestimates the torsional barrier of a chemical bond between two- and three-center-coordinated carbon atoms due to the inability of the potential to describe lone pair electrons”; and: “Brenner potential parameters derived from isolated hydrocarbon molecules and used in the literature to simulate various carbon systems may not be adequate to use for condensed phases, especially so in the presence of lone pair electrons”. In section 6.7.3 we introduced a bond-order (Brenner like) potential (LCBOPI⁺), that incorporates a much more flexible and transferable definition of the torsional interactions. In chapter 9 we will show that the conclusion of Wu *et al.* is not necessarily true for all BOPs; we will show how our definition of the torsional interaction is able to reproduce relevant features of liquid carbon, as described by density functional based molecular dynamics.

The carbon phase diagram according to the LCBOPI⁺

*That thou hast
the serenity for accepting things that cannot change,
the courage for changing things that thou canst change,
the wisdom for understanding the difference.*

after a Cherokee blessing

In this chapter we describe the numerical evaluation of the phase diagram of carbon, comprising graphite, diamond and the liquid, with the LCBOPI⁺. The chapter opens with a detailed description of the method used to calculate the phase boundaries. Section 8.2 reports the calculated phase diagram.

8.1 Methods

The properties of the liquid, graphite, and diamond phases were determined by Monte Carlo simulation. Coexistence lines were determined by locating points in the $P - T$ diagram with equal chemical potential for the two phase involved. To this purpose, we first determined the chemical potential for the liquid, graphite, and diamond at an initial state point ($P = 10$ GPa, $T = 4000$ K). Subsequently, the liquid/graphite, liquid/diamond, and graphite/diamond coexistence pressures at $T = 4000$ K were located. In turn, these coexistence points served as the starting point for the determination of the graphite melting, diamond melting, and graphite/diamond coexistence lines, obtained integrating the Clausius-Clapeyron equation (this procedure is also known as Gibbs-Duhem integration):

$$\frac{dT}{dP} = \frac{T\Delta v}{\Delta h} \quad (8.1)$$

where Δv is the difference in specific volume, and Δh the difference in molar enthalpy between the two phases (calculated as $h = u + Pv$, being u the potential energy per particle).

The first point is in turn accomplished in two sub-steps. Firstly an Helmholtz free energy (F) at a given volume (V) and temperature (T) can be calculated via thermodynamic integration. In a canonical system, coexistence between phases can be found via the Helmholtz double tangent construction, once extended F to other V and T integrating its gradient, a quantity that can be measured in a Monte-Carlo (MC) simulation (see e.g. [214]). As an alternative [215], the one we chose, one can transform F into the chemical potential μ (coinciding with the specific Gibbs free energy in a one-component system), the latter as a function of P and T , knowing accurately enough the equation of state of each phase. Coexistence at a given T is found at the P where the different μ cross.

For all phases, the free energies at the initial state point $F^{\mathfrak{X}}$ was determined by transforming the systems into a reference system F^{ref} of known free energy, using $U_\lambda = (1-\lambda)U^{\mathfrak{X}} + \lambda U^{\text{ref}}$. Here, $U^{\mathfrak{X}}$ and U^{ref} denote the potential energy function of the LCBOP1+ and the reference system, respectively. The transformation is controlled by varying the parameter λ continuously from 0 to 1. The free-energy change upon the transformation was determined by thermodynamic integration:

$$\begin{aligned} F^{\mathfrak{X}} &= F^{\text{ref}} + \Delta F^{\text{ref} \rightarrow \mathfrak{X}} = \\ &= F^{\text{ref}} + \int_{\lambda=0}^{\lambda=1} d\lambda \left\langle \frac{\partial U_\lambda}{\partial \lambda} \right\rangle_\lambda = \\ &= F^{\text{ref}} + \int_0^1 d\lambda \langle U^{\text{ref}} - U^{\mathfrak{X}} \rangle_\lambda \end{aligned} \quad (8.2)$$

The symbol $\langle \dots \rangle_\lambda$ denotes the ensemble average with the potential U_λ .

8.1.1 The Lennard-Jones liquid

For the liquid phase the reference system was taken to be a Lennard-Jones 12-6 (LJ) system, described by the well known interaction energy:

$$U^{LJ} = 4\epsilon \left(\left(\frac{\sigma}{r} \right)^{12} - \left(\frac{\sigma}{r} \right)^6 \right)$$

The reference free energy (F^{ref}) of the liquid is:

$$F^{\text{ref}} = F^{\text{LJ}} = F^{\text{id}} + F_{\text{LJ}}^{\text{ex}} \quad (8.3)$$

The ideal-gas contribution is:

$$\frac{\beta F^{\text{id}}}{N} = 3 \ln \Lambda + \ln \rho - 1$$

where N is the number of particles in the box, $\Lambda = h/\sqrt{2\pi m k_B T}$ is the de Broglie wavelength, m is the mass of one atom, and ρ is the number density.

The LJ liquid excess free energy ($F_{\text{LJ}}^{\text{ex}}$) has been accurately parameterized [216] by means of (NVT) MC and MD simulations.

The LJ σ parameter was determined by matching the first peak of the radial distribution functions ($g(r)$) of the LCBOP and LJ liquid at the same position, ensuring optimal similarity between the structure of the two liquids. The LJ ϵ parameter was chosen such that,

at the selected $T = 4000$ K, the LJ liquid was above the critical temperature: this is done in order to avoid possible unwanted transitions, since the thermodynamic integration method works under the hypothesis the no boundary between phases is ever crossed on varying λ . On the other hand, the liquid should not be too far from the critical temperature: in fact, the $g(r)$ given by the LCBOP⁺ (see chapter 9) has pronounced secondary peaks beyond the first coordination shell. Thus, a rather structured LJ liquid had to be preferred for the coupling. The requirements are matched by putting the liquid in proximity of the critical temperature.

8.1.2 The Einstein crystal

For the solid phases the Einstein crystal, whose free energy is analytically known, was taken as reference system [217]. For the Einstein solid, U^E is:

$$U^E = \frac{\alpha}{2} \sum_{i=1}^N (\mathbf{r}_i - \mathbf{r}_{i,0})^2$$

where the $\mathbf{r}_{i,0}$ are the equilibrium lattice positions of the particles. In the Einstein solid, the fixed equilibrium lattice positions are referred to an absolute frame, so that if a particle is moved, then the crystal as a whole cannot. When $\lambda = 0$ (i.e. the system is on the LCBOP⁺ side) the center of mass of the system (CoM) to drift: if L is the box size, the CoM mean square displacement $\langle r^2 \rangle_{CoM}$ becomes of the order of L^2 . Should this happen, the integral of Eq. 8.2 becomes sharply peaked for small values of λ . In fact, the particles are allowed to drift far away from their absolute equilibrium lattice positions, since the coupling with the Einstein solid is mild, but in Eq. 8.2 appears the energy $U^{\boxtimes} = U^E$, that can become uncontrollably large. In order to avoid to perform extremely long simulations to evaluate the integral for small λ , one can perform a simulation under the constraint that the CoM of the solid is fixed [217, 13, 218], so that $\langle r^2 \rangle_{CoM}$ is of the order of $\langle r^2 \rangle_0$, the mean square displacement of a particle from its lattice site in a real (i.e. interacting) crystal. This constraint calls for a slight modification of the Eq. 8.2. We label with $E(CM)$ the Einstein solid with fixed center of mass, $\boxtimes(CM)$ the LCBOP⁺ system with fixed center of mass, so that [217, 13, 218]:

$$\begin{aligned} F^{\boxtimes} &= F^{E(CM)} + \Delta F^{E(CM) \rightarrow \boxtimes(CM)} + \Delta F^{\boxtimes(CM) \rightarrow \boxtimes} = \\ &= F^{E(CM)} + \int_0^1 d\lambda \langle U^{\text{ref}} - U^{\boxtimes} \rangle_{\lambda} + \Delta F^{\boxtimes(CM) \rightarrow \boxtimes} \end{aligned} \quad (8.4)$$

Specifically:

$$\frac{\beta F^{E(CM)}}{N} = 3 \ln \Lambda - \frac{3}{2} \ln \left(\frac{2\pi}{\beta\alpha} \right) - \frac{3}{2N} \left(\ln \left(\frac{\alpha\beta}{2\pi} \right) + \ln N \right) \quad (8.5)$$

The last term on the right hand side represents the (finite size) correction for the fixing of the CoM: note its dependency on $1/N$.

$$\frac{\beta \Delta F^{\boxtimes(CM) \rightarrow \boxtimes}}{N} = -\frac{1}{N} \ln \frac{V}{N_{ws}} \quad (8.6)$$

where N_{ws} is the number of Wigner-Seitz cells in the simulation box. If n_{ws} is the number of atoms per Wigner-Seitz cell, $N_{ws} = N/n_{ws}$. Note that also this term, a purely finite size effect, vanishes in the thermodynamic limit.

In reporting the results (in the next section) we will group differently the terms of the previous three equations: it is indeed natural to group the terms proportional to $\frac{1}{N}$, so that:

$$\frac{\beta F^E}{N} = 3\ln\Lambda - \frac{3}{2}\ln\left(\frac{2\pi}{\beta\alpha}\right) \quad (8.7)$$

$$\frac{\beta\Delta F^{\frac{1}{N}}}{N} = -\frac{1}{N}\left(\frac{3}{2}\ln\left(N\frac{\alpha\beta}{2\pi}\right) + \ln\frac{V}{N_{ws}}\right) \quad (8.8)$$

The coupling of (hot) graphite to an Einstein crystal, whose average atomic positions are constrained to a fixed reference system, displayed a peculiar feature. Due to the softness of the interplanar interactions ($0.07 k_B T$ at 4000 K), graphite neighbouring sheets are allowed to slide. Also this is a finite size effect: to correct for this we found necessary to attach any sheet to its CoM, independently from the others*.

The Einstein crystal spring constant, α , was determined by requiring that the mean-squared displacement from the equilibrium lattice positions is equal for the Einstein crystal and the carbon crystal:

$$\frac{3}{\beta\alpha} = \left\langle \frac{1}{N} \sum_{i=1}^N (\mathbf{r}_i - \mathbf{r}_{i,0})^2 \right\rangle$$

Therefore α was fixed calculating the right hand side in a simulation with the LCBOP1+.

8.1.3 From the Helmholtz free energy to the chemical potential

The chemical potential μ along the 4000 K isotherm was obtained by integrating from the initial state point a fit, $P(\rho) = a + b\rho + c\rho^2$, through simulated (P,T) state points along the 4000 K isotherm. Here, ρ is the number density, and a , b , and c are fit parameters. This yields for the chemical potential [215]:

$$\beta\mu(\rho) = \frac{\beta F^{\mathfrak{X}}}{N} + \beta \left(\frac{a}{\rho^{\mathfrak{X}}} + b \ln \frac{\rho}{\rho^{\mathfrak{X}}} + b + c (2\rho - \rho^{\mathfrak{X}}) \right) \quad (8.12)$$

*Eq. 8.5 then becomes:

$$\frac{\beta F^{E(CM)}}{N} = 3\ln\Lambda - \frac{3}{2}\ln\left(\frac{2\pi}{\beta\alpha}\right) - \frac{3N_s}{2N} \left(\ln\left(\frac{\alpha\beta}{2\pi}\right) + \ln NN_s \right) \quad (8.9)$$

where N_s is the number of sheets. Eq. 8.6 becomes:

$$\frac{\beta\Delta F^{\mathfrak{X}(CM)\rightarrow\mathfrak{X}}}{N} = -\frac{N_s}{N} \ln \frac{V}{N_{ws}} \quad (8.10)$$

where, in $N_{ws} = N/n_{ws}$, one has to define the Wigner-Seitz cell within a graphite sheet; this leads to $n_{ws} = 2$. Eq. 8.8 becomes:

$$\frac{\beta\Delta F^{\frac{1}{N}}}{N} = -\frac{N_s}{N} \left(\frac{3}{2}\ln\left(NN_s\frac{\alpha\beta}{2\pi}\right) + \ln\frac{V}{N_{ws}} \right) \quad (8.11)$$

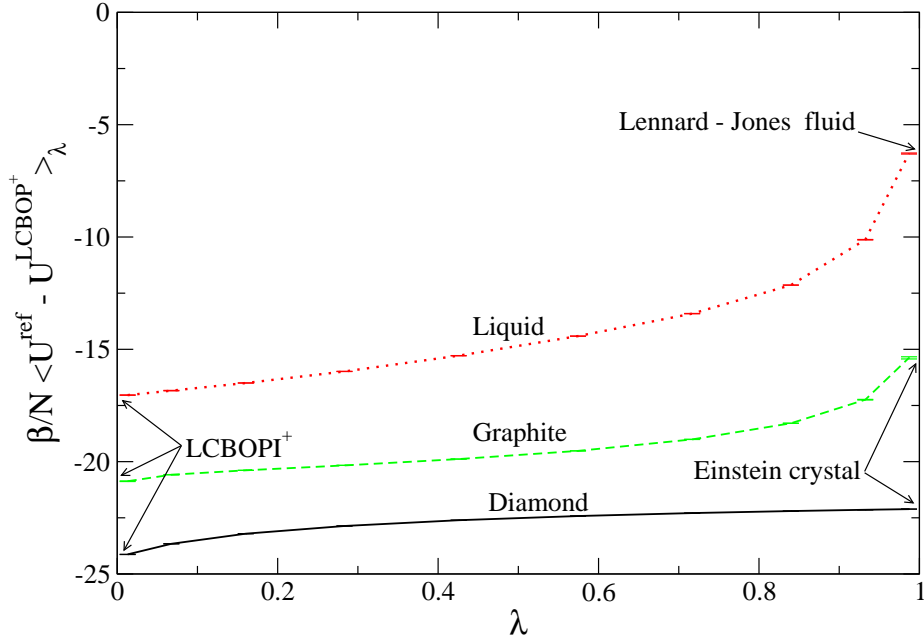


Figure 8.1: Plots of the quantity $\beta/N \langle U^{\text{ref}} - U^{\text{LCBOP}^+} \rangle_\lambda$ (see Eqs. 8.2 and 8.4) as a function of the coupling parameter λ for the liquid, graphite, and diamond. On the left side of the horizontal axis ($\lambda = 0$) is the pure LCBOP⁺, on the right side ($\lambda = 1$) is the reference system, i.e. the Lennard-Jones liquid for the liquid phase and two Einstein crystals (with different coupling constant) for graphite and diamond. The simulated ten points per phase are marked by their error bars, that are almost reduced to a single dash at this scale.

Here, $\rho^{\mathfrak{X}}$ denotes the number density at the initial state point, N the number of particles, and $\beta = 1/k_{\text{B}}T$, with k_{B} the Boltzmann constant. Details on this equation are given in appendix 8.3

8.2 Results

For calculating the three $F^{\mathfrak{X}}$ we performed independent Monte Carlo (MC) simulations for three phases. Three samples of 216 particles of the three systems were prepared, the solids in their lattice positions, and the liquid in a simple cubic arrangement. The three phases were equilibrated with NPT MC simulations at the chosen $T = 4000$ K and at $P = 10$ GPa[†]. The integer $N = 216$ permits the atoms to be arranged both in a defect-free diamond and cubic lattice, aligned with the sides of a cubic cell, while bonding perfectly across its faces to periodic-image atoms. The same requirements are fulfilled for 216 atoms in a defect-free graphite lattice, arranged in three sheets, but in a rectangular periodically replicated cell, with resulting edge-size ratios 1:1.5:1.7. The first, in-plane, ratio (1:1.5) is defined by the lattice structure, while the interplanar ratio (1:1.7) is pressure dependent. In fact, the rescaling of the box was allowed to be independent on the three axes for the equilibration of the solid phases, while kept intrinsically isotropic for the melting of the cubic crystal and

[†]For the correct application of the method it is not needed to have the three states at the same P . It is only required that the phases share a broad stable region in pressure at the chosen T .

the subsequent equilibration of the liquid phase. The equilibrium densities ρ^{\boxtimes} , expressed in 10^3 kg/m^3 , were 3.425 for diamond, 2.597 for graphite, and 2.421 for the liquid. Three configurations at the equilibrium volume were then chosen as starting points for the three thermodynamic integration. The value of α was set to 453000 and 39700 kJ/(mol nm²) for diamond and graphite, respectively. The parameters σ and ϵ for the LJ fluid were 0.127 nm and 31.84 kJ/mol.

	Graphite	Diamond
$\beta F^{\text{E}}/N$	-5.588	-1.933
$(\beta/N) \int d\lambda \langle U^{\text{ref}} - U^{\boxtimes} \rangle_{\lambda}$	-19.369 ± 0.006	-22.671 ± 0.002
$\beta F^{\frac{1}{N}}/N$	0.133	0.021
$\beta F^{\boxtimes}/N$	-24.824 ± 0.006	-24.5831 ± 0.002

	Liquid
$\beta F^{\text{id}}/N$	-10.697
$\beta F_{\text{LJ}}^{\text{ex}}/N$	-0.165
$(\beta/N) \int d\lambda \langle U^{\text{ref}} - U^{\boxtimes} \rangle_{\lambda}$	-14.275 ± 0.002
$\beta F^{\boxtimes}/N$	-25.137 ± 0.002

Table 8.1: Calculated values for the quantities in equations 8.4, 8.7, 8.8.

	a [GPa]	b [GPa nm ³]	c [GPa nm ⁶]
Liquid	89.972	-1.9654	0.011 092
Diamond	74.809	-3.6307	0.019 102
Graphite	108.29	-2.2707	0.011 925

Table 8.2: Parameters for the polynomial fitting of the 4000 K isotherms of the three phases, according to: $P(\rho) = a + b\rho + c\rho^2$.

The calculated values for the free energy for three phases, split in their contributions, are given in table 8.1. The values of λ for the sampling were defined by a 10-point Gauss-Legendre integration scheme. The scheme avoids the sampling of the systems at the two boundary values of λ . A 10 point scheme assures exact result whenever the integrand function of Eq. 8.2 ($\langle U^{\text{ref}} - U^{\text{LCBOPI}^+} \rangle_{\lambda}$) can be reasonably described with a polynomial up to order $2 * 10 + 1 = 21$. When $\lambda = 0,1$ the system performs its random walk on the basis of only one of the two potentials, thus in principle allowed to assume configurations completely avoided by the other potentials, in such a way that the integrand of Eq. 8.2 could diverge. Should this be the case, the integration scheme would yield a poor estimate of the integral. We thus ascertained that the integrand never indeed diverged at $\lambda = 0,1$. For the three phases, we run at each λ point an NVT MC simulation of 500000 cycles.

In Fig. 8.1 $\langle U^{\text{ref}} - U^{\text{LCBOPI}^+} \rangle_{\lambda}$ versus λ is shown. The absence of spurious phase boundary crossings throughout the integration over λ was checked by looking at the distribution

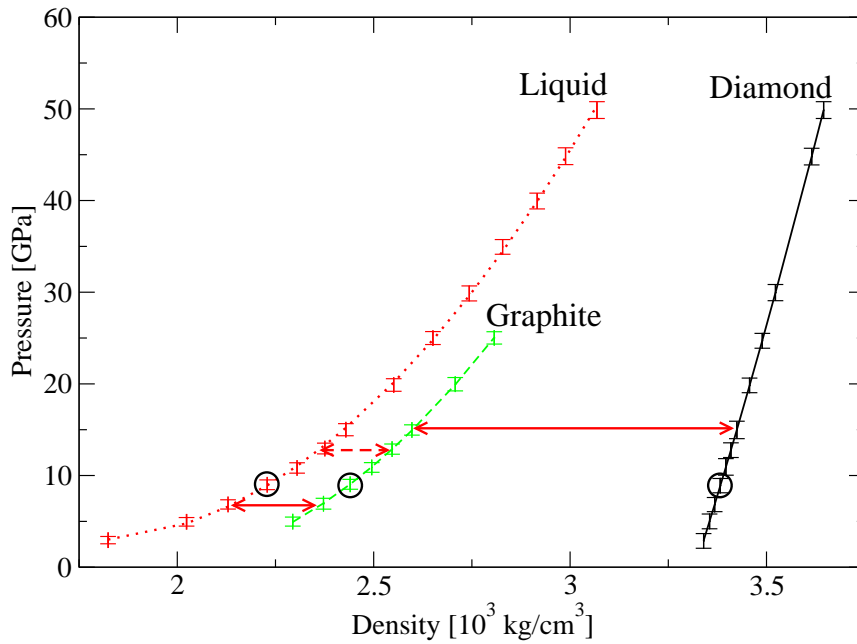


Figure 8.2: Equations of state at 4000K for the liquid, graphite, and diamond. The lines are the quadratic polynomial fits to the data. The circles indicate the points, at 10 GPa, where the thermodynamic integration (Eq. 8.2) was performed. The solid arrows connect coexisting (stable) points, i.e. liquid/graphite and graphite/diamond. The dashed arrow links the liquid/diamond coexisting point, metastable towards graphite.

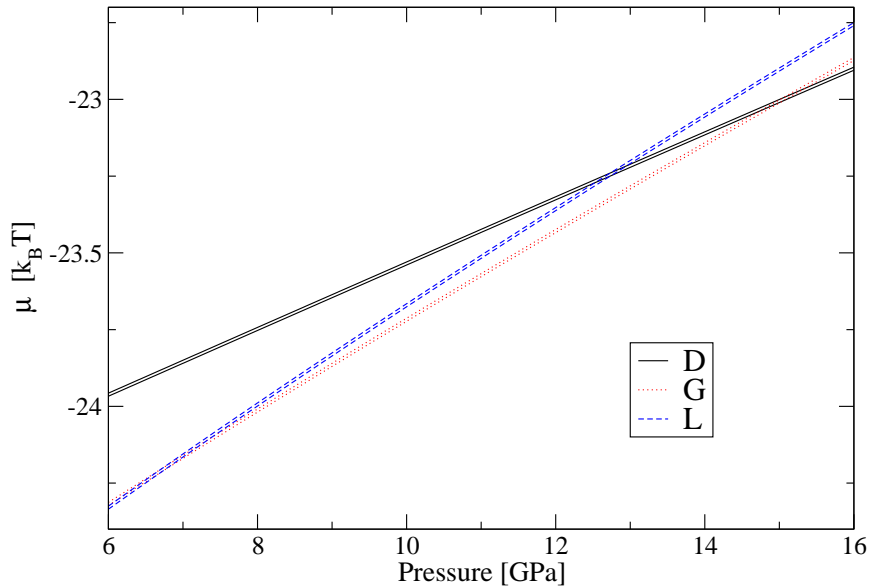


Figure 8.3: Plot of the chemical potential μ displaying the associated uncertainty intervals corresponding to $\pm\sigma$. These curves represent equation 8.12, but expressed as a function of pressure with the help of $P(\rho) = a + b\rho + c\rho^2$. The main source of error was the thermodynamic integration, being the uncertainty on the equations of state of at least an order of magnitude less.

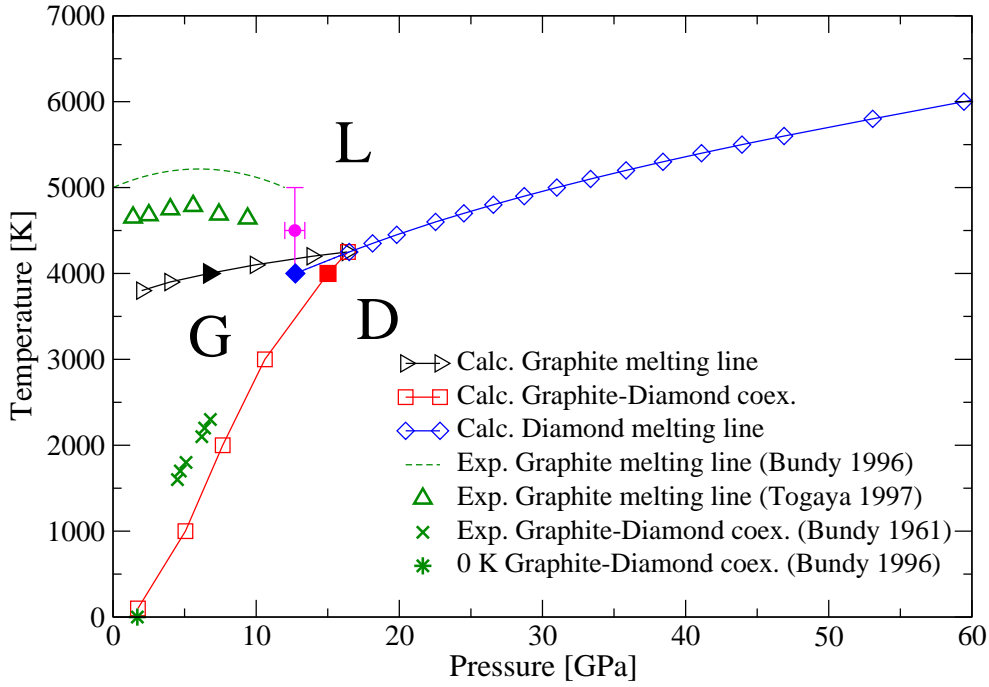


Figure 8.4: Phase diagram of carbon up to 60 GPa. The solid right triangle, square, and diamond are the three coexistence points found by equating the chemical potentials at 4000 K (see text). The open right triangles, squares, and diamonds are the calculated coexistence points, propagated via Gibbs-Duhem integration. The solid circle with error bars indicates the experimental estimate for the liquid/graphite/diamond triple point [205, 2, 210]. The dashed line is the experimental graphite melting line from Ref. [205]. The up triangles are graphite melting state points from Ref. [200]. The crosses represent experimental graphite/diamond coexistence from Ref. [176]. The asterisk represent the theoretical graphite/diamond coexistence at zero kelvin, as reported in Ref. [205].

of $(U^{\text{ref}} - U^{\text{LCBOPI}^+})^\ddagger$. Since the points were run in parallel in order to accumulate more statistics, only shorter independent simulations were performed by increasing and then decreasing λ , each new λ point starting from the final configuration of the previous. The absence of hysteresis in this process completely rules out phase boundary crossings. The isotherms for the three phases, calculated via NPT MC simulations together with their fit, are shown in Fig. 8.2.

The three μ curves, as given in 8.12, but expressed as functions of P , are shown in Fig. 8.3. The three curves, μ_L , μ_G , μ_D , as given in Eq. (8.12), intersect in pairs in three points (these points are shown as a solid triangle, square and diamond in Fig. 8.4). The intersections locate the graphite/liquid coexistence at 6.72 ± 0.60 GPa ($\mu_{\text{GL}} = -24.21 \pm 0.10 k_B T$), and the graphite/diamond coexistence at 15.05 ± 0.30 GPa ($\mu_{\text{GD}} = -23.01 \pm 0.03 k_B T$). The third intersection locates a diamond/liquid coexistence at 12.75 ± 0.20 GPa ($\mu_{\text{DL}} = -23.24 \pm 0.03 k_B T$). Even though both diamond and the liquid are there metastable, this point can be taken as the starting one for the Clausius-Clapeyron integration of the diamond melting line. Starting from the three coexistence points at 4000 K, the coexistence lines were traced by integrating the Clausius-Clapeyron equation

[‡]The distribution usually exhibits a bimodal shape in case of phase boundary crossing.

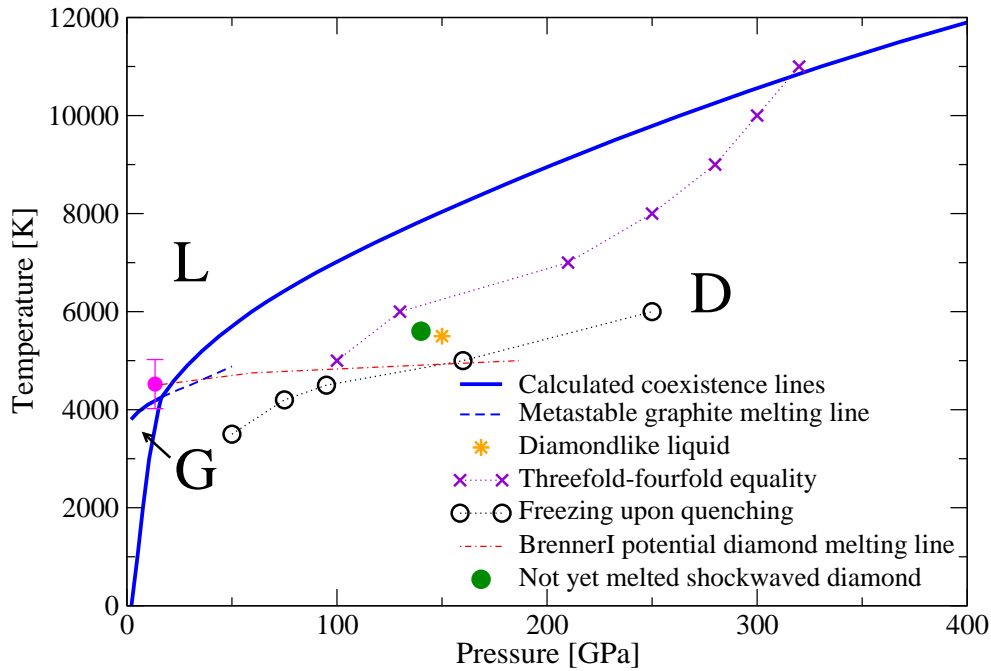


Figure 8.5: Phase diagram of carbon at all calculated pressures. The thick solid lines are our calculated phase boundaries. The dashed line is the metastable prolongation of the graphite melting line, from Gibbs-Duhem integration; the line stops just before the simulated graphite became unstable, displaying large density fluctuations. The dashed-dotted line departing from the experimental guess for the triple point (solid circle with error bar [205, 2, 210]) is the diamond melting line calculated in Ref. [214] with the BrennerI potential. The solid circle is the final point of the shock wave experiment of Ref. [191] at which diamond is not yet melted. The following features are discussed in the next chapter (see section 9.2): crosses mark the liquid with equal amount of three and four-fold atoms; circles represent state points in which the sample freezes; in the region in between the two series is the “diamond-like liquid”: the star is the point reported in Ref. [17].

using the trapezoidal-rule predictor-corrector scheme [219]. The new value of the coexisting P at a given T was taken when two iterations differed less than 0.01 GPa, this being the size of the single uncertainty in the calculation of dP/dT . This normally took 2-3 iterations to be obtained.

The calculated phase diagram in the $P - T$ plane is shown in Fig. 8.4 for the low pressure region, and in Fig. 8.5 for the full range of pressures and temperatures considered. Tab. 8.3 lists the densities of selected points on the coexistence lines. The three coexistence lines meet in a triple point at 16.4 ± 0.7 GPa and 4250 ± 10 K. The graphite/diamond coexistence line agrees very well with the experimental data. In the region near the liquid/graphite/diamond triple point, that has not been directly probed in experiments, the graphite/diamond coexistence line bends to the right, departing from the usually assumed straight line. Analysis of our data shows this is mainly due to the fast reduction with increasing pressure of the interplanar distance in graphite at those premelting temperature. This causes an enhanced increase of the density in graphite, yielding a decrease of dT/dP .

Table 8.4 shows the melting enthalpy Δh_m for graphite and diamond. These are calculated as the difference in enthalpy between the solid and the melt at coexistence. Our calcu-

Graphite melting line			
P [GPa]	T [K]	ρ_G [10^3 kg/m ³]	ρ_L [10^3 kg/m ³]
2.00	3800	2.134	1.759
6.70	4000	2.354	2.098
16.4	4250	2.623	2.414

Diamond melting line			
P [GPa]	T [K]	ρ_D [10^3 kg/m ³]	ρ_L [10^3 kg/m ³]
16.4	4250	3.427	2.414
25.5	4750	3.470	2.607
43.9	5500	3.558	2.870
59.4	6000	3.629	3.043
99.4	7000	3.783	3.264
148.1	8000	3.960	3.485
263.2	10000	4.286	3.868
408.1	12000	4.593	4.236

Table 8.3: Pressure (P), temperature (T), solid and liquid densities (ρ) along the melting lines.

Graphite melting line		
P [GPa]	T [K]	Δh_m [kJ/mol]
2.00	3800	68.8
5.24	3950	65.6
9.94	4100	67.8
16.4	4250	64.7

Diamond melting line		
P [GPa]	T [K]	Δh_m [kJ/mol]
16.4	4250	95.9
25.5	4750	111.5
43.9	5500	130.8
59.4	6000	143.9
99.4	7000	160.5
148.1	8000	174.7
263.2	10000	195.3
330.5	11000	208.1
408.1	12000	221.7

Table 8.4: Pressure (P), temperature (T), and melting enthalpy (Δh_m , calculated as the enthalpy of the liquid subtracted of the enthalpy of the underlying solid phase) along the melting lines.

lated melting enthalpies of graphite are sensibly lower than the values around 110 kJ/mol reported in shock heating melting experiments in the past years [205, 200], nonetheless our values retain the feature of being rather constant along the graphite melting line. No experimental data are known about the melting enthalpies of diamond: we note them increasing monotonically with temperature (and pressure).

The calculated graphite melting line is monotonically increasing in a small temperature range around 4000 K. In contrast to data inferred from experiments it shows no maximum and is at a somewhat lower temperature. In agreement with the experiments the coexistence temperature is only slowly varying with pressure. Inspection reveals that this behavior is due to 1) the limited variability of the melting enthalpy, and 2) a similar bulk modulus for liquid and graphite such that Δv is almost constant.

We have extended the calculation of the graphite melting line to the region in which both graphite and the liquid are metastable towards diamond, with the aim to look for a possible maximum in the line. The results are shown as a dashed line in Fig. 8.5. We stopped the Gibbs-Duhem integration at ~ 50 GPa, where the 216-particles graphite sample started showing huge volume fluctuations during the NPT sampling. The integration algorithm became unstable, forbidding any further analysis. Looking at this metastable melting line, it is clear that its slope does not continue to decrease with increasing pressure as in the stable region; thus, the hypothesis of an hidden maximum appears to be rejected.

The slope of the diamond melting line is consistent with the only experimental point available [191] (see Fig. 8.5). When compared to the diamond melting line of the Brenner model [214], the LCBOP1⁺ diamond melting line has a steeper slope yielding significantly higher temperatures for the diamond melting line.

In summary, this is the first time that carbon phase diagram comprising graphite, diamond, and the liquid has been calculated. The knowledge of the phase diagram predicted by the LCBOP1⁺ gives per se a deep insight into many of the open issues we summarized in the previous chapter. In the next two chapters we examine the nature of liquid carbon and study the interesting problem of diamond (homogeneous) nucleation, using the phase boundaries here reported as a reliable starting point.

8.3 Appendix. Chemical potential as a function of density

One can always write:

$$\begin{aligned}
 \beta\mu(\rho) &= \beta\mu(\rho^{\boxtimes}) + \beta\Delta\mu \\
 &= \beta\mu(\rho^{\boxtimes}) + \frac{\beta}{N} [F(\rho) - F(\rho^{\boxtimes}) + P(\rho)V - P(\rho^{\boxtimes})V^{\boxtimes}] \\
 &= \beta\mu(\rho^{\boxtimes}) + \frac{\beta}{N} \left[\int_{\rho}^{\rho^{\boxtimes}} \frac{\partial F}{\partial \rho} d\rho + \frac{P(\rho)}{\rho} - \frac{P(\rho^{\boxtimes})}{\rho^{\boxtimes}} \right]. \tag{8.13}
 \end{aligned}$$

Working out the integral:

$$\int_{\rho}^{\rho^{\boxtimes}} \frac{\partial F}{\partial \rho} d\rho = \int_{\rho}^{\rho^{\boxtimes}} \frac{PV}{\rho} d\rho = N \int_{\rho}^{\rho^{\boxtimes}} \frac{P}{\rho^2} d\rho \tag{8.14}$$

From the ansatz $P(\rho) = a + b\rho + c\rho^2$, one finds:

$$\int_{\rho}^{\rho^{\boxtimes}} \frac{a}{\rho^2} + \frac{b}{\rho} + c d\rho = \left[-\frac{a}{\rho} + \frac{a}{\rho^{\boxtimes}} + b\ln\rho - b\ln\rho^{\boxtimes} + c(\rho - \rho^{\boxtimes}) \right] \tag{8.15}$$

Putting this result in Eq. 8.13 and reordering the terms:

$$\begin{aligned}
 \beta\mu(\rho) &= \beta\mu(\rho^{\boxtimes}) - \frac{P(\rho^{\boxtimes})}{\rho^{\boxtimes}} + \beta \left[-\frac{a}{\rho} + \frac{a}{\rho^{\boxtimes}} + b\ln\rho - b\ln\rho^{\boxtimes} + c(\rho - \rho^{\boxtimes}) + \frac{a}{\rho} + b + c\rho \right] \\
 &= \frac{\beta F^{\boxtimes}}{N} + \beta \left[2c\rho + b(\ln\rho + 1) - c\rho^{\boxtimes} - b\ln\rho^{\boxtimes} + \frac{a}{\rho^{\boxtimes}} \right] \tag{8.16}
 \end{aligned}$$

The nature of liquid carbon: absence of a *first-order* liquid – liquid phase transition

Gh'è mië de fidàss trupàsc.

after Andrea S. Ghiringhelli

In this chapter we examine the issue of the liquid – liquid phase transition (LLPT) for carbon. A short review of the relevant findings is given in section 7.3. In the first section we describe the liquid at 6000 K as predicted by several bond order potentials (see Fig. 9.1 for the complete list) and compare the results with density functional (DF) based molecular dynamics (MD) calculation. The temperature was chosen to agree with the DF-MD based analysis of the liquid Wu *et al.* [14] (see paragraph 7.3.6). There the isotherm at 6000 K was originally chosen for two reasons. Firstly it is expected to be far from coexistence in the density interval studied; this assumption is based on the phase diagram calculated by Glosli and Ree [214] using one of the Brenner bond order potential [3] (the authors do not specify which parametrization they use). Secondly, the 6000 K isotherm is predicted by Glosli and Ree [2], with the BrennerI [3] bond order potential, to cross the liquid – liquid coexistence line. In the third section the analysis will be extended at all the relevant region of the phase diagram, supported by the calculation elucidated in the previous chapter. The chapter ends with the analysis of the structure of the so called “diamond-like” liquid.

9.1 Properties of liquid carbon, according to selected BOPs

9.1.1 Methods

We performed the Monte Carlo (MC) simulations of 128 particles in a cubic box with periodic boundary conditions with all the bond order potentials we chose for the comparison. We sampled at 6000 K the constant volume (NVT) ensemble for densities smaller than $2.5 \cdot 10^3 \text{ kg/m}^3$ and the constant pressure (NPT) ensemble for larger densities where

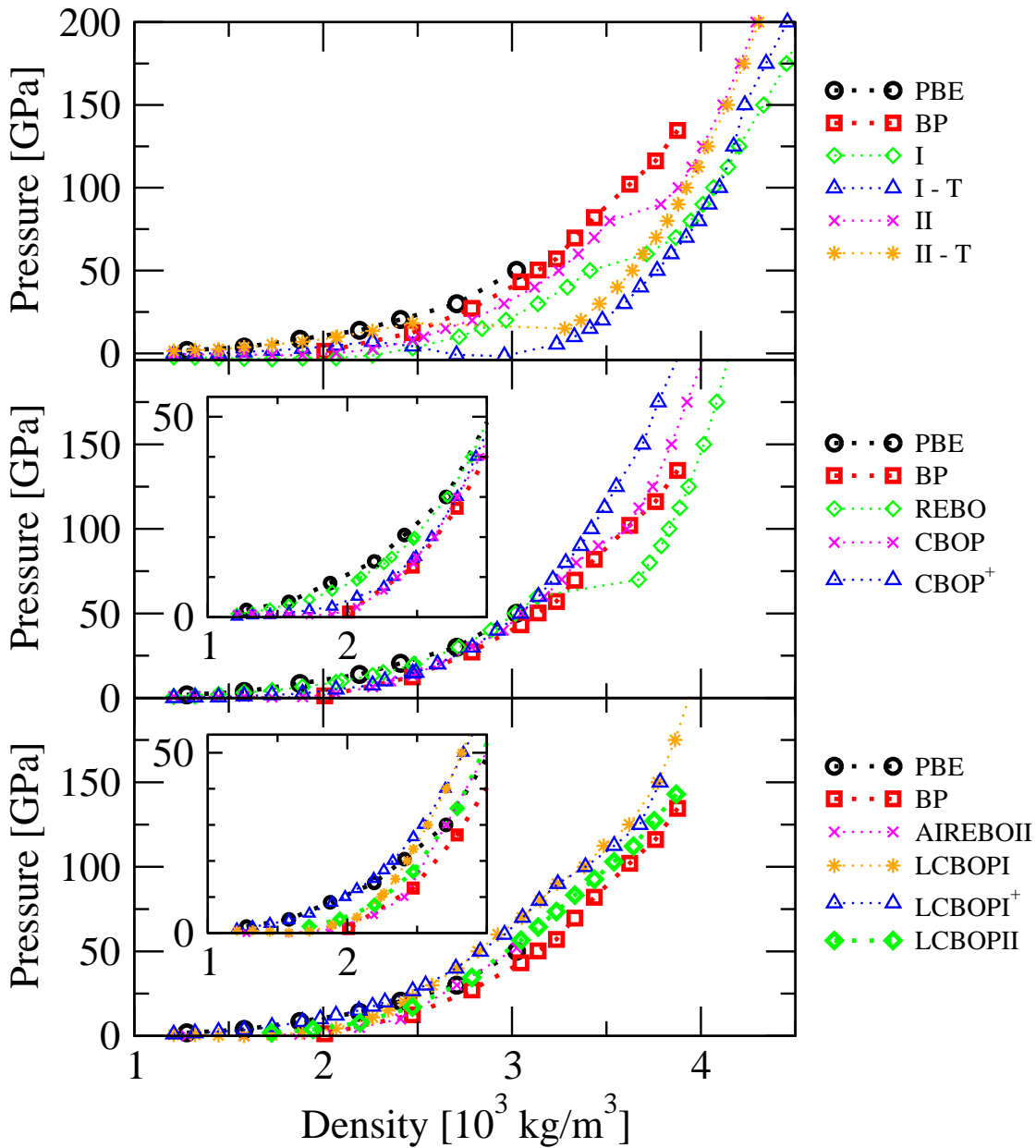


Figure 9.1: Equations of state for all the potential tested. The abbreviation ‘PBE’ and ‘BP’ refer to two parametrization of the gradient corrected density functional (see text), and are thought as reference data on these plots. The Brenner potentials are labelled ‘I’ and ‘II’ for their original version [3], i.e. without torsional interaction, and ‘I-T’ and ‘II-T’ for the version [4] with added torsional interactions. The REBO potential is shortly described in section 6.5 and presented in Ref. [130]: the data points come from our simulations. The CBOP is presented in Ref. [15]; with CBOP⁺ is labelled the CBOP with modified angular interactions and added torsional interactions, in the same way as for the LCBOPi⁺, but with appropriate parameters. The LCBOPi [15] and the LCBOPi⁺ are presented in sections 6.6 and 6.7. The LCBOPii is presented in chapter 11. The AIREBO potential is presented in Ref. [155] and its slight modification (called AIREBOII), together with the points reported here, are presented in Ref. [220].

the increase of pressure is steeper, with an overlap between the two regions to check for consistency. The pressure in the NVT simulation for the BOPs was calculated without virial evaluation, by means of virtual volume rescaling (see appendix 9.4).

We performed constant volume DF-MD simulations using the Car-Parrinello method [62] as implemented in the CPMD package [60]. The system consisted of 128 atoms in a cubic box with periodic boundary conditions at 9 densities and a temperature $T = 6000$ K, imposed by means of a Nosé-Hoover [94] thermostat. We used the Becke [79] exchange and Perdew [78] correlation gradient corrected functional (BP) with a plane wave basis set cut off at 35 Ry and sampled the Brillouin zone only in the gamma point. BP gives a correct description of bulk diamond. Each state point was studied for 5 ps, starting from a sample equilibrated via the LCBOP⁺; only minor structural changes occurred in the first tenths of ps. Since liquid carbon is metallic, we imposed a thermostat for the electronic degrees of freedom in order to ensure a proper implementation of the Car-Parrinello scheme [98] (see section 3.4).

9.1.2 Results

Fig. 9.1 shows the equations of state of all the mentioned potentials. All the points were calculated by us, except for the AIREBOII potential [155] points in the bottom panel, that come from Ref. [220], and the DF-MD data of Wu *et al.*, marked with PBE (vide infra). The data from Ref. [14] are calculated with a different functional (i.e. PBE, as labelled in Fig. 9.1) and a different cut-off energy (50 Ry). In view of the relatively low cut-off energy (35 Ry), we had to correct the pressures for the spurious contribution due to Pulay forces [102] (see appendix 9.5 for details about the method). In the density range where we can compare with the results of Wu *et al.* [14], the pressures that we compute are some 15% lower than those reported by Wu *et al.* The difference in calculated pressures between the two DF-MD simulations should be attributed to the use of a different functional. Differences in plane-wave cutoff and pseudopotential should not contribute significantly to this discrepancy, as both setups yielded good binding energies. We have checked that our samples were indeed liquid: over the whole isotherm we have observed diffusive behavior in both the MC-LCBOP⁺ and the DF-MD simulations, the latter indicating a self-diffusion coefficient at least of order $10^{-5}\text{cm}^2/\text{s}$.

The two series of DF-MD data are taken as reference, and thus presented in every panel. The original Brenner potentials [3], BrennerI and BrennerII, with and without torsional interactions [4], are in the top panel. The center panel is for the subsequent generation of short range potentials: REBO [130] and CBOP [15]. With CBOP⁺ is labelled the CBOP with modified angular interactions and added torsional interactions, in the same way as for the LCBOP⁺. The bottom panel groups the potentials with non-bonded interactions: AIREBOII, LCBOP⁺ and LCBOP⁺. The bottom panel also shows the equation of state as given by the LCBOP⁺, the potential that is presented in chapter 11*. The coordination fractions are shown in Figs. 9.2, 9.3, 9.4 with the same labelling criterion: for the AIREBOII potential no coordination data are available; ‘LCBOP⁺’ indicates an intermediate version of the LCBOP⁺, i.e. with the softened angular interactions at low coordination

*The properties of the liquid as predicted by the LCBOP⁺ are given in chapter 12; the purpose of this anticipation is to make it possible to have in a single glance the comparison of all the BOPs entering in the discussion throughout this thesis.

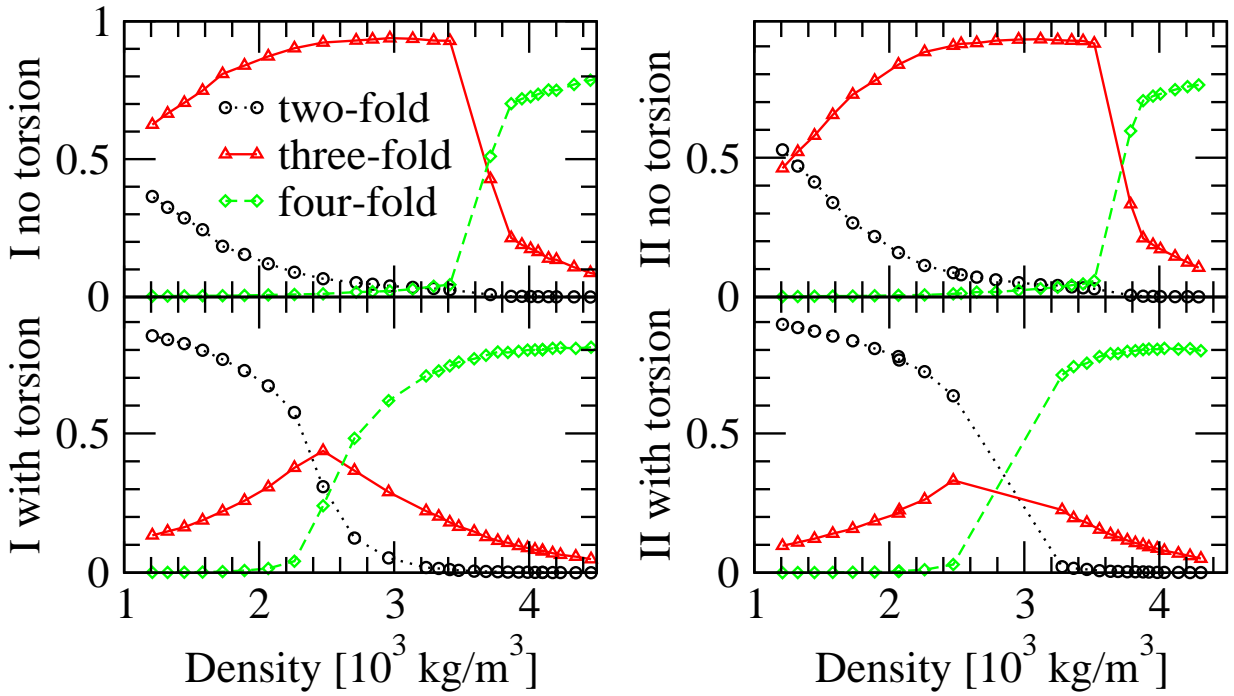


Figure 9.2: Coordination fractions for the Brenner potentials of Refs. [3, 4].

(section 6.7.2), but without torsional interactions. The DF-MD data, that are in the right bottom panel of Fig. 9.4, serve as reference data for the coordination fractions.

Looking at equations of state and coordination fractions, BrennerI and BrennerII with torsional interactions show the LLPT from a mainly two-fold to a mainly four-fold liquid, as

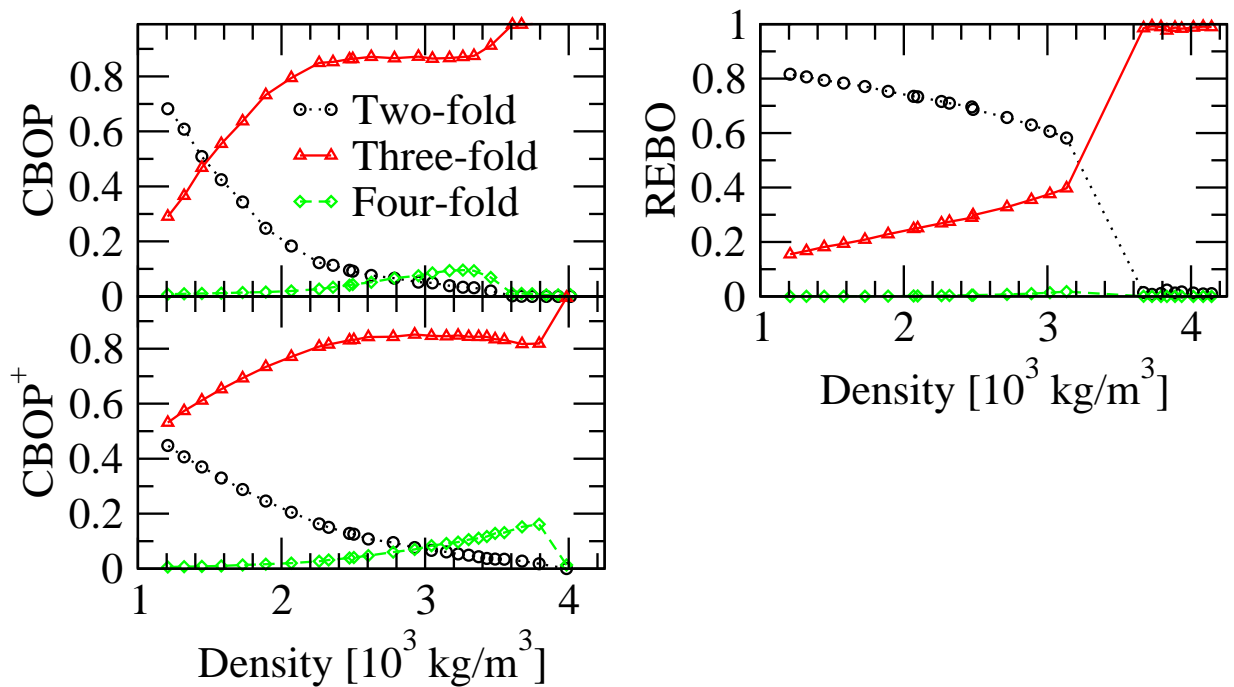


Figure 9.3: Coordination fractions for short range potentials [130, 15].

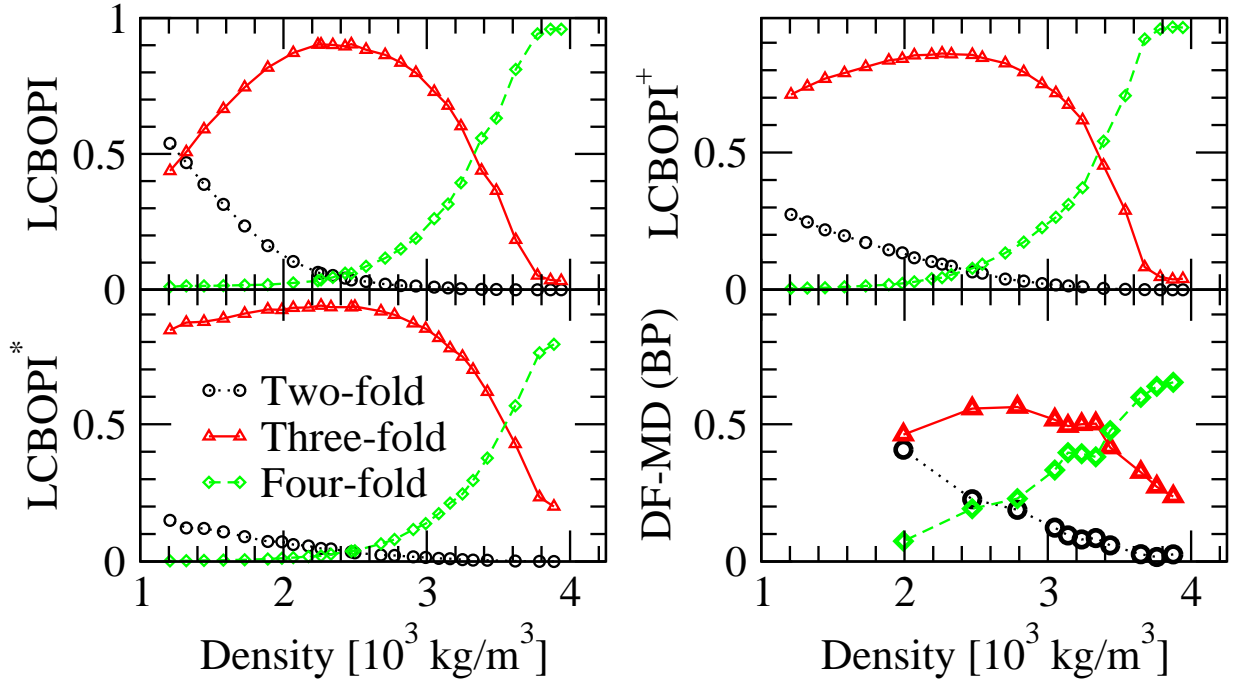


Figure 9.4: Coordination fractions for long range potentials and for the density functional (BP) calculations.

discussed in section 7.3.5. We show that also for the version without torsional interactions, the potentials present an abrupt transition from a mainly three-fold to a mainly four-fold liquid from density 3.4 to 3.8 10^3 kg/m³. The REBO potential displays a quite good reproduction of the DF-MD *equation of state* at lower densities (up to 3.2 10^3 kg/m³), but, also at low density, the structure of the liquid is far from the reference data (see Fig. 9.4, bottom right panel): two-fold atoms are predominant where DF-MD predicts three-fold to be. Furthermore, the liquid undergoes a LLPT at 3.2 10^3 kg/m³. The high density liquid is revealed to be, upon visual inspection of the snapshots, a completely three-fold graphite-like liquid consisting of almost defect-less sliding sheets that eventually get stuck upon further increasing of the pressure. We note that the transition occurred regularly upon compression for different, independent, samples. Note that the four-fold fraction remains always negligible. Also the CBOP and the CBOP⁺ present this spurious transition, but the predominance of three-fold sites in the lower density regime is correctly given by both these potentials. Note that the equation of state of CBOP is the one in better agreement with our DF-MD data. Nonetheless, as it is dramatically shown by the coordination fractions, a good equation of state is not sufficient to assess the accuracy of a potential.

With the introduction of non-bonded interactions, the fraction of four-fold becomes eventually non negligible at higher densities. For these potentials, the coordination fractions depict a similar scenario at high density, whereas the main differences are found at intermediate densities. The original potential, LCBOP, predicted a too stiff variation of the three-fold fraction, both when increasing, substituted by the two-fold predominance, and when decreasing, substituted by the four-fold sites. The introduction of softened angular correlation for low coordinated atoms, the case of LCBOP*, increased the stability of the three-fold sites versus two- and four-fold sites. The introduction of torsional interac-

tions, i.e. LCBOP⁺, yielded a picture closer to the reference data. Anyway the agreement remains qualitative since only the trends and the fold-type of dominant coordination is reproduced, while the absolute values are always shifted towards overestimation of the dominant fraction.

DF-MD predicts a marked switching of dominant coordination from three to four around $3.4 \cdot 10^3 \text{ kg/m}^3$. Judging from the isotherm of Fig. 9.1, the transition seems to be continuous with no sign of a van der Waals loop. These results are consistent with the tight binding MD simulations of Ref. [213]. In contrast, between 3.3 and $3.6 \cdot 10^3 \text{ kg/m}^3$, where the switch of dominant coordination takes place, the MC results based on the LCBOP⁺ display large fluctuations in density at the imposed pressure of 100 GPa, resulting in a slight bending of the isotherm of Fig.4.3.

Our results provide no evidence of a first-order transition but rather indicate a pronounced but continuous change of dominant coordination.

It is rather surprising that the LCBOP⁺ potential reproduces the transformation to a predominantly four-fold coordinated liquid, while the REBO potential does not. The latter is in fact a potential known to give rather accurate predictions in several environments [130]. The high temperature liquid is, anyway, the most demanding benchmark for a semiempirical potential, due to the presence of a large variety of local structures. It thus becomes crucial to have a reasonable estimate of the interaction energy for configurations that are very far from cluster and lattice structures in their minimum energy. Apparently, the isotropic long-ranged interactions play a crucial role in stabilizing the high density liquid. This behavior is rather puzzling as long-ranged interactions were predicted (see, e.g., Ref. [214]) to play a negligible role at these high densities. It has to be recognized that the Brenner original potentials, even without torsional interactions, present at a certain density the switch to the dominant four-fold coordination, but with a strongly first order LLPT, that is as spurious as the one predicted by the torsional interaction corrected versions.

Finally, we note that long-ranged interactions were introduced in Ref. [15] to describe three-fold coordinated graphitic phases, and no attempt was made to make the long range interactions dependent on the local environment. Torsional interactions appear to be important, since, without them, the calculated pressures would be too high for high densities and too low at low densities. We conjecture that the combination of torsional interactions, and long range forces is required to give the best description of the liquid.

9.2 Ruling out the liquid – liquid phase transition in the stable liquid region

In the previous chapter we reported our calculation of the phase diagram according to the LCBOP⁺. With the knowledge of the full melting lines, we can state that there is no LLPT in the stable liquid phase. One indication is the smoothness of the slopes of the melting lines. A further argument lies in the structure of the liquid near freezing. We determined several structural properties of the liquid at coexistence with the solid phases (the properties were calculated during the same simulations of the state points needed for the Gibbs-Duhem integration of the previous chapter). Fig. 9.5 shows the coordination fraction in the liquid along the coexistence lines with graphite and diamond. Since the coexistence lines are unimodal, the graph can be shown indifferently with density, pressure,

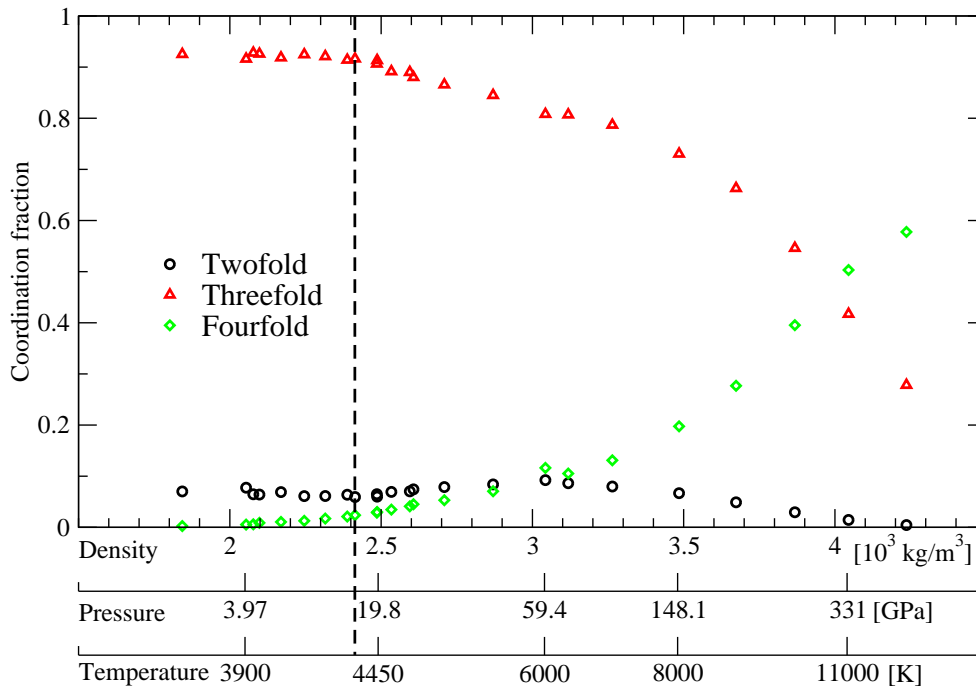


Figure 9.5: Coordination fraction of the liquid along the melting line(s). The melting lines are unimodal, thus fixing ρ , fixes also P and T . Anyway we chose the ρ scale to be linear. The dashed line is the liquid/graphite/diamond triple point.

or temperature on the horizontal axis. We chose to plot the graph with a linear scale in density. The dashed line is the graphite/diamond/liquid triple point. On the left hand side of the triple point, the liquid coexists with graphite, while on the right hand side it coexists with diamond. The three-fold and two-fold coordination fractions remain rather constant when the liquid coexists with graphite, with the four-fold slightly increasing, to account for the increase in density. Along the diamond melting line, on the right side of the dashed line, the three-fold coordinated atoms are gradually replaced by four-fold coordinated atoms. However, only at $(3.9 \cdot 10^3 \text{ kg/m}^3, 300 \text{ GPa}, \text{ and } 10500 \text{ K})$ the liquid has an equal fraction of three-fold and four-fold coordinated atoms. The change of dominant coordination is rather smooth; moreover, it is fully reversible, without signs of hysteresis, in the region around the swapping of dominant coordination. These results contradict the generally assumed picture (see e.g. Ref. [210]) that diamond melts into a four-fold coordinated liquid.

The interrelation between three and four-fold sites, was further investigated calculating the partial radial distribution functions ($2g_{ij}(r)$) of the liquid at 300 GPa, and 10500 K. Partial radial distribution functions are defined as the probability of finding a j -fold site at a distance r from a i -fold site[†]; the total radial distribution function g is recovered by: $g = \sum_i g_{ii} + 2 \sum_{i \neq j} g_{ij}$. We show the results in Fig. 9.6; we focus on the three predominant curves, describing the pair correlations between three-fold atoms (g_{33}), between four-fold atoms (g_{44}), and the cross pair correlation between three- and four-fold sites (g_{34}). Disre-

[†]The factor two multiplying the off-diagonal partial distribution functions ($g_{ij}(r)$, with $i \neq j$) is needed when those distributions are calculated according to the literature (e.g. Refs [221, 222]). The algorithm calculating the $g_{ij}(r)$ browses the pairs of particles only once, as is commonly done for the total $g(r)$. If the algorithm browsed over all the neighbours of each particle, the factor two would clearly not be needed.

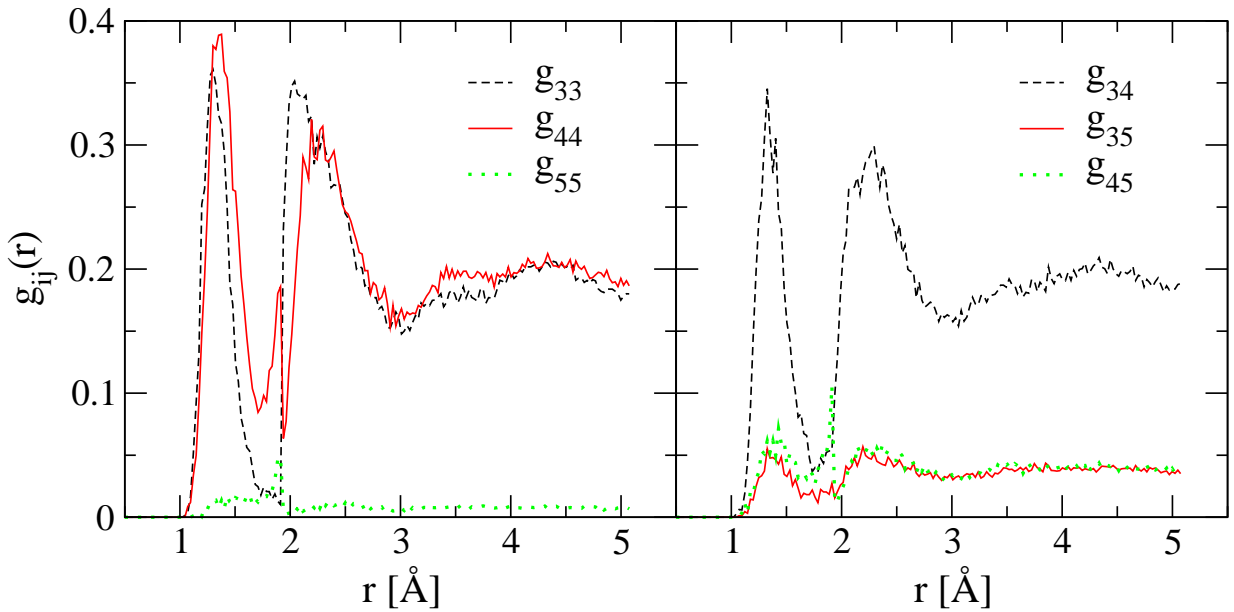


Figure 9.6: Partial distribution functions G_{ij} of the liquid at the calculated coexistence with diamond, at 10500 K and ~ 300 GPa, when three- and four-fold atoms are equally present. The left panel is for the diagonal contributions (i.e. for $i = j$), while the right panel is for the cross correlations (i.e. for $i \neq j$).

guarding the rather pronounced minimum in correspondence of the dip around 2\AA of the g_{33} and the g_{34} (see introduction to chapter 11 for a discussion of this problem), the similarity of three curves at all distances r is striking. The two sites are almost undistinguishable: in case of a tendency towards phase transition, one would expect some segregation of the two structures. In contrast, looking at distances within the first neighbours shell, a three-fold site seems to bond indifferently to a three- or a four-fold site, and viceversa. Furthermore, the partial structures up to the third, quite pronounced, peak at $\sim 4.5 \text{\AA}$, are almost the same for these three partial radial distribution functions.

We determined the properties of the metastable liquid in the stable diamond region. Fig. 8.5 shows the liquid $P - T$ state points (crosses) that exhibit an equal number of three and four-fold coordinated atoms. It ranges from high-pressure high-temperature region where the liquid is thermodynamically stable down into the diamond region, where the liquid is metastable for the LCBOP. The circles indicate state points in which the LCBOP liquid freezes in the simulation. Enclosed by the two set of points lies the diamond-like liquid[‡] addressed in the next section. This suggests that a (meta)stable liquid with a dominantly four-fold coordination may only exist for pressures beyond ≈ 100 GPa and could imply that the freezing of liquid into a diamond structure might be severely hindered for a large range of pressures beyond the graphite/diamond/liquid triple point. In Ref. [17] it is also pointed out that at 6000 K the equation of state shows a change of slope around the transition to the four-fold liquid. At even lower temperature this feature becomes more and more evident, but for temperatures lower than ~ 4500 K the liquid freezes into

[‡]A four-fold coordinated liquid with a rather pronounced diamond-like structure in the first coordination shell [17]).

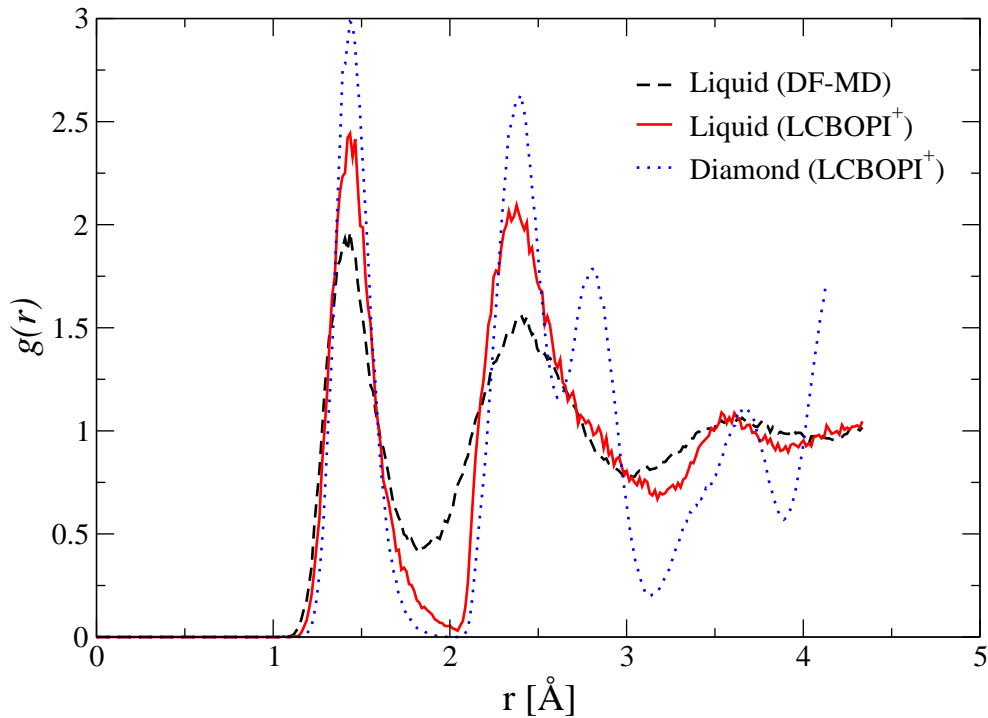


Figure 9.7: Pair correlation functions at 5000 K. Diamond (dotted curve) is at 150 GPa; the LCBOP⁺ liquid (solid curve) is at 150 GPa and $3.89 \cdot 10^3 \text{ kg/m}^3$; DF-MD liquid (dashed curve) is at $3.89 \cdot 10^3 \text{ kg/m}^3$.

a mainly four-fold coordinated amorphous structure. This observation is consistent with quenching MD simulations [223, 224] to obtain the tetrahedral amorphous carbon. In those simulations a mainly three-fold liquid freezes into an almost completely four-fold amorphous.

9.3 High pressure diamond-like liquid carbon

The state point in which the “diamond-like” liquid was analyzed in Ref. [17], at 5000 K and 150 GPa, was expected to be near the diamond/liquid coexistence on the basis of the shock wave experimental point [191] and of the only diamond melting line found in literature, calculated with the Brenner [3] bond order potential. The calculation of the phase diagram with the LCBOP⁺ revealed that the liquid was metastable in our simulation box, deep in the diamond stable region of the phase diagram. Both the DF-MD and LCBOP⁺ simulations of the mainly four-fold liquid carbon show a strong diamond like order, both in the typical distances and orientations of the bonds, as shown in Figs. 9.7, 9.8, and 9.9. Two two simulation methods agree in showing for the “diamond-like” liquid a mean square displacement much lower than for the mainly three-fold liquid.

In Fig. 9.7, we compare the pair correlations $g(r)$ of this metastable high density liquid with that of a stable bulk diamond at 5000 K and 150 GPa (also the LCBOP⁺ and DF-MD liquid samples were equilibrated at that temperature). One can see that up to the second neighbour shell the liquid has a structure almost as pronounced as diamond. The $g(r)$ ’s obtained by the LCBOP⁺ globally agree fairly well with the ones obtained by our

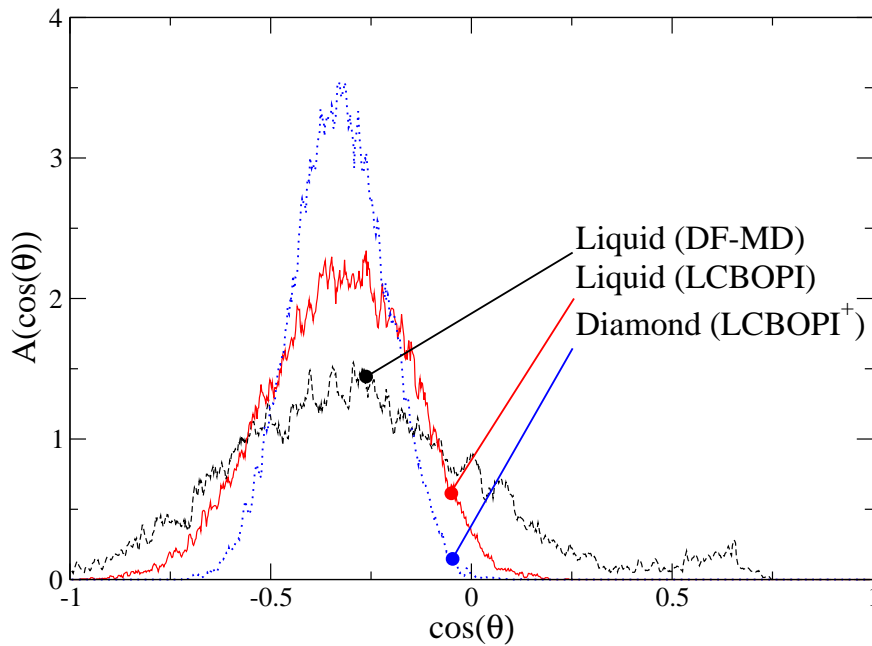


Figure 9.8: Angular correlation functions ($A(\cos(\theta))$) of first neighbours with state parameters as in Fig. 9.7.

DF-MD calculations, except around 2 \AA , where the LCBOPI⁺ minimum is too deep. In Fig. 9.8 we present the calculated angular correlation $g^{(3)}(\theta)$ for first neighbours, i.e. those atoms that fall within the short range cut-off of the LCBOPI⁺. Again, the first shell of neighbours in the liquid has a strong tetrahedral ordering, comparable to bulk diamond.

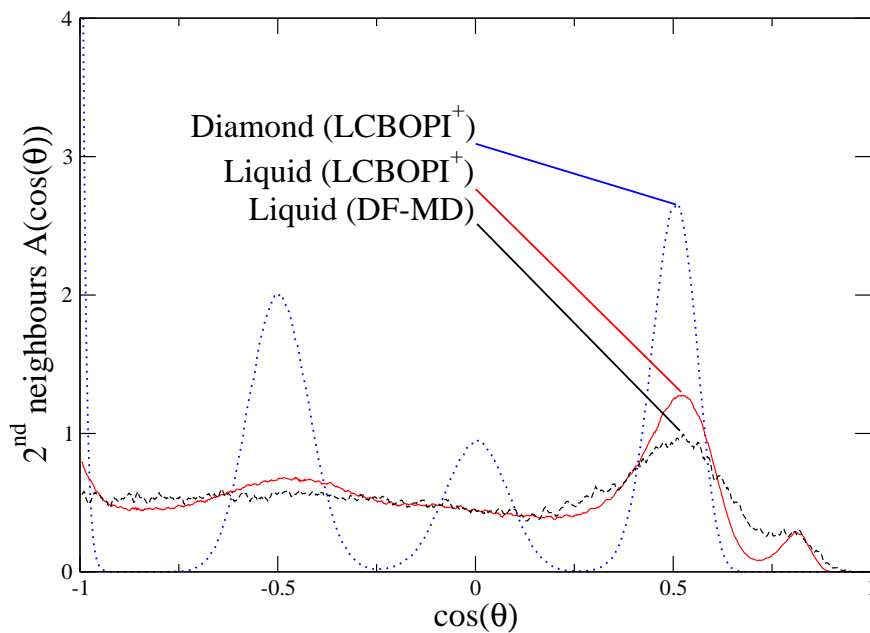


Figure 9.9: Angular correlation functions for second neighbours (see text) with state parameters as in Fig. 9.7. The peaks for the diamond are spread around the theoretical values for an fcc lattice of $-1, -0.5, 0, 0.5$, with weights $6/66, 24/66, 12/66, 24/66$.

To test how far the local diamond structure persists in the liquid, we define the angular correlation function for second neighbours (i.e. all those particles that are first neighbours of the first neighbours, excluding the central atom and the first-neighbor shell). Fig. 9.9 shows that, in the second-neighbor shell, the diamond structure is completely lost. Yet, the angular distribution is not structure-less: we find an average second shell coordination of 12 atoms, as in diamond, a peak around 60° and a shoulder at $\sim 35^\circ$; in a diamond lattice, the latter feature can be attributed to cross-correlations between the first and the second neighbour shells.

9.4 Appendix. Pressure estimation without evaluating the virial

At the present stage, we do not have carried out the force evaluation for the LCBOPs used throughout this work. In the calculation of the equation of state of the liquid we combined NPT and NVT simulations. The choice was made for statistical accuracy, preferring constant pressure estimation of the density when $|dP/d\rho|$ is high, and constant volume estimation of the pressure when $|d\rho/dP|$ is high. Since for the equation of state of the liquid is needed the estimate of the pressure in NVT simulations, we used a method that did not require the evaluation of the virial, and, to the purpose, forces. In practise we calculate pressure performing a “test” or “virtual” volume displacement, similar in spirit to the “ghost” particle insertion and removal when evaluating the chemical potential via the Widom [225] method. For a given configuration at a volume V , one can evaluate the total energy U_V . The same can be done for the configuration obtained rescaling the box and all the coordinates to a volume V' : the total energy is then $U_{V'}$. If $\Delta U = U_{V'} - U_V$, then the pressure can be evaluated as:

$$P = \rho k_B T - \frac{\langle \Delta U \rangle}{\Delta V} \quad (9.1)$$

This can be derived as follows [226, 227]. The partition function Q for the canonical ensemble is:

$$Q = \int_{\mathbf{r}} \frac{V^N}{\Lambda^{3N} N!} e^{-\beta U} d\mathbf{r} \quad (9.2)$$

where Λ is the de Broglie wavelength and $\beta = 1/k_B T$. The integration runs over all the configurations visited by the system. Pressure is the derivative with respect to the volume of the Helmholtz free energy:

$$P = - \left. \frac{dA}{dV} \right|_{N_i, T} \simeq - \frac{\Delta A}{\Delta V} = k_B T \frac{1}{\Delta V} \ln \frac{Q_{V'}}{Q_V} \quad (9.3)$$

The difference in free energy ΔA is calculated for a volume change $\Delta V = V' - V$.

From 9.2:

$$\frac{Q_{V'}}{Q_V} = \frac{\int_{\mathbf{r}} \frac{V'^N}{\Lambda^{3N} N!} \exp(-\beta U_{V'}) d\mathbf{r}}{\int_{\mathbf{r}} \frac{V^N}{\Lambda^{3N} N!} \exp(-\beta U_V) d\mathbf{r}} = \left\langle \left(\frac{V'}{V} \right)^N e^{-\beta \Delta U} \right\rangle \quad (9.4)$$

Where $\langle \dots \rangle$ denotes ensemble average over the canonical ensemble. Thus, from 9.3:

$$P = \frac{k_B T}{\Delta V} \ln \left\langle \left(\frac{V'}{V} \right)^N e^{-\beta \Delta U} \right\rangle \quad (9.5)$$

This expression is valid as soon as ΔV is small, so the derivative in 9.3 can be approximated by the finite difference ratio. If one fixes the ratio V'/V , then the above expression becomes:

$$P = \rho k_B T + \frac{1}{\Delta V} \ln \langle e^{-\beta \Delta U} \rangle \quad (9.6)$$

This expression is valid for any kind of potential, especially suited for discontinuous potentials. In fact, in the case of hard spheres ΔU would be either 0 or ∞ , so that the

exponential is the only way to treat ΔU . Anyway, for continuous potentials, one could avoid the evaluation of the exponential and the logarithm. We remind that the volume rescaling is virtual, so that the exponential does not have to be calculated anyway for the MC move. For small enough ΔV , ΔU can be so small that it is possible to approximate $\exp(x) \simeq 1 + x$ and subsequently $\ln(1 + x) \simeq x$, recovering indeed the 9.1. We *implemented* the pressure estimation with the 9.1, but we checked the use of the 9.6 is neither more accurate nor efficient (the error converges with comparable velocity, while the single evaluation is slightly more time expensive).

9.5 Appendix. Pressure evaluation in a constant volume CPMD simulation

For the DF-MD simulations, the pressure is evaluated as:

$$P = \rho k_B T + \frac{1}{3} \langle \text{Tr } \mathbf{\Pi} \rangle + P_{corr} \quad (9.7)$$

where $\langle \text{Tr } \mathbf{\Pi} \rangle$ is the ensemble average of the sum of the diagonal elements of the stress tensor $\mathbf{\Pi}$. P_{corr} is a correction term accounting for the fact that only the binding energy and not the (total) Kohn-Sham energy is converged for a plane-wave basis set usually employed in DF-MD simulation: this gives rise to a spurious contribution to the virial, known as the Pulay stress [102]. This contribution acts as a downward shift. The correction was estimated for all the NVT simulation involving carbon (in this chapter and in chapter 12). To the purpose, we performed short simulations at each density, at $E_{\text{cut}} = 120$ Ry, for which the total energy is almost converged, so that one can assume $P_{\text{corr}} \sim 0$. P_{corr} at the E_{cut} used in the simulations, i.e. 35 Ry, is then the difference in $\langle 1/3 \text{Tr } \mathbf{\Pi} \rangle$ between the simulations at the two cut-off energies.

Diamond nucleation

» *Alles, was geschieht* «, sagte sie, » *schreibst du auf*. «
» *Alles, was ich aufschreibe, geschieht* «, war die Antwort.

“Everything that happens, you write it.”, she argued.

“Everything that I write happens” was the answer.

10.1 Introduction

As a prime and most challenging application of the newly determined phase diagram of carbon via the LCBOP⁺ (see chapter 8), we aim to study the nucleation of liquid carbon into diamond. More specifically, we want to calculate the rate at which the liquid transforms into diamond and possibly find a relation between the rate and the mechanism of nucleation.

In recent years, methods for studying the homogeneous nucleation from a bulk and methods for recognizing ‘solid’ particles in the liquid have been developed (see e.g. Refs. [228, 229, 230] and references therein). Our study of diamond nucleation is based on this work, but also required various adaptations of the existing methods as carbon is rather different from systems studied earlier. Firstly, as shown in chapter 9, liquid carbon is rather structured, being a covalent liquid below its freezing line [22]. Thus, a definition of ‘solidity’ of a particle has to be rather restricted, in order to avoid the overestimation of the number of ‘solid’ particles and growing spurious structures. Secondly, simulations with bond order potentials, such as the LCBOP⁺ are computationally expensive, if compared e.g. to a Lennard-Jones interacting system [228, 229, 230]. Therefore, we employed in our study a computationally cheap method that yields a reasonable estimate of the nucleation rate.

It is well known that liquids can be cooled significantly below their freezing temperature. Pure water remains liquid if cooled down well below 0°C [231]. Even if the solid, crystal state is thermodynamically more stable, the system does not immediately crystallize due to the presence of a *free energy barrier*. In nature, as well as in most experiments, the freezing is triggered by some disturbances, such as the presence of impurities, walls, or shocks. This latter is the realm of *inhomogeneous* nucleation. We restrict to the case of *homogeneous* nucleation, in which only spontaneous fluctuations can lead the system to the thermodynamically stable state, the solid. According to classical nucleation theory (CNT, see appendix 10.7), nucleation is an activated process, i.e. a process that is difficult to

initiate spontaneously, but, when started, it proceeds very quickly. In CNT, this feature is modelled by postulating that the nucleation process proceeds via formation and growth of small solid nuclei in the melt. As it will become clear in the following, we do not rely on CNT in our simulation study of diamond nucleation. Yet, CNT helps us to introduce the vocabulary that is used when dealing with nucleation. Consider a pure liquid containing a spherical droplet of radius R of the same substance in its solid phase. In appendix 10.7 we show that the difference in Gibbs free energy between the pure liquid and the nucleus in the liquid is:

$$\Delta G = \Delta G^{\text{sol}} - \Delta G^{\text{liq}} = 4\pi R^2 \gamma + \frac{4}{3}\pi R^3 \rho_{\text{sol}} \Delta \mu \quad (10.1)$$

where γ is the surface free energy density, ρ_{sol} is the number density of the (bulk) solid phase, and $\Delta \mu = \mu^{\text{sol}} - \mu^{\text{liq}}$ is the difference in Gibbs free energy *per particle* between the liquid and the solid. The first term is a *surface* term: it scales with the surface of the droplet and is always positive due to the work needed to create an interface. The second term is a bulk term: it scales with the *volume* of the droplet and is always negative in our region of interest, i.e. where the solid is more stable than the liquid. The competition between the two terms gives rise to a maximum in the Gibbs free energy (see Fig. 10.1), at a certain *critical* radius R^* . The height of the barrier at R^* is $\Delta G^* = \Delta G(R^*)$:

$$\Delta G^* = \frac{16\pi\gamma^3}{3\rho_s^2(\Delta\mu)^2} \quad (10.2)$$

Here we want to note that ΔG^* is inversely proportional to $(\Delta\mu)^2$. This implies that the barrier is infinitely high at coexistence. Furthermore, near coexistence $\Delta\mu$ can be approximated by [232]:

$$\Delta\mu \simeq \Delta h_m \Delta^* T \doteq \Delta h_m \frac{T_m - T}{T_m} \quad (10.3)$$

where the last equality defines the *degree of undercooling* $\Delta^* T$. The term Δh_m is the difference in enthalpy between the coexisting solid and liquid phases (i.e. the latent heat released upon freezing). The higher the difference between the temperature of the system and the melting temperature, the higher $\Delta\mu$, the lower the free energy barrier ΔG^* . From statistical mechanics we know that a lower free energy barrier implies a higher probability that a spontaneous fluctuation leads the system to the top of the barrier. In a computer simulation, given the limitation on the system size and time length one can sample, only at very large undercooling a spontaneous nucleation can be seen. For instance, in Ref. [233] the sample of silicon, described by the Stillinger-Weber potential, was undercooled up to 40 % for a spontaneous nucleation to occur. For our system, spontaneous nucleation was not accessible, since the strength of the covalent bonds involved typically makes the system freeze into an amorphous at a 25 to 35 % undercooling, depending on the size of the simulated system.

The chapter is organized as follows. In section 10.2 we introduce the method we used for the nucleation procedure. In section 10.3 we describe the choice of the state points for the nucleation procedure and the method we used to identify ‘solid’ particles and recognize the biggest cluster; it also provides further details on the specific implementation of the nucleation method we used. Section 10.4 presents the results for the calculation of the rate constant at one selected state point, whereas in section 10.5 we present our calculation of the nucleation barrier for the same state point. Appendix 10.7 gives the details on the aspects of the Classical Nucleation Theory we refer to throughout the chapter.

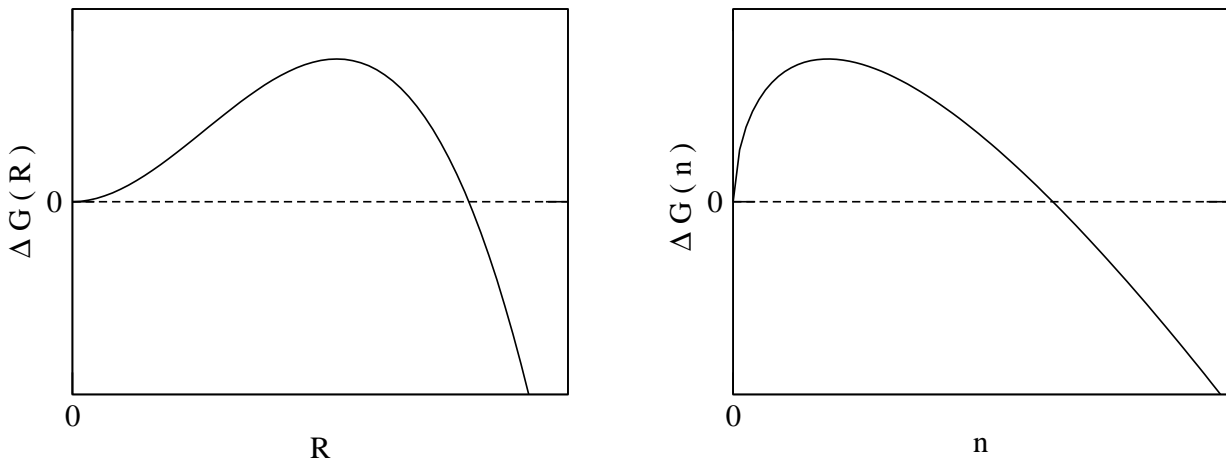


Figure 10.1: Plots of the CNT free energy barrier. The left panel shows the free energy as a function of the radius of the cluster, as in Eq. 10.1. On the right panel is shown the same free energy, but expressed as the number of particles in the nucleus $n = 4\pi R^3 \rho_{sol}/3$ (see Eq. 10.27).

10.2 Method: direct estimate of a rate constant

In the choice of a simulation method to calculate the nucleation rate of diamond from the liquid, we were limited by the computational effort needed to simulate a system size of the order of one thousand particles with the LCBOP⁺. The number of particles is dictated by the size of the critical nucleus, that should not interact with its periodic images. To give a rough idea, an energy evaluation in a Monte-Carlo (MC) move with the LCBOP⁺, is 100 to 1000 times slower than with a Lennard-Jones potential, when the two systems have the same number of particles and number density. We thus looked for a method to determine the rate constant, that required the minimum amount of computational effort. Recently, a method that served as a good starting point for our purposes has been proposed. This is known as Forward Flux Sampling [234] and has been designed to efficiently evaluate the rate constant of rare events.

10.2.1 The forward flux sampling algorithm

According to the Forward Flux Sampling method, a system is considered in which transitions can take place between an initial state \mathcal{A} and a final state \mathcal{B} , separated by a free energy barrier. Two regions of the phase space are identified as surrounded by the dividing hyper-surfaces $I_{\mathcal{A}}$ and $I_{\mathcal{B}}$, and assigned to the two states. The phase space is then partitioned by means of non intersecting interfaces. Here we assume that the transition can be described by only one coordinate* λ , so that the set of dividing interfaces, labelled $\{I_{\mathcal{A}}, I_1, \dots, I_n, I_{\mathcal{B}}\}$, is defined by the values assumed by λ : $\{\lambda_{\mathcal{A}}, \lambda_1, \dots, \lambda_n, \lambda_{\mathcal{B}}\}$. The coordinate λ is also referred to as ‘order parameter’, in the sense that it *orders* the state points along an oriented line. If an ensemble of trajectories starting from state \mathcal{A} is generated,

*The coordinate λ is a (scalar) function of the coordinates of all the particles in the system. In a system of N particles, λ is a function of $6N$ coordinates, $3N$ if one restricts to the configurational space (e.g. when dealing with a MC sampling, as in our case). The interfaces are indeed hyper-surfaces in the $6N$ (or $3N$) dimensional phase-space, and are constituted by all the points sharing a certain value of λ .

the rate constant $R_{\mathcal{A}\rightarrow\mathcal{B}}$ of the (forward) transition, from state \mathcal{A} to state \mathcal{B} reads:

$$R_{\mathcal{A}\rightarrow\mathcal{B}} \doteq \frac{\langle \phi_{\mathcal{A}}(I_{\mathcal{B}}) \rangle}{\langle h_{\mathcal{A}} \rangle} = \frac{\langle \phi_{\mathcal{A}}(I_{\mathcal{A}}) \rangle}{\langle h_{\mathcal{A}} \rangle} \mathcal{P}(I_{\mathcal{B}}|I_{\mathcal{A}}) \quad (10.4)$$

Here $\langle \dots \rangle$ denotes time average, $\phi_{\mathcal{A}}(I_{\mathcal{B}})$ is the net flux of the trajectories crossing interface $I_{\mathcal{B}}$ and coming from \mathcal{A} (i.e. identified by the characteristic function $h_{\mathcal{A}} = 1$), and $\mathcal{P}(I_{\mathcal{B}}|I_{\mathcal{A}})$ is the probability for a trajectory to cross $I_{\mathcal{A}}$ and then $I_{\mathcal{B}}$, without returning to \mathcal{A}^\dagger . Now we make use of the partitioning of the phase space and split the very low probability $\mathcal{P}(I_{\mathcal{B}}|I_{\mathcal{A}})$ into partial probabilities:

$$\mathcal{P}(I_{\mathcal{B}}|I_{\mathcal{A}}) = \mathcal{P}(I_1|I_{\mathcal{A}}) \left[\prod_{i=1}^{n-1} \mathcal{P}(I_{i+1}|I_i) \right] \mathcal{P}(I_{\mathcal{B}}|I_n) \quad (10.5)$$

The above expression is exact only when the partial probabilities are uncorrelated. The rare trajectories going from \mathcal{A} to \mathcal{B} are efficiently generated in a ratchet-like way. This means that a simulation is run, starting from state \mathcal{A} ; all the configurations crossing interface $I_{\mathcal{A}}$ are collected and the flux is estimated as [230]:

$$\frac{\langle \phi_{\mathcal{A}}(I_{\mathcal{A}}) \rangle}{\langle h_{\mathcal{A}} \rangle} = \frac{N^+}{V N_{MD} \tau_{MD}} \quad (10.6)$$

where N^+ is the number of positive crossings of $I_{\mathcal{A}}$, V is the volume of the sample, N_{MD} is the number of time-steps in a molecular dynamics (MD) simulation with time-step τ_{MD} for the integration of the equations of motion. Subsequently, M_i trial runs are generated for each interface I_i . In each trial run, a configuration from the collection at I_i is chosen at random and used to start a run, which is continued until the system crosses either I_{i+1} or $I_{\mathcal{A}}$. A counter N_{i+1} is updated for every crossing of I_{i+1} and the crossing configuration is stored. After the M_i trials, an estimate for the probability $\mathcal{P}(I_{i+1}|I_i)$ is N_{i+1}/M_i . The procedure is iterated until the state \mathcal{B} is reached (or all the trial trajectories has returned to \mathcal{A})[‡].

10.2.2 The parallel optimized FFS

Working on the nucleation in a ionic system, Valeriani *et al.* [236, 237] developed an improvement of the FFS method, in order to make it suitable for large scale computations on parallel machines. We further elaborated the method to efficiently apply it to our LCBOPI⁺

[†]In this review of the method, there is a slight difference if compared to the original formulation [234]: there the rate is expressed as the product of the flux crossing I_1 and the probability to go from I_1 to $I_{\mathcal{B}}$. $I_{\mathcal{A}}$ is used only to define the initial state: whenever this interface is crossed downwards, the system is defined to be returned to state \mathcal{A} . We have made this slight change to approach our method, that will be introduced from section 10.2.2 on, where the state \mathcal{A} is defined statistically, in a rather elegant manner.

[‡]FFS was not the first method that postulated a set of interfaces. This was previously done by the method known as Transition Interface Sampling (TIS [235, 230]). FFS and TIS are two methods sharing a similar spirit: Eqs. 10.4, 10.5, and 10.6 are the basis also for TIS. In the TIS method, the algorithm, robust but more computationally expensive if compared to FFS, follows trajectories started at interface I_i until they cross either I_{i-1} or I_{i+1} . This procedure permits to state that the distribution of phase space points at the interfaces is equal to the stationary distribution of states. In contrast to FFS, this powerful feature allows a sharp analysis of the mechanism of the transition.

interacting system. We used MC rather than MD. Also in our case, the nucleation rate is written as in Eq. 10.4, where time averages are substituted by ensemble averages. At the initial stage a simulation is run starting from \mathcal{A} and configurations crossing $I_{\mathcal{A}}$ are collected. When a MD code for the interacting potential is available, the preliminary run can be a MD simulation and the flux is computed via Eq. 10.6. In case only a MC code is available, a different expression for the flux has to be used, as explained in section 10.3.6.

Exploiting the pseudo-randomness of the MC trajectories, we run, for each collected configuration, a certain number $M_{\mathcal{A}}$ of trials, where trials differ in the seed for the series of pseudo-random numbers used. Configurations crossing I_1 are then collected and the process is iterated until $I_{\mathcal{B}}$ is reached. At each step, trajectories starting from I_i are followed until they either cross I_{i+1} or go back to the state \mathcal{A} . The procedure to decide whether the trajectory has returned to state \mathcal{A} will be explained in the next paragraph. If N_i is the number of configurations arrived at I_i , an estimate for the probability $\mathcal{P}(I_{i+1}|I_i)$ is $N_{i+1}/(M_{\mathcal{A}} N_i)$. In fact the denominator is the total number of attempted trajectories starting from I_i , while the numerator is the number of ‘winning’ events.

10.2.3 Definition of state \mathcal{A}

Valeriani *et al.* [237] proposed a very elegant test to establish whether the trajectory is returned to state \mathcal{A} . During the initial, unbiased simulation started from state \mathcal{A} , the histogram of the distribution of the order parameter λ is collected. From the distribution, the cumulative function $\mathcal{X}(x) = \mathcal{P}(\lambda \leq x)$ is constructed. The interface $I_{\mathcal{A}}$ is set at a value $\lambda_{\mathcal{A}}$ at which \mathcal{X} is equal to a preset value \mathcal{X}_{Th} , typically close to 1. Whenever in a trial run the system is found at a state point associated to a $\lambda \leq \lambda_{\mathcal{A}}$, a random number x_{rnd} is extracted. If $x_{\text{rnd}} > \mathcal{X}(\lambda)$, the system is defined to be returned to state \mathcal{A} and the trial run is stopped.

10.2.4 Parallelization and derived constraints

In our implementation, we employ a parallel algorithm. Once a given interface I_i is reached, each configuration is loaded onto a different CPU and run, in principle, $M_{\mathcal{A}}$ times. In this straightforward implementation the number of needed CPUs is equal to N_i , the number of ‘winning’ trajectories (i.e. trajectories collected at I_i). Since typically the number of available processors n_{CPU} is limited and N_i is not predictable, we proceed in the following way: out of the N_i configurations crossing I_i , we randomly select a fixed number of configurations, equal to n_{CPU} . In case $N_i < n_{\text{CPU}}$ the new n_{CPU} can be reduced to N_i , or a lower λ_i for I_i can be set (this last adjustment can be done without wasting computational time, as explained in paragraph 10.2.5). Furthermore, the length of each trial is impossible to predict, so that the total (real) time needed to perform $M_{\mathcal{A}}$ trials can vary by orders of magnitude. Yet, the total time a CPU can be used is typically set at the beginning of the simulation. This is not a problem, since all the trials are independent; we count in the denominator of the partial probability $\mathcal{P}(I_{i+1}|I_i)$ only the number of ended (i.e. crossing the next interface or going back to state \mathcal{A}) trials. In summary, at every interface, the partial probability is calculated as: $\mathcal{P}(I_{i+1}|I_i) = N_{i+1}/N_i^T$, where N_i^T is the number of ended trials starting from I_i , and both the numerator and the denominator of the probability are known afterwards, in a time constrained simulation.

10.2.5 Setting the interfaces

Interface $I_{\mathcal{A}}$ is set as explained in paragraph 10.2.3. Any other interface I_i can be set dynamically *after* the trial runs from I_{i-1} . The trials are run fixing an attempted \tilde{I}_i , but all the configurations with $\lambda > \lambda_i$ are collected with their λ value. At the end of all the trial runs, if the number of stored configuration N_i is not satisfactory (e.g. $N_i \ll n_{\text{CPU}}$), the interface λ_i can be set back to that λ_i^* at which N_i^* is satisfactory.

10.2.6 A comment on correlations among trajectories

Configurations collected at $I_{\mathcal{A}}$ are all independent. After crossing $I_{\mathcal{A}}$, the system has to return to state \mathcal{A} , in the statistical sense defined in paragraph 10.2.3, before a new crossing updates N^+ in Eq. 10.6 and the new configuration corresponding to that crossing is stored. From the collection of configurations at $I_{\mathcal{A}}$, independent sets can be grouped. When configurations are randomly selected among the set collected at an interface I_i (see paragraph 10.2.4), the configurations in the set after the selection are correlated by the selection procedure itself. This means that any set of configurations initially selected at $I_{\mathcal{A}}$ gives an overall estimate for the nucleation rate, according to Eq. 10.4, once $I_{\mathcal{B}}$ is reached. Statistics is improved by selecting another set at $I_{\mathcal{A}}$ and repeating the procedure to reach $I_{\mathcal{B}}$. The new estimate is independent from the previous; thus, quantities can be averaged and error bars are correctly calculated considering the quantities as independent. It would be wrong to compute the nucleation rate for any single configuration starting at $I_{\mathcal{A}}$ and averaging over all these initial configurations; this is because the overall probability of reaching $I_{\mathcal{B}}$, for a given initial configuration at $I_{\mathcal{A}}$, depends also on whether configurations, generated by this initial one and crossing any subsequent interface, are randomly selected, or not, to proceed to the next interface.

10.3 The setup for the diamond nucleation

10.3.1 The phase diagram

In Fig. 10.2 we show the same phase diagram we obtained from our free energy calculations (chapter 8), where the solid diamonds mark three state points at 20% undercooling that we selected for the nucleation procedure. The point ‘A’ at $P = 85$ GPa and at $T = 5000$ K is located in the region of the (metastable) “diamond-like” liquid (see section 9.3). The liquid has strong local diamond-like structure and is slowly diffusing (at least one order of magnitude slower than a mainly three-fold liquid at the same temperature). The point ‘(B)’, at $P = 30$ GPa and $T = 4000$ K, was chosen in the mainly three-fold region of the (metastable) liquid, but still far from the stable graphite domain. Point ‘(B)’ was chosen to investigate the possibility that in small clusters diamond- and graphite-like structures are competing. These two lattices are more similar than one would expect: as shown in Ref. [156], there is a simple path to transform graphite into diamond. Looking at Fig. 10.3:

1. starting from graphite, the interplanar distance, used as constraint, is decreased and the structure made relax;
2. graphite planes buckle so that the three bonds per particle at $\pi/3$ close out of plane and atoms move alternatively above and below the plane;

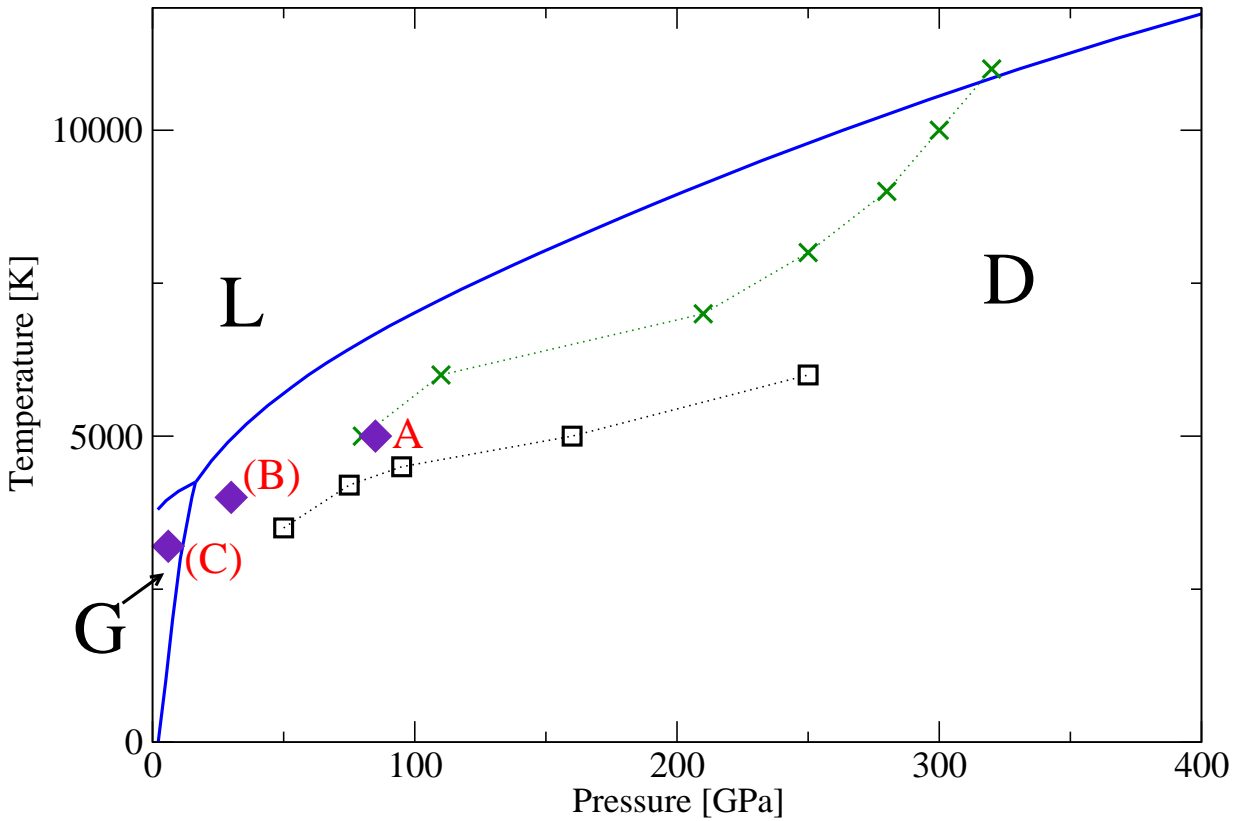


Figure 10.2: Phase diagram for carbon calculated with the $LCBOPI^+$ with the selected state points ('A', 'B', and 'C') for the nucleation process. The three points are at 20% undercooling. Point 'A' is at 85 GPa and 5000 K, point 'B' is at 30 GPa and 4000 K, and point 'C' is at 6 GPa and 3200 K. The letters 'L', 'G', and 'D' indicate liquid, graphite and diamond region of stability. Phase boundaries are the thick lines. The crosses are state point with equal fraction of three- and four-fold coordinated atoms; the squares indicate freezing upon quenching into an amorphous for 216 particles samples (see section 8.2 for discussion).

3. a fourth bond per atom is formed between approached layers, in order to give a perfect diamond lattice.

This is exactly the path followed to calculate the graphite to diamond energy barrier in section 11.3.3. In the bulk phases at 0 K the energy barrier between the two lattices is quite high (~ 0.4 eV per atom)[§], but, in a liquid at a temperature of several thousand kelvins, small clusters could be allowed to oscillate between the two structures.

The point 'C', at $P = 6$ GPa and $T = 3200$ K is in the region of stable graphite. Point 'C' was chosen aiming to see whether it is still possible to nucleate diamond in the region where graphite is more stable.

Results concerning the diamond nucleation in point 'A' are presented in this chapter, while the investigation of points 'B' and 'C' is left for future work. Nonetheless, in the next paragraph, we discuss the definition of 'solidicity' also in these latter points; we found

[§]And luckily the energy barrier is so high, otherwise diamond would easily convert into the more stable graphite, at room conditions!

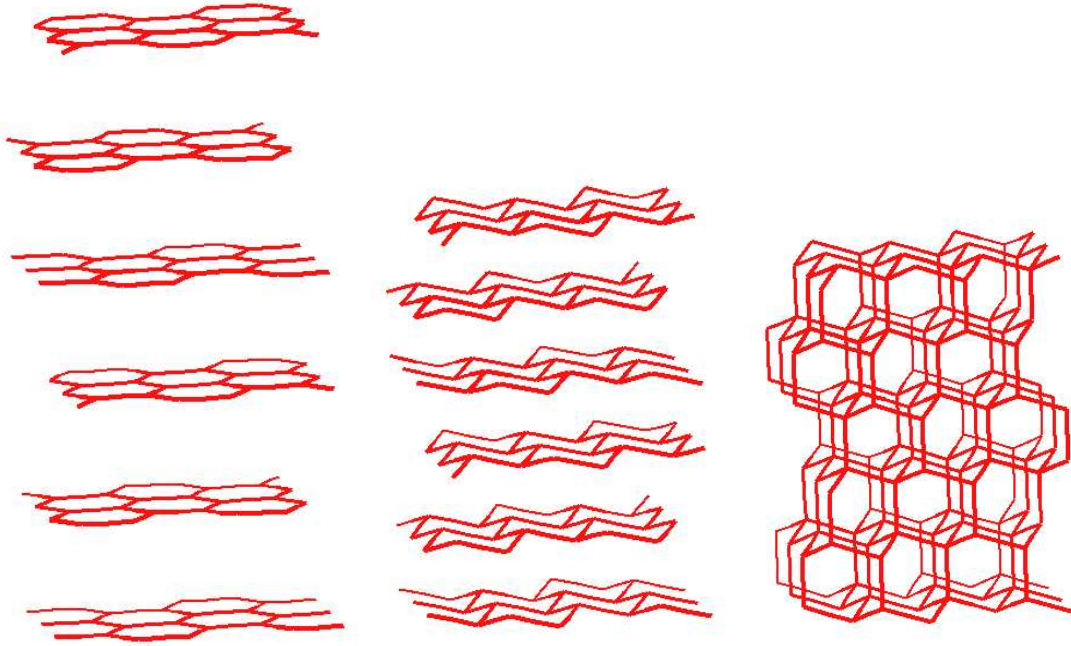


Figure 10.3: A possible path from graphite to diamond. The structure is relaxed via the LCBOPI⁺, with the constraint of the interplanar distance.

indeed that the definition of ‘solidicity’ has to be differently tuned, depending on whether the liquid is mainly three-fold, as is the case of points ‘(B)’ and ‘(C)’, or ‘diamond-like’, as in point ‘A’. To test the ‘solidicity’ algorithm, also points ‘(B)’ and ‘(C)’ were sampled until clusters of few tens of atom were identified.

10.3.2 Identification of the ‘solid’ cluster

To automatically select atoms that are part of a solid cluster, we started from the method developed by ten Wolde [228]. We introduced two modifications: we adopted overall a smooth definition of ‘first neighbour’ in the spirit of BOPs[¶]. More importantly, we had to deal with a liquid that is ‘not too different’, as concerning the local order, from the solid(s) into which it nucleates. This characteristic of liquid carbon asked for a strict definition of ‘solidicity’ of a particle.

We denote with \mathbf{r}_i and \mathbf{r}_j the positions of particle i and j , respectively; we denote with \mathbf{r}_{ij} the difference vector $\mathbf{r}_i - \mathbf{r}_j$, with r_{ij} its modulus $|\mathbf{r}_i - \mathbf{r}_j|$, with $\hat{\mathbf{r}}_{ij}$ the unit vector in the direction of \mathbf{r}_{ij} ($\hat{\mathbf{r}}_{ij} \doteq \mathbf{r}_{ij}/r_{ij}$).

For each atom i is defined a local (angular) order detector^{||}, as the average of the spherical

[¶]A similar concept was introduced in its MD simulations also by ten Wolde in order to avoid impulsive forces; here the smoothing is naturally following from the BOP framework.

^{||}Here we wish to make a clear distinction between an ‘order parameter’ and a ‘local order detector’, this latter usually referred to as ‘bond order parameter’ in literature. An ‘order parameter’, such as the biggest cluster size in this chapter, orders (or, better, projects) the phase space along a one dimensional axis. A ‘local order detector’ maps into a mathematical object the environment of an atom, in order to give a numerical information on the rather fuzzy concept of ‘order’ surrounding an atom. Furthermore, in this work (see e.g. chapter 6) we used ‘bond order’ with the completely different meaning of strength of a given bond, depending on the environment. We thus think that the old term of ‘bond order parameter’

harmonics $Y_{lm}(\hat{\mathbf{r}}_{ij})$ on all its neighbours j .

$$q_{lm}(i) \doteq \frac{1}{Z_i} \sum_{j \neq i} S_{p=3}^{\text{down}}(r_{ij}) Y_{lm}(\hat{\mathbf{r}}_{ij}) \quad (10.7)$$

where the sum extends over all the atoms (other than i); the smooth cut off function $S_{p=3}^{\text{down}}(r_{ij})$ is defined in Eq. 6.53, and the fractional number of neighbours Z_i is: $Z_i = \sum_{j \neq i} S_{p=3}^{\text{down}}(r_{ij})$. The components of the local order detector $q_{lm}(i)$ depend on the orientation of the reference frame. A rotational invariant form is:

$$q_l(i) \doteq \left(\frac{4\pi}{2l+1} \sum_{m=-l}^l q_{lm}^*(i) q_{lm}(i) \right)^{1/2} \quad (10.8)$$

where the $*$ denotes complex conjugate.

The quantity $q_l(i)$ has a definite value, at a given channel l and for a given crystalline structure [238]. For example $q_6(i)$ was used [238, 228, 230] to identify fcc and bcc structures in the liquid, while $q_4(i)$ was used [236] to help recognizing sc structures. In the original formulation [238], an even value of l was suggested since the definition of q_{lm} should be invariant upon inversion of the coordinates: this assumption is motivated by the fact that a bond does not change upon such an inversion. Spherical harmonics with even values of l are indeed symmetrical upon inversion, while they are anti-symmetrical when l is odd. We note that fcc, bcc, and sc structures are indeed inversion invariant structures. If one constructs an odd-valued $q_l(i)$, this would be identically null for this structures. Diamond and graphite lattices are different. In Fig. 10.4, we represent a portion of a graphite sheet. The three neighbours of the center atom see a local environment (represented by the bonds) that is obtained from the coordinate inversion of the local environment of the reference site (dashed bonds of the center atom). In other words, in shifting from one lattice site to any neighbouring one, the coordinates have to be inverted with respect to the starting lattice site, in order to reproduce the same environment. Note that the three neighbours of the reference site are all identical, i.e. one can translate from one to the other without changing the environment that is seen. The same holds in the diamond lattice with the four neighbours of a reference site, albeit it is much more difficult to display it on paper.

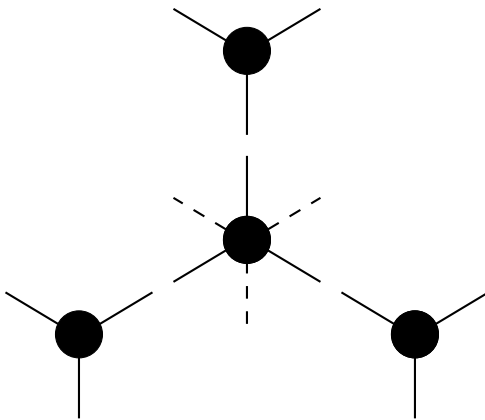


Figure 10.4: Schematic view of the graphite lattice. The three bonds of the lattice sites (circles) are represented by solid lines. The dashed lines from the center site are an inversion with respect to the site of its three bonds.

We looked for a local order detector that could recognize antisymmetrical structures. We found that the smallest odd l that gave non-zero value for the tetrahedral arrangement should be avoided, since rather confusing.

of diamond, $l = 3$, was the perfect local order detector for *both graphite and diamond lattices*. We show in Fig. 10.5 the distributions of $q_3(i)$ at 30 (left panel) and 85 GPa (right panel). The point at 30 GPa refers to the state point ‘(B)’ in Fig. 10.2, but the phases are shown at the melting temperature (5000 K). This is because the liquid at 20% undercooling is expected to have some ‘solid’ particles, while at coexistence ‘solid’ particles appear very rarely. Thus, the calibration of the local order detector has to be done where ‘solid’ particles in the liquid are not expected. In contrast, all the phases shown at 85 GPa are exactly in state point ‘A’. This is needed since, at the melting temperature at 85 GPa, the liquid has completely different features as compared to the 20% undercooled liquid at the same pressure. In fact (see Fig. 10.2), the diamond-like liquid is found only below a certain undercooling, at 85 GPa. In this case, we tuned the local order detector keeping in mind that some ‘solid’ particles *are* present at that undercooling. In the left panel both graphite and diamond are shown, together with the liquid, while in the right panel only the diamond is shown with the liquid, since, at the pressure of 85 GPa, graphite is mechanically unstable in a simulation. One can see that $q_3(i)$ is not sufficient to unambiguously distinguish between particles in the liquid and belonging to a lattice (equilibrated in a certain state point). Furthermore, we put as a comparison the distribution of $q_3(i)$ as given by a random orientation of four and three hard spheres around a reference hard sphere**; it is evident that liquid carbon has a strong angular ordering, due to covalent interactions.

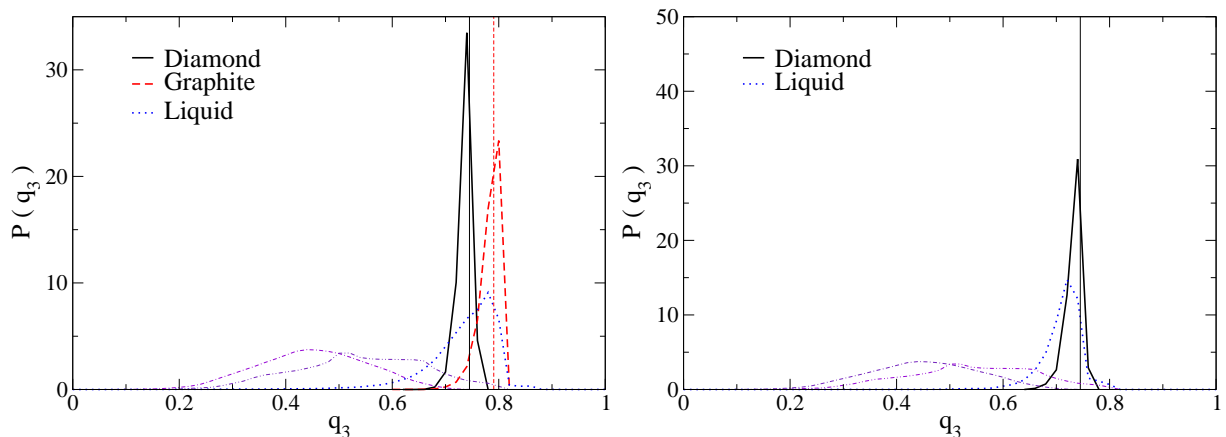


Figure 10.5: Distribution of $q_3(i)$, i.e. the scalar invariant of the local order detector, at 30 GPa (left panel) and 85 GPa (right panel). Solid lines are for diamond, dashed lines are for graphite, dotted line for the liquid. The ‘- · -’ lines and the ‘- -’ lines are for, respectively, three and four hard spheres, randomly distributed on the surface of a (bigger) sphere (see text). The vertical lines are the ideal value for the diamond (solid line, $q_3(i) = 0.745$) and graphite (dashed line, $q_3(i) = 0.791$). All the phases at 30 GPa are at the melting temperature (5000 K), while all the phases at 85 GPa are at 5000 K, i.e. the liquid is 20% undercooled.

To distinguish solid particles in the liquid we have to resort to the full information contained in $q_{3m}(i)$. The above described property of antisymmetry in diamond and

**The ratio between the distance between the centers of the hard spheres and their diameters was chosen 1.4, i.e. the ratio between the typical distance and the closest approach distance between carbon atoms in the liquid, as given by the radial distribution function in the typical liquid.

graphite lattices reflects in $q_{3m}(i)$ in this way: two neighbours in both lattices have the same absolute value of the $2l + 1$ components of $q_{3m}(i)$, but inverted signs. We define a normalized local order parameter as $\hat{q}_{lm}(i)$:

$$\hat{q}_{lm}(i) \doteq \frac{q_{lm}(i)}{\left(\sum_{m=-l}^l q_{lm}^*(i)q_{lm}(i)\right)^{1/2}} \quad (10.9)$$

For atoms that give a small (i.e. smaller than a chosen threshold) denominator in the above equation, all the components of $\hat{q}_{lm}(i)$ are put to zero, in order to avoid numerical instabilities. We then define a quantity which has the form of a inner product between the $\hat{q}_{3m}(i)$ referred to any two neighbours:

$$d_l(i,j) \doteq \sum_{m=-l}^l S_{p=3}^{down}(r_{ij}) \hat{q}_{lm}(i) \hat{q}_{lm}^*(j) \quad (10.10)$$

It is easily proved that $d_l(i,j)$ is a well defined real scalar, invariant upon exchange of the indexes. For ideal graphite and diamond lattice the $d_3(i,j)$ is identically -1 .

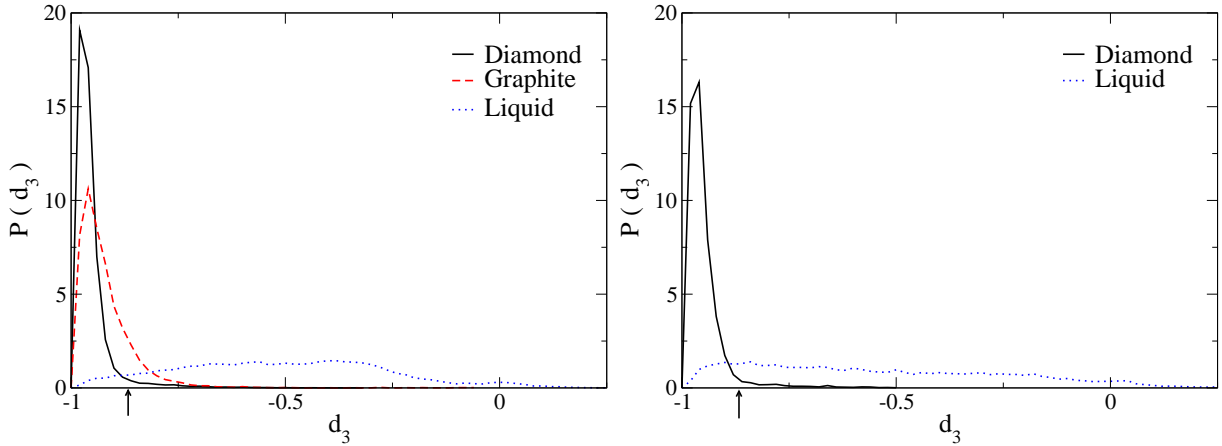


Figure 10.6: Distribution of $d_3(i,j)$, i.e. the inner product of the local order detectors for any pair of neighbours at 30 GPa (left panel) and 85 GPa (right panel). Solid lines are for diamond, dashed lines are for graphite, dotted lines for the liquid. All the phases at 30 GPa are at the melting temperature (5000 K), while all the phases at 85 GPa are at 5000 K, i.e. the liquid is 20% undercooled. The ideal value of $d_3(i,j)$ for both diamond and graphite is -1 .

In Fig. 10.6 we show the distribution of $d_3(i,j)$ for the same state points as in Fig. 10.5. The separation between liquid and solid is now pronounced. Particles that have a value of $d_3(i,j)$ close to -1 share a similar local structure. They are defined to be *connected*. More precisely, we defined as connected particles for which $d_3(i,j) \leq -0.87$; the choice is motivated by the observation (see Fig. 10.6) that most of the pairs of particles in the solids give a $d_3(i,j)$ smaller than -0.87 . To enhance the separation between solid and liquid particles, one can count the number of such connections [228]: it is intended that solid particles do have a number of connections close, if not equal, to the coordination in their ideal lattices.

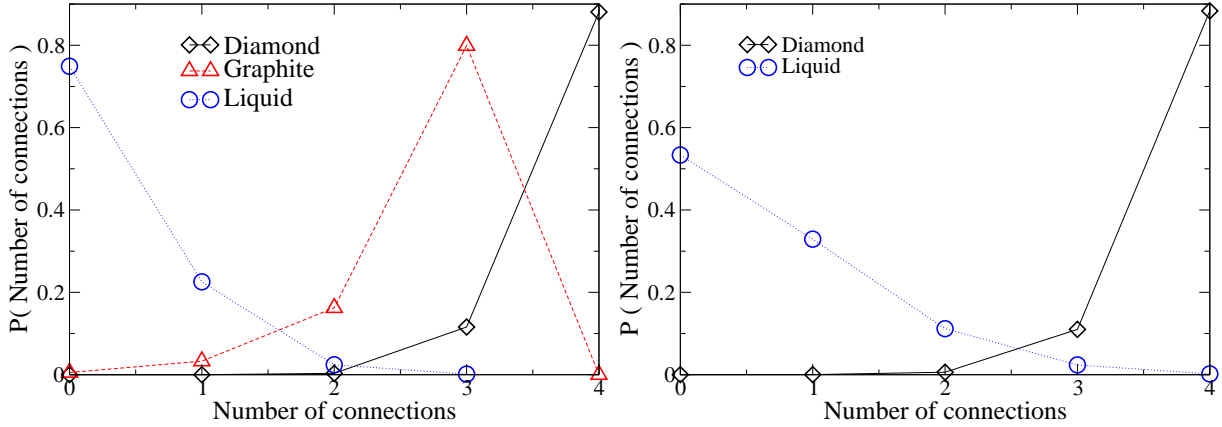


Figure 10.7: Distribution of the number of connections at 30 GPa (left panel) and 85 GPa (right panel). Diamonds connected with solid lines are for diamond, triangles connected with dashed lines are for graphite, circles connected with dotted lines for the liquid. All the phases at 30 GPa are at the melting temperature (5000 K), while all the phases at 85 GPa are at 5000 K, i.e. the liquid is 20% undercooled.

Fig. 10.7 shows an histogram of the number of connections between particles at 30 GPa (left panel) and 85 GPa (right panel). In both panels, diamond has mostly four connections with a small percentage of particles with only three connections. The distribution for graphite (only left panel) is split between three and two connections. The liquid at 30 GPa has mainly zero and one connections, with only a $\sim 3\%$ of particles counting two connections. We chose a *threshold of two connections* for defining ‘solidicity’; we note that only a $\sim 3\%$ of graphite particles would be erroneously counted as liquid (but they can still be counted as ‘surface’, vide infra section 10.3.3). The choice of the threshold for the diamond-like liquid revealed to be much more difficult. In this region we did not expect to have graphite structures, nor did we ever find them. On the other hand, the liquid, mainly four-fold coordinated, was also highly connected (see Fig. 10.7). An attempted threshold for ‘diamondicity’ at three connections led to the growth of branched structures, while the very strict choice of four connections led to no growth at all. Note that the histogram of connections at 85 GPa shows that ‘only’ a $\sim 4\%$ of particles have three connections. We could grow clusters that showed a convincing diamond structure with the following choice. We defined an average *connectivity*, as:

$$D_l(i) = \frac{1}{Z_i} \sum_{j \neq i} S_{p=3}^{\text{down}}(r_{ij}) d_l(i,j) \quad (10.11)$$

Fig. 10.8 shows $D_3(i)$ in state point ‘A’. A threshold of this parameter at -0.87 led to a satisfactory growth. The reason for the success of this last criterion can be found in its average nature. In fact, the satisfactory threshold was found to be the same value that defined one connection via $d_3(i,j)$: this means that ‘diamond’ particles need to have on the average four connections. A threshold of three connections would count as ‘diamond’ a particle that has three well correlated neighbours and a fourth possibly completely uncorrelated. Using $D_3(i)$, all four neighbours need to have some high correlation, even if not all four are asked to be strictly *connected*: this apparently leads to more compact, bulk-like, structures.

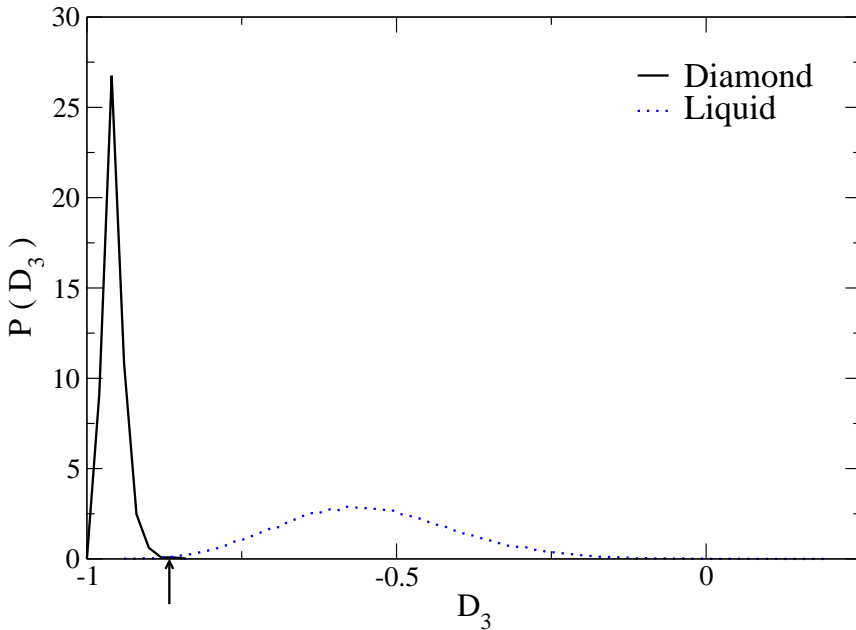


Figure 10.8: Averaged connectivity $D_3(i)$ at 85 GPa. The solid line is for diamond, whereas the dotted line is for the liquid. Both phases are at 5000 K, where the liquid is 20 % undercooled. The ideal value of $D_3(i)$ for the diamond lattice is -1

Once ‘solid’ (or ‘diamond’) particles are defined as satisfying the above criteria, all connected solid particles are counted as belonging to the same cluster.

10.3.3 ‘Surface’ particles

In our definition we had to be rather conservative in the identification of solid particles, due to the small range of connectivity, up to 4. In contrast, in a Lennard-Jones interacting system, the fcc solid has 12 connections [228, 230], while the typical liquid particle has hardly more than five connections. One can be rather generous in defining the threshold for ‘solidicity’ (e.g. 9 in [230] and 7 in [228]). An interesting observation [230] is that particles with at least 12 connections^{††} were found in the ‘interior’ of the clusters, while particles with 8-11 connections were found on the ‘surface’ of the clusters. This led to the idea of defining surface particles as those who are ‘solid’, but counting less than 12 connections. In our case we adopted a different procedure for defining surface particles: ‘surface’ particles were added to the solid particles afterwards, defined as those particles that had *at least one connection to a solid particle*. Algorithmically, one has first to find all the solid particles. Then a second sweep on the liquid particles identifies the ‘surface’ particles. Those ‘surface’ particles were then added to the solid and counted in the cluster size. The reason for adding surface particles is that a certain ordering is certainly present in particles with even only one connection (their $q_{lm}(i)$ has to be similar to that of the connected neighbour). The direct, ‘first-flush’ counting of singly connected particles as ‘solid’, was a-posteriori forbidden by the growth of percolating structures, while their ‘second-flush’ addition always led to meaningful, compact, clusters.

10.3.4 Algorithm for ‘solidicity’ in summary

In short, we give the algorithm to assign particles to a solid cluster in liquid carbon.

^{††}More than 12 connections were probably given by bcc ordered particles.

- The local order detector $q_{3m}(i)$ is calculated for every particle .
- The inner product $d_3(i,j)$ is calculated for every pair of neighbours.
- For the diamond-like liquid: the average connectivity $D_3(i)$ is calculated for each particle; particles for which $D_3(i) \leq -0.87$ are ‘diamond’ particles.
For the mainly three-fold liquid: neighbours for which $d_3(i,j) \leq -0.87$ are *connected*; a connection counter for both particles is incremented by one; particles with at least 2 connections are ‘solid’ particles.
- ‘Solid’ (or ‘diamond’) particles are grouped in clusters: namely connected solid particles belong to the same cluster.
- ‘Liquid’ particles with one connection to a solid particle in a cluster are counted as ‘surface’ of the cluster^{‡‡}. The size of a cluster is the sum of its ‘solid’ and ‘surface’ particles.

10.3.5 Choice of the box size: frozen nuclei analysis

In order to set the size of the simulation box, we estimate the size of the critical nucleus by what we can call the ‘frozen spherical nucleus’ method. To the purpose:

1. we equilibrated, via NPT MC simulations, a sample of 1000 particles in a cubic box, arranged in a diamond lattice, in state points ‘A’ and ‘B’ shown in Fig. 10.2; we only allowed isotropic cell fluctuations, to keep the box shape a cube;
2. particles comprised in a sphere of selected radius around a selected atom, were then fixed to the final position assumed in the equilibration run; the rest of the particles was melted in a NPT simulation at 10000 K and at the pressure of the selected state point;
3. still keeping the particles in the nucleus frozen, the rest of the sample was annealed at the melting temperature corresponding to the pressure of the selected state point;
4. all those samples containing nuclei that never ended in a complete (re)crystallization in the previous step were sampled at the initial state point, with particles in the nucleus released; this was achieved by running at the initial temperature the samples annealed in the previous step [†];
5. several samples were prepared for each selected radius: we considered as critical (spherical) nucleus size R^* , the size at which about half of the nuclei shrank to the liquid and half grew to the full box crystal. Consistently, nuclei smaller than the critical more likely shrank, while bigger nuclei almost always grew.

^{‡‡}In the case of the diamond-like liquid the criterion for a ‘liquid’ particle to be counted as ‘surface’ is: ‘at least one connection’. ‘Surface’ particles can be ascribed to two clusters, but two clusters linked by a ‘surface’ particle that is connected to solid particles in the two clusters are *not* merged into one cluster. These, rare, shared ‘surface’ particles are actually counted as belonging to both clusters.

[†]Samples that did not lead to re-crystallization at the melting temperature, always kept the number of particles in the nucleus equal to the number of the fixed particles, i.e. it never occurred that some particles attached to the nucleus unless this event avalanched towards the crystal.

After estimating in this way R^* , the *minimum* length of the (cubic) box edge for the nucleation procedure was set to $L_{\min} = 2R^* + r_2^{LR}$, where r_2^{LR} (see Eq. 6.53) is the range of the non bonded interactions for the LCBOP⁺. Its value is set to 6 Å (see Table 6.2). This choice prevents, in a box with edge equal to or bigger than L_{\min} , direct interactions between the replica of the nucleus, through the applied periodic boundary conditions. Possible indirect interactions have been neglected at this stage: these can arise from the extension of the ordering outside the surface of the critical nucleus, that we defined rather arbitrarily.

At state point ‘A’, i.e. in the diamond-like region of the metastable liquid, we found that the criticality criterion was matched by nuclei of radius $R^* = 5.8$ Å. Eleven neighbour shells, i.e. 159 particles, are comprised in a sphere of radius $R^* = 5.8$ Å centered on the atom located at the center of mass of the nucleus, in a 0 kelvin lattice at the selected pressure of 85 GPa. The number of fixed atoms after the equilibration procedure (step 1 above) was found indeed to be equal to 160. This R^* yields $L_{\min} = 17.6$ Å. In state point ‘A’, the liquid equilibrates at the specific volume of 5.65 Å³/atom. This implies that the smallest number of particles in the simulation box is 965. Aiming to nucleate diamond, the nucleation box cannot contain any number of particles, but a number that can yield a perfect lattice, given the periodic boundary conditions. Namely, for a cubic diamond lattice, the number of particles N has to be $N = 8n^3$, with n integer, to fit in a cubic box. We chose to perform the nucleation procedure with a sample of 1000 atoms.

At the state point ‘B’ the same procedure gave $R^* = 6.40$ Å, so that the critical cluster contained 191 particles; with a specific volume of 7.37 Å³/atom, this requires at least 902 particles in a cubic box of edge $L_{\min} = 18.8$ Å.

10.3.6 Monte Carlo ‘time-step’

For the LCBOP⁺, only a MC code is available. The rather cumbersome implementation of the force calculation, needed for a MD code, has not yet been carried out. The flux crossing I_A was calculated in a slightly different way, if compared to Eq. 10.6, namely:

$$\frac{\langle \phi_A(I_A) \rangle}{\langle h_A \rangle} = \frac{N^+}{V N_{MC} \tau_{MC}} \quad (10.12)$$

where N_{MC} is the number of MC sweeps[‡]. In order to estimate the MC ‘time-per-sweep’ τ_{MC} , we performed a DF-MD simulation in the same state point we chose for the nucleation process. We assumed that the system as described by the density functional behaves not too differently from the LCBOP⁺. As a justification, we proved that static properties of the LCBOP⁺ liquid, e.g. as described by the radial and angular distribution functions, are in reasonable agreement with DF-MD calculations (see chapter 9). The MC ‘time’ is calculated [239]:

$$\tau_{MC} = \frac{D_{MC}^*}{D_{MD}^*} \quad (10.13)$$

[‡]This quantity is also known as “moves per particle”: in a MC algorithm this means that a sweep is counted once a loop, comprising a number of attempted moves equal to the number of particles in the system, is completed. This does not mean that every particle is attempted to be moved in the sweep, since, for statistical reasons [13], at any attempted move, the particle is selected randomly; It is just in an average sense, that every particle is attempted to be moved each sweep.

where

$$D_{\text{MD}}^* = \lim_{t \rightarrow \infty} \frac{\langle [\mathbf{r}_i(t) - \mathbf{r}_i(t_0)]^2 \rangle_{\text{MD}}}{t} \quad (10.14)$$

is calculated in the MD run and

$$D_{\text{MC}}^* = \lim_{s \rightarrow \infty} \frac{\langle [\mathbf{r}_i(s) - \mathbf{r}_i(s_0)]^2 \rangle_{\text{MC}}}{s} \quad (10.15)$$

is calculated in the MC run. The brackets $\langle \dots \rangle_{\text{MD}}$ denotes time average and average over all particles; $\langle \dots \rangle_{\text{MC}}$ denotes ensemble average and average over all particles. The index s is updated every MC sweep. In a MC simulation, the quantity D_{MC}^* depends on the acceptance ratio, that in turn depends on the maximum displacement of the attempted move. Anyway, the definition of τ_{MC} is not ambiguous as soon as all the MC simulations are performed at constant *acceptance ratio*.

10.4 Results

For the carbon system described by the LCBOP⁺, the state \mathcal{A} is the liquid state (L), while the state \mathcal{B} is diamond (D). The order parameter λ was chosen to be the size of the biggest cluster (NBC), as recognized via the algorithm summarized in paragraph 10.3.4. Fig. 10.9 shows an excerpt of the evolution of the order parameter in an unbiased simulation, started in the liquid state, for a sample with 1000 atoms. The dashed line is NBC_L , i.e. the threshold for NBC , fixed putting the value of $\mathcal{X}_{Th} = 0.997^{\S}$. The threshold NBC_L defines the interface I_L defining the liquid. The arrows in Fig. 10.9 indicate the stored configurations. Note that in correspondence with the first arrow, there is more than one crossing of the NBC_L line. Only the first crossing was counted since the system was not judged to be returned to the liquid (following the procedure of paragraph 10.2.3), before recrossing.

10.4.1 Results at 85 GPa

For the sample of 1000 atoms, we grouped the configurations at I_L into two sets and performed two independent nucleation simulations. Subsequent interfaces were set at: $I_1 = 34$, $I_2 = 42$, $I_3 = 50$, $I_4 = 60$, $I_5 = 70$, $I_6 = 80$, $I_7 = 90$, $I_8 = 110$, $I_9 = 130$. At every interface 40 configurations were randomly selected to be propagated (this means $n_{\text{CPU}} = 40$). The configurations at I_L and at the subsequent interfaces were then used as starting points for the calculation of the free energy barrier (see section 10.5). The nucleation procedure was not followed until the complete crystallization. To have a box completely crystallized, one should have the growing cluster with an orientation close enough to one of the possible orientations compatible with the periodic boundary conditions. In contrast, the growing cluster has a free orientation and it is not likely that its orientation is compatible with the imposed periodic boundary conditions. Furthermore, the simulation time per trial rapidly

^{\S}The cumulative distribution \mathcal{X} was constructed considering the number of times the liquid was sampled; this occurred every 25 MC sweeps, since the determination of the order parameter is a rather expensive calculation. Thus, the liquid was defined as the state in which an unbiased trajectory is found for 997 out 1000 inspections.

increased: for clusters around size 100, the system could wander for a long time[¶] before either crossing the next interface or going back to the liquid. In fact, huge fluctuations in the cluster size were always observed: in a typical ‘winning’ trial, the cluster size decreased of several tens of atoms, before a sudden increase led the cluster crossing the next interface. This can be interpreted by arguing that the liquid surrounding the cluster is always rather ordered, so that the growing of the cluster is triggered by a sort of collective fitting into the diamond lattice of several particles, rather than by a one-to-one attachment. We stopped the nucleation procedure when the probability $\mathcal{P}(I_{i+1}|I_i)$ was larger than 1/2, assuming that the top of the nucleation barrier was reached and possibly overcome. This occurred in the 1000 particles sample on going from I_8 to I_9 , i.e. from size 110 to 130. Rather than the nucleation rate, we thus calculated the rate at which the top of the nucleation barrier is reached. This is an upper boundary for the real nucleation rate. We calculated the flux: $\Phi_L(I_L) = (4.2 \pm 0.2) 10^{-9} \text{ \AA}^{-3} \tau_{MC}^{-1}$. The conversion to the real time was (see Eq. 10.13): $\tau_{MC} = (9.0 10^{-6})/(2.2 10^{-4}) \text{ fs} = 0.04 \text{ fs}$ ^{||}. The crossing probability was: $\mathcal{P}(I_9|I_L) = (3.5 \pm 2.1) 10^{-5}$. In conclusion the 1000 particles sample gives a rate: $R = (3.7 \pm 2.5) 10^{-12} \text{ \AA}^{-3} \text{ fs}^{-1} = (3.7 \pm 2.5) 10^{33} \text{ m}^{-3} \text{ s}^{-1}$.

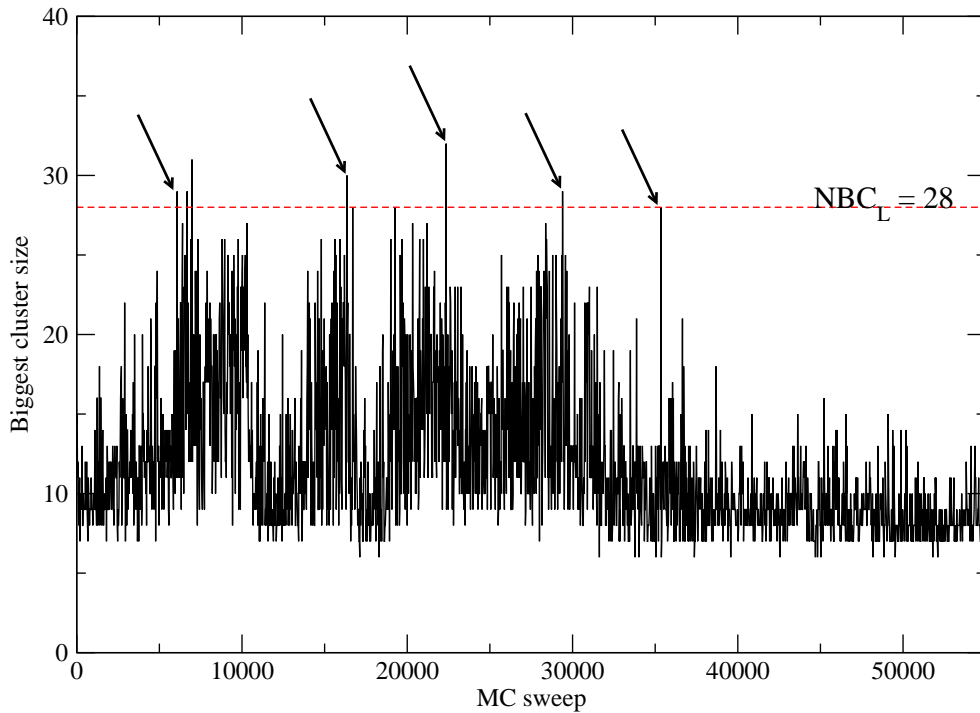


Figure 10.9: Evolution of the order parameter NBC in an unbiased simulation of a 1000 particles liquid. The dashed line is the NBC_L at the interface defining the liquid state. The arrows indicate stored configurations.

The nucleation procedure was stopped when a nucleus of size 130 was obtained. We checked the results obtained with 1000 particles with a sample containing 2744 particles. Here one we will refer to the 2744 particles sample as the ‘‘big sample’’ and to the 1000

[¶]To give a representative figure: from I_8 to I_9 we had ~ 12 hours *per trial* on a 3.4 GHz Intel® Xeon™.

^{||}The parameter D_{MD}^* was calculated from a 5 ps DF-MD run of 128 atoms at the same temperature and *density* of the LCBOP⁺ system.

particle one as the “small sample”. Note that in the big sample, at the same density as in the small sample, the biggest non directly self interacting spherical cluster counts 575 particles. The computational cost per MC sweep, needed to evaluate the bonded interactions with the LCBOP⁺ (as well as with any BOP), scales linearly with the number of particles in the system, since this cost depends on the average number of neighbours, when a dynamic list of them is book-kept. On the other hand, for the non-bonded interactions, an evaluation of the distance, in case the distance is shorter than a given cut-off, of the interactions between the trial-moved particle and all the other particles has to be performed every trial move. Thus, the computational cost per sweep scales quadratically with the system size, for samples that are not too big. We observed that the cost per sweep in the big sample was ~ 6 -7 times higher than with the small sample. Typically, the trial runs from one interface to the next were run for the same (real) time interval as for the small sample. This means that we had on the average 6-7 times less trial runs per configuration to deal with. We grouped the configurations at I_L into three sets. From each interface, 12 configurations (i.e. $n_{\text{CPU}} = 12$) per set were run. We used the same definition of I_L as for the small sample as well as all the interfaces up to I_9 . For the big sample, the flux at I_L is: $\Phi_L(I_L) = (7.7 \pm 0.8) 10^{-9} \text{ \AA}^{-3} \tau_{\text{MC}}^{-1}$. With the big sample, we found that the criterion “ $\mathcal{P}(I_{i+1}|I_i) > 1/2$ ” to define the top of the barrier was matched at an upward shifted NBC , if compared to the small sample. Two more interfaces were set, I_{10} and I_{11} , defined at the cluster sizes: $NBC_{10} = 150$ and $NBC_{11} = 175$. Two sets of initial configurations fulfilled the criterion at I_{11} and one set at I_{10} . We inspected the trials for the two sets yielding I_{11} fulfilling the criterion and we found that in both cases the partial probability to cross an interface at I^* at $NBC = 160$, coming from I_{10} , was bigger than $1/2$ too. We evaluated also for the third set $\mathcal{P}(I^*|I_{10})$, so that the average overall probability is: $\mathcal{P}(I^*|I_L) = (2.8 \pm 2.7) 10^{-5}$. The rate is: $R = (5.4 \pm 5.3) 10^{-12} \text{ \AA}^{-3} \text{ fs}^{-1} = (5.4 \pm 5.3) 10^{33} \text{ m}^{-3} \text{ s}^{-1}$. In the big sample case, as well as in the small sample one, we had indication that the transmission probability to interfaces beyond the ones we stopped keeps bigger than $1/2$ and increasing. However, the computational time per trial becomes there unpracticably long, so that only few trials could be completed and the statistics is very poor, implying that the results should be interpreted with care.

The big sample confirms at least the order of magnitude of the rate at which the top of the barrier is reached. The nucleation rate at that state point cannot be more than one order of magnitude lower, since, beyond the top of the barrier, the nucleation should proceed rather fast, due to its nature of activated process. If we compare our rate to the *nucleation* rate of order $10^{30} \text{ m}^{-3} \text{ s}^{-1}$, found at the same undercooling for the liquid argon, described by the Lennard Jones potential [240, 228], we see that the diamond-like carbon would nucleate (practically instantaneously in an ideal experiment) at a rate approximatively two orders of magnitude higher. Employing essentially the same method we used for diamond nucleation, Valeriani *et al.* [236] found a nucleation rate of order $10^{24} \text{ m}^{-3} \text{ s}^{-1}$ for NaCl described by the Fumi-Tosi potential. Thus, compared to carbon, NaCl nucleates into the crystal with a dramatically slower rate.

In Fig. 10.10 we show a cluster of size $NBC = 177$ (thus, one of the configurations that crossed I_{11}). In the top part of the figure, ‘diamond’ and ‘surface’ particles belonging to the biggest cluster in the sample are highlighted, while ‘liquid’ particles (together with ‘solid’ and ‘surface’ particles belonging to smaller clusters) were made smaller in size and shown to account for the size of the simulation box. In the bottom part the same cluster, without

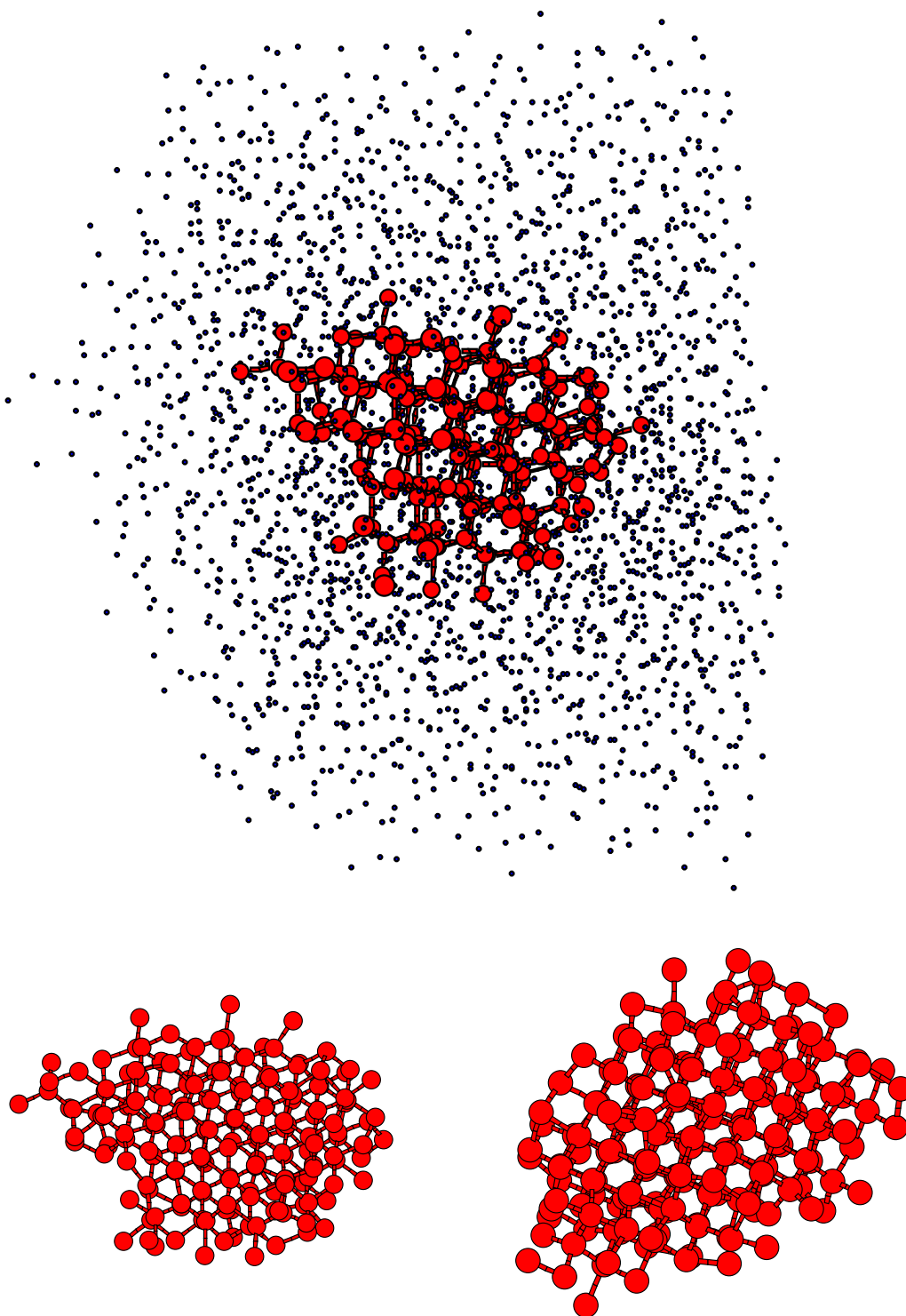


Figure 10.10: Three views of a cluster of size $NBC = 177$. In the top panel the atoms in the liquid are represented with spheres of smaller diameter than for the atoms in the cluster. In both the bottom panels the cluster is rotated by 90 degrees, with respect to the top panel.

the surrounding particles, is shown from other points of view. The diamond structure, with few defects, is evident from this snapshot.

10.5 Calculation of the free energy barrier via umbrella sampling

In addition to the nucleation procedure, we calculate the nucleation barrier in state point ‘A’ (see Fig. 10.2), for the small sample. In appendix 10.7 we show that the difference in free energy from a reference state (in our case the metastable liquid) can be written as a function of the biggest cluster size NBC , used as order parameter:

$$\Delta G = -\ln \frac{NBC}{N} \quad (10.16)$$

However, considering only the biggest cluster is an approximation that holds only for big, rare, clusters. In a simulation in the liquid state, clusters are normally small, ranging from size 5 (in the diamond-like liquid, 5 is the minimum size that can be defined for a cluster) to 35 (the biggest cluster seen in the simulation used for the free energy calculation). After equilibrating a liquid of 1000 particles at the state point ‘A’, we calculated the distribution of all clusters and determined the related free energy with Eq. 10.16. The result is shown in Fig. 10.11, up to the arrow. The point at size zero accounts for those rare configurations in which no cluster of any size was detected. Thus, in Fig. 10.11, we note that the reference status (the ‘normal’ liquid) most likely contains one or more cluster of size 5.

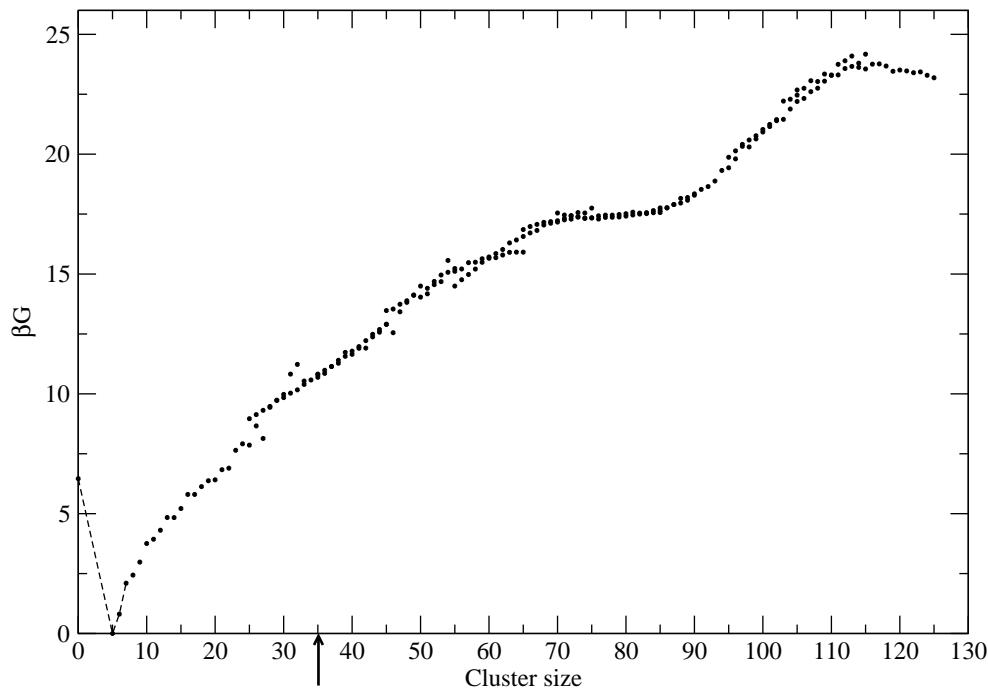


Figure 10.11: Gibbs free energy for the formation of a solid cluster of a given size. The points at small cluster sizes are connected to guide the eye. The arrow indicates the size of the biggest cluster histogrammed during the unbiased simulation.

In order to sample the distribution of clusters bigger than ~ 35 , we employed the method of the umbrella sampling. The umbrella sampling scheme was proposed [241] to handle situations where important contributions to the ensemble average come from configurations whose Boltzmann factor is small, thus leading to poor statistical accuracy (see also paragraph 10.7.2). We constructed overlapping windows of our order parameter, i.e. the biggest cluster size NBC . We used windows presenting hard walls; this means that the umbrella sampling algorithm proceeds in the following way. Every 25 MC sweeps, NBC is evaluated; if NBC is in the window, the present configuration is stored and the simulation continues unperturbed; if NBC is outside the window, the whole trajectory of 25 MC sweeps is rejected and the stored configuration is substituted to the present one. The windows, of width 20, were centered every 10 units, starting from size 40. This implies that two neighbouring windows overlapped by 10 units. Initial configurations were taken from the nucleation procedure (see previous section). Each window was simulated starting from 3 different configurations, for each initial configuration statistics were acquired for 250000 MC sweeps (i.e. we had 10000 entries, times 3, in the histogram, for each window). The distribution given at every window has to be rematched exploiting the overlapping intervals. We imposed that the *areas below the distribution curves of the overlapping interval agreed*. Practically, the data from the first window (up to size 35) are not rescaled, coming from an unbiased simulation; the distribution of the second window (from size 30 to 50) was rescaled to match the first window in the overlapping interval, and so on. The result is shown in Fig. 10.11.

The free energy barrier exhibits a maximum at size 115. Consistently, the nucleation procedure in the small sample revealed that more than one half of the trajectories starting from the interface at size 110 reached the interface at size 130. In the big sample this feature is systematically shifted to a size of 160. Incidentally, the cluster size of 160 corresponds to the ‘critical’ spherical cluster as found in the frozen nucleus analysis. It is therefore possible that the maximum in the free energy at 115 for the small sample is a finite size effect. This is possible, for instance, if indirect interactions between the replicas of the cluster are present. Following this argument, the particles that are “almost solid” would be more than those we count as ‘surface’, so that the cluster size, from a thermodynamical point of view could be sensibly bigger than what we measure.

Regarding the shape of the nucleation barrier, the presence of a shoulder around size 80 should be noted. A rather flat distribution in the window centered at size 80 is present also if each of the initial configurations for the window itself is histogrammed separately. Furthermore, in all the nucleation processes that we sampled, at both sample sizes, we found that the probability to reach the interface at size 90, starting from interface at size 80, was always approximatively double than the neighbouring probabilities, i.e. $70 \rightarrow 80$ and $90 \rightarrow 100^{**}$.

10.6 Summary and conclusions

In summary, in this chapter we illustrated the method and the results for the nucleation of diamond from the 20 % undercooled liquid carbon. Based on the Forward Flux Sampling method [234], we developed an efficient method to calculate the rate of nucleation, and a

^{**}The interface at 100 is not in the set mentioned in section 10.4.1, but it could be fictitiously added a posteriori, from the knowledge of the evolution of the biggest cluster size in every single trial.

method to recognize ‘solid’ (or ‘diamond’) particles in the liquid, based on the local order detector of Refs. [238, 228]. Due to the large computational cost, we could only arrive to a rough estimate of the rate to reach the top of the nucleation barrier for the diamond-like liquid carbon we discussed in chapter 9. We found this rate to be of the order of $10^{33} \text{ m}^{-3} \text{ s}^{-1}$ at 20 % undercooling. This is an enormously fast rate. Having reached the top of the barrier, we argue that the effective nucleation rate at that state point cannot be more than one order of magnitude lower than our estimate. We compared this rate to the value of order $10^{30} \text{ m}^{-3} \text{ s}^{-1}$, as found for liquid argon at the same undercooling [240, 228]; we also compared it to the much smaller rate of order $10^{24} \text{ m}^{-3} \text{ s}^{-1}$, calculated for NaCl with essentially the same method we presented here. In the nucleation procedure, we found that the top of the barrier was reached at the biggest cluster size ~ 115 for a sample of 1000 particles and at size ~ 160 particles for a sample of 2744 particles. The size ~ 160 agrees with the size predicted by a rough estimate made via the ‘frozen nucleus method’. We presented the calculation of the free energy barrier, by means of the umbrella sampling method, for a sample of 1000 particles in the same state point as for the nucleation procedure. The nucleation barrier presented a maximum at size 115. We argue that the discrepancy between the two sample sizes is due to finite size effect, if indirect interactions between periodic replicas of the critical cluster are postulated.

10.7 Appendix. Classical nucleation theory

We give here a selected overview of Classical Nucleation Theory. Namely, we restrict ourselves to a) the model for the calculation of the (free energy) nucleation barrier and b) the justification of the choice of the cluster size as order parameter *à la* Landau^{††} [242].

10.7.1 Free energy barrier

We consider two systems. The first system (I) contains the homogenous, metastable phase β . The second system (II) contains a nucleus of the stable phase α , immersed in the phase β . Given that the systems are at a certain temperature T and pressure P , and that they contain the same number of particles N , we want to compute the Gibbs free energy difference between the two systems. To the purpose, we first consider the difference in total internal energy. Assuming that this latter quantity is a homogeneous first-order function of the entropy S , the volume V , and the number of particle N , for system (I) it holds:

$$U^I = T^I S^I - P^I V^I + \mu^I N^I \quad (10.17)$$

where μ is the chemical potential. In system (II) we assume that the temperature T^{II} is constant throughout the system, but the same homogeneity does not necessarily holds for the chemical potential and the pressure (consider that the interface can sustain a pressure difference at equilibrium between the two phases). The total internal energy in system (II) can thus be written:

$$U^{II} = T^{II} S^{II} - P_\alpha^{II} V_\alpha^{II} - P_\beta^{II} V_\beta^{II} + \mu_\alpha^{II} N_\alpha^{II} + \mu_\beta^{II} N_\beta^{II} + \gamma A \quad (10.18)$$

where A is the area of the interface between phase α and β , and γ is the interfacial free energy density. The total volume of system (II) is $V^{II} = V_\alpha^{II} + V_\beta^{II}$, the total number of particle is $N^{II} = N_\alpha^{II} + N_\beta^{II}$. We can thus rewrite Eq. 10.18 in this form:

$$U^{II} = T^{II} S^{II} - P_\beta^{II} V^{II} + (P_\beta^{II} - P_\alpha^{II}) V_\alpha^{II} + \mu_\beta^{II} N^{II} + (\mu_\alpha^{II} - \mu_\beta^{II}) N_\alpha^{II} + \gamma A \quad (10.19)$$

Since the two systems have the same number of particles, temperature, and pressure (i.e. pressure of the phase β !), we have: $N^I = N^{II} = N$, $P^I = P_\beta^{II} = P$, and $T^I = T^{II} = T$. Moreover, the phase β is at the same thermodynamical state in both systems, so that $\mu^I = \mu_\beta^{II}$. We can now write the difference in Gibbs free energy between system (I) and (II):

$$\begin{aligned} \Delta G &= \Delta U + P\Delta V - T\Delta S = \Delta G^I - \Delta G^{II} = \\ &= (P_\beta^{II} - P_\alpha^{II}) V_\alpha^{II} + (\mu_\alpha^{II} - \mu_\beta^{II}) N_\alpha^{II} + \gamma A \end{aligned} \quad (10.20)$$

Up to here, no approximations have been made. A more useful expression is obtained via the assumptions:

- phase α is incompressible, i.e. $\rho_\alpha \doteq N_\alpha/V_\alpha$ is a constant. From thermodynamics, it holds $\partial G/\partial P|_T = V$, and $G = \mu N$, so that, at constant T, N :

$$d\mu = dP \frac{V}{N} = \frac{dP}{\rho} \quad (10.21)$$

^{††}The résumé of CNT we present here is heavily based on the bright summary that Daniele Moroni gave in appendix G of his PhD thesis [230].

If ρ is constant, we can integrate the latter relation, getting a linear dependence of μ on ρ :

$$\mu_{\alpha}^{II}(P_{\alpha}^{II}) = \mu_{\beta}^{II}(P_{\beta}^{II}) + \frac{P_{\alpha}^{II} - P_{\beta}^{II}}{\rho_{\alpha}} \quad (10.22)$$

Substituting this expression into Eq. 10.20, if we recognize that there $\mu_{\alpha}^{II} = \mu_{\alpha}^{II}(P_{\alpha}^{II})$, and $\mu_{\beta}^{II} = \mu_{\beta}^{II}(P_{\beta}^{II})$:

$$\Delta G = \gamma A + [\mu_{\alpha}^{II}(P_{\alpha}^{II}) - \mu_{\beta}^{II}(P_{\beta}^{II})] \rho_{\alpha} V_{\alpha}^{II} \quad (10.23)$$

- phase α is characterized by its bulk properties, in particular ρ_{α} is the density of bulk phase α .
- the nucleus is spherical, so that $A = 4\pi R^2$ and $V_{\alpha} = 4\pi R^3/3$, where R is the radius of the nucleus;
- the surface tension is independent of R .

With all these assumptions, Eq. 10.20, through, Eq. 10.23, is rewritten in the form:

$$\Delta G = 4\pi R^2 \gamma + \frac{4}{3} \pi R^3 \rho_{\alpha} \Delta \mu \quad (10.24)$$

where $\Delta \mu = \mu_{\alpha}^{II}(P_{\beta}^{II}) - \mu_{\beta}^{II}(P_{\beta}^{II}) < 0$ is the difference in chemical potential between phase α and β at the same pressure P_{β} . Eq. 10.24 is the same as Eq. 10.1, where α and β were the solid and the liquid phases, respectively. Taking the derivative of ΔG in Eq. 10.24 with respect to R , we get an expression for the critical radius:

$$R^* = \frac{2\gamma}{\rho_{\alpha} |\Delta \mu|} \quad (10.25)$$

that corresponds to a maximum in the free energy difference:

$$\Delta G^* = \frac{16\pi\gamma^3}{3\rho_{\alpha} \Delta \mu^2} \quad (10.26)$$

Finally, we can rewrite Eq. 10.24 as a function of the number of particles n in the nucleus ($n = 4\pi R^3 \rho_{\alpha}/3$):

$$\Delta G = 4\pi\gamma \left(\frac{3n}{4\pi\rho_{\alpha}} \right)^{2/3} + n\Delta\mu \quad (10.27)$$

yielding a critical nucleus of size:

$$n^* = \frac{32\pi\gamma^3}{3\rho_{\alpha}^2 |\Delta\mu|^3} \quad (10.28)$$

10.7.2 Equilibrium cluster distribution

We consider a system at homogeneous temperature T , and label with N_n the number of clusters of size n present at equilibrium. The system consists of N_1 monomers, N_2 dimers, \dots N_n n -mers, in a solvent of N_β particles in phase β . The total number of particles is N and we assume $N_\beta \gg N_n, \forall n$, so that $N \simeq N_\beta$. We rewrite Eq. 10.23 as:

$$\Delta G - \gamma A + n [\mu_\alpha(P) - \mu_\beta(P)] = \mu_n(P) - n\mu_\beta(P) \quad (10.29)$$

where the chemical potential of the cluster is defined as $\mu(P) \doteq \gamma A + n\mu_\alpha(P)$, and P stays for P_β . We consider and treat the system as an ideal solution, since we assume that the concentration of clusters is low enough so that they do not interact with each other. We thus use the equation of state of the ideal gas, substituted into Eq. 10.21, to integrate the chemical potential to a different pressure:

$$\mu_n(P_n) = \mu_n(P) + k_B T \ln(P_n/P) \quad (10.30)$$

where we chose the different pressure to be P_n , i.e. the partial pressure exerted by the cluster of size n .

Substituting into Eq. 10.29, we get:

$$\Delta G = \mu_n(P_n) - k_B T \ln(P_n/P) - n\mu_\beta(P) = -k_B T \ln(P_n/P) \quad (10.31)$$

In the last equality we have made use of the relation $\mu_n(P_n) = n\mu_\beta(P)$, that holds at equilibrium, if a cluster of n particles in phase α substitutes an equal number of particles in phase β . Raoult's law relates the ratio of the partial pressures to the ratio of the concentrations for an ideal solution: $P_n/P = N_n/N_\beta \simeq N_n/N$. We write:

$$\Delta G \simeq -k_B T \ln(N_n/N) \quad (10.32)$$

At this point we remind that, following the Landau definition of free-energy [242], this quantity is written as:

$$G(q) \doteq \text{constant} - \ln(q) \quad (10.33)$$

where q is an order parameter describing the state of the system.

By comparison of Eqs. 10.32 and 10.33, we recognize that the argument of the logarithm in Eq. 10.32 is the probability of having a cluster of size n . Thus:

$$\mathcal{P}(n) \doteq \frac{N_n}{N} = e^{-\beta \Delta G(n)} \quad (10.34)$$

that relates the cluster size distribution to the CNT free energy barrier. Histogramming the cluster size distribution of *all* the cluster in the system, yields ΔG . Unfortunately, in a numerical simulation, only relatively small clusters can be efficiently sampled, since configurations with big clusters are exponentially rare. Special techniques, such as the umbrella sampling method (see section 10.5) are to be used. To our purposes, this technique works biasing the sampled configurational phase space to those configuration containing a biggest cluster of given size. It is thus instructive to show that, when the system contains a cluster of big enough size, the distribution of the biggest cluster size, NBC , is a very good approximation of the distribution of all the cluster sizes. We can in fact write:

$$\mathcal{P}(n) = \sum_i i \mathcal{P}_i(n) \quad (10.35)$$

where $\mathcal{P}_i(n)$ is the probability of having i clusters of size n . Assuming that the formation of different clusters is uncorrelated, we can write $\mathcal{P}_i(n) = \mathcal{P}_1(n)^i$, so that:

$$\mathcal{P}(n) = \sum_i \mathcal{P}_1(n)^i \simeq \mathcal{P}_1(n) \doteq \mathcal{P}(NBC) \quad (10.36)$$

The last approximation holds since the probability of having one big cluster is small, so that the first term in the sum dominates. CNT comprises also a kinetic treatment of the nucleation process, that leads to an estimate of the nucleation rate. This is expressed as the product of the probability of having a critical nucleus of size n^* (i.e. Eq. 10.34 for n^*) times the so called kinetic pre-factor. This is built from information retrieved from the system containing the critical nucleus. We do not assume CNT to estimate the nucleation rate, since we use a method (see section 10.2) that directly yields this information. More details on CNT can be found in Ref. [230] and references therein.

The LCBOP II

... a coloro che verranno.

Luigia Cadario in Marin

11.1 Introduction

As shown in chapters 9 and 8, both the results for the liquid phase and the phase diagram, based on the LCBOP⁺, show a promising agreement with available data from ab initio Car Parrinello Molecular Dynamics (CPMD) [62] simulations and/or experimental data. For example, with the LCBOP⁺ no LLPT was found in agreement with DF-MD, most likely due to a weaker torsional interactions for conjugated bonds as compared to the extended Brenner II BOP. For the LCBOP⁺ these interactions were fitted to recent ab initio calculations [14] of the torsional barrier for such bonds. The pressure-volume isotherms at 6000 K from DF-MD simulations is reasonably well reproduced by the LCBOP⁺ as well as the trend in the coordination statistics over a wide range of densities, in contrast to Brenner's BOP's without *lr* interactions.

However, significant differences in the radial distribution function (rdf) for the liquid phase between DF-MD and LCBOP⁺ prompt to further improvement of the potential. Although the positions of the extrema in the rdf's at various densities are reproduced reasonably well, the minima and maxima according to the LCBOP⁺ are clearly more pronounced than those according to DF-MD [17]. In particular, the LCBOP⁺, and also Brenner's BOP's, give rise to a very deep minimum around the cut-off range for the short-range interactions. It is tempting to assign this effect to the strong gradients within the cut-off range, an artifact of the rigid cut-off. In order to clarify this point, we performed ab initio calculations of the dissociation energy curve for a single bond, as described in appendix 11.4, and compared it to those according to the LCBOP⁺ and the REBO potential. The comparison is shown in Fig. 11.1. Clearly, with a *sr* cut-off radius of 2.2 Å (2.0 Å for the REBO potential) the LCBOP⁺ cannot reproduce the energy of -2 eV at 2.2 Å in the single bond dissociation found in the DF-MD calculation. Note that beyond the *sr* cut-off radius there are only *lr* interactions between the two dissociating fragments, which give rise to an effective repulsion between the fragments in the range from 2.2 to 3.5 Å. For the REBO potential, the interaction between the fragments beyond 2 Å vanishes altogether. In this case, we may certainly assume that the ab initio results are more reliable, and obviously this discrepancy could very well be the reason for the mentioned difference in the liquid structure.

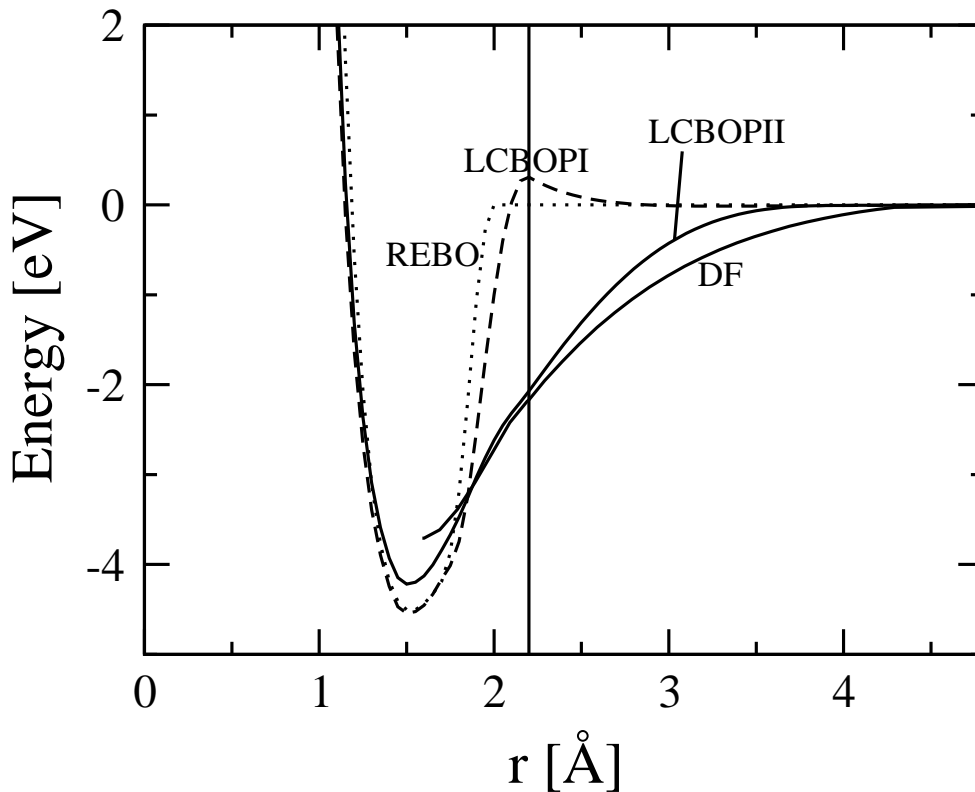


Figure 11.1: Binding energy for the single bond in $(\text{CH}_3)_3\text{C}-\text{C}(\text{CH}_3)_3$ as a function of the central C-C-distance, calculated by DF (dotted line), by LCBOP11 (solid line), by REBO potential and LCBOP1⁺ (dashed lines).

The above discrepancy inspired us to further improvements of the LCBOP1⁺. The resulting new potential is denoted LCBOP11. The many modifications and improvements of the LCBOP11, as compared to the LCBOP1⁺, require a complete description, which is given in Section 11.2. The LCBOP11 reproduces much better the dissociation energy curves for single, double and triple bonds by the addition of new attractive interactions between atoms at middle range (mr) distances between 1.7 and 4 Å. These mr interactions, which extend the covalent bonds where this is appropriate, depend on the mutual reactivity between atoms, which is quantified in terms of the bond angles and of the presence of dangling bonds, as described in Section 11.2.4. Further improvements of the LCBOP11 include i) an extended and more dynamic coordination dependence of the angular correlation, ii) a correction for anti-bonding states by the addition of a new term to the bond order, iii) an extended conjugation dependence of the torsional interactions based on ab initio calculations of the torsional barriers for a set of molecular configurations, iv) a new definition of the torsion angle not producing spurious torsion, and v) a completely new, and more natural interpolation approach for non-integer coordination states.

After the description of the LCBOP11 in Section 11.2, structural and elastic properties for solid phase structures, including the diamond (111) and (100) reconstructed surfaces will be presented and discussed in Section 11.3. In this Section we present also results concerning the geometry and energetics of the diamond to graphite transformation and of the vacancy in graphite and diamond as well as the prediction of the LCBOP11 for

the energy barrier for the formation of the so called 5-77-5 defect. In appendix 11.4, we give details of the DF calculations used to develop the LCBOP II. In the next chapter, the results of an extended study of liquid carbon according to the LCBOP II are given, covering a large pressure-temperature domain of the phase diagram, and are compared to ab initio data, where available.

11.2 The LCBOP II

For the LCBOP II, the total binding energy E_b for a system consisting of N_{at} is given by:

$$E_b = \frac{1}{2} \sum_{i,j}^{N_{at}} \left(S_{sr,ij}^{down} V_{ij}^{sr} + S_{sr,ij}^{up} V_{ij}^{lr} + \frac{1}{Z_i^{mr}} S_{mr,ij}^{up} V_{ij}^{mr} \right) \quad (11.1)$$

where $V_{ij}^{sr} = V^{sr}(r_{ij})$ describes the covalent, short range interactions, $V_{ij}^{lr} = V^{lr}(r_{ij})$ accounts for the long range non-bonded interactions and $V_{ij}^{mr} = V^{mr}(r_{ij})$ represents the remainder of bonded (attractive) interactions between atoms at middle range distances. Here $r_{ij} = |\mathbf{r}_i - \mathbf{r}_j|$ is the interatomic distance. The middle range attractive interaction, not present in the LCBOP I, is inspired and based on the ab initio calculations of the dissociation energy curves for single, double and triple bonds (see appendix 11.4). The prefactor $1/Z_i^{mr}$, where Z_i^{mr} is an effective middle range coordination number defined in Sec. 11.2.4, takes into account many body effects. The switch functions $S_{sr,ij}^{down} = S_{sr}^{down}(r_{ij})$, $S_{sr,ij}^{up} = S_{sr}^{up}(r_{ij})$ and $S_{mr,ij}^{up} = S_{mr}^{up}(r_{ij})$, described in detail in Sec. 11.2.1 provide a smooth connection between the various interaction contributions.

11.2.1 Switch functions

In the description of the LCBOP II, we will make use of two families of switch functions, $S^{down}(x)$ and $S^{up}(x)$, being defined as:

$$S^{down}(x) = \Theta(-x) + \Theta(x)\Theta(1-x)(1+2x+px^2)(1-x)^2 \quad (11.2)$$

and:

$$S^{up}(x) = 1 - S^{down}(x) \quad (11.3)$$

respectively, where $\Theta(x)$ is the heavyside step function. As shown in Fig. 6.2, the parameter p , ranging in the interval $[-3,3]$, offers a certain freedom in the choice of the shape of the switch function while staying monotonic within $x \in [0,1]$. To realize a switch as a function of a given quantity q (e.g. distance or coordination) within a desired interval $[q_{min}, q_{max}]$ the dimensionless argument x is defined as:

$$x = x(q) = \frac{q - q_{min}}{q_{max} - q_{min}} \quad (11.4)$$

In the description of the LCBOP II, each switch function, labeled by an appropriate subscript, is specified by the three numbers q_{min} , q_{max} and p , which are given in Table 11.4.

11.2.2 Short range potential V^{sr}

The potential V_{ij}^{sr} is a Brenner type of bond order potential similar to that of the LCBOPI, but with several important modifications. It reads:

$$V_{ij}^{sr} = V_{R,ij}^{sr} - B_{ij} V_{A,ij}^{sr} \quad (11.5)$$

where V_R^{sr} and V_A^{sr} are repulsive and attractive radial pair potentials given by:

$$V_R^{sr}(r) = A^{sr} \exp(-\alpha r) \quad , \quad (11.6)$$

$$V_A^{sr}(r) = B_1^{sr} \exp(-\beta_1 r) + B_2^{sr} \exp(-\beta_2 r) \quad . \quad (11.7)$$

The bond order B_{ij} includes the many body effects and is the sum of several terms:

$$B_{ij} = \frac{1}{2}(b_{ij} + b_{ji}) + F_{ij}^{conj} + A_{ij} + T_{ij} \quad (11.8)$$

where b_{ij} depends on the bond angles and F_{ij}^{conj} accounts for conjugation. New with respect to the LCBOPI are the terms A_{ij} and T_{ij} , which account for the effects of the presence of occupied anti-bonding states and of torsion respectively.

Term b_{ij}

The bond angle dependent part b_{ij} is given by:

$$b_{ij} = \left(1 + \sum_{k \neq i,j} S_Z^{down}(r_{ik}) H(\delta r_{ijk}) G(\cos \theta_{ijk}, Z_{ijk}) \right)^{-1/2} \quad (11.9)$$

where the summation runs over all neighbours k ($\neq j$) of i , θ_{ijk} is the bond angle between the bonds ij and ik and $\delta r_{ijk} = r_{ij} - r_{ik}$. The reduced coordination number Z_{ijk} is defined as:

$$Z_{ijk} = \sum_{l \neq i,j,k} S_{Z,il}^{down} = Z_i - S_{Z,ij}^{down} - S_{Z,ik}^{down} \quad (11.10)$$

where Z_i is the coordination of atom i defined as:

$$Z_i = \sum_{j \neq i} S_{Z,ij}^{down} \quad (11.11)$$

and $S_{Z,ij}^{down} = S_Z^{down}(r_{ij})$. As compared to the LCBOPI, we have modified the angular function G , making it coordination dependent in order to improve the energetics of configurations with small bond angles (at low coordination). Such a correction of the angular correlation was also included in the REBO potential, switching from the maximal to a weaker angular correlation for coordinations between 3.8 and 3.2*. We found that a good description of various small clusters, as those of Refs. [157, 158], required different angular functions for the coordinations two and three. Simulations for the liquid phase [17, 21],

*Note that ‘coordination’ of atom i is defined as Z_i (Eq. 11.11), thus allowed to be a non-integer number.

suggest that a weakening of the angular correlation for small angles is required for higher coordinations (i.e. $Z \geq 4$) as well. For the LCBOP II we have formulated a dynamic coordination dependence which smoothly interpolates the angular correlation for coordinations $Z_{ijk} \leq 8$.

Using the short notations $y = \cos\theta_{ijk}$ and $z = Z_{ijk}$, the angular function $G(y, z)$ reads:

$$G(y, z) = \Theta(y_0(z) - y)G_1(y) + \Theta(y - y_0(z))G_2(y, z) \quad (11.12)$$

where $G_1(y)$ is the angular function fitting the properties of the various bulk crystal lattices from chain to fcc as in the LCBOP I [15], and $G_2(y, z)$ gives a weaker angular correlation, as compared to $G_1(y, z)$, for low coordinations and small angles. The function G is presented in Fig. 11.2. The coordination dependent boundary value $y_0(z)$ where G_2 is smoothly matched to G_1 is given by:

$$y_0(z) = A_{y_0} + B_{y_0}(z + z^2) \quad (11.13)$$

For high coordination $y_0(z)$ becomes larger than one and $G(y, z) = G_1(y)$ for all angles. The functions $G_1(y)$ and $G_2(y, z)$ are given by:

$$G_1(y) = \begin{cases} g_{min} + (y + 1)^2 \sum_{n=0}^2 g_{1,n} y^n & -1 \leq y < -\frac{1}{2} \\ g_{gr} + (y + \frac{1}{2}) \sum_{n=0}^4 g_{2,n} y^n & -\frac{1}{2} \leq y < -\frac{1}{3} \\ g_{max} + (y - 1)^2 \sum_{n=0}^4 g_{3,n} y^n & -\frac{1}{3} \leq y \leq 1 \end{cases} \quad (11.14)$$

and:

$$G_2(y, z) = g_{z,max} + (1 - y)^2 \sum_{n=0}^2 g_{z,n} y^n \quad (11.15)$$

respectively, where:

$$g_{z,max} = g_{max} - (A_g + B_g z + C_g z^4)(1 - y_0)^3 \quad (11.16)$$

and:

$$g_{z,2} = \frac{D_g z^4}{1 + E_g z^4} \quad (11.17)$$

The coefficients $g_{z,0}$ and $g_{z,1}$ are fixed by the requirement of continuity of $G(y, z)$ up to the first derivative at $y = y_0(z)$, implying:

$$g_{z,1} = \frac{G'_1(y_0)}{(y_0 - 1)^2} - 2 \frac{G_1(y_0)}{(y_0 - 1)^3} - 2g_{z,2}y_0 \quad (11.18)$$

and:

$$g_{z,0} = \frac{G_1(y_0) - g_{z,max}}{(y_0 - 1)^2} - g_{z,1}y_0 - g_{z,2}y_0^2 \quad (11.19)$$

where $G'_1(y_0) = dG_1/dy|_{y_0}$.

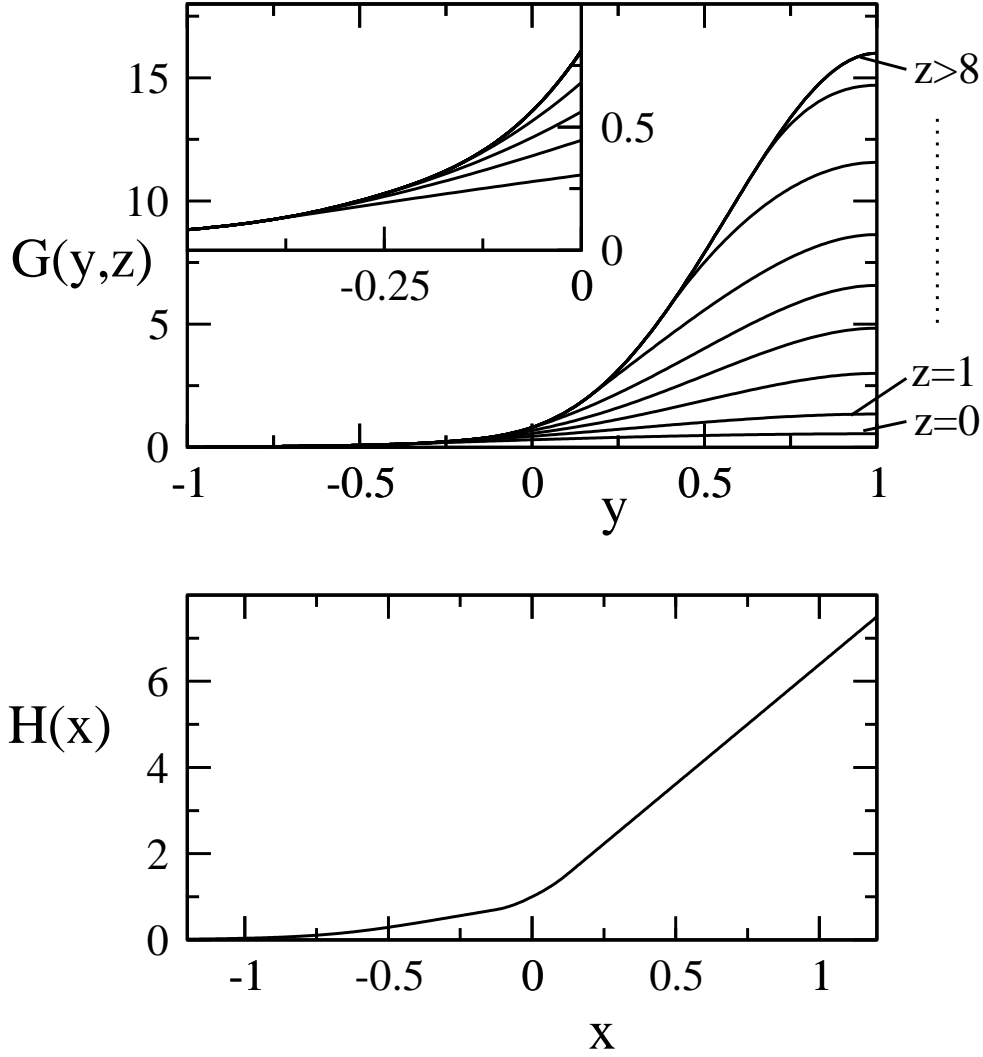


Figure 11.2: Top panel: function $G(y,z)$ (Eq. 11.12) for integer values of z . The inset shows that G_2 is smoothly matched to G_1 at a coordination dependent boundary value $y_0(z)$; the vertical axis of the inset is labeled on the right-hand side. Bottom panel: function $H(x)$ (Eq. 11.20).

The function $H(\delta r_{ijk})$ shown in Fig. 11.2 is almost the same as for the LCBOPI and reads:

$$H(x) = \begin{cases} H_1(x) = L \left(1 + \kappa(x+d) \left(\frac{1}{1 + (\kappa(x+d))^4} \right)^{1/4} \right) & x < -d \\ H_2(x) = 1 + C_1 x + \frac{1}{2} C_1^2 x^2 + C_4 x^4 + C_6 x^6 & -d \leq x \leq d \\ H_3(x) = R_0 + R_1(x-d) & x > d \end{cases} \quad (11.20)$$

with three independent parameters d , C_1 and C_4 and where L , κ , C_6 , R_0 and R_1 follow from continuity of H up to its second derivative at $x = \pm d$. By construction $d^2 H_1/dx^2|_{x=-d} = d^2 H_3/dx^2|_{x=d} = 0$, so that C_6 follows directly from $d^2 H_2/dx^2|_{x=d} = d^2 H_2/dx^2|_{x=-d} = 0$.

Furthermore, L and R_0 follow from continuity of H in $x = -d$ and $x = d$ respectively, leaving R_1 and κ to be found from continuity of the first derivative of H at $x = \pm d$.

Conjugation term F_{ij}^{conj}

We call atom j a full neighbour of atom i if $S_{Z,ij}^{down} = 1$. If $0 < S_{Z,ij}^{down} < 1$ then atom j is called a fractional neighbour. For the LCBOPI, as for Brenner's potentials, F_{ij}^{conj} is a function of the reduced coordination numbers Z_{ij} and Z_{ji} , and of the conjugation number Z_{ij}^{conj} . The number Z_{ij} is defined by:

$$Z_{ij} = Z_i - S_{Z,ij}^{down} \quad (11.21)$$

The values of F_{ij}^{conj} for integer Z_{ij} and Z_{ji} were fitted to known bond energies for equilibrium configurations with appropriate coordination environments[3, 15]. A cubic spline was used to extend F_{ij}^{conj} to non integer coordinations. In this interpolation approach, a situation where atom i has 2 full neighbours other than j gives the same argument $Z_{ij} = 2$ as a situation where atom i has one full neighbour other than j and two fractional neighbours $k_1 \neq j$ and $k_2 \neq j$ with $S_{Z,ik_1}^{down} + S_{Z,ik_2}^{down} = 1$ which can lead to unreasonable values for F_{ij}^{conj} . Therefore, for the LCBOPII, which we wish to be applicable also to the liquid phase where multiple fractional neighbours often occur, we propose an interpolation scheme which makes use only of the values of F_{ij}^{conj} for integer Z_{ij} and Z_{ji} . In this new approach, the above situation is interpolated as a weighted sum of one configuration with $Z_{ij} = 1$ (both fractional neighbours excluded), two configurations with $Z_{ij} = 2$ (one of the fractional neighbours included as full neighbour and the other excluded and viceversa) and one configuration with $Z_{ij} = 3$ (both fractional neighbours included as full neighbours). Mathematically, this can be written as:

$$F_{ij}^{conj} = \sum_{\{\sigma_k=0,1\}} \sum_{\{\sigma_l=0,1\}} W_{ij,\{\sigma_k\}} W_{ji,\{\sigma_l\}} F^{conj}(\tilde{Z}_{ij,\{\sigma_k\}}, \tilde{Z}_{ji,\{\sigma_l\}}, Z_{ij,\{\sigma_k\}}^{\{\sigma_l\}}) \quad (11.22)$$

where:

$$W_{ij,\{\sigma_k\}} = \prod_{k \neq j} (\sigma_k S_{Z,ik}^{down} + (1 - \sigma_k)(1 - S_{Z,ik}^{down})) \quad (11.23)$$

is a weight factor. The summation $\sum_{\{\sigma_k=0,1\}}$ runs over all possible sets of numbers $\{\sigma_k\}$, one number for each neighbour $k \neq j$ of i , with each σ_k assuming the value 0 or 1. Note however that $W_{ij,\{\sigma_k\}} = 0$ for all sets $\{\sigma_k\}$ containing a $\sigma_k = 0$ for a full neighbour $k \neq j$ of i . Therefore, the summation can be restricted to the fractional neighbours, putting $\sigma_k = 1$ for all full neighbours. The expression (11.22) requires only the values of F^{conj} for the integer arguments $\tilde{Z}_{ij,\{\sigma_k\}}$ (ranging between 0 and 3), defined as:

$$\tilde{Z}_{ij,\{\sigma_k\}} = \min(3, Z_{ij,\{\sigma_k\}}) \quad (11.24)$$

with

$$Z_{ij,\{\sigma_k\}} = \sum_{k \neq j} \sigma_k \quad (11.25)$$

The definition of the conjugation number $Z_{ij,\{\sigma_k\}\{\sigma_l\}}^{conj}$ is equivalent to that for the LCBOP I, but is presented here in a more transparent form. By construction it is a number between 0 and 1 and reads:

$$Z_{ij,\{\sigma_k\}\{\sigma_l\}}^{conj} = \frac{Z_{ij}^{el} + Z_{ji}^{el} - Z_{ij,min}^{el} - Z_{ji,min}^{el}}{Z_{ij,max}^{el} + Z_{ji,max}^{el} - Z_{ij,min}^{el} - Z_{ji,min}^{el} + \epsilon}, \quad (11.26)$$

where Z_{ij}^{el} is the fractional number of electrons supplied by atom i to the bond ij given by:

$$Z_{ij}^{el} = \frac{4 - \tilde{M}_{ij,\{\sigma_k\}}}{\tilde{Z}_{ij,\{\sigma_k\}} + 1 - \tilde{M}_{ij,\{\sigma_k\}}} \quad (11.27)$$

with $\tilde{M}_{ij,\{\sigma_k\}}$ the fractional number of saturated (i.e. with coordination at least four) neighbours $k \neq j$ of atom i . It is defined by:

$$\tilde{M}_{ij,\{\sigma_k\}} = \min(3, M_{ij,\{\sigma_k\}}) \quad (11.28)$$

where $M_{ij,\{\sigma_k\}}$ is given by:

$$M_{ij,\{\sigma_k\}} = \sum_{k \neq i,j} \sigma_k S_M^{up}(Z_{ki}) \quad (11.29)$$

with $Z_{ki} = Z_k - S_{Z,ki}^{down}$ according to Eq. 11.21. According to these definitions the minimal and maximal values of Z_{ij}^{el} , to be inserted into Eq. 11.26, are given by:

$$Z_{ij,min}^{el} = \frac{4}{\tilde{Z}_{ij,\{\sigma_k\}} + 1} \quad \text{and} \quad Z_{ij,max}^{el} = 4 - \tilde{Z}_{ij,\{\sigma_k\}} \quad (11.30)$$

respectively. We assume a linear dependence of $F_{ij,\{\sigma_k\}\{\sigma_l\}}^{conj}$ on $Z_{ij,\{\sigma_k\}\{\sigma_l\}}^{conj}$, i.e.:

$$F_{ij}^{conj} = (1 - Z_{ij,\{\sigma_k\}\{\sigma_l\}}^{conj}) F_{ij,0}^{conj} + Z_{ij,\{\sigma_k\}\{\sigma_l\}}^{conj} F_{ij,1}^{conj} \quad (11.31)$$

with $F_{ij,0}^{conj} = F^{conj}(\tilde{Z}_{ij,\{\sigma_k\}}, \tilde{Z}_{ji,\{\sigma_l\}}, 0)$ and $F_{ij,1}^{conj} = F^{conj}(\tilde{Z}_{ij,\{\sigma_k\}}, \tilde{Z}_{ji,\{\sigma_l\}}, 1)$ given in Table 11.5. In Eq. 11.26, ϵ is a very small positive number that prevents the numerical singularities occurring for coordination combinations $(\tilde{Z}_{ij,\{\sigma_k\}}, \tilde{Z}_{ji,\{\sigma_l\}}) = (0,0), (0,3), (3,0)$ and $(3,3)$, where $Z_{ij,\{\sigma_k\}\{\sigma_l\}}^{conj} = 0/\epsilon = 0$. Actually, for these combinations $F_{ij,0}^{conj} = F_{ij,1}^{conj}$ so that the value of $Z_{ij,\{\sigma_k\}\{\sigma_l\}}^{conj}$ becomes irrelevant.

Antibonding term A_{ij}

The term A_{ij} accounts for occupancy of anti-bonding states. When the supply of electrons from atom i to the bond ij , Z_{ij}^{el} , is not equal to that from atom j , Z_{ji}^{el} , bonding is relatively less effective. To illustrate this point, we refer to the configuration shown in Fig. 11.3. For the ij -bond with $Z_{ij,\{\sigma_k\}} = 1$ and $Z_{ji,\{\sigma_l\}} = 2$ with saturated neighbours $k \neq j$ of i and $l \neq i$ of j , yielding $Z_{ij,\{\sigma_k\}\{\sigma_l\}}^{conj} = 1$, we have $Z_{ij}^{el} = 3$ and $Z_{ji}^{el} = 2$. Instead of a bond energy somewhere between that of a double bond (6.2 eV, Ref. [130]) and that of a triple bond (8.4 eV, Ref. [130]), the bond energy for this bond is only about 5.8 eV, according to the LCBOP I, the LCBOP II, and the REBO potential, due to the unfavorable

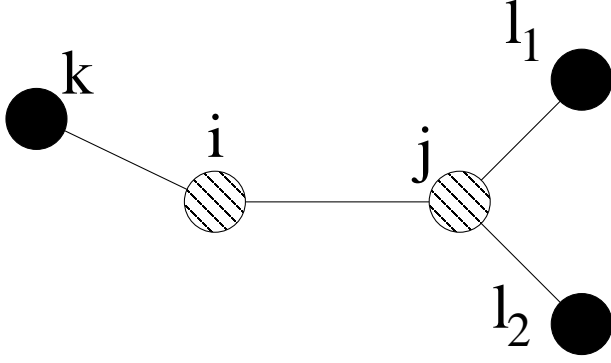


Figure 11.3: Example used to describe the term A_{ij} that accounts for occupancy of anti-bonding states (see text).

situation that not all electrons can make pairs, giving rise to an anti-bonding state being occupied by the lone electron. Conversely, if the neighbours k and l are unsaturated, yielding $Z_{ij,\{\sigma_k\}\{\sigma_l\}}^{conj} = 0$, the bond energy is equal to 5.2 eV . With the linear dependence in Eq. 11.31, the bond energy of this bond for $0 < Z_{ij,\{\sigma_k\}\{\sigma_l\}}^{conj} < 1$ is always between 5.2 eV and 5.8 eV for the LCBOPI and the REBO potential. However, when the two neighbours $l \neq i$ of atom j are saturated and the neighbour $k \neq j$ of atom i is unsaturated, we have $Z_{ij}^{el} = 2$ and $Z_{ji}^{el} = 2$, i.e. a proper double bond which should have a bond energy of about 6.2 eV . For this case, $Z_{ij,\{\sigma_k\}\{\sigma_l\}}^{conj} = 2/5$. In order to describe all these situations correctly we introduced the anti-bonding term A_{ij} , which, using the same interpolation approach as for the conjugation term, is given by:

$$A_{ij} = \sum_{\{\sigma_k=0,1\}}^l \sum_{\{\sigma_l=0,1\}}^l W_{ij,\{\sigma_k\}} W_{ji,\{\sigma_l\}} a_{ij}(\Delta_{el}) \quad (11.32)$$

where the summations are restricted to those configurations with $(Z_{ij,\{\sigma_k\}}, Z_{ji,\{\sigma_l\}})$ equal to $(1,1), (2,2), (1,2)$ or $(2,1)$ and where:

$$a_{ij}(\Delta_{el}) = \frac{\alpha_0 \Delta_{el}^2}{1 + 10|\Delta_{el}|} \quad (11.33)$$

with

$$\Delta_{el} = Z_{ij,\{\sigma_k\}}^{el} - Z_{ji,\{\sigma_l\}}^{el} \quad (11.34)$$

The function a_{ij} tends to a linear dependence on $|\Delta_{el}|$ while being continuous up to the first derivative at $\Delta_{el} = 0$. For $(Z_{ij,\{\sigma_k\}}, Z_{ji,\{\sigma_l\}})$ not equal to $(1,1), (2,2), (1,2)$ or $(2,1)$ the linear interpolation Eq. 11.31 is reasonable and the correction A_{ij} is not required.

Torsion term T_{ij}

Also for the torsion term T_{ij} , the same interpolation approach is used as for the conjugation term:

$$T_{ij} = \sum_{\{\sigma_k=0,1\}}^{\prime\prime} \sum_{\{\sigma_l=0,1\}}^{\prime\prime} W_{ij,\{\sigma_k\}} W_{ji,\{\sigma_l\}} t_{ij}(y_{ij,\{\sigma_k\}\{\sigma_l\}}, Z_{ij,\{\sigma_k\}\{\sigma_l\}}^{conj}) \quad (11.35)$$

where now the summations are restricted only to those configurations with $(Z_{ij,\{\sigma_k\}}, Z_{ji,\{\sigma_l\}}) = (2,2)$. The torsional term t_{ij} for each of these configurations depends on $y_{ij,\{\sigma_k\}\{\sigma_l\}} =$

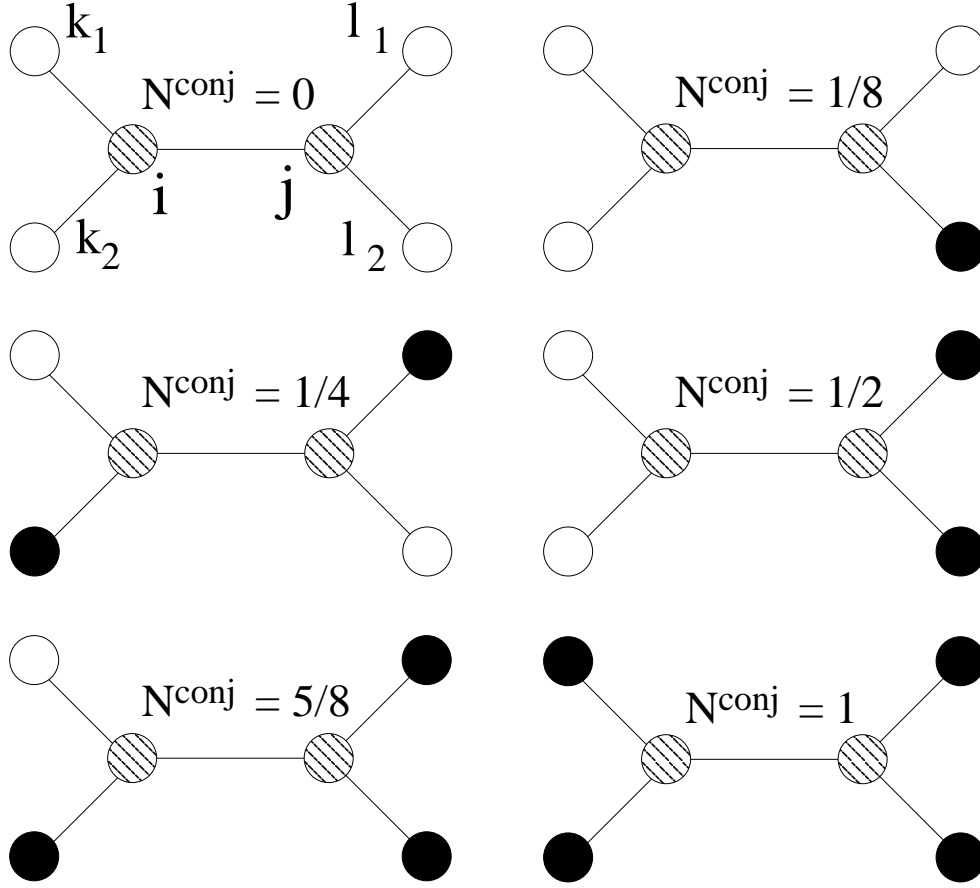


Figure 11.4: Schematic molecules with a central bond between two sp_2 sites (i and j , dashed circles), for all the possible values of Z^{conj} (Eq. 11.26) with integer coordinated neighbours. White circles represent three-fold (sp_2) sites, while black circles are for four-fold (sp_3) sites.

$\cos(\omega_{ij,\{\sigma_k\}\{\sigma_l\}})$ with $\omega_{ij,\{\sigma_k\}\{\sigma_l\}}$ the torsion angle and on the conjugation number $Z_{ij,\{\sigma_k\}\{\sigma_l\}}^{conj}$ for this configuration. The DF calculations of the torsional barrier for the 6 cases of Fig. 11.4, shown in Fig. 11.5, display a rather complex dependence of the torsional barrier on each of the possible conjugation numbers. Fitting this behaviour led us to the following form for t_{ij} :

$$t_{ij}(\tilde{y}, \tilde{z}) = \begin{cases} \tau_1(\tilde{z}) (\tilde{y}^2(1 - \tilde{y}^2))^2 & \tilde{z} \leq \frac{1}{8} \\ \tau_2(\tilde{z})(1 - \tilde{y}^2)(2 - \tilde{y}^2)^2 & \tilde{z} > \frac{1}{8} \end{cases} \quad (11.36)$$

where we used the short notations $\tilde{y} = \cos(\omega_{ij,\{\sigma_k\}\{\sigma_l\}})$ and $\tilde{z} = Z_{ij,\{\sigma_k\}\{\sigma_l\}}^{conj}$ and where:

$$\tau_1(\tilde{z}) = A_t (\tilde{z} - 1/8)^2 \quad (11.37)$$

$$\tau_2(\tilde{z}) = \frac{B_{t1}(\tilde{z} - 1/8)^2 (\tilde{z} + B_{t2}\Delta_{el}^2[\Delta_{el}^2 - (2/3)^2])^2 (1 - B_{t3}\tilde{z})}{B_{t4} + (\tilde{z} - 1/8)^2} \quad (11.38)$$

For the LCBOPI⁺ (see section 6.7) the torsion angle was defined as the angle between the vector product of \mathbf{r}_{ij} with \mathbf{r}_{ik} and the vector product of \mathbf{r}_{ij} with \mathbf{r}_{jl} , as for the REBO potential. The total torsion term T_{ij} was the sum of contributions from the torsion angles

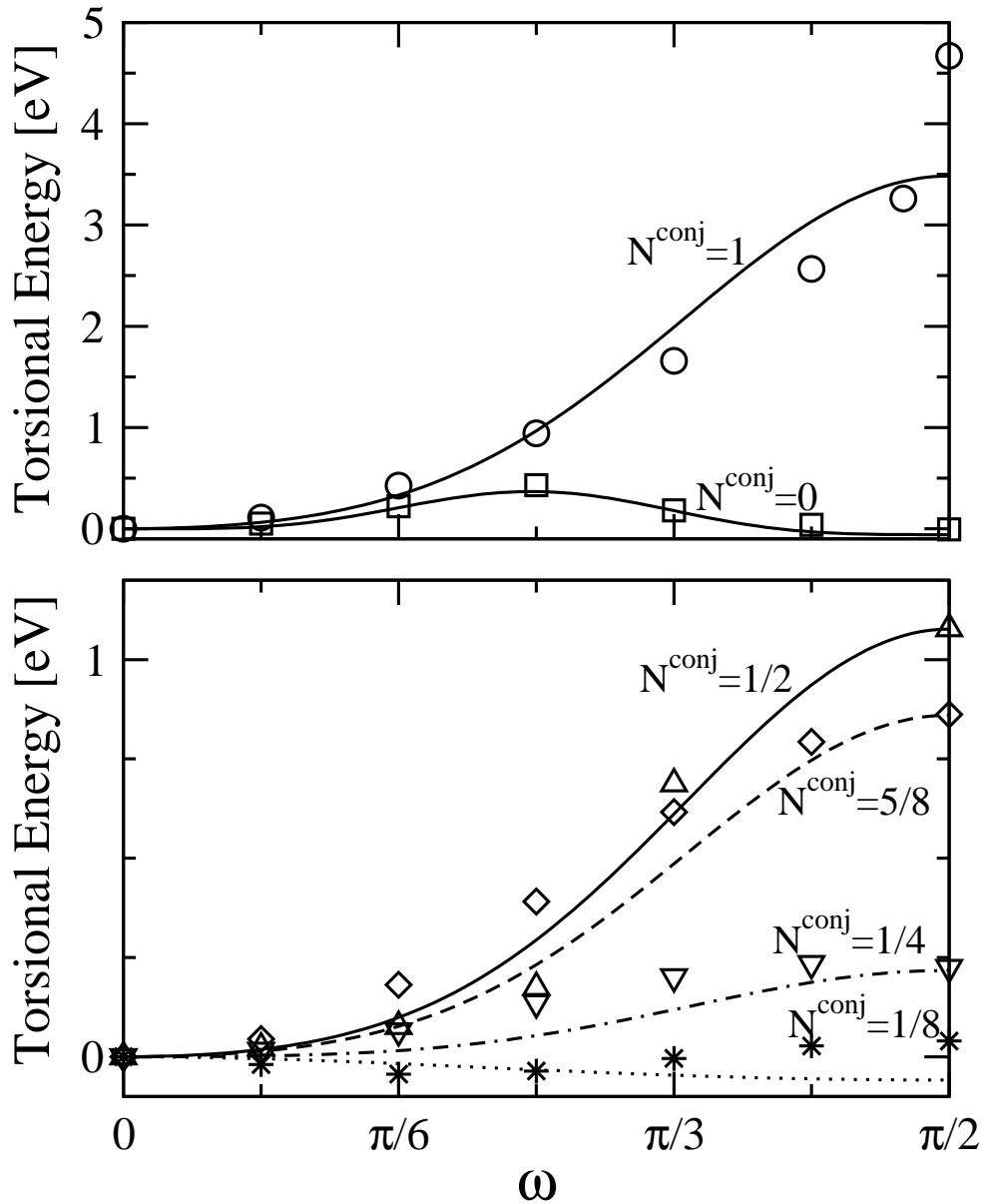


Figure 11.5: Torsional barriers according to the LCBOP11 and our DF calculations for the six values of Z^{conj} corresponding to the molecules schematically represented in Fig. 11.4. Symbols represent the DF results, curves the fits obtained by the LCBOP11. Top panel: torsional barriers for the extreme values of Z^{conj} , related to the conjugated ($Z^{\text{conj}}=0$, squares and dashed curve) and double bonds ($Z^{\text{conj}}=1$, circles and solid curve). Bottom panel: intermediate values of Z^{conj} : $1/8$ (stars and dotted curve), $1/4$ (down triangles and dashed-dotted curve), $1/2$ (up triangles and solid curve) and $5/8$ (diamonds and dashed curve). Note the complex behaviour of the curves for the values $1/2$ and $5/8$, where the barrier at $\pi/2$ is higher for $Z^{\text{conj}}=1/2$ than for $Z^{\text{conj}}=5/8$.

from all pairs of these vector products. However, apart from the problematic singularity occurring when \mathbf{r}_{ik} or \mathbf{r}_{jl} is parallel to \mathbf{r}_{ij} this definition of the torsion term gives a non-zero torsion for many situations, like the one shown in Fig. 11.6 where there is actually

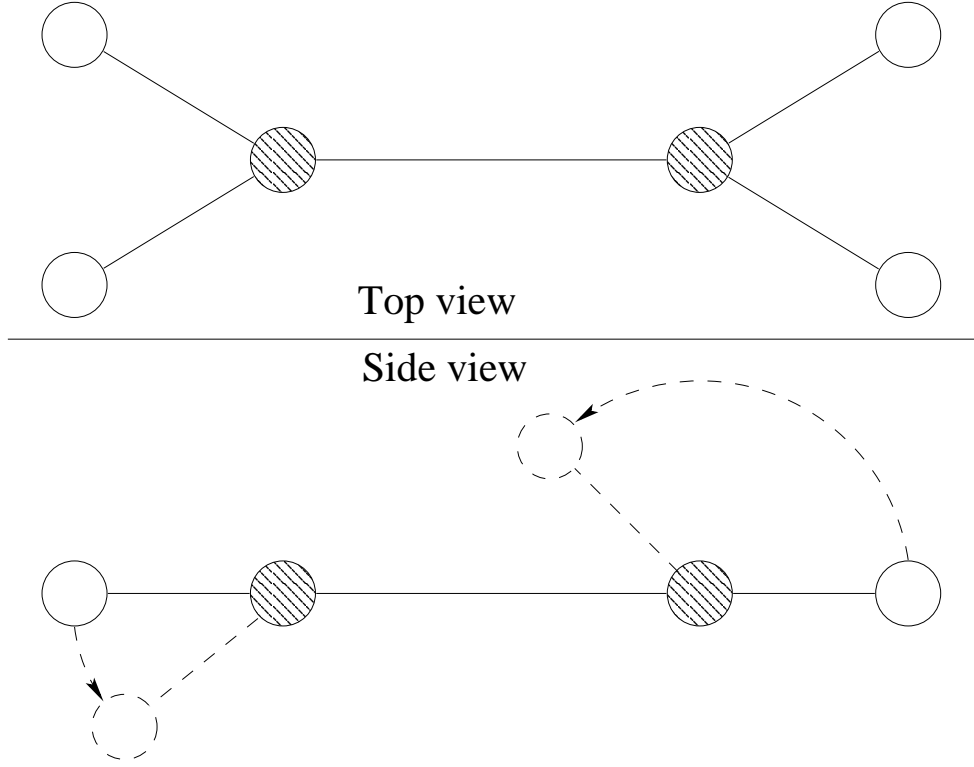


Figure 11.6: Scheme to show a case with no torsion, according to our definition. Starting from the molecule in its planar configuration, out of plane bending described by dashed lined arrows leave $\tilde{y} = 0$, thus giving the torsional term $T_{ij} = 0$. Only the twisting around the central bond gives a $\tilde{y} \neq 0$. In contrast, older definition of the torsions, such as in Refs. [4, 130, 155], gave a spurious nonzero torsional contribution for the bending shown in this figure.

no torsion at all. For example, it gives a non-zero torsion for the dimer bond on the reconstructed (001) surface, leading to a too large dimer bond distance (1.555 Å for the LCBOP-I and 1.546 Å for the REBO potential against the experimental value 1.37 Å). Therefore, for the LCBOP-II we have formulated a different expression for the torsion angle which does not give 'spurious torsion' and interpolates well for any configuration. For each configuration where two bonded atoms i and j both have two other neighbours (k_1, k_2) and (l_1, l_2) respectively, characterized by the two sets of numbers $\{\sigma_k\}$ and $\{\sigma_l\}$, we define a single torsion angle through:

$$\tilde{y} = \cos(\omega_{ij, \{\sigma_k\} \{\sigma_l\}}) = \frac{\mathbf{t}_{ijk} \cdot \mathbf{t}_{jil}}{|\mathbf{t}_{ijk}| |\mathbf{t}_{jil}|} \quad (11.39)$$

where the vector \mathbf{t}_{ijk} is given by:

$$\mathbf{t}_{ijk} = \hat{\mathbf{r}}_{ij} \times \hat{\mathbf{w}}_{ijk}^- + (\hat{\mathbf{r}}_{ij} \cdot \hat{\mathbf{w}}_{ijk}^-) (\hat{\mathbf{r}}_{ij} \times \hat{\mathbf{w}}_{ijk}^+) \quad (11.40)$$

with:

$$\hat{\mathbf{w}}_{ijk}^- = \frac{\hat{\mathbf{r}}_{ik_1} - \hat{\mathbf{r}}_{ik_2}}{|\hat{\mathbf{r}}_{ik_1} - \hat{\mathbf{r}}_{ik_2}|}, \quad \hat{\mathbf{w}}_{ijk}^+ = \frac{\hat{\mathbf{r}}_{ik_1} + \hat{\mathbf{r}}_{ik_2}}{|\hat{\mathbf{r}}_{ik_1} + \hat{\mathbf{r}}_{ik_2}|} \quad (11.41)$$

and $\hat{\mathbf{r}}_{ij} = \mathbf{r}_{ij}/|\mathbf{r}_{ij}|$. We note that the definition Eq.(11.40) becomes equivalent to the one of the REBO potential for the standard case of rotation around the axis $\hat{\mathbf{r}}_{ij}$.

11.2.3 Long range potential V^{lr} .

The functional form of the long-range (i.e. non-bonded) pair potential V_{ij}^{lr} is the same as for the LCBOPI:

$$V^{lr}(r) = (\theta(r_0 - r)V_1^{lr}(r) + \theta(r - r_0)V_2^{lr}(r)) S_{lr}^{down}(r) \quad (11.42)$$

where V_i^{lr} ($i = 1,2$) are ordinary Morse functions plus a shift:

$$V_i^{lr}(r) = \epsilon_i (e^{-2\lambda_i(r-r_0)} - 2e^{-\lambda_i(r-r_0)}) + v_i. \quad (11.43)$$

and $S_{lr}^{down}(r)$ smoothly cuts off the long range interactions beyond 6 Å. The two Morse functions are connected continuously up to the second derivative in $r = r_0$, implying $\epsilon_1 = \epsilon_2\lambda_2^2/\lambda_1^2$ and $v_1 = \epsilon_1 - \epsilon_2$ with $v_2 = 0$. The values of the parameters have slightly changed as compared to those for the LCBOPI, leading to an optimal fit of the compressibility in the direction perpendicular to the layers, namely $4.324 \cdot 10^{-3} \text{ \AA}^3/\text{meV}$ to be compared to the experimental value $4.326 \cdot 10^{-3} \text{ \AA}^3/\text{meV}$ [243, 244]. This long range part binds the graphitic layers at the experimental equilibrium distance of 3.35 Å, the binding energy being 25 meV/at [15].

11.2.4 Middle range potential V^{mr}

The middle range attractive interactions in Eq. 11.1, representing an important novelty of the LCBOPII, are environment dependent. They depend on bond angles and on the presence of 'dangling bonds' as quantified by the dangling bond number Z^{db} defined in the following. It reads:

$$V_{ij}^{mr} = \begin{cases} S_{db}^{down}(x_{ij}^{db})S_{\gamma,0}^{up}(\gamma_{ij})V_{0,ij}^{mr} + S_{db}^{up}(x_{ij}^{db})\tilde{S}_{\gamma,1}^{up}(\gamma_{ij})V_{1,ij}^{mr} & 0 \leq Z_{ij}^{db} \leq 1 \\ S_{db}^{down}(x_{ij}^{db})\tilde{S}_{\gamma,1}^{up}(\gamma_{ij})V_{1,ij}^{mr} + S_{db}^{up}(x_{ij}^{db})S_{\gamma,2}^{up}(\gamma_{ij})V_{2,ij}^{mr} & 1 < Z_{ij}^{db} \leq 2 \\ S_{db}^{down}(x_{ij}^{db})S_{\gamma,2}^{up}(\gamma_{ij})V_{2,ij}^{mr} & 2 < Z_{ij}^{db} \leq 3 \end{cases} \quad (11.44)$$

where:

$$x_{ij}^{db} = Z_{ij}^{db} - I_{ij}^{db} \quad (11.45)$$

with $I_{ij}^{db} = \text{Int}(Z_{ij}^{db})$ (i.e. the largest integer smaller than Z_{ij}^{db}). The dangling bond number Z_{ij}^{db} is defined as:

$$Z_{ij}^{db} = 4 - \sum_{k \neq i,j} S_{Z_{ik}}^{down} Z_{ki}^{el} \quad (11.46)$$

where Z_{ki}^{el} is the number of electrons from atom k available for the bond ki , defined by:

$$Z_{ki}^{el} = \frac{4 - S_{sat}^{down}(Z_{ki})M_{ki}}{Z_{ki} + 1 - S_{sat}^{down}(Z_{ki})M_{ki}} \quad (11.47)$$

with

$$M_{ki} = \sum_{m \neq i} S_Z^{down}(r_{km}) S_M^{up}(Z_{mk}) \quad (11.48)$$

and $S_{sat}^{down}(Z_{ki})$ goes to zero for $Z_{ki} \geq 3$, i.e. when atom k is saturated.

In Eq.(11.44) the attractive potentials $V_{n,ij}^{mr} = V_n^{mr}(r_{ij})$ are simple polynomials cut off smoothly:

$$V_n^{mr}(r_{ij}) = A_n^{mr} \Theta(r_1^{mr} - r_{ij})(r_1^{mr} - r_{ij})^3 \quad (11.49)$$

$$V_2^{mr}(r_{ij}) = A_2^{mr} \Theta(r_2^{mr} - r_{ij})(r_2^{mr} - r_{ij})^2 \quad (11.50)$$

for situations with $n=0, 1$ dangling bonds and 2 dangling bonds respectively. For $Z_{ij}^{db} \geq 3$ we set $V_{ij}^{mr} = 0$. In the presence of dangling bond(s) the middle range attraction is stronger than without dangling bond(s). The parameter γ_{ij} is related to the bond angles by:

$$\gamma_{ij} = \frac{1}{1 + (B/Z_{ij}) \sum_{k \neq i,j} (1 + \cos\theta_{ijk})^4}. \quad (11.51)$$

For small angles, γ_{ij} becomes small. If γ_{ij} is smaller than the lower bounds of the switch functions $S_{\gamma,n}^{up}$, then $V_{ij}^{mr} = 0$ according to Eq.(11.44). According to the definition of Z_{ij}^{db} , $Z_{ij}^{db} = 0$ for each of the equilibrium bulk phases, i.e. chain, graphite, diamond etc. The lower bound of $S_{\gamma,0}^{up}$ is chosen such that the middle range interaction vanishes for each of these bulk phases. So the middle range interaction does not affect the equilibrium properties of these phases to which the short range potential, combined with the given V^{lr} , is fitted, but it only affects the energetics for bond breaking and formation. The lower bound for the switch functions $S_{\gamma,n}^{up}$ depends also on the dangling bond number, favoring the attraction when dangling bond(s) are involved. In order to make the attraction for a single bond more directional than that for a double bond, we took:

$$\tilde{S}_{\gamma,1}^{up} = (S_{\gamma,2}^{up})^2 \quad (11.52)$$

The middle range coordination number Z_i^{mr} is defined as:

$$Z_i^{mr} = \left(\frac{(\sum_j \tilde{v}_{ij})^2}{\sum_j \tilde{v}_{ij}^2} \right)^{\delta_{mr}} \quad (11.53)$$

where we used the short notation $\tilde{v}_{ij} = S_{mr,ij}^{up} V_{ij}^{mr}$ and where δ_{mr} is a correlation exponent. The larger δ_{mr} , the larger Z_i^{mr} , the stronger is the middle range correlation. Without this correlation (i.e. $\delta_{mr} = 0$) the middle range contribution tends to become too large and gives unrealistic configurations with accumulation of atoms in the middle range. On the basis of simulations for the liquid phase at various densities, we took $\delta_{mr} = 1/2$. With this exponent the middle range correlation is equivalent with the correlation in the embedded atom potentials and the total middle range energy of atom i becomes:

$$E_i^{mr} = \frac{1}{2} \frac{\sum_j \tilde{v}_{ij}}{Z_i^{mr}} = \frac{1}{2} \sqrt{\frac{\sum_j \tilde{v}_{ij}^2}{(\sum_j \tilde{v}_{ij})^2}} \sum_j \tilde{v}_{ij} = -\frac{1}{2} \left(\sum_j \tilde{v}_{ij}^2 \right)^{1/2} \quad (11.54)$$

The minus sign appear due to the fact that $\tilde{v}_{ij} \leq 0$ for all pairs ij . With this mr contribution, a reasonable agreement of the dissociation energy curves calculated by the LCBOPII and by DF is obtained, as shown in Fig.11.7 for single, double and triple bonds.

All parameters of the LCBOPII are given in Tables 11.5 and 11.4.

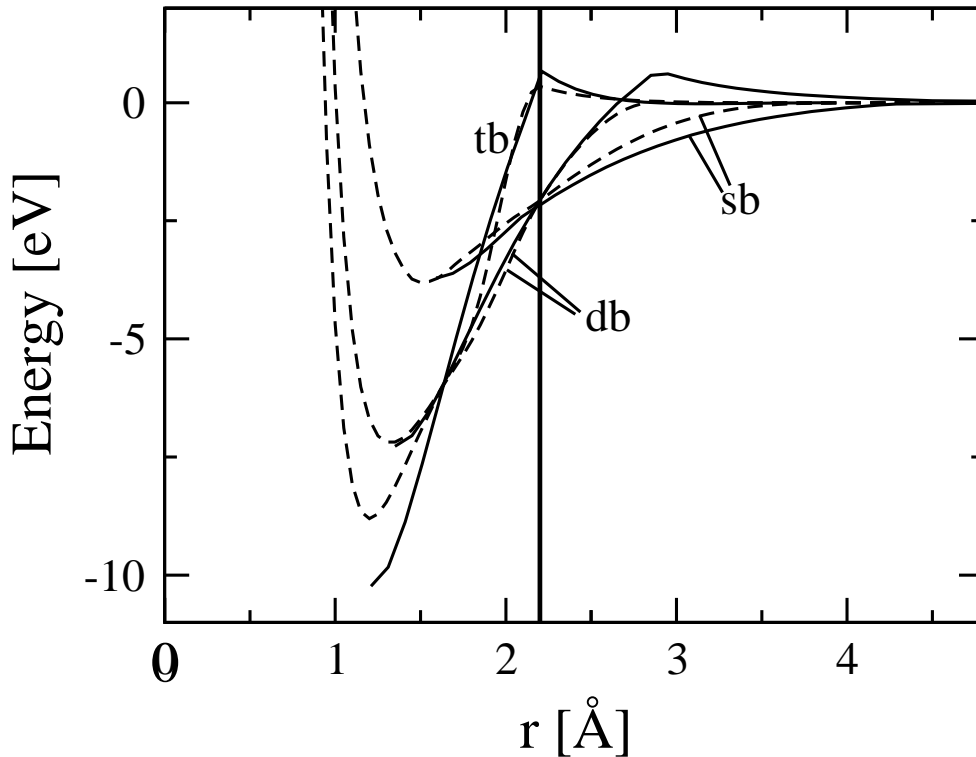


Figure 11.7: Binding energy for $(\text{CH}_3)\text{C}\equiv\text{C}(\text{CH}_3)$ (triple bond, *tb*), $(\text{CH}_3)_2\text{C}=\text{C}(\text{CH}_3)_2$ (double bond, *db*), and $(\text{CH}_3)_3\text{C}-\text{C}(\text{CH}_3)_3$ (single bond, *sb*), calculated by DF (dashed curves) and the LCBOP II (solid curves) as described in the text. To determine the parameters A_1^{mr} and A_2^{mr} of Eq. 11.50, we impose the energy of the central single and double bonds, stretched to 2.2 Å (vertical line), to be equal to the corresponding DF value.

11.3 Properties

The LCBOP II accounts by construction for the structural and elastic properties of most crystalline structures of carbon and for these quantities gives values very close to the LCBOP I [15]. Conversely, it gives a more accurate description of more complex structures, such as the reconstructed surfaces of diamond, and of the energetics of phase transformations and structural defects.

11.3.1 Bulk equilibrium structures and elastic constants.

In Table 11.1 we give the values of the equilibrium interatomic distance d_{CC} , binding energy E_b and stretching force constant F_c for different crystalline structures, compared to the reference values of Refs. [3, 130, 187, 149]. Table 11.1 can be directly compared to Table I of Ref. [15] containing also the values for the LCBOP I and the REBO potential. The values of the LCBOP I⁺ are the same as for the LCBOP I. In Table 11.2 we give the elastic force constants for diamond and graphite compared to the results of Refs. [245] and [246] respectively.

Z	$d_{CC}(\text{\AA})$	$E_b(\text{eV/atom})$	$F_C(\text{eV/\AA}^2)$
1 (di)	1.315 (1.315)	3.081 (3.163)	
2 (ch)	1.325 (1.330)	6.089 (6.175)	62.29 (59.67)
2 (tb)	1.200 (1.200)	8.524 (8.424)	98.85 (99.86)
3 (gr)	1.420 (1.420)	7.374 (7.374)	43.95 (43.57)
4 (d)	1.544 (1.544)	7.349 (7.349)	29.27 (29.52)
6 (sc)	1.770 (1.765)	4.760 (4.689)	
12(fcc)	2.170 (2.170)	2.759 (2.759)	

Table 11.1: Bond distances d_{CC} , binding energies E_b and stretching force constants F_C calculated by the LCBOP-II for the coordination Z of a C_2 dimer bond (di), a linear chain (ch), the triple bond (tb) and the crystalline structures graphite (gr), diamond (d), simple cubic (sc) and face centered cubic (fcc). The binding energy for graphite includes the interlayer binding energy described by V_{lr} . In parenthesis we give the reference values of Refs. [3, 130, 187, 149].

Elastic force constants (in eV/\AA^3) for graphite (gr) and diamond (d). In parenthesis the reference values of Ref. [246] for graphite and Ref.[245] for diamond.	
c_{11} (gr)	6.551 (6.616)
c_{66} (gr)	2.763 (2.746)
c_{11} (d)	6.718 (6.718)
c_{44} (d)	3.604 (3.604)

11.3.2 Diamond (111) and (001) reconstructed surfaces

The energy and structure of crystalline surfaces results from a delicate balance of forces due to undercoordinated atoms at the surface and represent a severe test for interatomic

	Ref.	LCBOP-II	REBO*	REBO	LCBOP-I+
(111)(2X1)					
E_{surf}	1.87	1.2807	1.01	1.91	1.59
d_{12}	1.43	1.460	1.437	1.445	1.455
d_{13}	1.54	1.539	1.559	1.527	1.535
d_{24}	1.54	1.540	1.565	1.534	1.545
d_{35}	1.61 1.62	1.643	1.621	1.644	1.626
d_{46}	1.65 1.64	1.647	1.653	1.690	1.664
(001)(2X1)					
E_{surf}	2.12	1.99	2.14	2.61	2.60
d_{12}	1.37	1.444	1.443	1.546	1.555
d_{13}	1.50	1.519	1.556	1.539	1.521
d_{34}	1.57	1.621	1.602	1.605	1.606
d_{35}	1.55	1.541	1.555	1.549	1.543

Table 11.3: Surface energy (in $\text{eV}/(\text{unit cell of the unreconstructed surface})$) and interatomic distances (in \AA) of the relaxed (2×1) -Pandey-reconstructed (111) and of (2×1) reconstructed (001) surfaces, with the same notation of Fig.6 and Table IV of Ref.[15]. Notice that the REBO potential data in Table IV of Ref.[15] are indicated here as REBO* and refer to the REBO potential without torsional interactions, i.e. with $b_{ij}^{DH} = 0$.

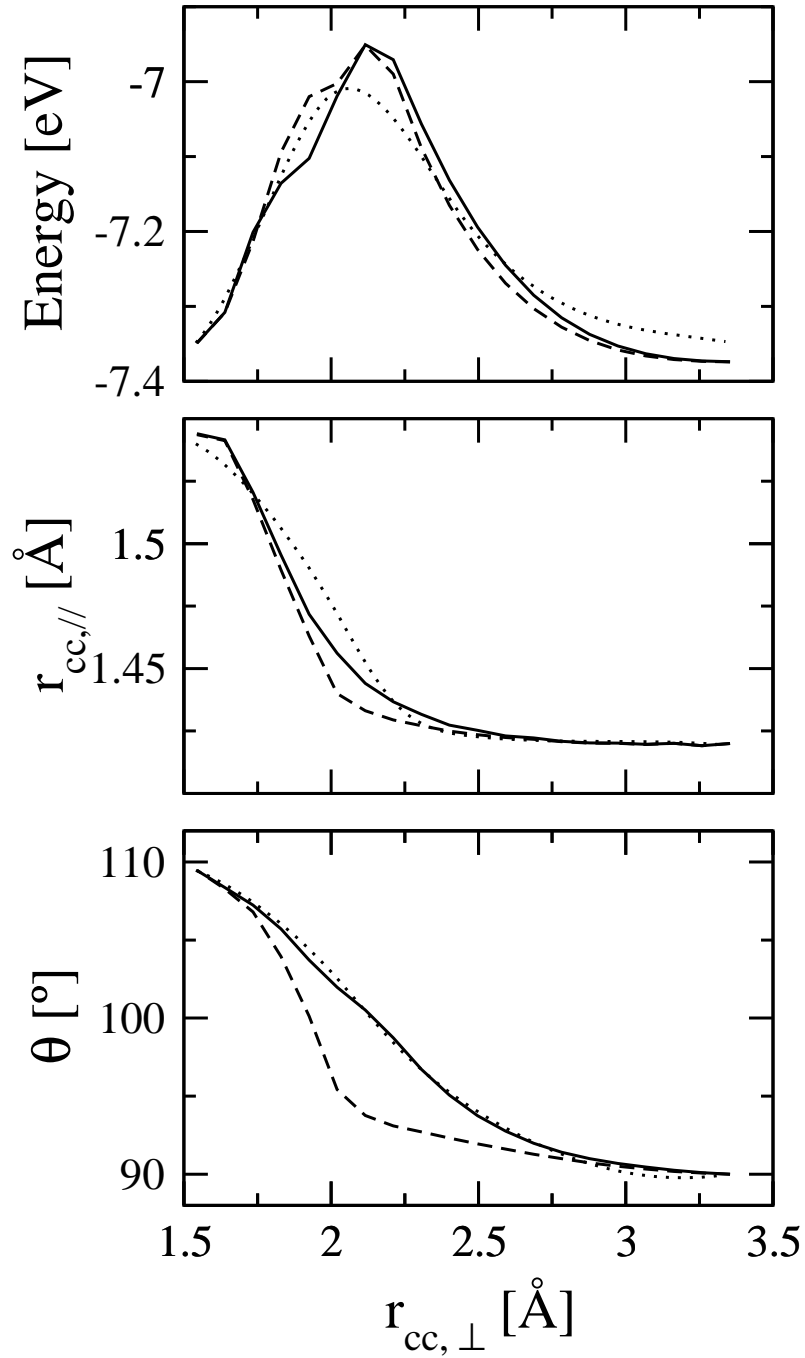


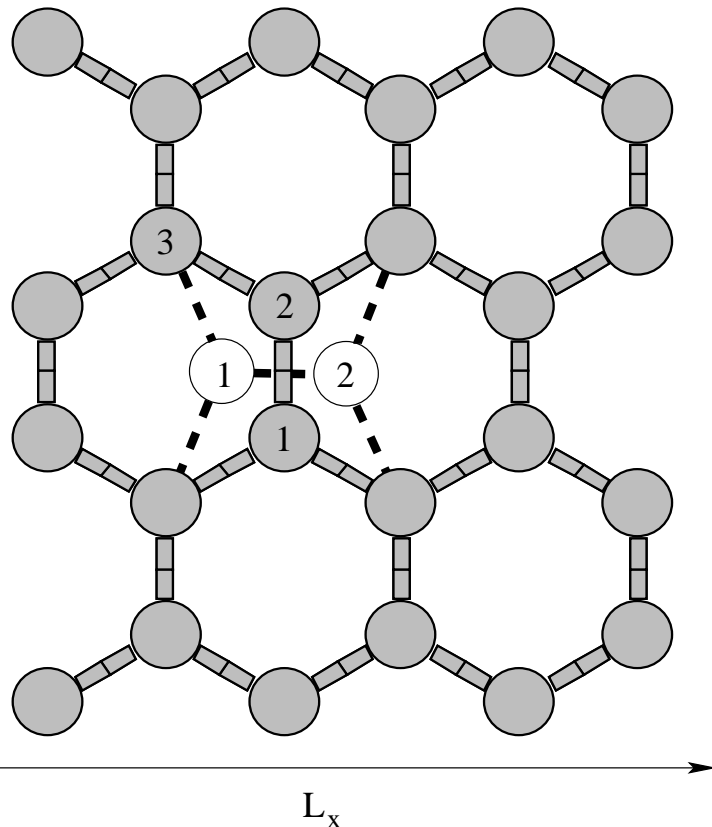
Figure 11.8: The reaction path of the bulk diamond to graphite transformation as a function of $r_{cc,\perp}$ (in \AA), the carbon-carbon distance perpendicular to the (111) bilayers that transform into graphitic layers, (in \AA), compared with the *ab initio* results from Ref. [156]. The path is characterized by: the energy barrier E (in eV) (top panel), b) the intraplanar carbon-carbon distance, $r_{cc,\parallel}$ (in \AA) (middle panel), and c) the buckling angle θ (in degrees) (bottom panel). Solid line: LCBOP II; dashed line: LCBOP I⁺; dotted line: Ref. [156].

potentials. In Table 11.3 we give the surface energy and the interatomic distances of the relaxed (2×1) -Pandey-reconstructed (111) and of the (2×1) reconstructed (001) surfaces, with the same notation of Fig.6 and Table IV of Ref.[15]. It is important to notice that the (2×1) reconstruction of the (001) surface does not imply any torsion of the bonds whereas a torsional contribution is present for the $(111)(2\times 1)$. With the definition of torsion of the LCBOP II both situations are correctly described, whereas the REBO potential and the LCBOP I⁺ give a spurious torsion for the $(001)(2\times 1)$ surface, leading to the too large value of the d_{12} distance (see Table 11.3).

11.3.3 Graphite to diamond transformation.

The transformation from graphite to diamond occurs via a reaction path that can be parametrized by one reaction coordinate, the carbon-carbon distance $r_{CC,\perp}$ between two atoms in adjacent (111) bilayers evolving towards graphitic planes. The ab initio results of Fahy et al. [156], for the energy barrier E , intraplanar carbon-carbon distance $r_{CC,\parallel}$ and buckling angle θ are compared in Fig. 11.8 with the results of the LCBOP II and also the LCBOP I⁺. Notice that only the barrier height has been used in the fitting procedure as it has been done also for the LCBOP I. The structural details of the transformation along the reaction path are much better reproduced by the LCBOP II. The agreement with the ab initio results is satisfactory.

Figure 11.9: Illustration of the formation of the 5-77-5 defects in graphite in a roughly square sample with side L_x . We show how the defect is formed by rotation of $\pi/2$ of the bond between atoms 1 and 2, transforming four hexagons into two pentagons and two heptagons, whence the 5-77-5 name of the defect. A rotation of the bond between atoms 2 and 3 gives an equivalent transformation.



11.3.4 Vacancy in diamond and vacancy in graphite

We have calculated by DF the energy of formation of a vacancy in diamond, $E_{vac}^d = 5.64$ eV and in a single layer of graphite $E_{vac}^{gr} = 7.90$ eV to determine the values of the parameters $F_{23,1}^{conj} = F_{32,1}^{conj}$ and $F_{21,0}^{conj} = F_{12,0}^{conj}$ respectively. Previous DF calculations gave $E_{vac}^d = 7.2$ eV [247] and $E_{vac}^{gr} = 7.6$ eV [248]. The LCBOP-II gives $E_{vac}^d = 6.78$ eV and $E_{vac}^{gr} = 7.90$ eV. For both graphite and diamond, according to our DF calculations the first neighbours move

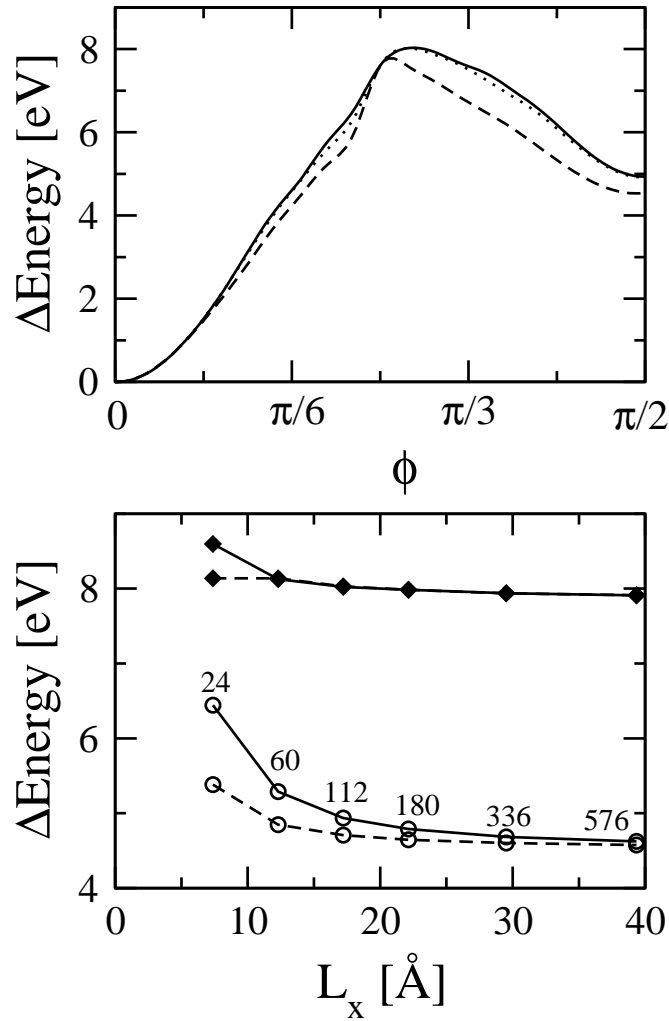


Figure 11.10: Bottom panel: barrier height (filled diamond) and formation energy (empty circles) of the 5-77-5 defect calculated for rotation of the 1–2 (solid line) and 2–3 (dashed line) bonds as a function of the side L_x of the samples defined in Fig. 11.9. As indicated, the total number of atoms in the sample ranges between 24 and 576. One can see that the two estimates converge only for the largest sizes. For the largest sample we show in the top panel the calculated energy as a function of the rotation angle ϕ for three cases: graphene, i.e. a single layer of graphite (dashed line), graphene with positions constrained into the plane (dotted line) and bulk graphite (solid line). As expected, the last two cases are almost undistinguishable and at slightly higher energy than for graphene with out-of-plane relaxation.

away radially from the vacancy up to a distance of 1.52 Å and 1.73 Å, to be compared to LCBOP-II values 1.44 Å and 1.67 Å, for graphite and diamond respectively. The distance between first and second neighbours of the vacancy is 1.40 Å for graphite and 1.50 Å for diamond, in good agreement with our DF data of 1.40 Å and 1.49 Å, respectively.

11.3.5 The 5-77-5 defect of graphite.

The energetics of defect formation is very relevant for understanding diffusion and growth. An important defect in graphite is the so called 5-77-5 topological defect shown in Fig. 11.9 which is formed by rotating a carbon-carbon bond by $\pi/2$ within a graphitic sheet, implying a transformation of four hexagons into two pentagons and two heptagons. This rotation is also called a Stone-Wales transformation [249] and plays an important role in the formation of fullerenes and nanotubes. A tight-binding calculation by Pan et al. [250] for this defect resulted in a formation energy of 4.43 eV, a value much lower than the 10.4 eV previously found by Kaxiras and Pandey by means of ab initio calculations [248]. The discrepancy is attributed by Pan et al. to a too small sample of 18-atoms used in Ref. [248], making unreliable also the activation barrier of 13.7 eV calculated in this paper. In Fig. 11.10 we show the prediction of the LCBOP-II for these quantities that indeed confirm that formation and activation energy of this defect markedly depends on the sample size and shape. Notice that the defect can be obtained in two equivalent ways, by rotating the bond between atoms indicated as 1 and 2 or that between atoms indicated as 2 and 3 in Fig. 11.9. However the calculated energies become equal only in the limit of large samples. In the bottom panel of Fig. 11.10 we give the values of barrier height and formation energy of this defect calculated for rotation of the 1 – 2 and 2 – 3 bonds as a function of the side L_x of the, periodically repeated, samples as shown in Fig. 11.9. One can see that the results for these two cases converge only for very large sizes.

For the largest sample we show in the top panel of Fig. 11.10 the calculated energy as a function of the rotation angle ϕ for three cases, for graphene, i.e. a single layer of graphite, for a single layer of graphite with positions constrained into the graphite plane and for bulk graphite. As expected the last two cases are almost undistinguishable and at slightly higher energy than for graphene with out-of-plane relaxation.

11.4 Appendix. Detail of density functional calculations

The functions t_{ij} (Eq. 11.35) and V_{ij}^{mr} (Eq. 11.44) are fitted to ab initio DF results calculated to this purpose by means of the CPMD package [60]. We used the spin polarized local density functional with BP [79, 78] gradient correction. The Kohn-Sham states were expanded in a plane-wave basis set sampled at the Γ point in the Brillouin zone, and truncated at a kinetic energy of 90 Ry. Semi-local norm-conserving Martins-Troullier pseudopotentials [113] were used to restrict the number of electronic states to those of the valence electrons. The pseudopotential was constructed with a valence-electron configuration s^2p^2 , using core-radii of 1.23 a.u. for both s and p orbitals. The pseudopotential was transformed into the Kleinman-Bylander form [114] with p orbitals as the local term. All calculations were performed using an isolated cubic cell.

Torsional barriers

In the spirit of Refs. [14, 220], we calculated by DF the torsional barriers for the bond between the two three-fold coordinated atoms i and j (shaded circles in Fig. 11.4) for three-fold (white circles) or four-fold (black circles) coordination of the other neighbours. The number Z^{conj} smoothly increases with the number of four-fold sp^3 neighbours. The cases with $Z^{conj} = 0$ (i.e. with a conjugated π_z orbital) and $Z^{conj} = 1$ (i.e. the double bond) correspond to the two molecules studied in Ref. [14]. Hydrogen atoms were used to obtain the correct coordination of the four peripheral atoms.

After geometrical optimization of the planar configuration, we twisted the molecule around the axis through i and j , in steps of $\frac{\pi}{12}$; at each step we optimized the electronic wavefunction without allowing any structural relaxation, in order to have the energy barrier as function of the twisting angle only. The results, shown by symbols in Fig. 11.5, were used to fit the parameters of t_{ij} for the LCBOPII. Note that for the LCBOPII only the coordination of the peripheral atoms, and not the actual positions of the further neighbours not shown in Fig. 11.4, is relevant for the energy of the bond ij .

Dissociation energy curves

We estimated the energies needed to dissociate a single, double or triple bond by describing model molecules as described in the following, to fit the parameters A_1^{mr} and A_2^{mr} in Eq. 11.50. Since the LCBOPII does not describe carbon-hydrogen bonds, we compared DF results for the double bond in $(\text{CH}_3)_2\text{C}=\text{C}(\text{CH}_3)_2$ with the structure with $Z^{conj} = 1$ in Fig. 11.4, i.e. we considered the stretching of the bond between atom i and j , each bonded to other two sp_3 atoms. Analogously, for a single bond we compared $(\text{CH}_3)_3\text{C}-\text{C}(\text{CH}_3)_3$ to a case with i and j each bonded to three sp_3 sites, and, for the triple bond $(\text{CH}_3)\text{C}\equiv\text{C}(\text{CH}_3)$ was compared to a case with i and j each bonded to one sp_3 site. After geometrical optimization, we stretched the central bond in steps of 0.1 Å and optimized the wavefunction without allowing any relaxation. The dissociation curves calculated by DF are reliable when the bond lengths are not too far from their equilibrium value. The dissociation energy was defined as the difference between twice the Kohn-Sham energy of one isolated

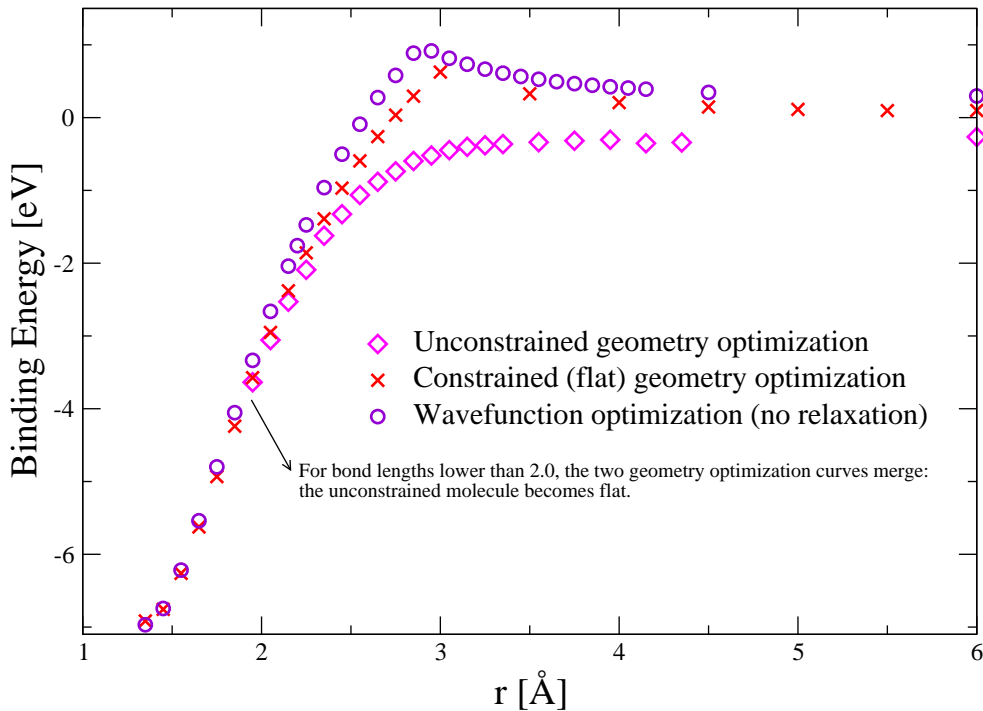


Figure 11.11: Calculated dissociation curves for the double bonded molecule $(\text{CH}_3)_2\text{C}=\text{C}(\text{CH}_3)_2$.

fragment after dissociation and the Kohn-Sham energy of the molecule in its equilibrium geometry. The binding energy has the opposite sign.

As shown in Fig. 11.7, the dissociation of the triple bond is already fairly well described by the potential $V^{lr}(r)$. The parameters A_1^{mr} and A_2^{mr} were obtained by fitting the results obtained for single and double bond, respectively. They were fitted to have the energy of the molecule with the central bond stretched to 2.2 Å equal to the DF binding energy at the same elongation. Note that 2.2 Å is the cut-off of V_{ij}^{sr} . Beyond 2.2 Å the DF results are not a priori reliable, particularly for the unpaired spin of the two fragments. Therefore, consistently with Ref.[251], we assumed that there is no barrier in the formation of the single bond and smoothly connected the curve to zero for $r > 6$ Å.

For the double bond (see Fig. 11.4) we found a small barrier for the formation of the bond at 2.9 Å if the molecule was kept in the planar configuration. Allowing relaxation during the dissociation, the molecule found a dissociation path without any barrier, evolving to a chair configuration from bond length 2.2 Å on. The middle range potential for the double dangling bond cannot account for this steric difference. Therefore we fitted the parameters to a dissociation barrier lower than the DF one, as shown in Fig. 11.7.

11.5 Appendix. Parameters for the LCBOP II

Switch	q	q_{min}	q_{max}	p
S_{sr}^{down}	r_{ij}	1.7	2.2	3.0
S_{lr}^{down}	r_{ij}	5.5	6.0	0
S_{db}^{down}	x_{ij}^{db}	0.0	1.0	0
S_{mr}^{up}	r_{ij}	1.7	2.2	-2.0
S_M^{up}	Z_{ki}	2.0	3.0	0
$S_{\gamma,0}^{up}$	γ_{ij}	0.34	0.93	0
S_Z^{down}	r_{ij}	1.7	2.2	-3.0
S_{sat}^{down}	Z_{ki}	3.0	4.0	0
$S_{\gamma,2}^{up}$	γ_{ij}	0.30	0.93	0

Short range potential V^{sr}						
V_R	A^{sr}	=	53026.92614	α	=	6.74750993
V_A	B_1^{sr}	=	27618.35706	β_1	=	6.34503890
	B_2^{sr}	=	34.07142502	β_2	=	1.19712839
G	g_{min}	=	0.0020588719	g_{gr}	=	0.0831047003
	g_{max}	=	16.0			
	$g_{1,0}$	=	0.7233666272	$g_{1,1}$	=	1.7334665088
	$g_{1,2}$	=	1.8701997632			
	$g_{2,0}$	=	0.73994527795	$g_{2,1}$	=	-1.999211817
	$g_{2,2}$	=	-17.43251545			
	$g_{2,3}$	=	-33.96127110	$g_{2,4}$	=	-44.65392079
	$g_{3,0}$	=	-15.19	$g_{3,1}$	=	-25.6168552398
	$g_{3,2}$	=	-21.51728397			
	$g_{3,3}$	=	0.9899080993	$g_{3,4}$	=	13.66416160
	A_{y_0}	=	-0.4	B_{y_0}	=	0.01875
	A_g	=	5.6304664723	B_g	=	0.1516943990
	C_g	=	0.009832975891			
	D_g	=	-0.189175977654	E_g	=	0.050977653631
H	d	=	0.14	C_1	=	3.335
	C_4	=	220.0	For $C_6, L, \kappa, R_0,$ and R_1 see text.		

Table 11.4: Parameters of the LCBOP II, part one. In the “Switch” table, the distances ($q = r_{ij}$) are in Å. In the “Short range potential” table A^{sr} , B_1^{sr} , and B_2^{sr} are in eV; r_{ij} and d are in Å; α , β_1 , β_2 , and C_1 are in Å⁻¹; C_4 is in Å⁻⁴; all the other parameters in these tables are dimensionless.

		Short range potential V^{sr} (continued)			
F_{ij}^{conj}	$F_{ij,0}^{conj}$				
		$Z_{ji} = 0$	$Z_{ji} = 1$	$Z_{ji} = 2$	$Z_{ji} = 3$
	$Z_{ij} = 0$	0.0000	0.0207	-0.0046	-0.1278
	$Z_{ij} = 1$	0.0207	0.0000	-0.0365	-0.1043
	$Z_{ij} = 2$	-0.0046	-0.0365	0.0000	-0.0273
	$Z_{ij} = 3$	-0.1278	-0.1043	-0.0273	0.0000
	$F_{ij,1}^{conj}$				
		$Z_{ji} = 0$	$Z_{ji} = 1$	$Z_{ji} = 2$	$Z_{ji} = 3$
	$Z_{ij} = 0$	0.0000	0.0584	0.0416	-0.1278
	$Z_{ij} = 1$	0.0584	0.1379	0.0062	-0.1243
	$Z_{ij} = 2$	0.0416	0.0062	0.0936	-0.0393
	$Z_{ij} = 3$	-0.1278	-0.1243	-0.0393	0.0000
	A_{ij}	α_0	=	0.95	
	T_{ij}	A_t	=	-13.15290988672	
		B_{t1}	=	-0.0486839615974	B_{t2} = 3.8
B_{t3}		=	0.62	B_{t4} = 0.005	
Middle range potential V^{mr}					
	r_1^{mr}	=	4.0	r_2^{mr}	= 2.9
	A_0^{mr}	=	-0.2345	A_1^{mr}	= -0.67
	A_2^{mr}	=	-4.94		
Long range potential V^{lr}					
	r_0	=	3.715735		
	λ_1	=	1.338162	λ_2	= 2.260479
	ϵ_2	=	2.827918	ϵ_1	= $\epsilon_2 \lambda_2^2 / \lambda_1^2$
	v_1	=	$\epsilon_1 - \epsilon_2$	v_2	= 0.0

Table 11.5: Parameters of the LCBOP II, part two. A_0^{mr} , A_1^{mr} , and A_2^{mr} are in eV; v_1 , ϵ_1 , and ϵ_2 are in meV; r_1^{mr} , r_2^{mr} , r_0 , are in Å; λ_1 , and λ_2 are in Å⁻¹; all the other parameters are dimensionless.

The LCBOPII: performance in the liquid

*Marco Polo describe un ponte, pietra per pietra.
— Ma qual è la pietra che sostiene il ponte? — chiede Kublai Kan.
— Il ponte non è sostenuto da questa o quella pietra,
— risponde Marco, — ma dalla linea dell'arco che esse formano.
Kublai Kan rimane silenzioso, riflettendo. Poi soggiunge: — Perché mi parli delle pietre? È solo dell'arco che m'importa.
Polo risponde: — Senza pietre non c'è arco*

*Marco Polo describes a bridge, stone by stone.
— Which is the stone that holds the bridge? — Kublai Kan asks.
The bridge is not held by this or that stone, — Marco answers, — but by the arch line that the stones design.
Kublai Kan stays silent, thinking. Then he adds: — Why do you tell me about stones? It is only about the arch that I care of.
Polo replies: — Without stones there is no arch.*

12.1 Introduction

The liquid phase of carbon provides one of the most severe benchmarks for testing the accuracy and transferability of the long range carbon bond order potential (LCBOPII) introduced in the previous chapter.

The purpose of this chapter is two-fold. Firstly, we will compare the LCBOPII liquid with density functional theory based molecular dynamics (DF-MD) simulations and simulation data from the literature. Note that no reliable experimental data are available at these extreme conditions. Secondly, we extend the DF-MD data for the liquid to a wider range of the phase diagram employing the LCBOPII, exploiting the fact that LCBOPII simulations are orders of magnitude faster than DF-MD simulations.

The present chapter is organized as follows. In section 12.2 we describe the simulation methods employed, both for the classical potentials (i.e. the LCBOPII and the LCBOP⁺) and for DF-MD. In section 12.3 we describe the equation of state (EoS, $P = P(\rho, T)$) of

liquid carbon, and propose a polynomial fit for the EoS. In section 12.4 we present the distribution of sp -, sp_2 -, sp_3 -coordinated sites over a wide range of densities and temperatures. Our analysis shows the impressive recovering of reference data. Subsequently, in section 12.5 we present the radial distribution functions ($g(r)$) at several densities and temperatures. We discuss both total $g(r)$ and partial $g(r)$ for atoms with specific coordinations. In section 12.6 we briefly report the behaviour of the angular distribution functions at different state points. Sections from 12.3 to 12.6 are naturally split in two parts, the first comparing LCBOP II with reference data, and the second with properties for state points not extensively covered in literature. We conclude in section 12.7 with a brief resume, conclusions, and an outlook.

12.2 Methods

All the simulations with the LCBOP II are performed using the Metropolis Monte Carlo (MC) algorithm, in the constant volume (NVT) ensemble. Systems consisted of 128 and 1000 atoms in a periodically replicated cubic box. Initial configuration were generated starting from a cubic arrangement that was melted at the highest probed temperature (15000 K). Subsequently, the temperature for the systems were fixed at 7 values (15000, 10000, 8000, 7000, 6000, 5000, 4500 K), and the systems were equilibrated for $5 \cdot 10^5$ MC moves per particle, followed by a production run of 10^6 MC moves per particle. The 128 particles samples were used to compare the results of the LCBOP II with calculated DF-MD data or with data taken from literature. The 1000-particle MC simulations with the LCBOP II were used to generate the bulk of the data presented in this paper. The local structure of the liquid, i.e. the coordination fractions and the radial and angular distribution functions show a negligible dependence on the system size. However, some collective properties, such as pressure and internal energy, show a small but non-negligible system size dependence. Typically, the 128 and 1000-particle systems show a pressure difference of 3% and an internal energy difference of 0.3% in energy. We selected 15 densities * ranging from $3.99 \cdot 10^3 \text{ kg/m}^3$ to $1.73 \cdot 10^3 \text{ kg/m}^3$. The lowest density was chosen to be near the graphite melting line [16]. The pressure was calculated via virtual volume displacements. If V is the volume of the sample, its potential energy is U_V at a given configuration. The energy of the sample rescaled to a volume V' is then $U_{V'}$. In the limit of $V'/V \rightarrow 1$, and with V' fixed as well as V , then:

$$P = \rho k_B T - \frac{\langle U_{V'} - U_V \rangle}{V' - V} \quad (12.1)$$

where $\langle \dots \rangle$ denotes the average in the NVT ensemble. This method avoids the measurement of forces, not needed in MC simulations.

A small part of the simulated state points are in the region of the phase diagram where the liquid is metastable with respect to diamond.

We have not carried out a numerical evaluation of the phase diagram predicted by the LCBOP II, evaluation that was done in Ref. [16] for the LCBOP I⁺. Yet, using direct free-energy difference calculations we determined the liquid freezing line for the LCBOP II from

*The complete list of densities, in units of 10^3 kg/m^3 is: 3.99, 3.87, 3.75, 3.64, 3.54, 3.44, 3.33, 3.24, 3.14, 3.05, 2.79, 2.47, 2.19, 1.95, 1.73. Points are naturally thicker where the $|dT/dP|$ is higher, see section 12.3.

the freezing line of the LCBOP^{I+} determined in Ref. [16]. We sampled with the LCBOP^{I+} a liquid and a diamond sample at the same phase point on the calculated diamond melting line and at intervals a virtual swapping between the two potentials is performed. This means that the energy of independent configurations during this run was evaluated also with the LCBOP^{II}. We call u_{I+} the energy per particle given by the LCBOP^{I+} at a certain configuration and u_{II} , the same quantity as given by the LCBOP^{II} at the same configuration, and $\Delta u = u_{II} - u_{I+}$. Under the hypothesis that the portions of phase space sampled by the two potentials have considerable overlap, their difference in chemical potentials in the same phase point can be directly estimated from a simulation by using:

$$\beta\Delta\mu_x = -\ln\langle\exp(-\beta\Delta u)\rangle_{I+}$$

where $\Delta\mu_x = \mu_x^{II} - \mu_x^{I+}$ is the difference in chemical potentials between the LCBOP^{II} and the LCBOP^{I+}, x is either l for the liquid or d for diamond, $\beta = 1/k_B T$, and $\langle\dots\rangle_{I+}$ denotes ensemble average with the LCBOP^{I+}. At the initial state point, it holds:

$$\begin{aligned}\Delta\mu_0 &= \Delta\mu_{d,0} - \Delta\mu_{l,0} = \mu_{d,0}^{II} - \mu_{d,0}^{I+} - (\mu_{l,0}^{II} - \mu_{l,0}^{I+}) = \\ &= \mu_{d,0}^{II} - \mu_{l,0}^{II} \doteq \Delta\mu_0^{II}\end{aligned}$$

in fact $\mu_{d,0}^{I+} - \mu_{l,0}^{I+} = 0$ for the choice of the simulation point. The last equality defines $\Delta\mu_0^{II}$, that in general is non zero. The melting T for the LCBOP^{II} at the chosen P can be estimated using the thermodynamic relation:

$$\left.\frac{\partial\beta\Delta\mu^{II}}{\partial\beta}\right|_P = h_d^{II} - h_l^{II}$$

where h_d^{II} and h_l^{II} are the specific enthalpies for the diamond and the liquid, evaluated with the LCBOP^{II} and $\Delta\mu^{II}$ is now the difference in chemical potentials between the two phases at any state point. The above differential equation can be readily solved with the trapezoidal rule in the framework of predictor-corrector algorithms. To the purpose the predictor is evaluated with the help of $h_{d,0}^{II}$ and $h_{l,0}^{II}$ calculated in one simulation for the liquid and one for the diamond with the LCBOP^{II} at the chosen state point. Then:

$$\frac{1}{k_B\bar{T}_m^{II}} = \frac{\Delta\mu_0^{II}}{h_{l,0}^{II} - h_{d,0}^{II}} + \frac{1}{k_B T_m^{I+}}$$

where T_m^{I+} is the diamond melting T at the chosen pressure the LCBOP^{I+}, \bar{T}_m^{II} is the predictor for the diamond melting T for the LCBOP^{II} at the same pressure, and $\Delta\mu_0^{II}$ is at T_m^{I+} . With a simulation a the predicted temperature \bar{T}_m^{II} , \bar{h}_d^{II} and \bar{h}_l^{II} are now calculated. Hence, the corrected melting temperature \hat{T}_m^{II} is:

$$\frac{1}{k_B\hat{T}_m^{II}} = \frac{\Delta\mu_0^{II}}{\frac{1}{2}(h_{l,0}^{II} + \bar{h}_l^{II} - (h_{d,0}^{II} + \bar{h}_d^{II}))} + \frac{1}{k_B T_m^{I+}}$$

We chose $T = 6000$ K, which gave $P = 59.44$ GPa for the coexistence for the LCBOP^{I+} [16]. We calculated $\beta\Delta\mu_d = -0.005$, and $\beta\Delta\mu_l = -0.210$. For the LCBOP^{II} $h_d = -313.4$ kJ/mol and $h_l = -429.2$ kJ/mol. It is important to note that the distributions of both the internal energy and the volume for the LCBOP^{I+} and the LCBOP^{II} show significant overlap,

and that the values of $(U_{\text{LCBOPII}} - U_{\text{LCBOPI}^+})$ are bound within reasonable values since the LCBOP $^+$ and the LCBOPII are rather similar. Both features are required for an accurate estimate of the chemical potential difference using Eq. 12.2. The predictor-corrector scheme gave a converged value of $T_m^{II} = 5505$ K in only two iterations. From the calculation at the final T_m^{II} of Δh and Δv (i.e. the difference in enthalpy and specific volume between the liquid and diamond), it is possible to evaluate the slope of the melting line with the Clausius-Clapeyron equation: $dT/dP = T\Delta v/\Delta h$. The slope was evaluated as 28.04 K/GPa. We compare it to the very close value of 28.97 K/GPa as given by the LCBOP $^+$ at the same pressure.

The DF-MD simulations were performed in the NVT ensemble, using the Car-Parrinello [62] method as implemented in the CPMD package [60]. The electronic structure was calculated using the Kohn-Sham formulation of density functional theory employing the gradient-corrected density functional in its BP [79, 78] parametrization. The system consisted of 128 atoms in a periodically replicated cubic cell. The Kohn-Sham states were expanded in a plane-wave basis set sampled at the Γ point in the Brillouin zone, and truncated at a kinetic energy (E_{cut}) of 35 Ry. This cut-off ensured the convergence of the binding energy for small clusters within 5 kJ/mol per bond. We restricted the number of electronic states to those of the valence electrons by means of semi-local norm-conserving Martins-Troullier pseudopotentials [113]. We constructed the pseudopotential with a valence-electron configuration s^2p^2 , using core-radii of 1.23 a.u. for both the $l = s$ and $l = p$. The pseudopotential was transformed into the Kleinman-Bylander form [114] with $l = p$ as the local term. The ionic temperature was controlled via a Nosé-Hoover thermostat [94]. As in our DF-MD simulations liquid carbon is metallic, a proper implementation of the Car-Parrinello method requires the electronic degrees of freedom to be coupled to a thermostat. Here we coupled a Nosé-Hoover chain thermostat to the electronic degrees of freedom with a target energy of 0.25 eV and a coupling frequency of 15000 cm^{-1} . The target energy was estimated using the procedure proposed by Blöchl and Parrinello [98]. The coupling frequency of 15000 cm^{-1} was chosen to be within the dominant frequencies of the wavefunctions, determined from a DF-MD simulation with fixed ion positions. The initial points were taken from equilibrated LCBOPII configurations at the same density and temperature. These were equilibrated for about 0.5 ps, followed by a production run of 5 ps. Pressures were evaluated with the method explained in appendix 9.5.

12.3 Equation of state

12.3.1 Comparison

Fig. 12.1 shows $\rho - P$ state points along the 6000 K isotherm obtained with DF-MD and the LCBOPII. For comparison we have also plotted results from literature: data obtained with DF-MD employing the BPE functional [14], and data obtained with the LCBOP $^+$ [17] and the AIREBOII potential [220]. The difference in calculated pressures between the two DF-MD simulations should be attributed to the use of a different functional. Differences in E_{cut} and pseudopotential should not contribute significantly to this discrepancy, as both setups yielded good binding energies. Compared to the DF-MD results, the LCBOPII improves the performance of the LCBOP $^+$ by lowering the pressure towards the DF-MD

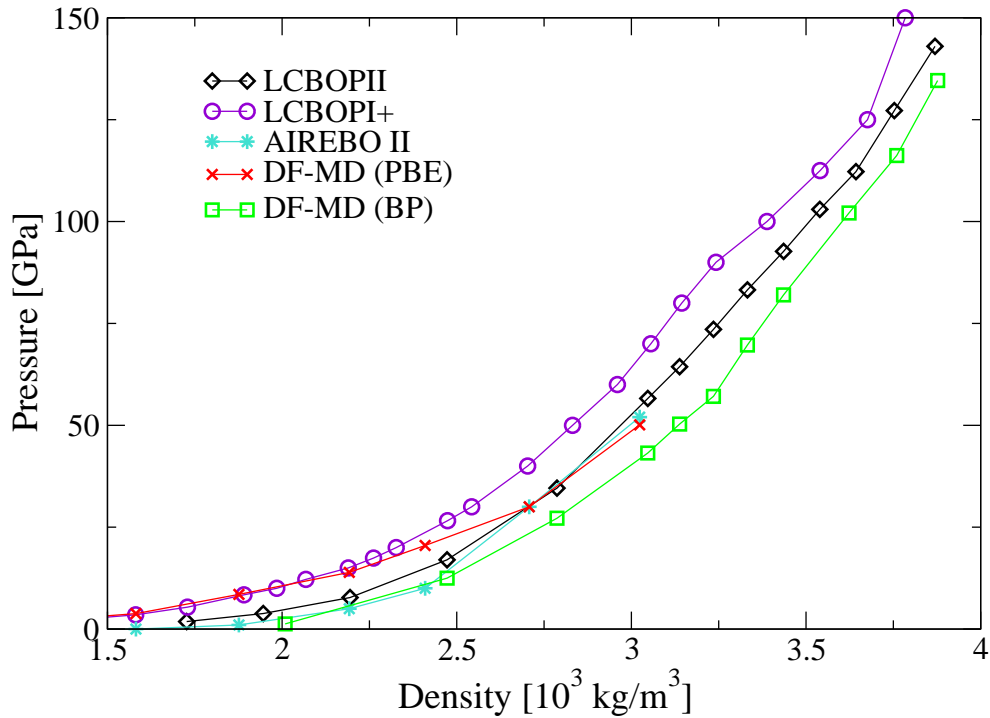


Figure 12.1: Calculated equations of state for the LCBOP II and DF-MD employing the BP functional. The statistical error for the pressure is smaller than the symbol size. Note, that the DF-MD results for the 9 highest densities are also reported in Ref. [17]. For comparison results obtained with the LCBOP I+ [17], the AIREBO II potential [220], and DF-MD employing the PBE functional [14] are shown. From these last two series, a point at $1.28 \cdot 10^3 \text{ kg/m}^3$ is not shown.

result and by suppressing the decrease of the slope of the density-pressure curve around $3.3 \cdot 10^3 \text{ kg/m}^3$. The results for the AIREBO II potential [220] are similar to that of the LCBOP II. The early short-range potentials CBOP and REBO do reproduce the DF-MD data for the EoS reasonably well for low densities, but fail at higher densities beyond the spurious LLPT. For the REBO potential, this is shown in Ref. [17].

12.3.2 Predictions

In Fig. 12.2 we have plotted the pressure-density curves for 7 isotherms from 4500 K to 15000 K. Also the estimated coexistence line is plotted. In the stable region all curves show a regular monotonic increase of the slope of the curve. In the undercooled region we observe for the 4500 K and 5000 K isotherms, in a small density region around $3.3 \cdot 10^3 \text{ kg/m}^3$, a decrease of the slope. For the LCBOP I+, this wiggling of the pressure-density curve was a pronounced feature at 6000 K, and associated with a rapid switching of the dominant coordination from three- to four-fold. For the LCBOP II, the same coordination change occurs in the wiggling region around $3.3 \cdot 10^3 \text{ kg/m}^3$ of the 4500 and 5000 K isotherms (see below).

A wiggle in the ρ - P equation of state denounces a sudden decrease of the isothermal compressibility ($1/\rho \text{ d}P/\text{d}\rho$). Thinking pressure as the leading parameter, in this region the liquid reacts to an increase of pressure with an increase of density, higher than at the

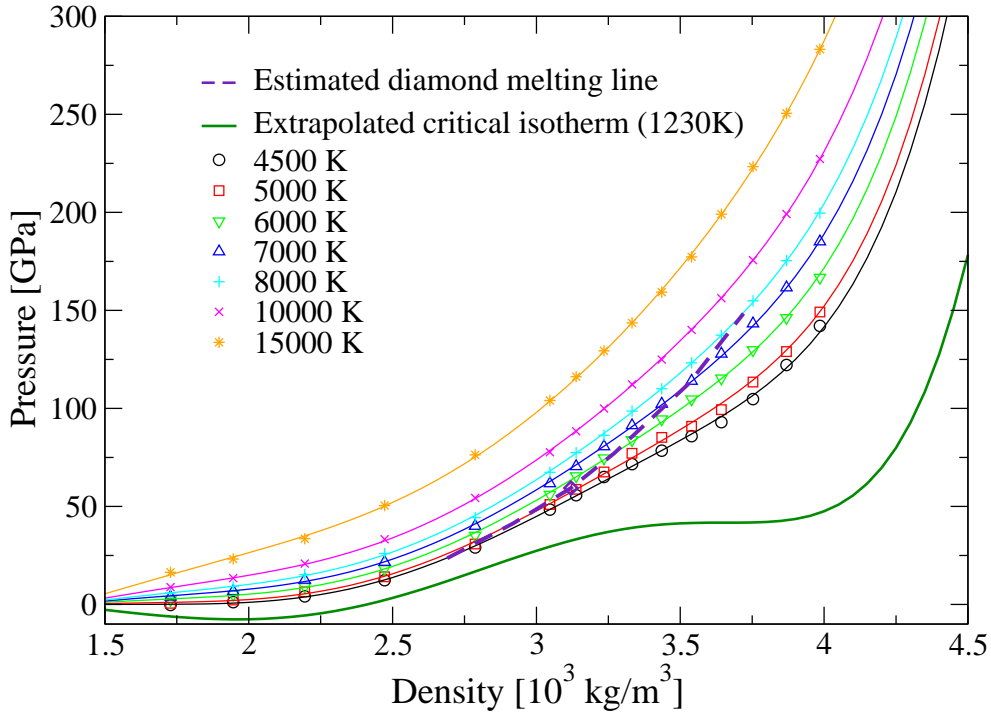


Figure 12.2: Equations of state for the LCBOP11 at seven different temperatures: 4500 K (circles), 5000 K (squares), 6000 K (diamonds), 7000 K (triangles), 8000 K (plus), 10000 K (crosses), 15000 K (stars). Each temperature is sampled at 15 different densities. Error bars, not shown, are within the symbol size. The relative error is around 1% at the highest pressure and increases up to 10% at the lowest (i.e. smaller than 5 GPa). The thick line at the bottom is the extrapolated critical isotherm, at 1230 K. It has a horizontal inflection point at density $3.66 \cdot 10^3 \text{ kg/m}^3$ and pressure 41.74 GPa. The dashed line is the estimated diamond melting line, started from the calculated point shown as a diamond (at 5505 K, 59.4 GPa, and $3.12 \cdot 10^3 \text{ kg/m}^3$, see section 12.2), and prolonged assuming constant dT/dP .

surrounding densities. This is understandable thinking that on the left and on the right of the wiggle, the liquid needs mainly to shorten covalent bonds to increase density. In the transition region, a bigger increase of density is readily achieved receiving an extra neighbour. Given the shape of the lower temperatures equation of state, nothing would prevent to speculate the existence of a liquid – liquid phase transition at even lower temperatures, eventually a first order one. We observed that samples at temperatures lower than $\sim 4000 \text{ K}$ rather froze, especially at densities higher than $3 \cdot 10^3 \text{ kg/m}^3$. This makes the speculation impossible to prove with this sample size. A (much) bigger sample size and a careful annealing could reveal a scenario similar to liquid water, with its liquid – liquid phase transition hidden in the glass region [57, 45, 47].

We employed a polynomial function to fit the calculated LCBOP11 equation of state:

$$\begin{aligned}
 P(\rho, T) = & (\rho - \rho_0)(c_1 + c_2T + c_3T^2 + c_4T^3) + (\rho - \rho_0)^2(c_5 + c_6T + c_7T^2 + c_8T^3) + \\
 & + (\rho - \rho_0)^3(c_9 + c_{10}T + c_{11}T^2 + c_{12}T^3) + (\rho - \rho_0)^4(c_{13} + c_{14}T) + \\
 & + (\rho - \rho_0)^5(c_{15} + c_{16}T) + (\rho - \rho_0)^6(c_{17} + c_{18}T)
 \end{aligned} \tag{12.2}$$

The parameters of the fit function are given in table 12.1 and are obtained by minimizing the square of the difference between the calculated and fitted pressures. The functional

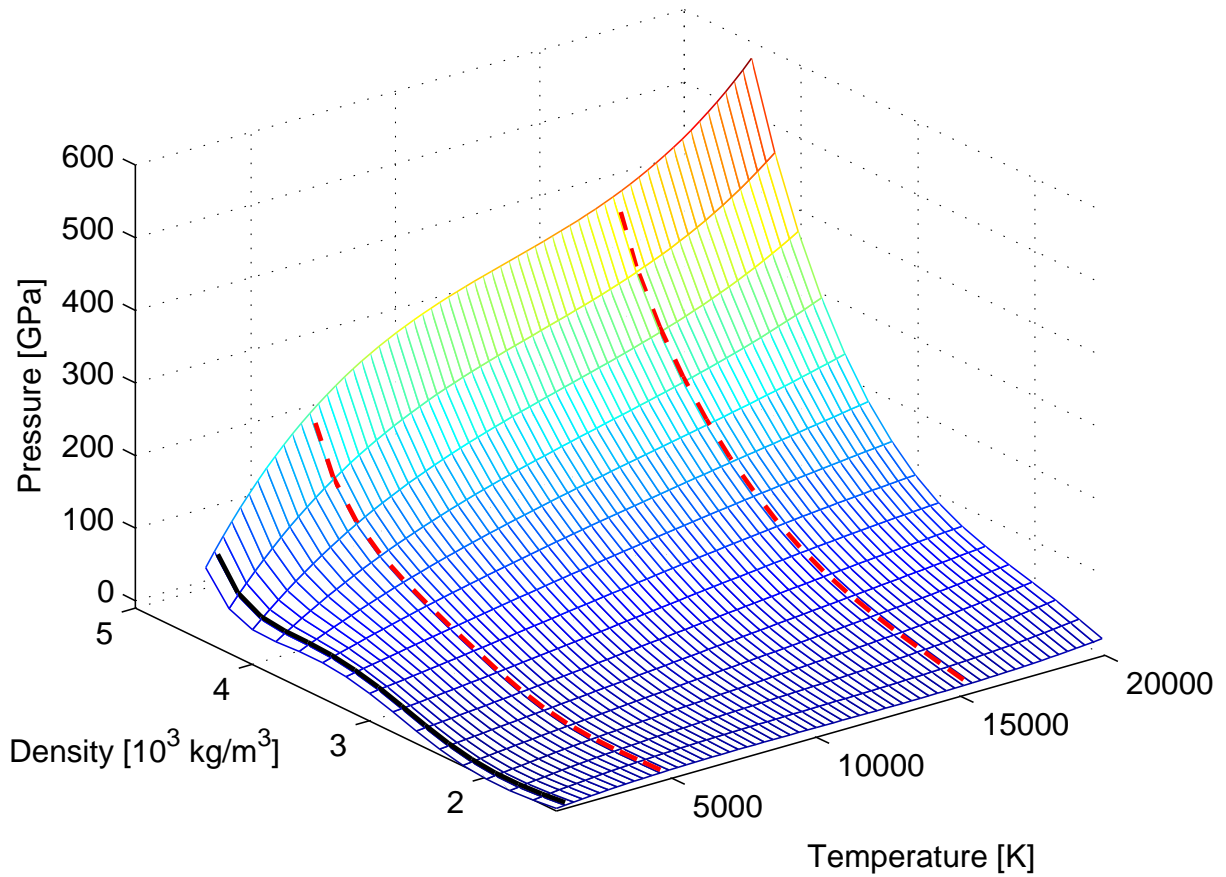


Figure 12.3: Three dimensional plot of the fitted equation of state, $P = P(\rho, T)$. The solid line is the critical isotherm (at 1230 K), while the two dashed lines are the two extreme isotherms of the simulated state points (i.e. 4500 and 15000 K).

form is fully empirical and designed to have a minimum number of parameters needed to describe all the features of the data points. The fit could possibly be employed outside the region of calculated state points. A reasonable extension for the density would be a range between ~ 1.5 to $\sim 4.5 \cdot 10^3 \text{ kg/m}^3$.

The polynomial fit reproduces the wiggling of the 4500 and 5000 K isotherms for the undercooled liquid. It is tempting to explore the behavior of the fit at lower temperatures, beyond the region of calculated state points. At these temperatures the liquid is even more undercooled. With decreasing temperatures the wiggles become more pronounced, yielding an inflection point with zero slope in the $P - \rho$ plane for the 1230 K isotherm at $3.66 \cdot 10^3 \text{ kg/m}^3$, and 41.74 GPa. This behaviour is typical for the critical isotherm. At lower temperatures the isotherms of the fit function show a van der Waals loop, indicating a first-order phase transition associated with a density change. However, in our simulations the system freezes below 4000 K, especially at densities higher than $3 \cdot 10^3 \text{ kg/m}^3$. Hence it would be rather speculative to propose the presence of a liquid – liquid phase transition. Still it might be interesting to explore the undercooled liquid by considering (much) larger system size and perform careful annealing to see if a scenario similar to that of liquid water, with its speculated liquid – liquid phase transition hidden in the glass region [57, 45, 47] would appear.

c_1 :	-3.22435447999	10^7	J
c_2 :	9.88711221869	10^3	J K ⁻¹
c_3 :	-6.05245942342	10^1	J K ⁻²
c_4 :	1.63510457127	10^5	J K ⁻³
c_5 :	2.53078007240	10^4	J m ³ kg ⁻¹
c_6 :	-9.47985686674	10^1	J m ³ kg ⁻¹ K ⁻¹
c_7 :	1.20616311340	10^{-3}	J m ³ kg ⁻¹ K ⁻²
c_8 :	-3.42300962915	10^{-8}	J m ³ kg ⁻¹ K ⁻³
c_9 :	-2.49596407210	10^1	J m ⁶ kg ⁻²
c_{10} :	-2.04475278536	10^{-4}	J m ⁶ kg ⁻² K ⁻¹
c_{11} :	-5.00834553350	10^{-7}	J m ⁶ kg ⁻² K ⁻²
c_{12} :	1.41814229613	10^{-11}	J m ⁶ kg ⁻² K ⁻³
c_{13} :	5.24835967149	10^{-2}	J m ⁹ kg ⁻³
c_{14} :	2.60371540562	10^{-6}	J m ⁹ kg ⁻³ K ⁻¹
c_{15} :	-3.08370110012	10^{-6}	J m ¹² kg ⁻⁴
c_{16} :	-2.44955788712	10^{-10}	J m ¹² kg ⁻⁴ K ⁻¹
c_{17} :	5.24072792404	10^{-9}	J m ¹⁵ kg ⁻⁵
c_{18} :	-3.22777913222	10^{-14}	J m ¹⁵ kg ⁻⁵ K ⁻¹
ρ_0 :	1.35694366721		kg m ⁻³

Table 12.1: Parameters of Eq. 12.2.

Fig. 12.4 shows the binding energy per particle at all the simulated state points. We note that at all temperatures there is a minimum in binding energy at $2.5 \cdot 10^3 \text{ kg/m}^3$. The almost perfectly parabolic dependency on density of the binding energy at the highest temperature, is step by step lost upon decreasing temperature. At the two lowest temperatures there appear pronounced wiggles as in the EoS. Reminding that all the reported points come from equally long simulations, the increase of the size of the error bars at lower temperature can be explained by the fact that the diffusion of the liquid is there slower. Thus, the system explore a smaller region of the phase space in the same number of attempted moves, giving a bigger uncertainty in the determination of the average binding energy.

12.4 Coordination

12.4.1 Comparison

The local coordination of atoms is determined by counting neighbours using the smoothed cutoff functions defined for the LCBOP-II. Specifically, we employed the following cut-off radii: atoms closer than 0.17 nm to a given atom are counted as its integer neighbours, atoms further than 0.22 nm are not counted, and atoms in between are partially counted, by means of the cut-off function $S_{Z,ij}^{\text{down}}$ (Eq. 11.11). This implies that a coordination fraction equal to e.g. three can be given by two integer and two partial neighbours. This definition is consistently employed throughout the following analysis, in any situation the definition of neighbour come into play (i.e. for the partial radial distribution functions and the angular total and partial distribution function). Here we should note that in

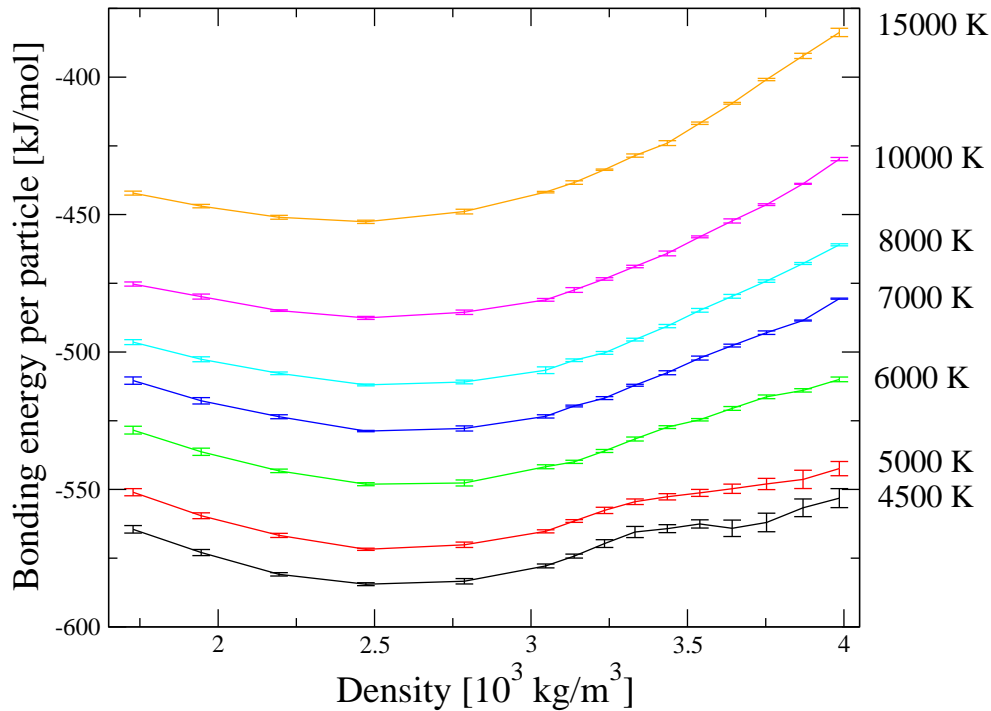


Figure 12.4: Energy per particle at all the temperatures. The symbol coding is the same as for Fig. 12.2.

literature various alternative definitions of the coordination fractions are employed. These may yield different values for a similar atomic configuration. Hence, a direct comparison of coordinations fractions with literature data should be done with some care, a point also noted by Marks [223]. Fig. 12.5 shows the coordination fractions calculated with the LCBOPII and DF-MD along the 6000 K isotherm. For comparison also the results for the LCBOP⁺ from Ref. [17] are shown. We see that, except for a slight overestimation of the three-fold fractions in the low-density regime, the LCBOPII results reproduce the DF-MD data very well, both for the density dependence as for the absolute values. The LCBOPII improves the predictions of the LCBOP⁺: at densities up to $\sim 3.4 \cdot 10^3 \text{ kg/m}^3$, the LCBOPII predicts less three-fold and more two- and four-fold sites, thus getting closer to the DF-MD data. At higher densities, where the LCBOP⁺ overestimated the four-fold fraction, the coordination fractions predicted by the LCBOPII almost perfectly recover the DF-MD data. Five-fold coordinated atoms (not shown in Fig. 12.5) only appear in the high-density region. At $3.75 \cdot 10^3 \text{ kg/m}^3$ the fraction for the LCBOPII is 0.1, slightly larger than DF-MD value of 0.07. Note that this is a remarkable achievement of the potential, as the structures used to develop the LCBOPII did not have five-fold coordination. We also note that in the high density range, short range BOPs hardly show coordination beyond three, while for the LCBOP⁺ the five-fold fraction remained negligible. The appearance of five-fold coordinated structures in LCBOPII calculations is due to the presence of the "middle range" part in the potential and to the softening of angular correlations. In fact, in older BOPs as well as in the LCBOP⁺, a small angle such as 60 degree had a significant energetic penalty, fitted to a twelve-fold structure (i.e. an fcc lattice) that applied also for five-fold sites. With the LCBOPII the penalty at small angle for this lower coordination has been reduced (see Eq. 11.12). As already shown in Ref. [17] the REBO potential yields

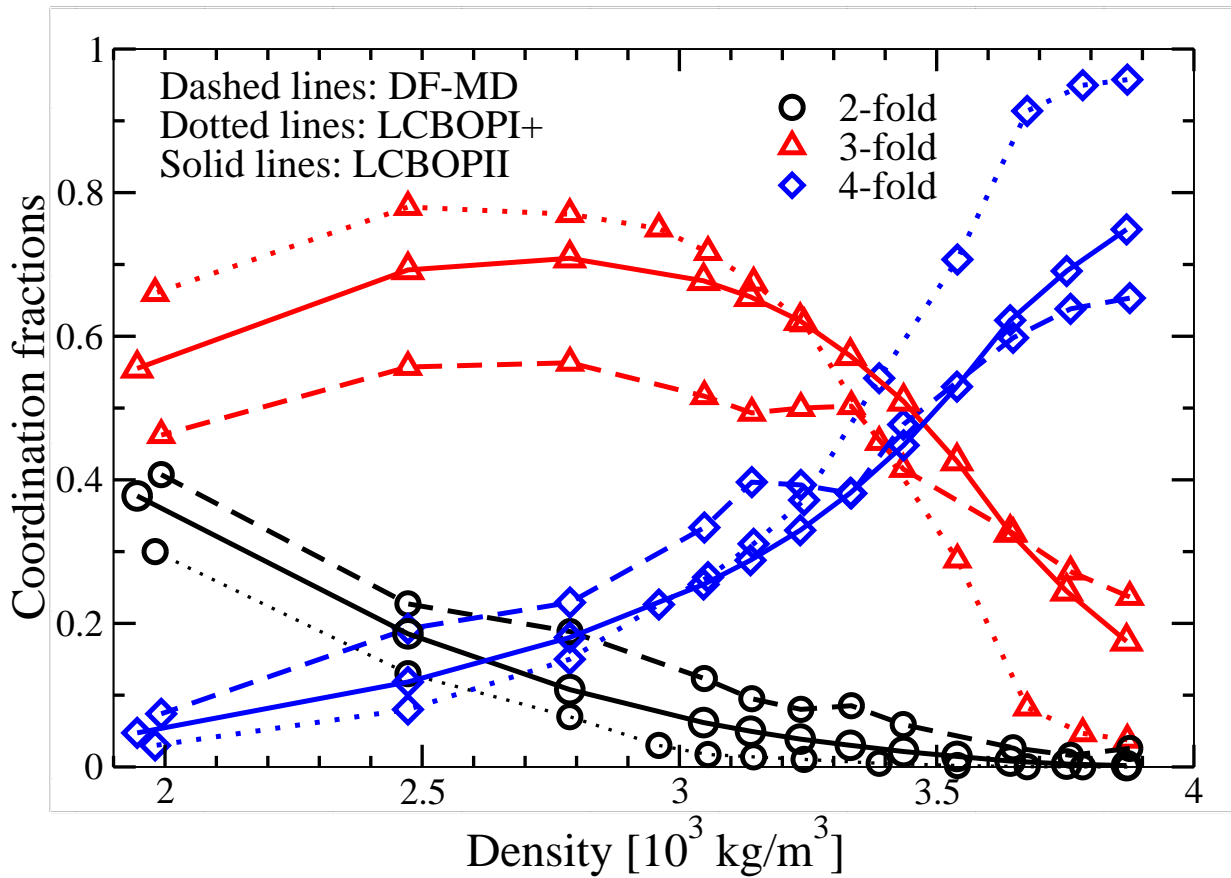


Figure 12.5: Comparison of coordination fractions at 6000 K between the LCBOP11 (solid lines) and reference data coming from our own DF-MD (dashed lines). Data at density $2.79 \cdot 10^3 \text{ kg/m}^3$ and higher are the same shown in Ref. [17]. Circles always represents two-fold sites, triangles three-fold, and diamonds four-fold. Five-fold sites are not shown but can be deduced by subtraction, since no atoms with a single bond (one-fold) or six-fold sites were observed at these densities. The error bars, not shown, are within the symbol size, ~ 0.01 for the LCBOP11, and ~ 0.02 for the DF-MD points.

a negligible four-fold fraction at all the densities: the three-fold atoms replace the two-fold upon increasing density, until the spurious LLPT at which all the atoms become three-fold. The transition is also appears for CBOP, but the fraction of four-fold atoms raises until $\sim 10\%$ before the transition. No data regarding coordinations in the liquid are available for the AIREBO11 potential, while the environment dependent potential (EDIP) introduced by Marks [147] is similar to the LCBOP11 in reproducing the DF-MD coordination fractions at 5000 K [223].

12.4.2 Predictions

In Fig. 12.6 we show the average coordination fractions at several temperatures. For clarity two-, three-, four-, and five-fold coordination fractions are shown in different panels, respectively from top to bottom. The fraction of six-fold coordinated atoms were negligible at all simulated state points. One-fold coordinated atoms appear only in a small amount (a few %) at the lowest densities, and are not shown. Considering the density de-

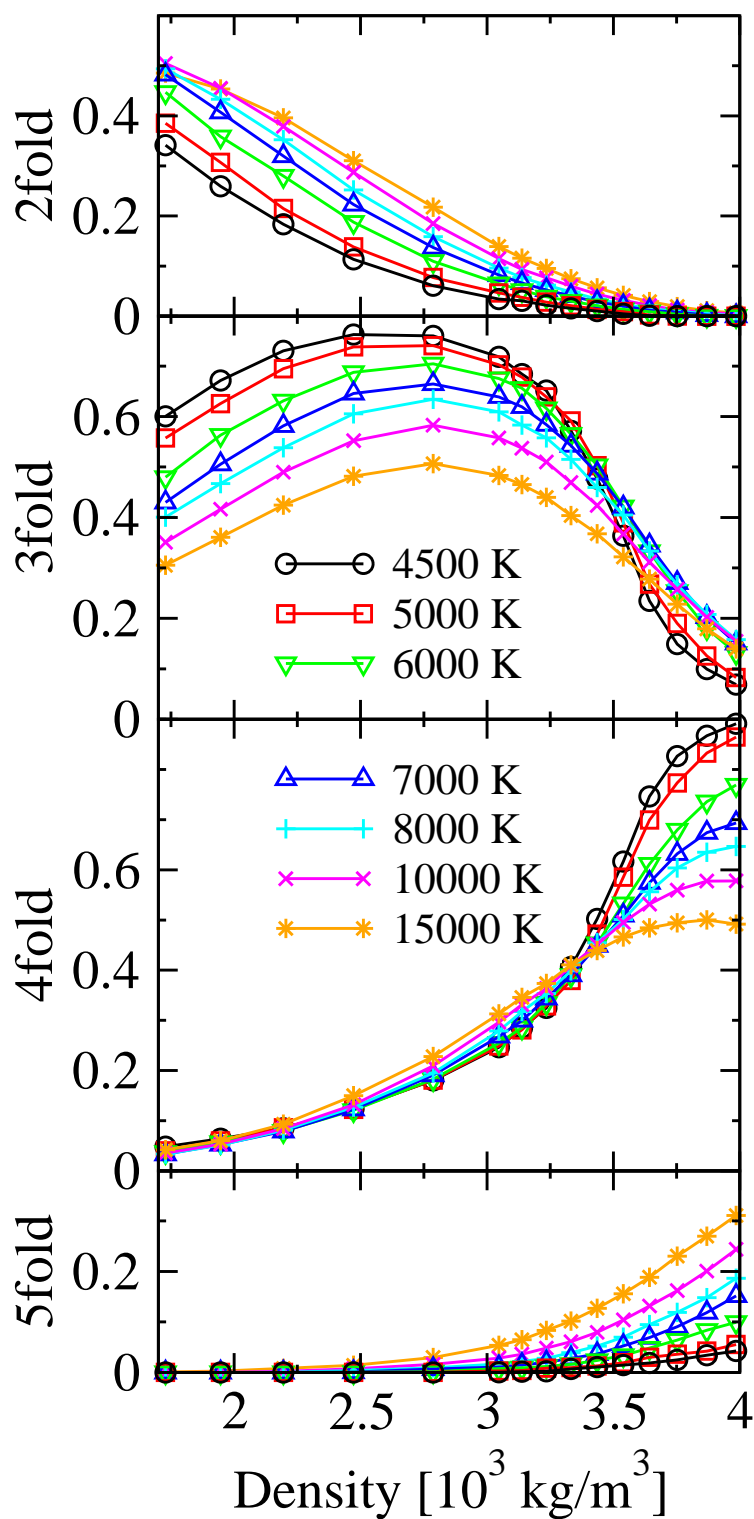


Figure 12.6: Coordination fractions at seven temperatures according to the LCBOP11. The symbol code is the same as for Fig. 12.2. Each panel shows a different coordination fraction intervals but y-axes share the same unit, so that they can be directly compared. The error bars, not shown, would be smaller than the symbol size, typically around 0.01.

pendence, we observe that, for all temperatures, the atoms are mainly two- and three-fold coordinated in the low density region, with the two-fold sites gradually replaced by three- and four-fold sites upon increasing density. At 6000 K the two- and three-fold fractions match around $\rho = 1.73 \cdot 10^3 \text{ kg/m}^3$. Note that the maximum of the three-fold fraction is at $\rho \sim 2.75 \cdot 10^3 \text{ kg/m}^3$ for all temperatures. Beyond this density the dominant coordination is three- and four-fold. The three-fold sites are replaced by four-fold sites over a relatively short density range around $\rho = 3.4 \cdot 10^3 \text{ kg/m}^3$. The five-fold fraction only appears with a significant fraction in the high-density region and shows a marked temperature dependence. This also implies a stronger temperature dependence of the four-fold fraction in the high-density region.

12.5 Radial distribution function

12.5.1 Comparison

In Figs. 12.7 we present the radial distribution functions (RDFs) obtained for the LCBOP II, LCBOP I⁺, and DF-MD at four selected densities along the 6000 K isotherm. Taking DF-MD as a reference, we see that the LCBOP II is a major improvement with respect to the LCBOP I⁺. In particular the minimum between the first and second shell is now properly described. Here we should note that the RDF and the coordination fractions, at $\rho = 3.75 \cdot 10^3 \text{ kg/m}^3$ were used as a test system in the development of the potential.

The figures also show that the LCBOP II reproduces the DF-MD values for the peak positions, and the height of the second and third peak. Only the first-peak height is slightly overestimated by the LCBOP II, consistent with the fact that the LCBOP II showed larger values for the higher coordination numbers (Fig. 12.5).

Figs. 12.8 compare the LCBOP II RDFs for a liquid at $2.9 \cdot 10^3 \text{ kg/m}^3$ at four different temperatures with 64-atom DF-MD data from Ref. [252], calculated using the local density (LDA) functional. This figure makes clear that, up to 12000 K, also the temperature dependence is well reproduced by the LCBOP II. The temperature dependence is typical for a liquid: the peak heights decrease with increasing temperature, while minima increase, indicating a gradual loss of structure. It is striking that all the curves cross at the same points at $g(r) = 1$. In fact, at ~ 0.165 , ~ 0.230 , and $\sim 0.285 \text{ nm}$, the value of $g(r)$ is 1, regardless of the temperature.

12.5.2 Predictions

Fig. 12.9 shows radial distribution functions for four selected densities at 6000 K. These four densities are chosen with the following criterion: density $1.73 \cdot 10^3 \text{ kg/m}^3$ is the lowest sampled and show almost equality of two- and three-fold fractions; density $2.79 \cdot 10^3 \text{ kg/m}^3$ show the maximum three-fold fraction amongst the densities; density $3.44 \cdot 10^3 \text{ kg/m}^3$ has about equal fraction of three- and four-fold sites; density $3.99 \cdot 10^3 \text{ kg/m}^3$ is the highest sampled and show a rather consistent fraction of five-fold sites. These selected fractions will be analyzed at the same temperature by means of the partial radial distribution functions, total, and partial angular distribution functions in the following sections.

In Fig. 12.9 we see that the position of the first peak is rather constant, whereas the position of the second peak moves markedly inwards with increasing density. This is

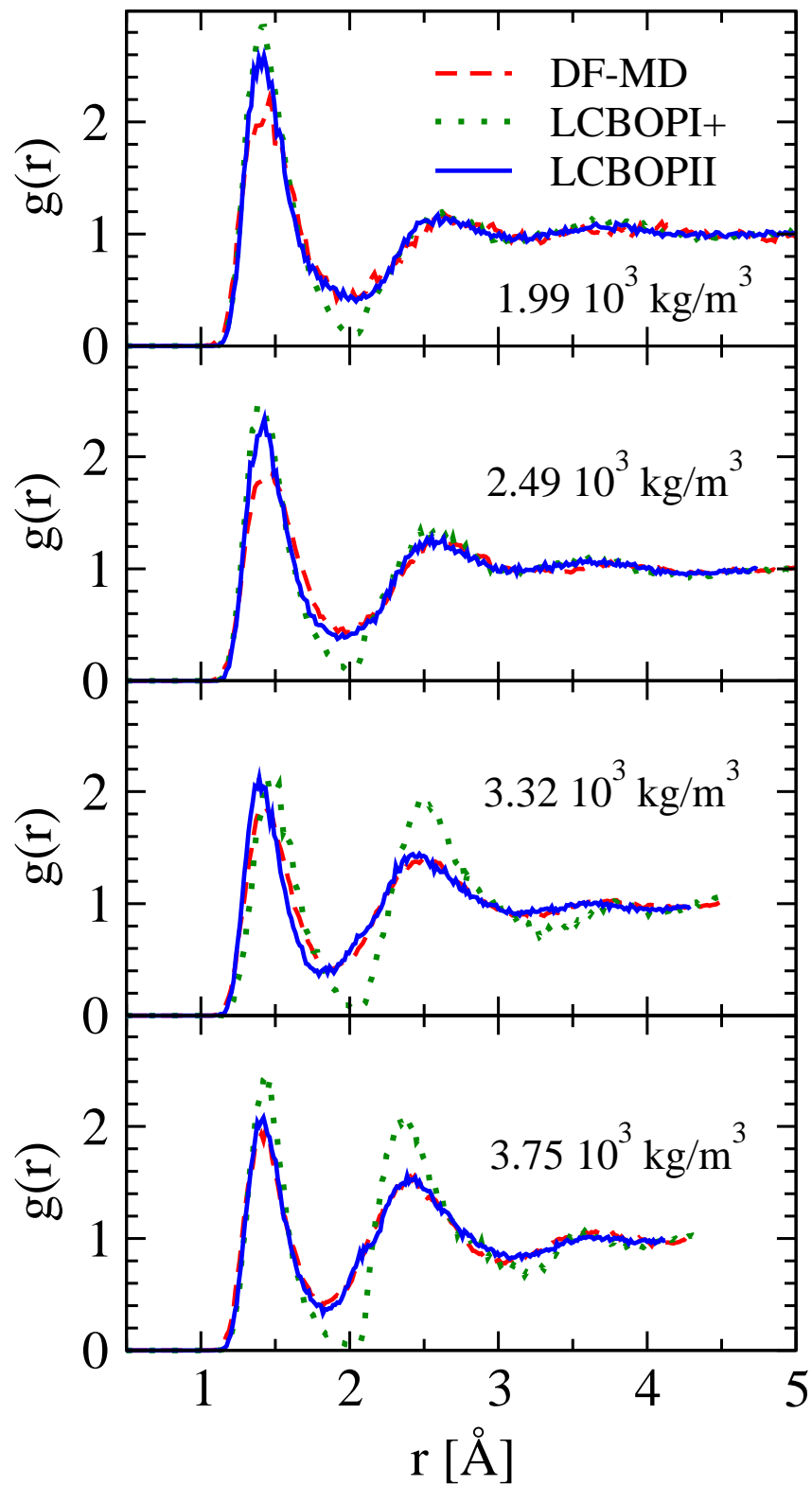


Figure 12.7: Comparison of the radial distribution functions at 6000 K and four selected densities between the LCBOPiII (solid lines), the LCBOPi+ (dotted lines), and the reference data taken from our own DF-MD simulations (dashed lines).

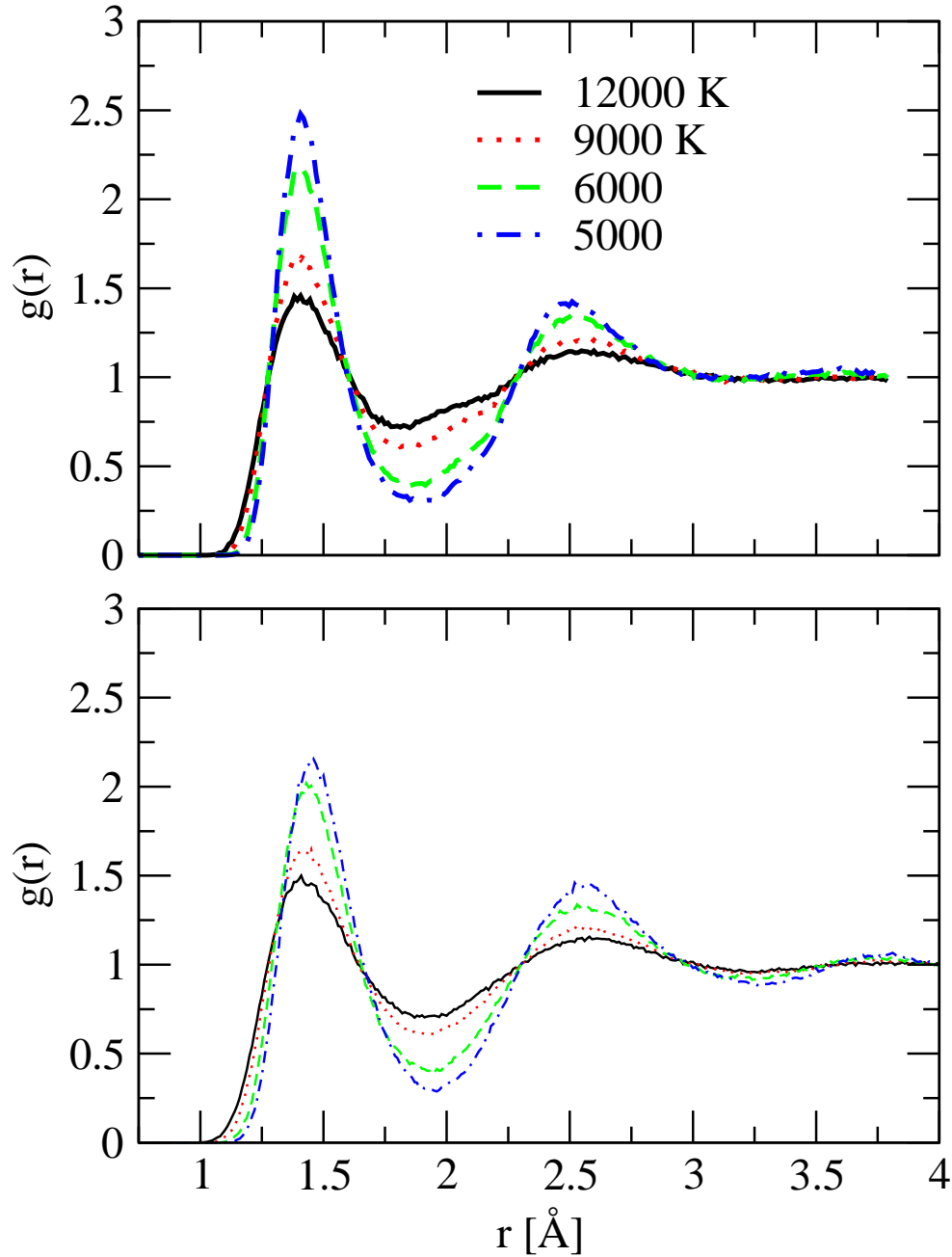


Figure 12.8: Comparison of the radial distribution functions at $2.9 \cdot 10^3 \text{ kg/m}^3$ and four temperatures between the LCBOP11 (top panel) and reference data taken from Ref. [252] (bottom panel). Solid lines are at 12000 K, dotted lines at 9000 K, dashed lines at 6000 K, and dotted-dashed lines are at 5000 K.

consistent with the findings of other DF-MD [252] and tight binding [213] calculations of liquid carbon, and is also seen in simulations of other covalently bonded liquids [253]. The height of the first peak decreases significantly when the density goes from 1.73 to $2.79 \cdot 10^3 \text{ kg/m}^3$. This should be attributed to the change in the coordination pattern, going from mixed two- three-fold to mainly three-fold. Upon further increase of the density it keeps the same height. In contrast, the second peak height increases gradually upon

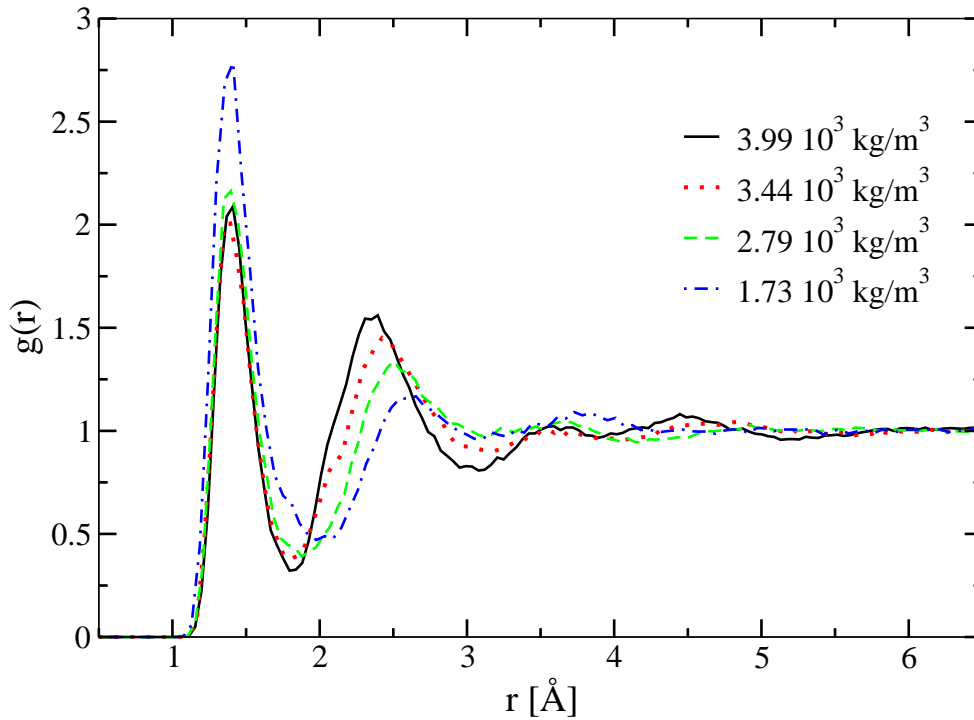


Figure 12.9: Radial distribution functions at 6000 K and four selected densities for the LCBOPII. Density 1.73 and $3.99 \cdot 10^3 \text{ kg/m}^3$ are respectively the lowest and the highest sampled. At the lowest density two-fold and three-fold are present with the same fraction. Density $2.79 \cdot 10^3 \text{ kg/m}^3$ shows the maximum in the fraction of three-fold coordinated atoms. Density $3.44 \cdot 10^3 \text{ kg/m}^3$ has almost the same amount of three- and four-fold sites. These same selected densities are analyzed in their partial distribution functions (Figs. 12.10, 12.11, 12.12, 12.13), angular distribution functions (Fig. 12.15), 2^{nd} shell angular distribution functions, and 2^{nd} shell coordinations (Figs. 12.16 and 12.17).

increasing density, while the dip between these two peaks decreases softly.

12.5.3 Partial radial distribution functions

We performed a further analysis of the liquid structure by examining the spatial correlation between the positions of carbon atoms with a specific coordination. We determined partial radial distribution functions (PRDF) $2g_{ij}(r)$, defined as the probability of finding a j -fold site at a distance r from an i -fold site. We have found some dependence of the PRDFs on the value of the cut-off radii used in the definition of neighbours. However, important features such the positions of peaks and minima, and the relative height of the peaks inside the same g_{ij} , appear to be rather independent of the cut-off radii.

In Figs. 12.10, 12.11, 12.12, and 12.13 we show the partial radial distribution functions at 6000 K at the same four selected densities of Fig. 12.9. At a density of $1.73 \cdot 10^3 \text{ kg/m}^3$ the dominant coordinations are two- and three-fold both appearing with an equal fraction. Fig. 12.10 shows that the positions of the first peaks of g_{22} and g_{33} are at 0.133 and 0.142 nm, typical for a sp and sp^2 type of bonding, respectively.

This agrees with the DF-MD results of Ref. [222] yielding an average bond length from g_{22} of 0.135 nm at $2.00 \cdot 10^3 \text{ kg/m}^3$ and 5000 K. The PRDF among two-fold coordinated

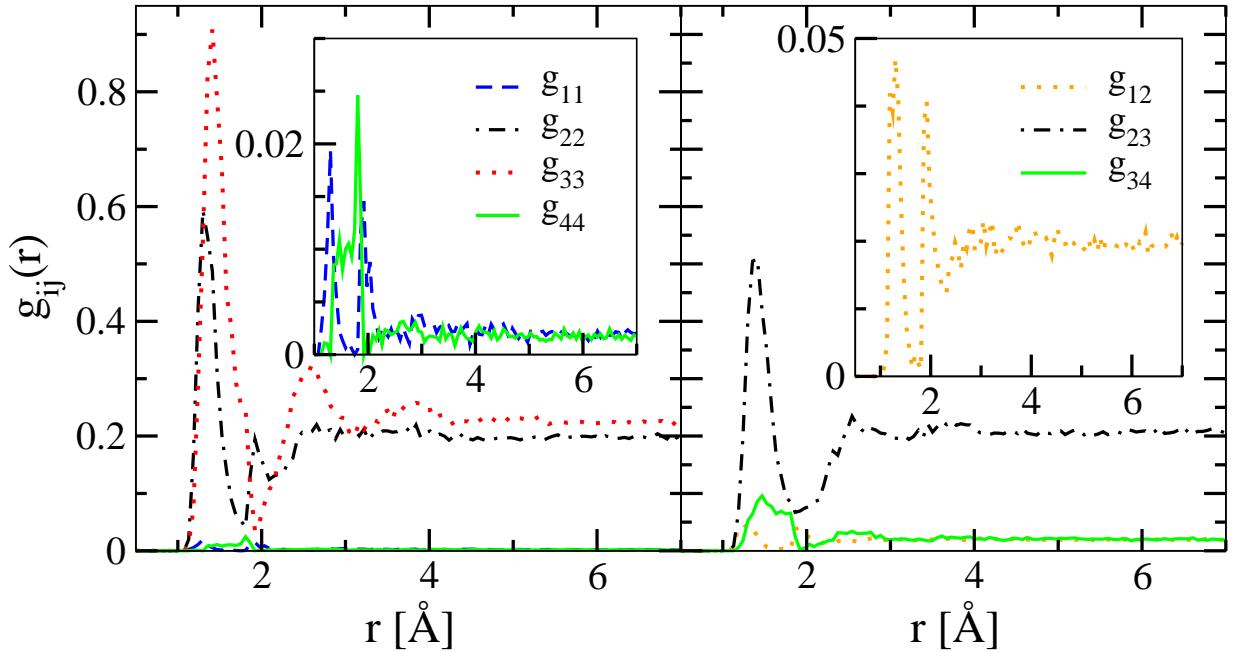


Figure 12.10: Partial radial distribution functions (g_{ij}) at $1.73 \cdot 10^3 \text{ kg/m}^3$ and 6000 K for the LCBOP-II. The left panel is for the diagonal terms (i.e. $i = j$): the dotted line here for the g_{11} , the dashed-dotted line is for the g_{22} , the dotted line for the g_{33} , solid line for the g_{44} . The inset shows magnified the g_{11} and the g_{44} . The right panel is for the cross terms (i.e. $i \neq j$): the dotted line here for the g_{12} (also shown magnified in the inset), the dashed-dotted line is for the g_{23} , the solid line is for the g_{34} . All the g_{ij} that are not shown are negligible. The total RDF is given by: $g = \sum_i g_{ii} + 2 \sum_i \sum_{j \neq i} g_{ij}$.

atoms (g_{22}), apart from the first peak due to nearest neighbours, is rather structure-less. This suggests that there are hardly any straight chains of three or more subsequent two-fold coordinated carbons. Conversely, a second and a third peak in the radial distribution appears among the three-fold coordinated atoms (g_{33}). Together with a visual analysis of liquid configurations, the PRDFs of Fig. 12.10 suggest the liquid structure to be a mixture of short bent chains and rings that are often mutually connected. Some of the chains end at a one-fold site. The relatively large first peak of g_{34} shows that the small fraction of four-fold coordinated atoms is mainly bonded to three-fold coordinated atoms. Occasionally there appear isolated dimers and bent trimers, as can be inferred from g_{11} (not shown) and visual inspection.

At density $2.79 \cdot 10^3 \text{ kg/m}^3$ the three-fold sites are at their maximum probability. At this density the g_{44} preserves the broadness of the first peak, even if here a 20% of four-fold sites is already counted. The ratio between the second and the first peak position for g_{33} gives a value higher than the $\sqrt{3}$ that is, incidentally, the lattice ratio in perfect graphite.

At a density of $3.44 \cdot 10^3 \text{ kg/m}^3$ the dominant coordinations are three- and four-fold, both almost equally represented. Fig. 12.12 shows substantial structure for all PRDFs with almost equal peak heights, indicating good mixing among three- and four-fold coordinated atoms. Note that the PRDFs at this density are rather structured. For g_{44} the position of the first two peaks and minima coincide with those of diamond. Also the ratio of the heights of the first two peaks, ≈ 1.6 , is similar to that of diamond. These observations are

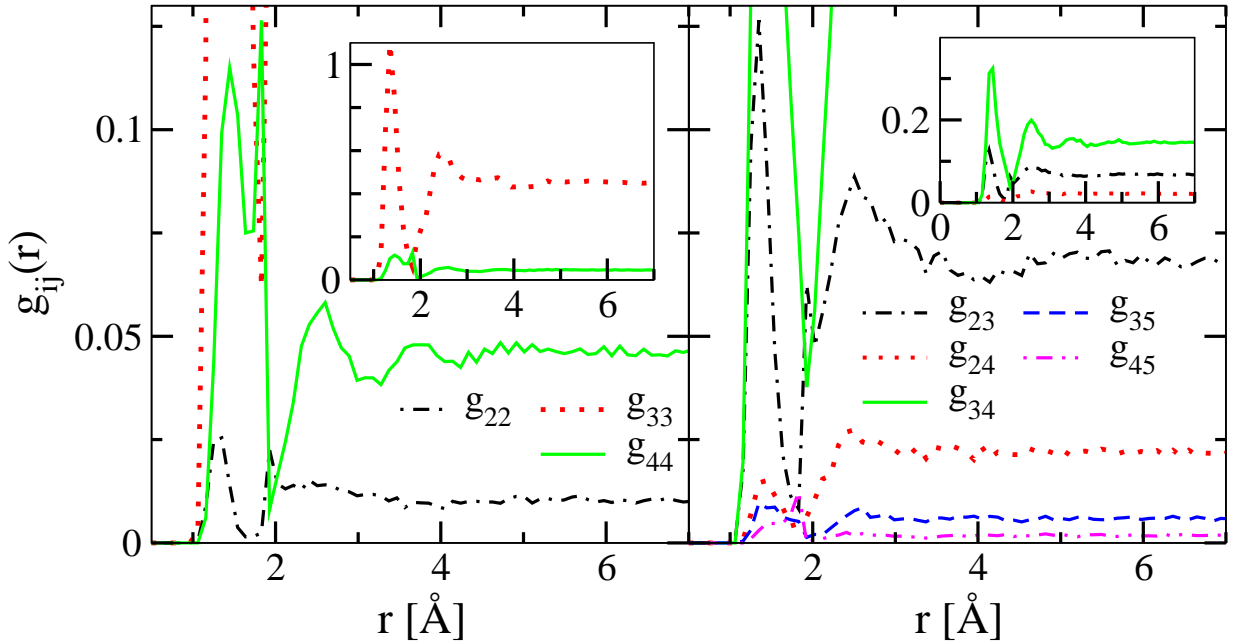


Figure 12.11: Partial radial distribution functions (g_{ij}) at $2.79 \cdot 10^3 \text{ kg/m}^3$ and 6000 K , where the population of three-fold atoms is the highest, for the LCBOP11. The left panel is for the diagonal terms (i.e. $i = j$): the dashed-dotted line for the g_{22} , the dotted line for the g_{33} , solid line for the g_{44} . In the inset is shown the full g_{33} , together with the g_{44} . The right panel is for the cross terms (i.e. $i \neq j$): the dashed-dotted line is for the g_{23} , the dotted line is for the g_{24} , the solid line is for the g_{34} , the dashed line is for the g_{35} , the dashed-double-dotted line is for the g_{45} . The inset is for the complete g_{34} , together with the g_{23} and g_{24} . All the g_{ij} that are not shown are negligible. The total RDF is given by: $g = \sum_i g_{ii} + 2 \sum_i \sum_{j \neq i} g_{ij}$.

consistent with the observation of Ref. [17] that a mainly four-fold coordinated liquid has a diamond-like structure up to the second shell of neighbours. The positions of the first peak and minimum of g_{33} are slightly but noticeably smaller than those of g_{44} . The small differences among the PRDFs in the positions of peaks and minima should be attributed to differences in bond-length for sp_2 and sp_3 type of bonding.

The ratio between the second and first peak position is around the lattice ratio for perfect diamond ($\sqrt{8/3}$) for g_{44} ; for g_{33} the ratio is higher than the ratio for perfect graphite ($\sqrt{3}$). Thus the almost exact $\sqrt{3}$ ratio between the peaks in the full $g(r)$ at this density is only a coincidence. In contrast, in Ref. [213] the authors infer from the same observed ratio in the total radial distribution function some graphitic structure at this density.

At the highest density considered ($3.99 \cdot 10^3 \text{ kg/m}^3$) the liquid is mainly four-fold coordinated with a small fraction of three- and five-fold coordinated atoms. The PRDFs at this density reveal a local diamond-like structure for the four-fold coordinated atoms, and show that the three- and five-fold coordinated atoms are mainly connected to four-fold coordinated atoms.

The partial distribution functions at temperatures above and below 6000 K (not shown here), have a temperature dependence similar to that of the total RDFs (Fig. 12.8: With

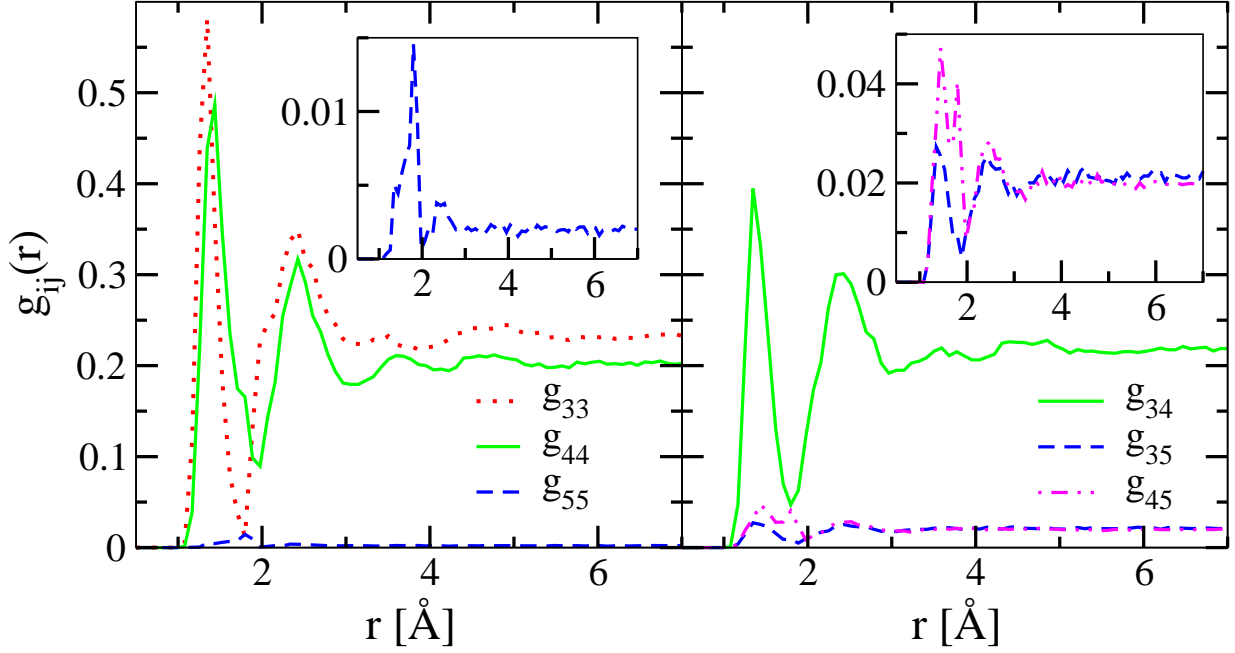


Figure 12.12: Partial radial distribution functions (g_{ij}) for the LCBOP-II at $3.44 \cdot 10^3 \text{ kg/m}^3$ and 6000 K , with almost equal fraction of three- and four-fold coordinated atoms. The left panel is for the diagonal terms (i.e. $i = j$): the dotted line for the g_{33} , solid line for the g_{44} , the dashed line for the g_{55} (also shown magnified in the inset). The right panel is for the cross terms g_{23} . (i.e. $i \neq j$): the solid line is for the g_{34} , the dashed line is for the g_{35} , the dashed-double-dotted line is for the g_{45} . In the inset are shown magnified the g_{35} and the g_{45} . All the g_{ij} that are not shown are negligible. The total RDF is given by: $g = \sum_i g_{ii} + 2 \sum_i \sum_{j \neq i} g_{ij}$.

increasing temperature, peaks tend to flatten and broaden, but in such a way that the radial positions of the maxima are preserved.

12.6 Angular distribution function

The angular distribution function ($A(\cos(\theta))$) is determined as the distribution of the the dot products ($\cos(\theta)$) of the pairs of vectors drawn from a reference atom to any two other atoms within a cutoff radius r_{co} of the reference atom. Note that, using $\cos(\theta)$ as the independent variable, equally spaced sampling points cover equal amounts of the surface of the unitary sphere; in fact the surface element is proportional to $d\cos(\theta)$. In literature one often finds the angular distribution functions defined as depending on the angle θ (i.e. $A(\theta)$); in this case, one has to normalize with $(\sin(\theta))^{-1}$ (being the surface element proportional to $\sin(\theta)d\theta$).

12.6.1 Comparison

In Fig. 12.14 we show the comparison of the angular distribution functions between LCBOP-II and DF-MD calculations at the same densities as for the radial distribution function (see Fig. 12.7). The overall agreement is impressive also in this case. The position of the

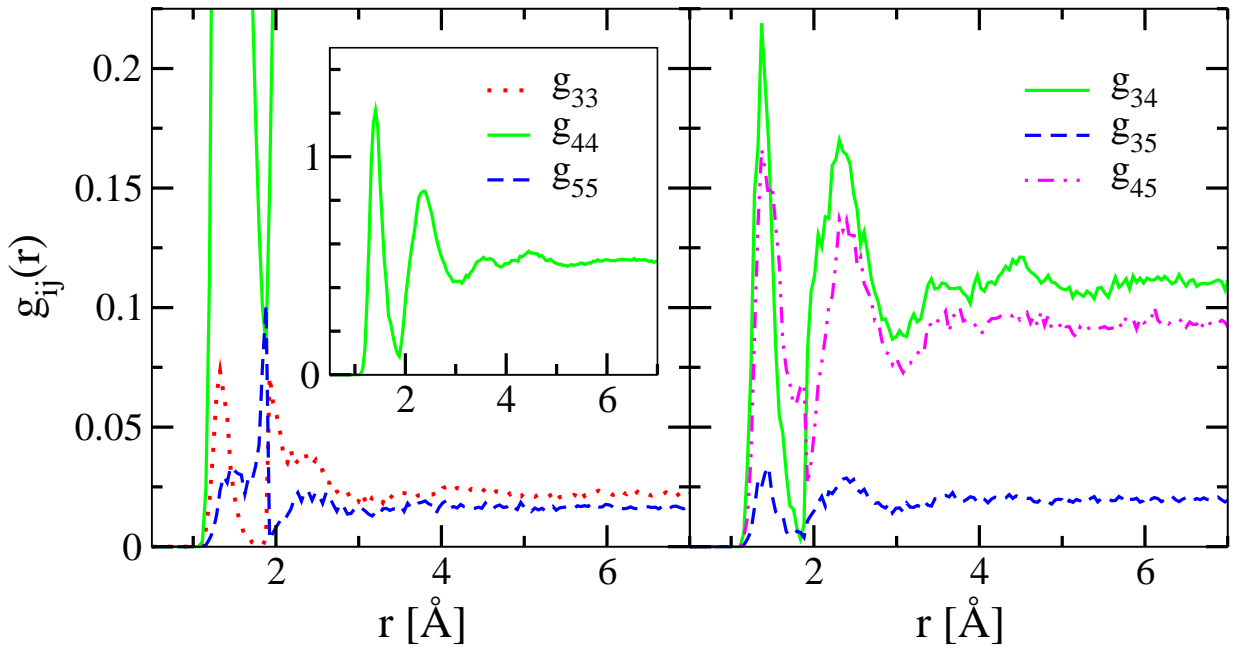


Figure 12.13: Partial radial distribution functions (g_{ij}) at $3.99 \cdot 10^3 \text{ kg/m}^3$ and 6000 K for the LCBOPII. The left panel is for the diagonal terms (i.e. $i = j$): the dotted line for the g_{33} , solid line for the g_{44} , the dashed line for the g_{55} ; in the inset is shown the complete g_{33} . The right panel is for the cross terms (i.e. $i \neq j$): the solid line is for the g_{34} , the dashed line is for the g_{35} , the dashed-double-dotted line is for the g_{45} . All the g_{ij} that are not shown are negligible. The total RDF is given by: $g = \sum_i g_{ii} + 2 \sum_i \sum_{j \neq i} g_{ij}$.

main peak together with its broadness is well recovered at all densities. Compared to the LCBOPI⁺, this is a significant improvement as the results of Ref. [17] showed that there was only a qualitative agreement between the LCBOPI⁺ and DF-MD, with the LCBOPI⁺ underestimating the presence of sub 90 degrees structures. The improvement of the LCBOPII over the LCBOPI⁺ should be attributed to the softening of the angular part in the potential yielding a lower energy for four-fold coordinated structures at small angles. As for the RDFs, the major discrepancies are at lower densities: in this case the position and/or the broadness of the secondary peak at low angles is only qualitatively reproduced. A discussion on the nature of this secondary peak comes at the end of this section.

12.6.2 Predictions

Fig. 12.15 shows the total and partial angular distribution functions at the four selected densities of Fig. 12.7. Looking at the total distributions (thick solid lines), the figures show that at the highest density ($3.99 \cdot 10^3 \text{ kg/m}^3$) the angular distribution is peaked near the tetrahedral angle ($\cos(\theta) = -1/3$), typical for diamond. Upon decreasing density, to $1.73 \cdot 10^3 \text{ kg/m}^3$, the peak position moves towards a value around $\cos(\theta) = -0.5$, i.e., the angle typical for hexagonal graphite. For all densities the distribution near the peak is rather symmetric with a Gaussian-like shape. Note also that the distributions are broad, and cover angles from 50 degrees to 180 degrees. At all densities, the tail at small angles features a local maximum around 50-60 degrees. These peaks are also present in our DF-

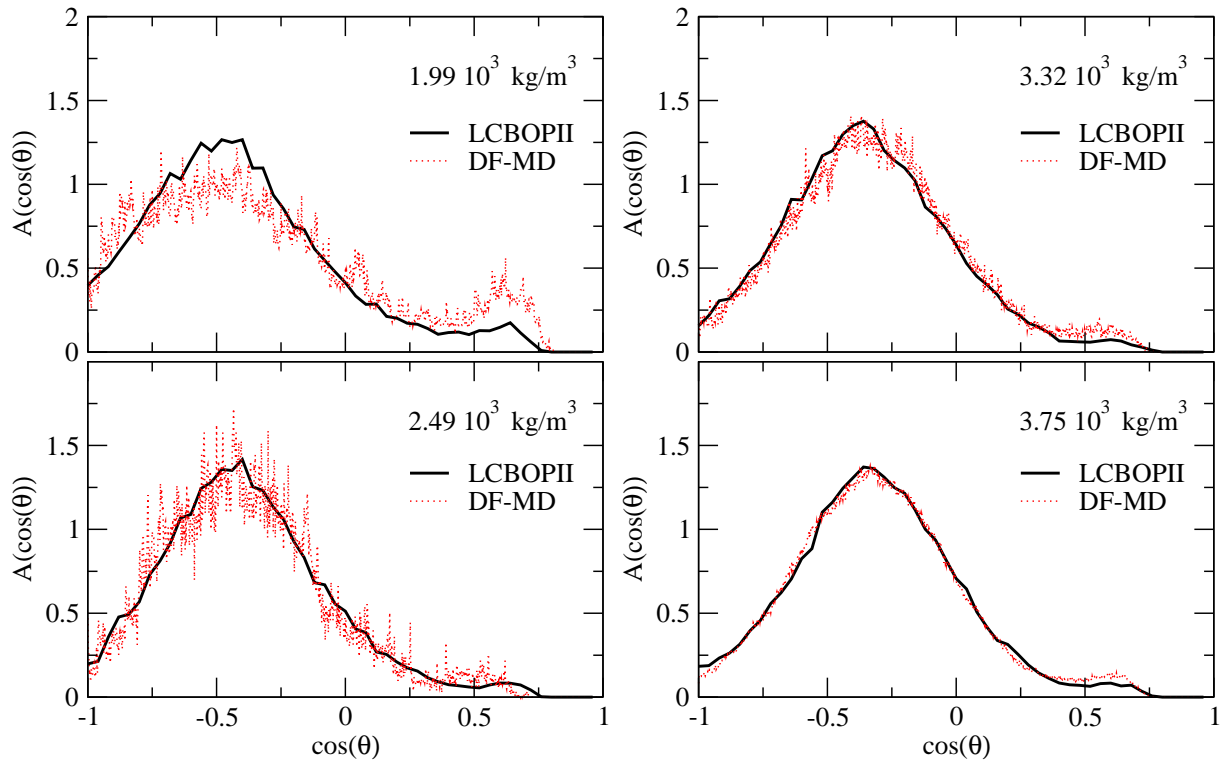


Figure 12.14: Angular distribution functions at 1.99 (top left panel), 2.49 (bottom left), 3.32 (top right), and $3.75 \cdot 10^3 \text{ kg/m}^3$ (bottom right), comparing DF-MD (dotted lines) with the LCBOP2 (solid lines).

MD simulations (see Fig. 12.14 and 9.8) as well as in earlier DF-MD simulations [223, 252]. Upon visual inspection of the atomic configurations (see Fig. 12.18), we could relate the peaks to nearly equilateral triangular structures. These peculiar triangular structures, present at all densities, occasionally merge in pairs in a rhombohedral structure. It is remarkable that the LCBOP2 is able to recover also this feature. To make a comparison, the environment dependent potential proposed by Marks [147], uses a definition of the angular correlations with a harmonic functional shape, Gaussian-softened at angles far from the preferred one (at a given coordination): in Ref. [223], Marks reports Gaussian-shaped angular correlation functions without any sign of a minor peak at small angles.

Going back to Fig. 12.15, we now focus on the partial angular distribution functions (padf's). In literature, two different ways of defining padf's are found. Following *one definition* (see e.g. [223]), with padf's denoted by A_x , one considers the probability of finding bonds at a certain (cosine of the) angle, as seen from an atom of a selected coordination type (so, $x = sp, sp_2, sp_3, 5\text{-fold}$), whatever is the coordination of its neighbours. Thus, in this case, the sum of the partial is the total angular distribution functions. Following the *other definition* (see e.g. [222]), with the padf's denoted by A_{ij} , one considers the probability of finding bonds at a certain (cosine of the) angle, where one of the bond is between two atoms of selected coordination type (i and j in A_{ij} indicate the number of neighbours of the two reference atoms), whatever the coordination of the third atom involved. In the bottom panels is shown only a part of these functions, namely those in which the particle constituting the bond are of the same coordination type.

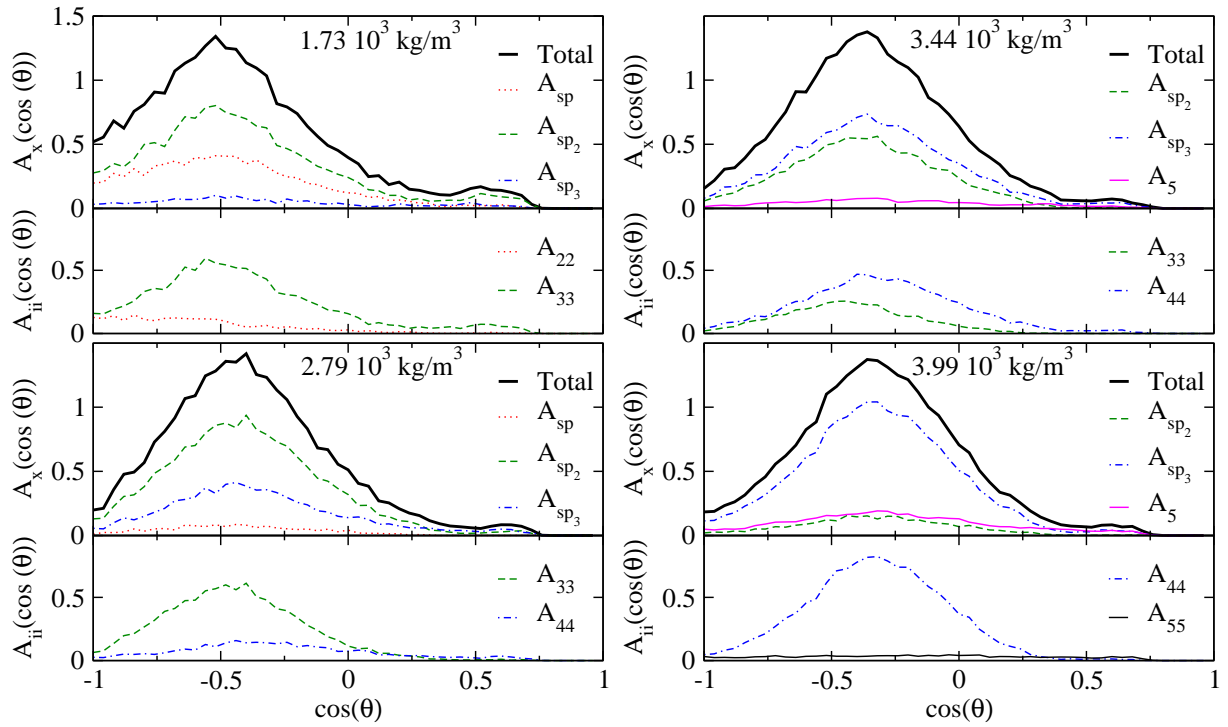


Figure 12.15: Total and partial angular distribution functions at 1.73 (top left panel), 2.79 (bottom left), 3.44 (top right), and $3.99 \cdot 10^3 \text{ kg/m}^3$ (bottom right). Each panel is divided into two sub-plot, the top one showing the total angular distribution function and the A_x (i.e. the probability of finding two bonds at given $\cos\theta$ as seen from a site x , whatever the coordination of its neighbours); each bottom subplot carries the A_{ii} (i.e. the probability of finding bonds at a certain $\cos\theta$, where one of the bond is between two atoms of the same selected coordination type, i , whatever the coordination of the third atom involved).

The results for A_x are shown in the top sub-plot of each panel in Fig. 12.15 (together with the total distribution): these partial distributions follow the peak position of their total distributions, at a lower height, yielding a poor information.

The results for A_{ii} (i.e. the A_{ij} for alike sites, where $i = j$) are shown in the bottom sub-plot of each panel in Fig. 12.15. They show clear distinct features for the different coordination types: the most striking example is at $3.44 \cdot 10^3 \text{ kg/m}^3$ where A_{33} has its maximum at $2\pi/3$, while A_{44} at the tetrahedral angle ($\cos\theta = -1/3$). At the lowest density, $1.73 \cdot 10^3 \text{ kg/m}^3$, the A_{22} show a flat distribution from π to $2\pi/3$, and then the distribution mildly drops to zero. The structures depicted there are portion of chains, that are allowed to bend indifferently from the linear configuration up to an angle of $2\pi/3$. The angular distribution is a property connected to a bond, rather than to a particle: this is why the A_{ii} carries much more information than the A_x .

We also determined the angular distribution of bonds to the second neighbours. Fig. 12.16 shows the results at the four selected densities at 6000 K . The prominent feature is a peak at $\pi/3$ at all densities. At angles larger than $\pi/2$ the distribution is rather flat, with more oscillations at higher densities. Peculiar is the secondary peak at small angles. At the highest density the peak is at $\sim 2\pi/10$; upon decreasing density the peak shifts slightly at smaller angles, decreasing in importance and converting into a shoulder of the primary peak

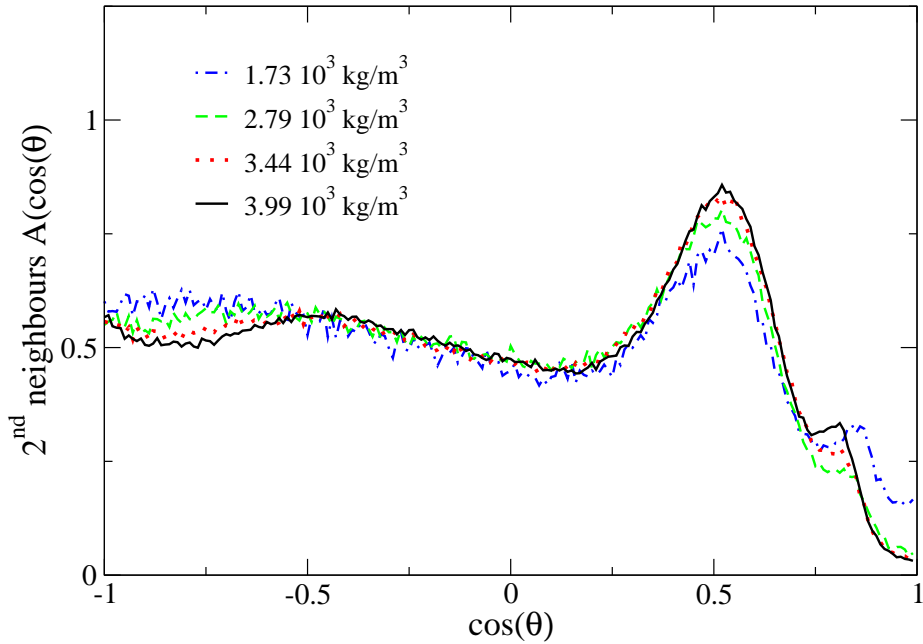


Figure 12.16: Second shell angular distribution function at 4 selected densities.

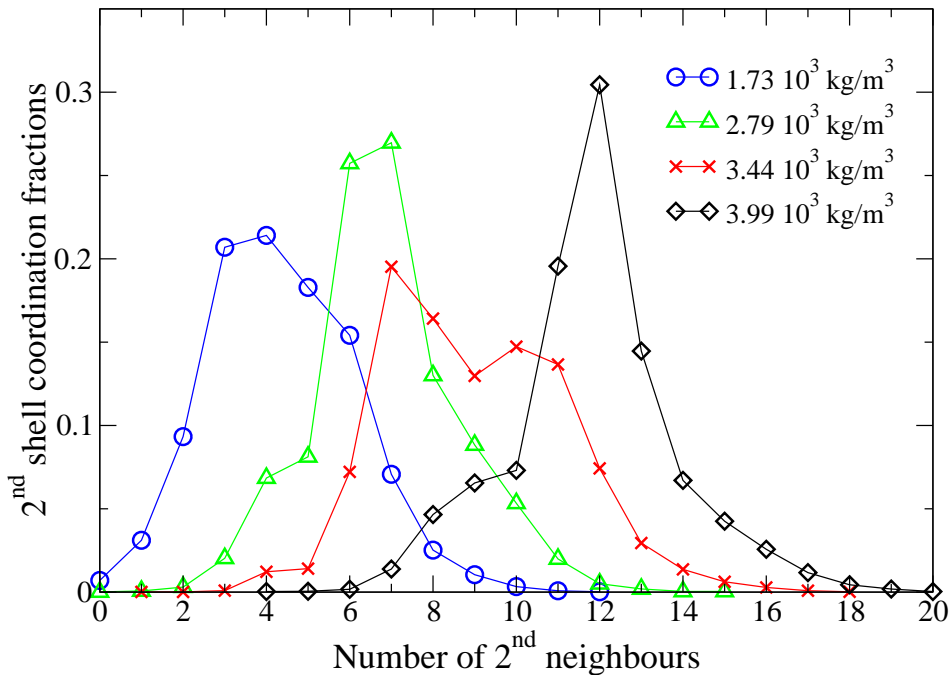


Figure 12.17: Histogram of the 2nd neighbours fraction at 4 selected densities.

at $\pi/3$, and then increases again, but at $\sim \pi/3$. It is instructive to compare these values to the lattice values for diamond and graphite. Second shell angular correlations of diamond show (see figure 9.9) entries at π , $2\pi/3$, $\pi/2$, and $\pi/3$, with weights 0.09, 0.36, 0.18, and 0.36, respectively. In addition, an angle of $\sim 2\pi/10$ is found in cross correlations between the first and second shell. Second shell angular correlations of graphite have entries π , $2\pi/3$, and $\pi/3$, with weights 0.2, 0.4, and 0.4, respectively. Besides, the angle $\pi/6$ is found

in cross correlations between the first and second shells and between second and third shells. The similarity between the liquid and the solid structures continues in the number of second neighbours. Fig. 12.17 shows the histograms of the number of second neighbours at the same phase point as in the previous figure. Where three- (at $2.79 \cdot 10^3 \text{ kg/m}^3$) and four-fold (at $3.99 \cdot 10^3 \text{ kg/m}^3$) are predominant, the number of second neighbours is peaked around 6-7 and 12, respectively, i.e. similar to graphite and diamond. Incidentally, the average second neighbours coordination of 12 atoms for the highest density considered confirms, as we noticed in section 9.3, that metastable liquid carbon has a diamond-like structure. Where three- and four-fold atoms have the same fraction (at $3.44 \cdot 10^3 \text{ kg/m}^3$), the distribution is bimodal, with peaks around 7 and 10. The second neighbours coordination at the lowest density contains some curious features: namely a nonzero population of zero-fold and one-fold second neighbours coordinated atoms. These two entries can be explained as follows: atoms with zero second neighbours are part of a dimer, while atoms with only one second neighbour are every two end atoms of a chain. This observation, together with the peak at coordination 3-4, confirms the structure depicted in section 12.5.3 for the lowest density liquid.

12.7 Conclusions

In summary, in this chapter we showed the performance of the newly introduced LCBOPII [20] for the description of the liquid carbon. We explicitly compared the equation of

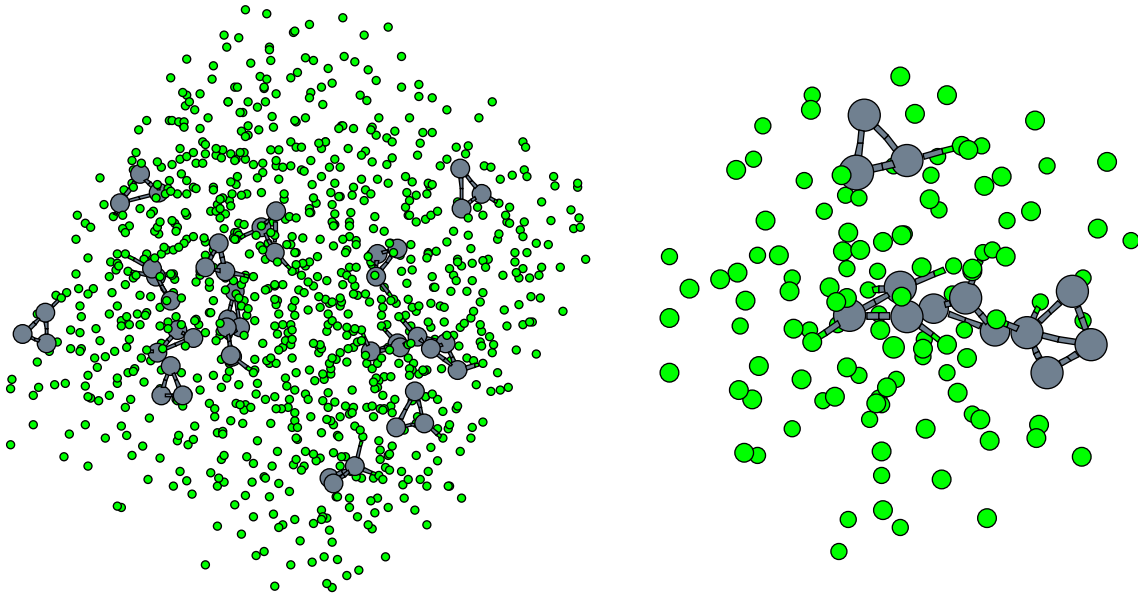


Figure 12.18: Snapshots of the liquid at $1.73 \cdot 10^3 \text{ kg/m}^3$ and 6000 K. In the left panel is shown a 1000 particle system, sampled via the LCBOPII; in the right panel is shown a snapshot of a 128 particle sample simulated via DF-MD. All the neighbouring atoms having at least one bond-angle smaller than 60 degrees are shown enlarged, and we explicitly show only the bonds involving them; bonds are drawn when two atoms are closer than 1.7 \AA (i.e. the r_{min} of the S_{sr}^{down} of the LCBOPII, see Table 11.5).

state, the coordination fraction, and the radial distribution function of the LCBOP II with reference data from density functional based simulations. We extended the analysis of the liquid in region not covered from other reference data. On the basis of the equation of state, the coordination fractions, the radial distributions function, and the angular distribution functions, we show the extreme accuracy and transferability of the LCBOP II. Looking at the calculated equation of state, we argue that a (first order) liquid – liquid phase transition could only be found in a deeply undercooled liquid. It is not clear if these condition can ever be reached. In simulation this would at least require a large system size and a very careful cooling from a stable liquid. On the basis of the partial radial distribution function at a density where three- and four-fold sites are equally present, we provide a further argument against a phase separation: the likeness of the partial radial distribution functions suggests, at 6000 K, a negligible strain energy amongst atoms of three- and four-fold coordination.

The present results are a first application of the LCBOP II in studies of condensed phase carbonic materials under extreme conditions. It is well suited for the study of various other type of carbonic materials. Future extensions of the LCBOP II could involve the incorporation of other elements such as hydrogen, oxygen, nitrogen, and various metals. This would open the way to the study of advanced nano-sized materials.

Who is we?

A note of the author

- *What is your name?*
- *My name is Legion; for we are many.*

In contrast to Latin-derived languages like Italian, the English language dislikes discourages the use of impersonal forms such as “It has been found . . .”, “It has been used . . .”. Thus, this as the great majority of the doctorate theses, is populated by sentences whose subject is “We”. A reasonable question that might arise in the reader’s mind would concern the identity of the persons that accompanied the author of the thesis, the one whose name is engraved below the title in the first page, to constitute the “We”. In the following the author will unveil those, all but secret, identities.

Chapters 2, 3, and 6 (up to section 6.7) are introductions in the form of a review whose possible worthiness should be attributed to the author only. Thus, there, “We” is indeed “the author”, unless, in some derivations, due to a commonly adopted figure of speech, the reader, if he likes, is invited to be part of the fellowship.

The final part of chapter 6, in which the LCBOP⁺ is introduced, Jan Los, Evert Jan Meijer, Annalisa Fasolino, and Daan Frenkel worked with the author for the model shown therein. The same impressive set of co-authors the author features for chapters 8 and 9, regarding the results obtained with the LCBOP⁺ in different aspects of carbon at extreme conditions.

In chapters 4 and 5, about liquid phosphorus, “We” is Evert Jan Meijer with the author.

For the historical review of chapter 7 the author must acknowledge the collaboration of his wife, Sara Iacopini, whom the author, for this chapter but not only, owes to more than he will ever admit.

In chapter 10, the author is accompanied by Chantal Valeriani, Evert Jan Meijer, and Daan Frenkel.

Chapter 11 is mainly a work of Jan Los, thus the author makes a step backward, putting himself within the other co-authors, i.e. Evert Jan Meijer and Annalisa Fasolino.

Finally, chapter 12 counts as co-authors Jan Los, Annalisa Fasolino, and Evert Jan Meijer.

Summary

This thesis orbits around carbon and phosphorus, studied by means of computer experiments.

At the beginning of this work these two chemical elements were considered good candidates for showing the so-called liquid – liquid (first order) phase transition. In solids, phase transitions are well-known and well-understood phenomena both at normal conditions and at high pressures. In contrast to crystals, no robust, consistent theory for the liquid phase has been created, yet. Phase transitions in disordered systems, such as liquids, are not well-understood. The very concept of the existence of such transitions in simple liquids has not yet reached a universal consensus; this is due to their counterintuitive nature and to experimental difficulties in the validation: the candidate transitions either occur at extreme pressure and/or temperature or appear in metastable regions (e.g. are hidden by competing solidification).

In liquid phosphorus, at pressure ~ 1 GPa and temperature ~ 1300 K an experimental tour-de-force [1] showed the occurrence of a first order phase transition between two liquids of different structure. Analysis of the x-ray data suggested that at those conditions a molecular *fluid*^{*}, made of tetrahedral P₄ molecules, reversibly transforms into a network liquid. The network structure of the liquid is due to the covalent bonding of phosphorus. In short, a covalently bonded system prefers certain lengths and angles. These preferred lengths and angles vary with the number of bonds. Thus, in the liquid, even if the system remains rather disordered, only certain structures are allowed and normally few bonds per atom are present, thus suggesting the picture of a network.

For liquid carbon no experiments are available, due to the extreme high temperatures (more than at least 4000 K) and pressures (order of GPa) at which carbon would exhibit its liquid phase. Nonetheless, theoretical speculations [210] led to the commonly accepted picture of graphite (the low pressure solid phase of carbon) melting into a mainly three-fold coordinated liquid, thus resembling the lattice structure, and diamond (the higher pressure solid phase) melting into a mainly four-fold coordinated liquid. It was thought that these two liquids could have been separated by a first order transition phase boundary.

In chapter 2 we review a simple model that accounts for transitions in simple liquids. This is achieved by treating the liquid as a mixture of two species: an atom (or a molecule) belongs to one of the two species accordingly to the local structure surrounding it. Under certain conditions such a liquid can macroscopically separate into two liquid phases in which the relative population of the two species is radically different. This leads to the appearance of two liquids, with different thermodynamical properties. The chapter ends with a review of the most famous (speculated) liquid – liquid phase transition, the one in water, and of two model (toy) interaction potentials that can exhibit a liquid – liquid phase transition.

We studied phosphorus exclusively by means of a simulation technique that is known as *ab initio* molecular dynamics. In molecular dynamics, the dynamics of a system of point particles, interacting via some given potential, is generated by numerically integrating its (newtonian)

^{*}In fact, the system is at a temperature above the gas/liquid critical point.

equations of motion. In ab initio molecular dynamics the interacting potential is not given a priori, but rather calculated from the (more or less approximated) knowledge of the electronic density of the system. In chapter 3 we introduce the ab initio molecular dynamics scheme, worldwide known as Car-Parrinello molecular dynamics (CPMD) [62], we used. We pay particular attention in explaining how constant temperature and constant pressure simulations are performed within the ab initio molecular dynamics scheme of our choice.

In chapter 4 we analyze the issue of the liquid – liquid phase transition in phosphorus. We performed constant temperature – constant pressure CPMD simulations of a system of 64 phosphorus atoms. These were originally arranged in 16 tetrahedra. Upon increasing pressure at constant temperature (1500 K), at 6.25 GPa we find the break up of the molecules, to give the formation of a network liquid. The transition is accompanied by the abrupt increase (of about 30%) of the density of the system. Together with a careful analysis of the structure and dynamics of the two phases, and a comparison to available experimental data, we suggest a possible mechanism that seeds the first order transition. We argue that the almost contemporary spontaneous break up of one bond in each of three neighbouring tetrahedral molecules, can lead to the formation of a chain of these unstable ‘butterfly’ molecules. The appearance of this last structure may trigger the overall transition.

In chapter 5 we continue the analysis of the liquid – liquid phase transition in phosphorus at higher temperatures. To do this, we follow several isotherms or isobars in order to collect phase points in which transitions spontaneously occur in our simulated system. The idea is to have information on the position of the critical point that must end the liquid – liquid phase transition coexistence line. At the temperature of 3100 K and the pressure of 1 GPa we obtain a transition that can be thought of as near-critical; at temperature 3500 K and pressure 0.5 GPa we find a super-critical transition[†]. At these state points, we observe the phenomenon of the formation of new tetrahedra; these comprise atoms belonging to different tetrahedra at the beginning of the simulation. The lifetime of these ‘newly formed’ tetrahedra is variable, sometimes comparable to the whole simulation time. Observing the samples along a slow cooling at the fixed pressure of 0.5 GPa, down to temperature 2500 K, the phenomenon of the reformation becomes more and more frequent.

In chapter 6 we introduce the class of bond order potentials, which includes the potential we have developed to study carbon. To the purpose, we give a two-fold theoretical justification of the functional form that is used for this class of potentials, then we review some bond order potentials successfully used in the last 20 years; subsequently we present the original preliminary form of our bond order potential, the so-called LCBOP, long range carbon bond order potential, as published in Ref. [15]; we conclude introducing the modified form of the LCBOP, i.e. the LCBOP⁺, that we used in chapters 8, 9, and 10 for our calculations.

In chapter 7 we aim at giving a complete picture of the ideas put forward in the scientific community about the phase diagram of carbon, when its bulk phases graphite, diamond, and the liquid(s) are taken into account. The chapter is presented following a historical perspective. In particular, we review every article that concerned the topic of the possible liquid – liquid phase transition for (liquid) carbon.

In chapter 8 we present our calculation of the phase diagram of carbon, comprising graphite, diamond and the liquid. Coexistence was found by equating the free energies of the three phases. Free energies were evaluated by means of thermodynamic integration. We find a graphite/diamond coexistence line very close to experimental data. We find a positive slope for the diamond melting line, consistently with shock–wave experiments. We find a T-vs-P graphite melting line always with a positive slope, in contrast to experiments that show a maximum. We

[†]A super-critical transition occurs at temperatures above the critical temperature. It is no longer a first-order transition.

discuss the possible causes of this discrepancy, that we think mainly due to the out-of-equilibrium conditions of the experiments. We find a graphite/diamond/liquid triple point at 16.4 ± 0.7 GPa and 4250 ± 10 K, i.e. at a somewhat lower temperature than *expected* from experiments.

In chapter 9 we analyze the structure of the liquid carbon. We rule out the presence of a liquid – liquid phase transition in the region of the phase diagram we investigated. We find that diamond melts into a mainly three-fold coordinated liquid, from the graphite/diamond/liquid triple point up to ~ 300 GPa, contrary to the common assumption. We find that undercooled liquid carbon can have a diamond-like structure, i.e. a local coordination that closely resembles the diamond lattice. We also show in detail the shortcomings, in the description of the liquid structure, of other bond order potentials that are used nowadays.

In chapter 10 we address the topic of the homogeneous nucleation of diamond from the bulk. Homogeneous nucleation is an activated process, i.e. a process that is difficult to initiate spontaneously, but, when started, proceeds very quickly. More precisely, "difficult to initiate" means that the spontaneous fluctuation that initiates the process is very unlikely. In our system we can estimate, afterwards, that a spontaneous nucleation could have occurred only once in a hundred years of simulation. To cope with this unlikeliness, we adapted to our case a recently developed technique [237] devised to study *rare events*. The technique we adopted, as many other rare events methods, relies on the definition of solid particles in the liquid. The underlying assumption, taken from classical nucleation theory (briefly accounted in this same chapter) is that when putting the liquid in a state point in which a certain lattice structure is thermodynamically more stable, an initially small cluster of the solid structure grows with difficulty until it reaches a certain critical size; thenceforth the growth of the cluster proceeds very rapidly. Thus, we adapted to our case an existing algorithm [238] that distinguishes solid particles in the liquid, looking at their spatial correlations. The rare event method we used allows us to estimate the nucleation rate. We successfully obtained paths from the liquid to the diamond for the diamond-like liquid we describe in the previous chapter: we find the enormously fast nucleation rate of 10^{33} nuclei per cubic meter per second.

In chapter 11 we present an overall improvement of the bond order potential used in previous chapter, yielding the LCBPOPII. The improvement was mainly motivated by the need to overcome two known problems of the LCBOP I (as well as the LCBOP⁺): for the LCBOP I the formation of a bond has to overcome a ~ 0.3 eV barrier at ~ 2.1 Å. This is not always true: when atoms have dangling bonds, the formation of the bond may occur without an energy barrier. We introduce a *middle range* potential that flexibly accounts for those dangling bond configurations. Furthermore, the preferred angles between covalent bonds involving a given atom depend on the number of those bonds. The LCBOP I accounts only roughly for this dependence, while for the LCBOP II we make this dependence highly transferable (i.e. able to account for structures not used to design the potential). These problems of the LCBOP I leads to a certain "stiffness" in the liquid phase description, that reflects in structural quantities, whereas the qualitative behaviour of this potential is always satisfactory. The LCBOP II yields an impressive quantitative reproduction of reference data.

In chapter 12, we thoroughly analyze structural properties of liquid carbon with the aid of the LCBOP II. We confirm the absence of a liquid – liquid phase transition in the stable liquid region. From the analysis of the equation of state in the region we could investigate, we argue that such a liquid – liquid phase transition is possible only in the metastable liquid region, at a very low temperature (with a critical point at ~ 1200 K); the direct observation of this transition is hindered by the freezing, possibly into an amorphous solid, of the system. This speculated transition would be similar to the one already speculated for water.

Samenvatting

Dit proefschrift draait om koolstof en fosfor, bestudeerd met computerexperimenten.

Aan het begin van dit onderzoek zijn deze twee chemische elementen gekozen als goede kandidaten om de zogenaamde (eerste orde) faseovergang vloeistof-vloeistof te bestuderen. In vaste stoffen zijn faseovergangen uitgebreid bestudeerd en goed begrepen, zowel onder normale omstandigheden als onder hoge druk. Voor de vloeibare fase is daarentegen nog geen degelijke, consistente theorie ontwikkeld. Over faseovergangen in ongeordende systemen, zoals vloeistoffen, is weinig bekend. Er is zelfs geen overeenstemming of deze overgangen in eenvoudige vloeistoffen daadwerkelijk bestaan. Dit komt doordat het een tegenintuïtief verschijnsel is en experimenteel moeilijk te valideren: de mogelijke overgangen vinden alleen plaats bij hoge druk en/of temperatuur of in een metastabiel gebied (waar de overgang naar vaste stof de vloeistof-vloeistofovergang verbergt).

Met een knap staaltje experimenteel werk [1] is een eerste orde faseovergang gemeten in fosfor tussen twee vloeibare fasen met een verschillende structuur bij een druk van ~ 1 GPa en een temperatuur van ~ 1300 K. De resultaten van röntgendiffractie wijzen op een reversibele overgang van een moleculair fluidum*, bestaande uit tetraëdrische P_4 -moleculen, naar een netwerk-vloeistof. De covalente bindingen in fosfor zorgen voor de netwerkstructuur. Kort gezegd geeft een covalent systeem de voorkeur aan specifieke bindingslengtes en -hoeken, die afhangen van het aantal bindingen per atoom. Daarom zijn zelfs in een behoorlijk ongeordende vloeistof slechts bepaalde structuren toegestaan. Normaal gesproken zijn er maar enkele bindingen per atoom aanwezig, waardoor het geheel er als een netwerk uitziet.

Voor vloeibare koolstof zijn er geen experimentele gegevens beschikbaar, vanwege de extreem hoge temperaturen (minimaal 4000 K) en drukken (ordegrootte GPa) waarbij de vloeistoffase bestaat. Uit theoretische overwegingen [210] is desondanks het algemeen geaccepteerde beeld ontstaan dat gesmolten grafiet (de vaste fase van koolstof bij lage druk) een voornamelijk driewaardig gecoördineerde vloeistof is en gesmolten diamant (de vaste fase bij hoge druk) voornamelijk vierwaardig. Aangenomen werd dat de fasegrens tussen deze twee vloeistoffen een eerste orde overgang is.

In hoofdstuk 2 behandelen we een simpel model om faseovergangen in eenvoudige vloeistoffen te beschrijven. Hierbij wordt de vloeistof als een mengsel van twee stoffen beschouwd; afhankelijk van de plaatselijke structuur om een atoom of molecuul behoort het tot een van beide stoffen. Onder bepaalde omstandigheden kan dit mengsel scheiden in twee vloeibare fasen, met elk een zeer verschillende verhouding tussen de twee

*Bij deze temperatuur bevindt het systeem zich boven het gas-vloeistof kritieke punt.

stoffen. De twee vloeistoffen die hierdoor ontstaan, hebben verschillende thermodynamische eigenschappen. Aan het eind van het hoofdstuk wordt de bekendste (veronderstelde) vloeistof-vloeistofovergang besproken, die in water. Ook behandelen we twee sterk vereenvoudigde modelpotentialen voor de interactie, waarmee een vloeistof-vloeistoffaseovergang beschreven kan worden.

Voor het onderzoek naar fosfor hebben wij uitsluitend gebruik gemaakt van een simulatietechniek die bekend staat als *ab initio* moleculaire dynamica. De moleculaire dynamica beschrijft de beweging in een systeem van puntdeeltjes met een gegeven onderlinge interactie door middel van numerieke integratie van de bewegingsvergelijkingen van Newton. Bij *ab initio* moleculaire dynamica is de interactiepotentiaal niet a priori bekend, maar wordt berekend uit de (min of meer benaderde) electronendichtheid van het systeem. In hoofdstuk 3 introduceren we de door ons gebruikte *ab initio* moleculaire dynamica methode, wereldwijd bekend als Car-Parrinello moleculaire dynamica (CPMD)[62].

In hoofdstuk 4 gaan we dieper in op de vloeistof-vloeistoffaseovergang in fosfor. We hebben CPMD-simulaties gedaan aan een systeem van 64 fosforatomen bij constante temperatuur en druk. Aan het begin van de simulatie zaten de atomen in 16 tetraëders. Bij verhoging van de druk bij een constante temperatuur van 1500 K zien we bij 6,25 GPa dat de moleculen zich herschikken tot een netwerkvlloeistof. Tegelijkertijd wordt de dichtheid van het systeem abrupt ongeveer 30% hoger. Aan de hand van een nauwkeurige analyse van de structuur en dynamica van de twee fasen en vergelijking met beschikbare experimentele gegevens, stellen wij een mechanisme voor dat de eerste orde overgang verklaart. We beargumenteren dat het bijna gelijktijdig, spontaan breken van een binding in elk van drie aangrenzende tetraëders kan leiden tot een ketting van onstabiele ‘vlinder’-moleculen. Het ontstaan van deze structuur stimuleert een volledige overgang.

In hoofdstuk 5 vervolgen we de studie van de vloeistof-vloeistoffaseovergang in fosfor bij hogere temperaturen. Hiertoe volgen we verschillende isothermen en isobaren om toestanden te vinden die in simulaties een spontane overgang vertonen. Het doel is om informatie te vinden over de plaats van het kritieke punt, dat zich moet bevinden aan het eind van de vloeistof-vloeistofcoëxistentielijn. Bij een temperatuur van 3100 K en een druk van 1 GPa vinden we een overgang die gezien kan worden als bijna-kritisch; bij 3500 K en 0,5 GPa vinden we een superkritische overgang[†]. Onder deze omstandigheden nemen we de vorming van nieuwe tetraëders waar uit atomen die aan het begin van de simulatie tot andere tetraëders behoorden. De levensduur van deze nieuw-gevormde tetraëders verschilt en kan in de orde van de totale simulatietijd zijn. Wanneer de systemen langzaam gekoeld worden tot een temperatuur van 2500 K bij een constante druk van 0,5 GPa, wordt er steeds vaker herschikking van de tetraëders waargenomen.

In hoofdstuk 6 introduceren we de ‘bond order’ potentialen, inclusief de door ons ontwikkelde potentiaal voor koolstof. We verantwoorden de functionele vorm van de potentialen aan de hand van twee theorieën en behandelen een aantal bond order potentialen waarmee in de afgelopen 20 jaar goede resultaten zijn behaald. Vervolgens presenteren we onze bond order potentiaal in haar oorspronkelijke vorm, de zogenaamde LCBOP (‘long range carbon bond order potential’), zoals die gepubliceerd is in Ref. [15]. Tot slot introduceren we de aangepaste vorm van LCBOP, namelijk LCBOP⁺, die in hoofdstuk 8, 9 en 10 gebruikt wordt in onze berekeningen.

[†]Een superkritische overgang vindt plaats bij temperaturen boven de kritische temperatuur en is geen eerste orde overgang meer.

In hoofdstuk 7 proberen we vanuit een historisch perspectief een compleet beeld te schetsen van de ideeën die binnen de wetenschappelijke gemeenschap leven over het fase-diagram van koolstof, met zijn bulkfasen grafiet, diamant en vloeistof(fen). In het bijzonder bespreken we elk artikel dat ingaat op de mogelijke vloeistof-vloeistoffaseovergang van (vloeibaar) koolstof.

In hoofdstuk 8 presenteren we het door ons berekende fase-diagram van koolstof, dat grafiet, diamant en vloeistof bevat. Coëxistentie is gevonden door de vrije energieën van de drie fasen te bepalen door middel van thermodynamische integratie. We vinden een grafiet-diamantcoëxistentielijn die zeer goed overeenkomt met experimentele data. Overeenkomstig met schokgolfexperimenten vinden we dat de smeltpuntslijn van diamant een positieve helling heeft. Ook bij de smeltpuntslijn van grafiet driewaardig gecoördineerde vloeistof (T tegen P) vinden we een positieve richtingscoëfficiënt, terwijl experimenten een maximum laten zien. We behandelen mogelijke oorzaken van dit verschil, waarvan wij denken dat het grotendeels te verklaren is doordat de experimenten bij niet-evenwichtsomstandigheden zijn uitgevoerd. Wij vinden een grafiet-diamant-vloeistof tripelpunt bij $16,4 \pm 0,7$ GPa en 4250 ± 10 K, dus bij een iets lagere temperatuur dan op basis van experimenten *verwacht*.

In hoofdstuk 9 analyseren we de structuur van vloeibaar koolstof. We sluiten de mogelijkheid van een vloeistof-vloeistoffaseovergang uit in het gebied van het fase-diagram dat we hebben bestudeerd. Wij vinden dat gesmolten diamant vanaf het tripelpunt tot ~ 300 GPa een voornamelijk driewaardige gecoördineerde vloeistof is, in tegenstelling tot hetgeen in het algemeen wordt aangenomen. Wij zien dat onderkoeld vloeibaar koolstof een diamantachtige structuur kan hebben, dat wil zeggen, een plaatselijke coördinatie die sterk lijkt op het diamantrooster. We laten gedetailleerd zien welke tekortkomingen andere, nog steeds gebruikte, bond order potentialen hebben bij de beschrijving van de vloeistofstructuur.

In hoofdstuk 10 gaan we in op de homogene nucleatie van diamant vanuit de bulk. Homogene nucleatie is een geactiveerd proces: een proces dat moeilijk spontaan op gang komt, maar snel voortschrijdt wanneer het eenmaal begonnen is. Nauwkeuriger gezegd, "moeilijk op gang komen" betekent dat de spontane fluctuatie die het proces opstart erg zeldzaam is. Achteraf gezien kunnen we voor ons systeem afleiden dat spontane nucleatie ongeveer één keer in honderd simulatiejaren voor zou komen. Om toch dit proces te kunnen bestuderen, hebben we gebruik gemaakt van een onlangs ontwikkelde techniek [237] voor simulatie van zeldzame gebeurtenissen. Net als veel andere methoden voor zeldzame gebeurtenissen, hangt deze techniek af van de definitie die gehanteerd wordt voor vaste deeltjes in de vloeistof. De onderliggende aanname komt uit de klassieke nucleatietheorie (die eveneens kort besproken wordt): wanneer vloeistof geplaatst wordt in een toestand waar een bepaalde kristalstructuur thermodynamisch stabiel is, dan groeit er met moeite een klein cluster van deze vaste structuur. Vanaf een bepaalde kritische grootte groeit het cluster juist erg snel. We hebben een bestaand algoritme [238] aangepast aan onze situatie om vaste deeltjes in de vloeistof te herkennen door naar hun ruimtelijke correlaties te kijken. De methode voor zeldzame gebeurtenissen die wij hebben gebruikt, maakt het mogelijk om een schatting te maken van de nucleatiesnelheid. Het is ons gelukt om paden te vinden die lopen van de diamantachtige vloeistof, zoals eerder beschreven, naar de vaste stof diamant: we vonden een enorm hoge nucleatiesnelheid van 10^{33} nuclei per kubieke meter per seconde.

In hoofdstuk 11 stellen we een algehele verbetering voor van de bond order potentiaal uit het eerdere hoofdstuk, hetgeen de LCBOP II oplevert. De verbetering werd voor-

namelijk ingegeven door de wens twee bekende problemen van de LCBOP I (en ook de LCBOP⁺) op te lossen: voor de LCBOP I is er een barrière voor de vorming van bindingen van $\sim 0,3$ eV bij $\sim 2,1$ Å. Dit is niet altijd correct: wanneer atomen bindingsplaatsen beschikbaar hebben, dan vormt de binding zich zonder energiebarrière. Wij introduceren een ‘middle range’ potentiaal die rekening houdt met dergelijke beschikbare bindingsplaatsen. De gewenste hoeken tussen covalente bindingen van een bepaald atoom hangt ook af van het aantal bindingen. De LCBOP I houdt hier slechts globaal rekening mee, terwijl voor de LCBOP II de afhankelijkheid in hoge mate overdraagbaar is (dat wil zeggen dat LCBOP II ook bruikbaar is voor structuren die bij het ontwerp van de potentiaal niet zijn meegenomen). Bij LCBOP I zorgen deze problemen voor een soort ‘stijfheid’ in de beschrijving van de vloeibare fase. Dit is terug te zien in de kwantitatieve structuur; de potentiaal gedraagt zich kwalitatief wel goed. De LCBOP II reproduceert de referentiegegevens ook kwantitatief uitzonderlijk goed.

In hoofdstuk 12 onderzoeken we de structuur van vloeibaar koolstof nauwkeurig met behulp van de LCBOP II. De afwezigheid van een vloeistof-vloeistoffaseovergang in het stabiele vloeistofgebied wordt bevestigd. Uit de analyse van de toestandsvergelijking in het door ons onderzochte gebied kunnen we afleiden dat een dergelijke vloeistof-vloeistoffaseovergang alleen mogelijk is in de metastabiele vloeistof bij een zeer lage temperatuur (met een kritiek punt bij ~ 1200 K). Directe waarneming van deze overgang wordt tegengewerkt door bevriezing van het systeem, mogelijk naar een amorfe fase. Deze veronderstelde overgang zou dan gelijk zijn aan de vermoede overgang in water.

Synopsis

Il lavoro di ricerca che ha portato alla stesura di questa tesi è stato svolto ad Amsterdam. Questi tesi, prevedibilmente, tratta di diamanti. Ma non solo. L'obiettivo è più ampio, ovvero più ambizioso. Tesi di questa tesi è che anche i liquidi semplici, elementali, possono esibire comportamenti inaspettati, al variare della pressione e della temperatura. Il discorso nelle precedenti pagine quindi s'aggira - cauto - intorno a due liquidi elementali, quelli del fosforo e del carbonio, liquidi la cui coesione è dovuta a legami covalenti. Legami che hanno una lunghezza e una direzionalità piuttosto ben definite. Definizione che mal s'accorda con la "flessibilità" richiesta ad un atomo nella fase liquida.

In un liquido i cui atomi interagissero attraverso forze non direzionali e additive, all'aumentare della pressione aumenterebbe gradualmente il numero dei primi vicini di ogni atomo, sì che la densità del liquido aumenterebbe parimenti gradualmente. A dire che l'equazione di stato avrebbe andamento liscio, senza brusche variazioni; 'smooth', dicono con efficace voce onomatopeica i cugini albionici. È questo il caso dell'argon liquido, per citare solo il caso più studiato, almeno tra i teorici.

Di contro, in un liquido colavente l'aumento dei primi vicini di un atomo non sarebbe così indolore, perché preferenze angolari e non additività dei legami* renderebbero più spesso energeticamente sfavorevole l'ingresso di un nuovo vicino. Del resto, nemmeno accorciare legami è una strada percorribile a lungo, data la loro rigidità. La teoria ammette che queste condizioni possano dare luogo a una transizione di fase nel liquido. Da liquido a liquido. Tra due diversi gradi di disordine. Pittoricamente si potrebbe pensare ad un aumento improvviso e collettivo di coordinazione (numero di primi vicini) ad una certa pressione, causa di un salto in densità. Il liquido cambierebbe bruscamente la struttura locale qualora la pressione divenisse troppo alta per supportare la struttura termodinamicamente favorevole a basse pressioni. È altresì noto che elementi che danno legami covalenti (ma non sono i soli), mostrino fasi cristalline diverse a diverse pressioni e/o temperature, che differiscono per la struttura del reticolo. Si specula che le transizioni nei liquidi siano in qualche modo imparentate con queste transizioni nei solidi. Si consideri che in un diagramma di fase usuale i solidi occupano la regione a bassa temperatura, mentre il (i) liquido (liquidi) occupa (occupano) la regione a più alta temperatura (se l'immaginazione facesse difetto, ci si riferisca alla figura 2.2, ad esempio). Nei liquidi succederebbe in maniera meno mercata, ma parimenti macroscopicamente visibile, ciò che nei solidi è così noto e studiato. Questa in nuce la natura delle transizioni liquido - liquido. Il fatto che queste transizioni,

*Con 'non additività' si intende che l'energia di due legami afferiti allo stesso atomo non è il doppio dell'energia di un singolo legame. Questo perché il nuovo legame interferisce con il precedente (o i precedenti).

stigmatizzate da un salto finito di densità ad una certa data pressione, esistano in natura è ancora tesi non universalmente condivisa.

Oggetto del capitolo 2 è la rivisitazione di un modello che giustifichi l'evenienza delle transizioni liquido – liquido. Questo vien fatto ipotizzando un liquido semplice come miscela di due specie liquide, laddove le particelle dello stesso elemento appartengono ad una ovvero all'altra specie a seconda dell'ordine locale in cui dette particelle sono immerse. La teoria delle miscele binarie ammette che, sotto alcune condizioni, siffatto liquido si separi in due liquidi, aventi la popolazione relativa delle due specie piuttosto diversa. In aggiunta alla teoria classica delle miscele binarie, qui si capisce bene che particelle ascritte ad una specie possano passare all'altra; per cui, non si osserva tipicamente una separazione di fase in due liquidi, quanto una transizione repentina tra una certa popolazione relativa ad un'altra molto diversa con una piccola variazione dei parametri di stato, come ad esempio la pressione o la temperatura. Di qui la transizione di fase. Nel proseguo del capitolo si riporta doverosamente l'esempio più celebre di transizione di fase liquido – liquido: quello relativo all'acqua, per quanto il fenomeno sia solo oggetto di una ipotesi che pare essere non verificabile. Il capitolo chiude con la descrizione di due potenziali modelli, reperiti in letteratura, che mostrano una transizione liquido – liquido. Questi potenziali cercano di afferrare le condizioni fisiche necessarie per dar luogo alla transizione liquido – liquido.

Questo lavoro tesi fa uso validativo elettivo della simulazione al calcolatore, operando ciò che gli addetti definiscono – talora provocatoriamente – come “esperimenti al calcolatore”, per investigare due elementi, principalmente nella loro fase liquida. Si sono scelti, tra i covalenti, il fosforo e il carbonio. Il fosforo perchè detiene la più spettacolare evidenza sperimentale di transizione liquido – liquido [1]. Ulteriori indagini sperimentali [108] hanno chiarito che questa transizione liquido – liquido è peculiare, nel senso che uno dei liquidi, il meno denso, è in realtà super-critico, rispetto alla transizione a gas. Meglio sarebbe parlare, in questo caso, di fluido. Detto fluido lo si pensa, suffragati da analisi strutturali ai raggi X, costituito intieramente di molecole P_4 , in forma tetraedrica. Alla pressione di circa 1 GPa e alla temperatura di circa 1300 K, le molecole costituenti il fluido si romperebbero simultaneamente a dare un liquido covalente, ad una densità di un 30% superiore a quella del fluido molecolare alla stessa pressione.

Il carbonio lo si è scelto perchè disquisizioni teoriche e simulazioni precedenti questo lavoro avevano indicato la possibilità di una transizione del prim'ordine, da un liquido dall'aspetto “grafitico” ad uno dall'aspetto “diamantico” (vedasi la sezione 7.3 per un'analisi bibliografica della vicenda). Nel carbonio la presenza di una transizione liquido – liquido porterebbe a interessanti conseguenze sulla formazione delle fasi solide, la grafite ed il diamante. Infatti, una simile transizione ammetterebbe certamente un punto critico: qualora la temperatura critica non si discostasse enormemente da quella di fusione, allora le fluttuazioni al punto critico connesse avrebbero una ricaduta sulla dinamica della nucleazione della fase solida [228].

Il fosforo è stato studiato, nei capitoli 4 e 5, con il metodo della dinamica molecolare ab initio, secondo cui le interazioni tra gli atomi, pensati come particelle classiche, sono ricavate da informazioni quantistiche, mercè la “teoria del funzionale di densità”. La teoria viene esposta, per sommi capi, nel capitolo 3. Simulazioni atomistiche e a maggior ragione simulazioni ab initio danno spesso informazioni non immediatamente correlabili agli esperimenti, specie in materia di transizioni di fase. Il problema risiede principalmente nell'esiguo numero di particelle che è possibile simulare. Per ottenere risultati nel tempo

stabilito dei 4 anni di dottorato, non si è potuto andare oltre i 64 atomi di fosforo, inizialmente raggruppati in 16 tetraedri. Tenendo presente il precedente caveat, nel fosforo si è invero trovata la transizione cercata. A 1500 K, si è osservato che aumentando da 0,5 GPa la pressione gradualmente, in modo da far di volta in volta equilibrare il sistema, a 6,25 GPa i tetraedri si rompono per dar luogo ad una fase atomica, a maggiore densità. Lusso riservato al simulatore, è possibile guardare, con un programma di visualizzazione, il movimento delle 64 particelle, onde ravvisarvi eventuali meccanismi peculiari. In effetti, si è potuto notare che la transizione vera e propria viene sempre anticipata da un evento particolare: a tre tetraedri vicini si rompe un legame ciascuno e queste tre “farfalle” (vedasi figura 4.12) si uniscono in una catena. Questa struttura è piuttosto stabile, rispetto alla singola “farfalla” di fosforo, la cui vita è comprensibilmente breve. Ben presto la rottura dei tetraedri si propaga a tutto il campione. Nel capitolo 5 si è inseguita la transizione nel fosforo a più alte temperature, obiettivo l’avvicinarsi al punto critico onde poterne stimare la posizione. In questo caso, il contenuto numero di particelle simulate limita ancor di più la portata euristica dell’indagine. Eppure si è potuta trovare una transizione a 3100 K e 1 GPa rivelante segnali di prossima criticità, mentre a 3500 K e 0.5 GPa la transizione era pressochè continua, specie in riferimento alla densità, che restava identica alla rottura dei tetraedri. Nell’ultimo caso, la rottura dei tetraedri non era totale; non solo, si è osservata la formazione di alcuni tetraedri composti da atomi che all’inizio della simulazione appartenevano a tetraedri diversi; tetraedri la cui vita media poteva essere ora breve ora paragonabile alla durata totale della simulazione.

Per il carbonio si pensò di adottare un modello per le interazioni (vale a dire un potenziale) di stampo classico, volendo sacrificare un poco di accuratezza alla maggiore velocità di calcolo. La questione si è posta in modo piuttosto delicato, perché, fin dall’inizio di questo lavoro, si fece chiaro che modelli diversi davano risultati preoccupantemente diversi, specie riguardo al verificarsi stesso della transizione di fase nel liquido. Si è quindi sviluppato un potenziale, collaborando strettamente con gli sviluppatori di uno ottimo preesistente [15] e da quel potenziale medesimo dipartendoci, che fosse sì computazionalmente (relativamente) leggero, ma che non introducesse fenomeni spuri. Il potenziale che si è sviluppato appartiene alla classe dei potenziali “a ordine di legame”. Si è perciò pensato opportuno l’anteporre alla sua discussione un’introduzione e teorica e storica della classe cui appartiene (capitolo 6). In particolare si è data una doppia giustificazione teorica della particolare forma funzionale adottata dai potenziali “a ordine di legame”, nonché un’analisi delle specifiche scelte di implementazione per alcuni membri della classe che hanno avuto un certo successo diffuso, nella ventennale storia della classe stessa. A conclusione del capitolo si introducono nei dettagli il potenziale di Los e Fasolino [15], servito da base al lavoro sul carbonio, e la sua modifica, che si è resa in prima istanza necessaria alla sua applicazione nella fase liquida.

Nel capitolo 7 si vorrebbe intrattenere il lettore ancora con un discorso storico su argomento scientifico, in aperta critica alla comune tendenza, nella comunità scientifica, di affidarsi a finestre di memoria storica di pochi anni, se non mesi. Quante volte è capitato di sentir definire vecchio un lavoro degli anni ’90 del secolo testè conclusosi? Se le tecniche e sperimentali e simulative progrediscono ad una velocità vertiginosa, le idee appaiono spesso molto più lente ad evolversi. Spesso, pescando in articoli degli albori del secolo ventesimo, capita di imbattersi in considerazioni di portata quasi profetica, considerando i mezzi. Altre volte, idee del tutto fuorvianti tendono a farsi dogma, tranne poi scoprire

che il loro autore le aveva solo tentativamente suggerite. Nel piccolo mondo di questa tesi, si è cercata ogni informazione possibile sullo studio del diagramma di fase del carbonio, in riferimento alle sue celebri fasi solide, la grafite e il diamante, e al liquido (o, secondo alcuni, i liquidi) ottenuto dalla loro fusione.

Il capitolo 8 presenta i metodi e i risultati relativi al calcolo del diagramma di fase del carbonio, limitatamente alla finestra di temperatura e pressione dove diamante, grafite e liquido sono stabili. Il che vuol dire che la pressione considerata è dell'ordine dei gigapascal (decine di migliaia di atmosfere). Le temperature vanno dallo zero assoluto a 10000 K, visto che il liquido si forma dai 4000 K in su, a seconda della pressione e della fase solida da fondere. Il calcolo del diagramma di fase è uno dei tour-de-force in cui l'autore di questa tesi si è prodotto. Calcolare le linee di coesistenza nel diagramma pressione-temperatura di una sostanza ha implicato eguagliare le energie libere delle diverse fasi coinvolte. Il calcolo delle energie libere è uno dei più laboriosi che si possano incontrare nel regno della simulazione atomistica. Il lettore smaliziato saprà che le energie libere assolute non sono calcolabili in tempi umani, visto che la loro stima richiederebbe il visitare una parte almeno rappresentativa di *tutto* lo spazio delle fasi riferito al sistema in esame. Ci si accontenta, ed è già tanto, di calcolare la *differenza* in energia libera delle fasi in gioco da stati o sistemi di riferimento per cui, deo gratia, l'energia libera si può calcolare analiticamente. Ed è ciò che è stato fatto per poter scrivere questo capitolo, mercè una tecnica nota come "integrazione termodinamica". Il diagramma di fase così calcolato presenta (figure 8.4 e 8.5) una linea di coesistenza tra grafite e diamante che giace molto vicina ai punti sperimentali. La temperatura di fusione del diamante cresce al crescere della pressione, così come i pochi esperimenti in merito suggeriscono. In contrasto con gli esperimenti, il calcolo trova una temperatura di fusione della grafite sempre crescente; gli esperimenti trovano un massimo in temperatura di fusione alla pressione di circa 6 GPa, sebbene la temperatura massima misurata sia scesa di circa 1000 K in 30 anni di esperimenti. Nel capitolo si delineano ipotesi sull'origine di questo indubbio discostarsi dagli esperimenti: per citare un solo argomento e rimandando il lettore al capitolo, vien chiaro che gli esperimenti sono tutti stati fatti fuori equilibrio e che essi riportano, più che la temperatura di fusione, la temperatura di instabilità meccanica della grafite rispetto al liquido, tracciando così, più che una linea di fusione, una linea spinodale.

Nel capitolo 9 il palcoscenico è finalmente approntato per affrontare la questione della transizione liquido – liquido nel carbonio. Orbene, in accordo con altrui calcoli ab initio [14] che sono apparsi durante il presente lavoro di ricerca, non si è trovata traccia dell'attesa transizione. È sì vero che il liquido a pressioni relativamente basse, in corrispondenza della fusione della grafite, ha aspetto "grafitico" (gli atomi tendono a coordinarsi con tre vicini, formando con loro approssimativamente un piano, mentre gli angoli di legame valgono in media $2\pi/3$ radianti), ma il diamante, sino a circa 300 GPa, fonde nondimeno in un liquido piuttosto "grafitico". Il liquido "diamantico" (dove gli atomi hanno preferibilmente quattro vicini, trovandosi ciascuno mediamente al centro di un tetraedro) si ritrova nella regione dove esso è metastabile rispetto al diamante, a pressioni non minori di circa 100 GPa (un milione di atmosfere). Con metastabile si intende un liquido al di sotto della temperatura di solidificazione (definire "di congelamento" temperature di diverse migliaia di kelvin pare assurdo) che, per ragioni cinetiche, tarda ad "accorgersi" che il cristallo sarebbe a quel punto termodinamicamente più stabile. Il carbonio liquido sottoraffreddato può quindi trasformarsi in un viscosissimo liquido "diamantico" prima di solidificare. Nella

lettura di questo capitolo, si spera che il lettore non sia troppo sconcertato nello scoprire, eventualmente, che il diamante non è termodinamicamente stabile a pressione ambiente. La figura 11.8 dovrebbe rassicurarlo, visto che la probabilità che la gemma si trasformi in grafite è resa evanescente dalla enorme barriera energetica, di circa 0.6 eV, che ogni atomo di diamante dovrebbe superare per trasformarsi in grafite.

Ed ecco, finalmente, i diamanti. Nel capitolo 10 si è cercato di iniziare a capire, forti del potenziale e del relativo diagramma di fase, sotto che condizioni si formino i diamanti. “Why diamonds?”, perché i diamanti? titolava originariamente il progetto per cui 4 anni fa l’autore ha cominciato a simulare e studiare i liquidi covalenti. Studiare come il carbonio liquido si trasforma in diamante, ossia la nucleazione del diamante, ha imposto all’autore un secondo tour-de-force. La nucleazione cui si è mirato è quella cosiddetta “omogenea”, cioè quella per cui il fenomeno è esclusivo prodotto delle fluttuazioni che naturalmente agitano il liquido (o la materia in genere). In contrasto si dice “eterogenea” la nucleazione in cui qualche corpuscolo estraneo (un atomo di un’altra sostanza) o qualche causa geometrica (una parete) o meccanica (un urto) esterna si dice che agiscano da “seme”. È facile accorgersi che in natura la nucleazione è più etero che omogenea, eppure lo studio simulativo della seconda fornisce solitamente più chiarezza riguardo al meccanismo della nucleazione stessa. La nucleazione omogenea è un fenomeno attivato: rarissimamente si innesca, tranne poi procedere piuttosto velocemente. Negli esperimenti al calcolatore questi eventi rari sono veramente rari, a causa del fatto che un secondo di un campione reale verrebbe simulato in tempi che possono facilmente aggirarsi sul milione d’anni. Per questo si utilizzano tecniche che tentano di favorire il verificarsi dell’evento raro pur senza perdere informazione sulla probabilità che l’evento raro si verifichi. Per questo capitolo si è adattato alle caratteristiche del sistema carbonio un metodo di recente sviluppo [237]. L’idea è quella di assumere che la nucleazione si produca per crescita di un nucleo di particelle che nel liquido si dispongono, casualmente, a guisa di cristallo. Questo nucleo talvolta cresce: appena raggiunta una certa dimensione detta critica, le particelle del liquido tenderebbero ad attaccarsi velocemente al nucleo sicché tutto il campione solidifica nel cristallo[†]. La ricetta che il metodo usato propone, consente di inseguire quei piccoli nuclei che spontaneamente si formano nel liquido (anche nelle scale di tempi accessibili al simulatore) e simularle ad oltranza finché essi non raggiungono dimensione critica. Si è trovato che il liquido “diamantico” nuclea precipitevolissimamente al rateo di 10^{33} nuclei per metro cubo per secondo.

Insieme alle applicazioni del potenziale per il carbonio, modificato secondo quanto riportato nel capitolo 6, si è sentito necessario lavorare ulteriormente sul miglioramento del potenziale, sempre insieme a Jan Los e Annalisa Fasolino. Infatti, *qualitativamente* il potenziale usato riproduceva sempre e soddisfacentemente le caratteristiche del liquido, così come suggerite dalle assai più dispendiose, in quanto a sforzo computazionale, simulazioni ab initio. Diverse considerazioni vanno riferite alla descrizione delle fasi solide, laddove la riproducibilità anche *quantitativa* dei dati di riferimento (ora ab initio, ora, ove disponibili, sperimentali) si è sempre dimostrata notevole fin dalla prima formulazione del potenziale. Il riprodurre *quantitativamente* le caratteristiche strutturali del liquido alle diverse pressioni e temperature ha richiesto un profondo ripensamento del potenziale. Il risultato di questo lavoro certoso è riportato nei capitoli 11 e 12. Nel primo di questi

[†]A meno che non si siano sviluppati altri di questi nuclei che, una volta “incontratisi”, potrebbero dar luogo ad un solido costituito di diversi nuclei diversamente orientati, quel che si dice essere un policristallo.

capitoli si descrive in minuziosi dettagli il potenziale stesso, mentre nel secondo si analizza il comportamento del potenziale nel liquido, e nella sua capacità di riprodurre i dati di riferimento, e nelle sue potenzialità predittive. In quest'ultimo capitolo si adombra l'ipotesi che una transizione liquido – liquido per il carbonio sia riscontrabile a temperature piuttosto basse, con una temperatura critica ben al di sotto della temperatura di congelamento, anche per un campione di poche centinaia di atomi. Se detto punto critico, stimato a circa 42 GPa e 1200 K, esiste, allora le fluttuazioni ad esso connesse, ancora potrebbero giocare un ruolo importante nella nucleazione della fase solida in regioni non necessariamente ad esso prossime del diagramma di fase.

Bibliography

- [1] Y. KATAYAMA, T. MIZUTANI, W. UTSUMI, O. SHIMOMURA, M. YAMAKATA, and K. FUNAKOSHI, *Nature* **403**, 170 (2000).
- [2] J. N. GLOSLI and F. H. REE, *Phys. Rev. Lett.* **82**, 4659 (1999).
- [3] D. W. BRENNER, *Phys. Rev. B* **42**, 9458 (1990), Erratum: *Phys. Rev. B* **46**, 1948 (1992).
- [4] D. W. BRENNER, J. H. HARRISON, C. T. WHITE, and R. J. COLTON, *Thin Solid Films* **206**, 220 (1991).
- [5] E. RAPOPORT, *J. Chem. Phys.* **46**, 2891 (1967).
- [6] S. STRÄSSLER and C. KITTEL, *Phys. Rev.* **139**, A758 (1965).
- [7] I. L. APTEKAR and E. G. PONYATOVSKY, *Phys. Met. Metallogr.* **25**, 10 (1968).
- [8] I. A. KORSUNSKAYA, D. S. KAMENETSKAYA, and I. L. APTEKAR, *Fiz. metal. metalloved.* **34**, 942 (1972), English version in: *Phys. Met. Metallogr. (USSR)* **34**, 39 (1972).
- [9] V. V. BRAZHKIN, S. V. POPOVA, and R. N. VOLOSHIN, *High Pressure Research* **15**, 267 (1997).
- [10] H. TANAKA, *Phys. Rev. E* **62**, 6968 (2000).
- [11] L. M. GHIRINGHELLI and E. J. MEIJER, *J. Chem. Phys.* **122**, 184510 (2005).
- [12] L. M. GHIRINGHELLI and E. J. MEIJER, (2005), in preparation.
- [13] D. FRENKEL and B. SMIT, *Understanding Molecular simulation*, Academic Press, San Diego, California, 2002.
- [14] C. J. WU, J. N. GLOSLI, G. GALLI, and F. H. REE, *Phys. Rev. Lett.* **89**, 135701 (2002).
- [15] J. H. LOS and A. FASOLINO, *Phys. Rev. B* **68**, 024107 (2003).
- [16] L. M. GHIRINGHELLI, J. H. LOS, E. J. MEIJER, A. FASOLINO, and D. FRENKEL, *Phys. Rev. Lett.* **94**, 145701 (2005).
- [17] L. M. GHIRINGHELLI, J. H. LOS, E. J. MEIJER, A. FASOLINO, and D. FRENKEL, *Phys. Rev. B* **69**, 100101(R) (2004).
- [18] L. M. GHIRINGHELLI, J. H. LOS, E. J. MEIJER, A. FASOLINO, and D. FRENKEL, *J. Phys.: Condens. Matter* **17**, S3619 (2005).
- [19] L. M. GHIRINGHELLI, C. VALERIANI, E. J. MEIJER, and D. FRENKEL, (2005), in preparation.

- [20] J. H. LOS, L. M. GHIRINGHELLI, E. J. MEIJER, and A. FASOLINO, *Phys. Rev. B* **72** (2005), in press.
- [21] L. M. GHIRINGHELLI, J. H. LOS, A. FASOLINO, and E. J. MEIJER, *Phys. Rev. B* **72** (2005), in press.
- [22] M. P. TOSI, *J. Phys.: Condens. Matter* **6**, A13 (1994).
- [23] E. A. GUGGENHEIM, *Mixtures*, Clarendon Press, Oxford, 1952.
- [24] E. RAPOPORT, *Phys. Rev. Lett.* **19**, 345 (1967).
- [25] E. RAPOPORT, *J. Chem. Phys.* **48**, 1433 (1968).
- [26] P. DEBYE and A. M. BUECHE, *J. Appl. Phys.* **20**, 518 (1949).
- [27] E. W. FISHER, *Physica A* **210**, 183 (1993).
- [28] R. PIAZZA and S. IACOPINI, *The European Physical Journal E* **7**, 45 (2002).
- [29] A. JAYARAMAN, R. C. NEWTON, and J. M. McDONOUGH, *Phys. Rev.* **159**, 527 (1967).
- [30] R. BELLISENT, C. BERGMAN, R. CEOLIN, and J. P. GASPARD, *Phys. Rev. Lett.* **59**, 661 (1987).
- [31] D. A. YOUNG, *Phase Diagrams of the Elements*, University of California Press, Berkeley, 1991.
- [32] O. OHTAKA, H. ARIMA, H. FUKUI, W. UTSUMI, Y. KATAYAMA, and A. YOSHIASA, *Phys. Rev. Lett.* **92**, 155506 (2004).
- [33] D. ISHIKAWA, M. INUI, K. MATSUDA, K. TAMURA, S. TSUTSUI, and A. Q. R. BARON, *Phys. Rev. Lett.* **93**, 097801 (2004).
- [34] V. V. BRAZHKIN, R. N. VOLOSHIN, S. V. POPOVA, and A. G. UMNOV, *Phys. Lett. A* **154**, 413 (1991).
- [35] A. G. UMNOV and V. V. BRAZHKIN, *High Pressure Research* **13**, 233 (1995).
- [36] V. V. BRAZHKIN, R. N. VOLOSHIN, and S. V. POPOVA, *Pis'ma v ZhETF* **50**, 424 (1989), English translation in : *JETP Letters* **50**, 424 (1989).
- [37] C. A. ANGELL, S. BORICK, and M. GRABOW, *J. of Non-cryst. Solids* **205**, 463 (1996).
- [38] P. BEAUCAGE and N. MOUSSEAU, *J. Phys.: Condens. Matter* **17**, 2269 (2005).
- [39] A. G. UMNOV and V. V. BRAZHKIN, *High Temp. - High Pressure* **25**, 221 (1993).
- [40] S. T. WEIR, A. C. MITCHELL, and W. J. NELLIS, *Phys. Rev. Lett.* **76**, 1860 (1996).
- [41] V. V. BRAZHKIN, R. N. VOLOSHIN, S. V. POPOVA, and A. G. UMNOV, *High Pressure Research* **6**, 363 (1992).
- [42] C. J. ROBERTS, A. Z. PANAGIOTOPOULOS, and P. G. DEBENEDETTI, *Phys. Rev. Lett.* **77**, 4386 (1996).
- [43] P. H. POOLE, M. HEMMATI, and C. A. ANGELL, *Phys. Rev. Lett.* **79**, 2281 (1997).

- [44] J. P. IITIE, *Phys. Rev. Lett.* **63**, 398 (1989).
- [45] H. E. STANLEY, S. V. BULDYREV, M. CANPOLAT, O. MISHIMA, M. R. SADR-LAHIJANY, A. SCALA, and F. W. STARR, *Phys. Chem. Chem. Phys.* **2**, 1551 (2000).
- [46] P. G. DEBENEDETTI, *Metastable Liquids*, Princeton University Press, 1996.
- [47] G. FRANZESE, G. MALESCIO, A. SKIBINSKY, S. BULDYREV, and H. STANLEY, *Nature* **409**, 692 (2001).
- [48] E. F. BURTON and W. F. OLIVER, *Proc. R. Soc. Lond. A* **153**, 166 (1936).
- [49] O. MISHIMA, L. D. CALVERT, and E. WHALLEY, *Nature* **310**, 393 (1984).
- [50] O. MISHIMA, L. D. CALVERT, and E. WHALLEY, *Nature* **314**, 76 (1985).
- [51] P. H. POOLE, F. SCIORTINO, U. ESSMANN, and H. E. STANLEY, *Nature* **360**, 324 (1992).
- [52] P. H. POOLE, F. SCIORTINO, U. ESSMANN, and H. E. STANLEY, *Phys. Rev. E* **48**, 3799 (1993).
- [53] H. TANAKA, *J. Chem. Phys.* **105**, 5099 (1996).
- [54] S. HARRINGTON, R. ZHANG, P. H. POOLE, F. SCIORTINO, and H. E. STANLEY, *Phys. Rev. Lett.* **78**, 2409 (1997).
- [55] F. SCIORTINO, P. H. POOLE, U. ESSMANN, and H. E. STANLEY, *Phys. Rev. E* **55**, 727 (1997).
- [56] S. HARRINGTON, P. H. POOLE, F. SCIORTINO, and H. E. STANLEY, *J. Chem. Phys.* **107**, 7443 (1997).
- [57] O. MISHIMA and H. E. STANLEY, *Nature* **396**, 329 (1998).
- [58] S. V. BULDYREV, G. FRANZESE, N. GIOVAMBATTISTA, G. MALESCIO, M. R. SADR-LAHIJANY, A. SCALA, A. SKIBINSKY, and H. E. STANLEY, *Physica A* **304**, 23 (2002).
- [59] H. LEE and R. SWEDENSEN, *Phys. Rev. B* **64**, 214102 (2001).
- [60] CPMD, version 3.3, developed by J. Hutter, A. Alavi, T. Deutsch, M. Bernasconi, S. Goedecker, D. Marx, M. Tuckerman, and M. Parrinello, MPI für Festkörperforschung and IBM Zurich Research Laboratory (1995-1999).
- [61] A. SZABO and N. S. OSTLUND, *Modern Quantum Chemistry - Introduction to Advanced Electronic Structure Theory*, McGraw-Hill Publishing Company, New York, 1989.
- [62] R. CAR and M. PARRINELLO, *Phys. Rev. Lett.* **55**, 2471 (1985).
- [63] G. PASTORE, E. SMARGIASSI, and F. BUDA, *Phys. Rev. A* **44**, 6334 (1991).
- [64] D. MARX and J. HUTTER, in *Modern Methods and Algorithms of Quantum Chemistry Proceedings, Second Edition*, edited by J. GROTEENDORST, Forschungszentrum Jülich, 2000, it can be found at <http://www.fz-juelich.de/nic-series/>.
- [65] F. A. BORNEMANN and C. SCÜTTE, *Numer. Math.* **78**, 359 (1998).
- [66] P. HOHENBERG and W. KOHN, *Phys. Rev.* **136**, B864 (1964).

- [67] W. KOHN and L. J. SHAM, *Phys. Rev. A* **140**, 1133 (1965).
- [68] D. M. CEPERLEY and B. J. ALDER, *Phys. Rev. Lett.* **45**, 566 (1980).
- [69] H. B. SHORE, J. H. ROSE, and E. ZAREMBA, *Phys. Rev. B* **15**, 2858 (1977).
- [70] F. W. KUTZLER and G. S. PAINTER, *Phys. Rev. Lett.* **59**, 1285 (1987).
- [71] P. MLYNARSKI and D. R. SALAHUB, *Phys. Rev. B* **43**, 1399 (1991).
- [72] C. S. WANG, B. M. KLEIN, and H. KRAKAUER, *Phys. Rev. Lett.* **54**, 1852 (1985).
- [73] W. WEBER, *Phys. Rev. Lett.* **58**, 1371 (1987).
- [74] T. C. LEUNG, C. T. CHAN, and B. N. HARMON, *Phys. Rev. B* **44**, 2923 (1991).
- [75] R. Q. HOOD, M. Y. CHOU, A. J. WILLIAMSON, G. RAJAGOPAL, and R. J. NEEDS, *Phys. Rev. Lett.* **78**, 3350 (1997).
- [76] R. Q. HOOD, M. Y. CHOU, A. J. WILLIAMSON, G. RAJAGOPAL, and R. J. NEEDS, *Phys. Rev. B* **57**, 8972 (1998).
- [77] D. C. LANGRETH and M. J. MEH, *Phys. Rev. B* **28**, 1809 (1983), Erratum: *Phys Rev B* **29**, 2310 (1984).
- [78] J. P. PERDEW, *Phys. Rev. B* **33**, 8822(R) (1986), Erratum *Phys. Rev. B* **34**, 7406 (1986).
- [79] A. D. BECKE, *Phys. Rev. A* **38**, 3098 (1988).
- [80] C. LEE, W. YANG, and R. G. PARR, *Phys. Rev. B* **37**, 785 (1988).
- [81] J. P. PERDEW, J. A. CHEVARY, S. H. VOSKO, K. A. JACKSON, M. R. PEDERSON, D. J. SINGH, and C. FIOLEHAI, *Phys. Rev. B* **46**, 6671 (1992).
- [82] A. D. BECKE, *J. Chem. Phys.* **96**, 2155 (1992).
- [83] B. G. JOHNSON, P. M. W. GILL, and J. A. POPLE, *J. Chem. Phys.* **98**, 5612 (1993).
- [84] X. J. KONG, C. T. CHAN, K. M. HO, and Y. Y. YE, *Phys. Rev. B* **42**, 9537 (1990).
- [85] G. ORTIZ, *Phys. Rev. Lett.* **45**, 11328 (1992).
- [86] A. GARCIA, C. ELSSER, J. ZHU, S. G. LOUIE, and M. L. COHEN, *Phys. Rev. B* **46**, 9829 (1992).
- [87] E. FERMI, *Nuovo Cimento* **11**, 157 (1934).
- [88] J. C. PHILLIPS and L. KLEINMAN, *Phys. Rev.* **116**, 287 (1959).
- [89] D. VANDERBILT, *Phys. Rev. B* **41**, 7892(R) (1990).
- [90] K. LAASONEN, R. CAR, C. LEE, and D. VANDERBILT, *Phys. Rev. B* **43**, 6796(R) (1991).
- [91] M. FUCHS and M. SCHEFFER, *Comput. Phys. Commun.* **119**, 67 (1999).
- [92] H. C. ANDERSEN, *J. Chem. Phys.* **72**, 2384 (1980).
- [93] S. NOSÉ, *Mol. Phys.* **52**, 255 (1984).

- [94] W. G. HOOVER, *Phys. Rev. A* **31**, 1695 (1985).
- [95] W. G. HOOVER, *Phys. Rev. A* **34**, 2499 (1985).
- [96] G. J. MARTYNA, M. L. KLEIN, and M. E. TUCKERMAN, *J. Chem. Phys.* **97**, 2635 (1992).
- [97] M. E. TUCKERMAN and M. PARRINELLO, *J. Chem. Phys.* **101**, 1302 (1994).
- [98] P. E. BLÖCHL and M. PARRINELLO, *Phys. Rev. B* **45**, 9413 (1992).
- [99] P. E. BLÖCHL, *Phys. Rev. B* **65**, 104303 (2002).
- [100] M. PARRINELLO and A. RAHMAN, *Phys. Rev. Lett.* **45**, 1196 (1980).
- [101] P. Focher, Ph.D. Thesis: *First-principle studies of structural phase transformations* (SISSA, Trieste, 1994).
- [102] P. G. DACOSTA, O. H. NIELSEN, and K. KUNC, *J. Phys. C: Solid State Phys.* **19**, 3163 (1986).
- [103] P. FOCHER, G. L. CHIAROTTI, M. BERNASCONI, E. TOSATTI, and M. PARRINELLO, *Europhys. Lett.* **26**, 345 (1994).
- [104] Y. AKAHAMA, W. UTSUMI, S. ENDO, T. KIKEGAWA, H. IWASAKI, O. SHIMOMURA, C. T. YAGI, and S. AKIMOTO, *Physics Letters A* **122**, 129 (1987).
- [105] D. R. PECK, *Mellor's comprehensive treatise on inorganic and theoretical chemistry*, volume 8, pp. 149–227, Longman, London, 1971.
- [106] T. MORISHITA, *Phys. Rev. Lett.* **87**, 105701 (2001).
- [107] Y. KATAYAMA, *J. Non-Cryst. Solids* **312-314**, 8 (2002).
- [108] G. MONACO, S. FALCONI, W. A. CRICHTON, and M. MEZOUAR, *Phys. Rev. Lett.* **90**, 255701 (2003).
- [109] J. S. KANE and J. H. REYNOLDS, *J. Chem. Phys.* **25**, 342 (1956).
- [110] R. O. JONES and D. HOHL, *J. Chem. Phys.* **92**, 6710 (1990).
- [111] D. HOHL and R. O. JONES, *Phys. Rev. B* **50**, 17047 (1994).
- [112] Y. SENDA, F. SHIMOJO, and K. OSHINO, *J. Phys.: Condens. Matter* **14**, 3715 (2002).
- [113] N. TROULLIER and J. L. MARTINS, *Phys. Rev. B* **43**, 1993 (1991).
- [114] L. KLEINMAN and D. M. BYLANDER, *Phys. Rev. Lett.* **48**, 1425 (1982).
- [115] J. P. PERDEW and A. ZUNGER, *Phys. Rev. B* **23**, 5048 (1981).
- [116] S. KRISTYÁN and P. PULAY, *Chem. Phys. Lett* **229**, 175 (1994).
- [117] J. PÉREZ-JORDÁN and A. BECKE, *J. Chem. Phys.* **233**, 134 (1995).
- [118] E. J. MEIJER and M. SPRIK, *J. Chem. Phys.* **105**, 8684 (1996).
- [119] A. K. RAPPÉ, C. J. CASEWIT, K. S. COLWELL, W. A. G. III, and W. M. SKIFF, *J. Am. Chem. Soc.* **114**, 10024 (1992).

- [120] Private communication with Y. Katayama.
- [121] L. PAULING and M. SIMONETTA, *J. Chem. Phys.* **20**, 29 (1952).
- [122] J. C. DORE and J. GRANADA, *Mol. Phys.* **46**, 757 (1982).
- [123] M. MISAWA, *J. Chem. Phys.* **93**, 6774 (1990).
- [124] A. KORNATH, A. KAUFMANN, and M. TORHEYDEN, *J. Chem. Phys.* **116**, 3323 (2002).
- [125] W. B. STRETT and D. J. TILDESLEY, *Proc. R. Soc. Lond.* **A348**, 485 (1976).
- [126] J. TERSOFF, *Phys. Rev. Lett.* **56**, 632 (1986).
- [127] J. TERSOFF, *Phys. Rev. B* **37**, 6991 (1988).
- [128] J. TERSOFF, *Phys. Rev. B* **38**, 9902 (1988).
- [129] J. TERSOFF, *Phys. Rev. Lett.* **61**, 2879 (1988).
- [130] D. W. BRENNER, O. A. SHENDEROVA, J. A. HARRISON, S. J. STUART, B. NI, and S. B. SINNOTT, *J. Phys.: Condens. Matter* **14**, 783 (2002).
- [131] D. W. BRENNER, O. A. SHENDEROVA, and D. A. ARESHKIN, in *Reviews in Computational Chemistry*, edited by K. B. LIPKOWITZ and D. B. BOYD, volume 5, Wiley-VCH, New York, 1998.
- [132] C. A. COULSON, *Proceedings of the Royal Society of London. Series A, Mathematical and Physical Sciences* **169**, 413 (1939).
- [133] G. C. ABELL, *Phys. Rev. B* **31**, 6184 (1985).
- [134] P. W. ANDERSON, *Phys. Rev. Lett.* **21**, 13 (1968).
- [135] P. W. ANDERSON, *Phys. Rev.* **181**, 25 (1969).
- [136] J. D. WEEKS and P. W. ANDERSON, *J. Chem. Phys.* **58**, 1388 (1973).
- [137] A. STREITWIESER, *Molecular Orbital Theory*, Wiley, New York, 1961.
- [138] J. FERRANTE, J. R. SMITH, and J. H. ROSE, *Phys. Rev. Lett.* **50**, 1385 (1983).
- [139] A. P. SUTTON, *Electronic Structure of the Materials*, Clarendon Press, Oxford, 1993.
- [140] R. HAYDOCK, V. HEINE, and M. J. KELLY, *J. Phys. C* **5**, 2845 (1972).
- [141] L. PAULING, *The Nature of the Chemical Bond, 3rd ed.*, Cornell University Press, Ithaca, NY, 1960.
- [142] J. H. ROSE, J. R. SMITH, and J. FERRANTE, *Phys. Rev. B* **28**, 1835 (1983).
- [143] A. P. SUTTON, M. W. FINNIS, D. G. PETTIFOR, and Y. OHTA, *J. Phys.: Condens. Matter* **21**, 35 (1988).
- [144] M. W. FINNIS and J. E. SINCLAIR, *Philos. Mag.* **A50**, 45 (1984).
- [145] F. H. STILLINGER and T. WEBER, *Phys. Rev. B* **31**, 5262 (1985).

- [146] J. F. JUSTO, M. Z. BAZANT, E. KAXIRAS, V. V. BULATOV, and S. YIP, *Phys. Rev. B* **58**, 2539 (1998).
- [147] N. A. MARKS, *Phys. Rev. B* **63**, 035401 (2001).
- [148] M. T. YIN and M. L. COHEN, *Phys. Rev. Lett.* **45**, 1004 (1980).
- [149] M. T. YIN and M. L. COHEN, *Phys. Rev. B* **29**, 6996 (1984).
- [150] K. J. CHANG and M. L. COHEN, *Phys. Rev. B* **30**, 5376 (1984).
- [151] A. Y. LIU, M. L. COHEN, and K. C. K. M. A. TAMOR, *Phys. Rev. B* **43**, 6742 (1991).
- [152] S. B. SINNOTT, O. A. SHENDEROVA, C. T. WHITE, and D. W. BRENNER, *Carbon* **36**, 1 (1998).
- [153] A. PETUKHOV and A. FASOLINO, in *Technical Proceedings of the ICCN 2001 Int. Conf. on Computational Nanoscience*, Applied Computational Research Society, also at <http://www.cr.org/publications/ICCN2001/>.
- [154] J. CHE, T. CAGIN, and W. A. GODDARD III, *Theor. Chem. Acc.* **102**, 346 (1999).
- [155] S. J. STUART, A. B. TUTEIN, and J. A. HARRISON, *J. Phys. Chem.* **14**, 6472 (2000).
- [156] S. FAHY, S. T. LOUIE, and M. L. COHEN, *Phys. Rev. B* **34**, 1191 (1986).
- [157] K. RAGHAVACHARI and J. S. BINKLEY, *J. Chem. Phys.* **87**, 2191 (1987).
- [158] K. KOBAYASHI, N. KUTITA, H. KUMAHORA, and K. TAGO, *Phys. Rev. B* **45**, 11299 (1992).
- [159] L. SALEM, *The Orbital Theory of Conjugated Systems*, W. A. Benjamin Inc., New York, 1966.
- [160] H. W. KROTO, J. R. HEATH, S. C. O'BRIEN, R. F. CURL, and R. E. SMALLEY, *Nature* **318**, 162 (1985).
- [161] S. IIJIMA, *Nature* **354**, 56 (1991).
- [162] H. W. B. ROOZEBOOM, *Die heterogenen Gleichgewichte*, Braunschweig, volume 1, 1901.
- [163] G. TAMMAN, *Zeit. Phys. Chem* **69** (1909).
- [164] F. D. ROSSINI and R. S. JESSUP, *J. Res. Nat'l. Bur. Stds.* **21**, 491 (1938).
- [165] O. I. LEIPUNSKII, *Uspekhi Khim.* **8**, 1519 (1939).
- [166] M. J. BASSET, *J. Chem. Radium* **10**, 217 (1939).
- [167] P. W. BRIDGMAN, *J. Chem. Phys.* **15**, 92 (1947).
- [168] R. LILJEBLAD, *Arkiv Kemi* **8**, 423 (1955).
- [169] R. BERMAN and F. SIMON, *Z. Elektrochem.* **59**, 333 (1955).
- [170] F. P. BUNDY, H. T. HALL, H. M. STRONG, and R. H. WENTORF, *Nature* **176**, 51 (1955).
- [171] F. P. BUNDY, *J. Chem. Phys.* **38**, 618 (1963).

- [172] M. T. JONES, *National Carbon Research Laboratories* (1958), Report PC-3.
- [173] J. E. HOVE, Some physical properties of graphite as affected by high temperature and irradiation, in *Industrial Carbon and Graphite*, Society of Chemical Industries, London, 1958.
- [174] P. S. DECARLI and J. C. JAMIESON, *Science* **133**, 1821 (1961).
- [175] B. J. ALDER and R. H. CHRISTIAN, *Phys. Rev. Lett.* **7**, 367 (1961).
- [176] F. P. BUNDY, *J. Chem. Phys.* **38**, 631 (1963).
- [177] A. E. GORESY and G. DONNAY, *Science* **161**, 363 (1968).
- [178] A. G. WHITTAKER, *Science* **200**, 4343 (1978).
- [179] V. I. KASATOCHIN, V. V. SAORANSKY, and B. N. SMIRNOV, *Dokl. Akad. Nauk SSSR* **217**, 796 (1974).
- [180] P. P. K. SMITH and P. R. BUSECK, *Science* **216**, 984 (1982).
- [181] VANVECHTEN, *Phys. Rev. B* **7**, 1479 (1973).
- [182] R. GROVER, *J. Chem. Phys.* **71**, 3824 (1979).
- [183] T. VENKATESAN, D. C. JACOBSON, J. M. GIBSON, B. S. ELMAN, G. BRAUNSTEIN, M. S. DRESSELHAUS, and G. DRESSELHAUS, *Phys. Rev. Lett.* **53**, 360 (1984).
- [184] G. GALLI, R. M. MARTIN, R. CAR, and M. PARRINELLO, *Science* **250**, 1547 (1990).
- [185] J. C. JAMIESON, *Science* **161**, 363 (1963).
- [186] F. P. BUNDY, *Physical Chemistry* (1969), Roozeboom award lecture, 25 October, 1969.
- [187] M. T. YIN and M. L. COHEN, *Phys. Rev. Lett.* **50**, 2006 (1983).
- [188] M. T. YIN, *Phys. Rev. B* **30**, 1773 (1984).
- [189] R. BISWAS, R. M. MARTIN, R. J. NEEDS, and O. H. NIELSEN, *Phys. Rev. B* **35**, 1987 (1987).
- [190] S. FAHY and S. G. LOUIE, *Phys. Rev. B* **36**, 3373 (1987).
- [191] J. W. SHANER, J. M. BROWN, A. C. SWENSON, and R. G. MCQUEEN, *J. Phys. (Paris) Colloq.* **45**, C8 (1984).
- [192] M. TOGAYA, in *Science and Technology of New Diamond*, KTK/TSPC, Tokyo, 1990.
- [193] M. ROSS, *Nature* **292**, 435 (1981).
- [194] M. P. GRUMBACH and R. M. MARTIN, *Phys. Rev. B* **54**, 15730 (1996).
- [195] D. K. BRADLEY, J. H. EGGERT, D. G. HICKS, P. M. CELLIERS, S. J. MOON, R. C. CAUBLE, and G. W. COLLINS, *Phys. Rev. Lett.* **93**, 195506 (2004).
- [196] E. I. ASINOVSKII, A. V. KIRILLIN, and A. V. KOSTANOVSKII, *High Temperature* **35**, 704 (1997).

- [197] J. W. SHANER, J. M. BROWN, A. C. SWENSON, and R. G. MCQUEEN, *J. Phys.* **45**, 235 (1984).
- [198] G. POTTLAGHER, R. S. HIXSON, R. S. MELNITZKY, E. KASCHNITZ, M. A. WINKLER, and H. JAGER, *Termochim. Acta* **218**, 183 (1993).
- [199] A. CEZAIRLIYAN and A. P. MILLER, *Int. J. Thermophys.* **11**, 643 (1990).
- [200] M. TOGAYA, *Phys. Rev. Lett.* **79**, 2474 (1997).
- [201] A. G. WHITTAKER and P. L. KINTNER, Carbon vapor pressure in the range 3450 to 4500 K and evidence for melting at ~ 3800 K, in *Abstract of the 12th biennial conf. on carbon*, Pittsburgh, Pa., 1975.
- [202] I. I. ALTHERTUM, W. FEHSE, and M. PIRANI, *Z. Elektrochem.* **31**, 313 (1925).
- [203] G. J. SCHOESSOW, *Phys. Rev. Lett.* **21**, 11 (1968).
- [204] J. HEREMANS, C. H. OLK, G. L. EESLEY, J. STEINBECK, and G. DRESSELHAUS, *Phys. Rev. Lett.* **60**, 5 (1988).
- [205] F. P. BUNDY, W. A. BASSETT, M. S. WEATHERS, R. J. HEMLEY, H. K. MAO, and A. F. GONCHAROV, *Carbon* **34**, 141 (1996).
- [206] E. I. ASINOVSKII, A. V. KIRILLIN, A. V. KOSTANOVSKII, and V. E. FORTOV, *High Temperature* **36**, 716 (1998).
- [207] M. MUSELLA, C. RONCHI, M. BRYKIN, and M. SHEINDIN, *J. Appl. Phys.* **84**, 2530 (1998).
- [208] A. FERRAZ and N. H. MARCH, *Phys. Chem. Liq.* **8**, 289 (1979).
- [209] M. VAN THIEL and F. H. REE, *High Pressure Research* **10**, 607 (1992).
- [210] M. VAN THIEL and F. H. REE, *Phys. Rev. B* **48**, 3591 (1993).
- [211] N. S. FATEEVA and L. F. VERESHCHAGIN, *Pis'ma. Zh. Eksp. Teor. Fiz.* **13**, 157 (1971).
- [212] E. PONYATOVSKY, *J. Phys.: Condens. Matter* **15**, 6123 (2003).
- [213] J. R. MORRIS, C. Z. WANG, and K. M. HO, *Phys. Rev. B* **52**, 4138 (1995).
- [214] J. N. GLOSLI and F. H. REE, *J. Chem. Phys.* **110**, 441 (1999).
- [215] J. ANWAR, D. FRENKEL, and M. G. NORO, *J. Chem. Phys.* **118**, 728 (2003).
- [216] J. K. JOHNSON, J. A. ZOLLWEG, and K. E. GUBBINS, *Molecular Physics* **78**, 591 (1993).
- [217] D. FRENKEL and J. C. LADD, *J. Chem. Phys.* **81**, 3188 (1984).
- [218] J. M. POLSON, E. TRIZAC, S. PRONK, and D. FRENKEL, *J. Chem. Phys.* **112**, 5339 (2000).
- [219] D. A. KOFKE, *J. Chem. Phys.* **98**, 4149 (1993).
- [220] O. KUM, F. H. REE, S. J. STUART, and C. J. WU, *J. Chem. Phys.* **119**, 6053 (2003).
- [221] G. GALLI, R. M. MARTIN, R. CAR, and M. PARRINELLO, *Phys. Rev. Lett.* **63**, 988 (1989).
- [222] G. GALLI, R. M. MARTIN, R. CAR, and M. PARRINELLO, *Phys. Rev. B* **42**, 7470 (1990).

- [223] N. A. MARKS, *J. Phys.: Condens. Matter* **14**, 2901 (2002).
- [224] N. A. MARKS, N. C. COOPER, D. R. MCKENZIE, D. G. MCCULLOCH, P. BATH, and S. P. RUSSO, *Phys. Rev. B* **65**, 075411 (2002).
- [225] B. WIDOM, *J. Phys. Chem.* **39**, 2808 (1963).
- [226] R. EPPENGA and D. FRENKEL, *Mol. Phys.* **52**, 1303 (1984).
- [227] J. V. V. I. HARISMIADIS and A. Z. PANAGIOTOPOULOS, *J. Chem. Phys.* **105**, 8469 (1996).
- [228] P. R. TEN WOLDE, *Numerical Study of Pathways for Homogeneous Nucleation*, 1997, It can be downloaded from:
<http://www.amolf.nl/publications/theses/wolde/wolde.html>.
- [229] H. E. A. HUITEMA, M. J. VLOT, and J. P. VAN DER EERDEN, *J. Chem. Phys.* **111**, 4714 (1999).
- [230] D. MORONI, *Efficient Sampling of Rare Event Pathways*, 2005, It can be downloaded from:
<http://www.science.uva.nl/~moroni/thesis.html>.
- [231] D. B. FAHRENHEIT, *Phil. Trans. Roy. Soc.* **39**, 78 (1724).
- [232] D. TURNBULL and J. C. FISHER, *J. Chem. Phys.* **17**, 71 (1949).
- [233] W. C. SWOPE and H. C. ANDERSEN, *Phys. Rev. B* **41**, 7042 (1990).
- [234] R. J. ALLEN, P. B. WARREN, and P. R. TEN WOLDE, *Phys. Rev. Lett.* **94**, 018104 (2005).
- [235] T. S. VAN ERP, D. MORONI, and P. G. BOLHUIS, *J. Chem. Phys.* **118**, 7762 (2003).
- [236] C. VALERIANI, E. SANZ, and D. FRENKEL, *J. Chem. Phys.* **122**, 194501 (2005).
- [237] Private communication with E. Sanz and C. Valeriani.
- [238] P. J. STEINHARDT, D. R. NELSON, and M. RONCHETTI, *Phys. Rev. B* **28**, 784 (1983).
- [239] H. E. A. HUITEMA and J. P. VAN DER EERDEN, *J. Chem. Phys.* **110**, 3267 (1999).
- [240] P. R. THE WOLDE, M. J. RUIZ-MONTERO, and D. FRENKEL, *J. Chem. Phys.* **104**, 9932 (1996).
- [241] G. M. TORRIE and J. P. VALLEAU, *J. Comp. Phys.* **23**, 187 (1977).
- [242] L. D. LANDAU and E. M. LIFSHITZ, *Statistical Physics*, Pergamon Press, Oxford, 1969.
- [243] W. W. R. NICKLOW and H. G. SMITH, *Phys. Rev. B* **5**, 4951 (1972).
- [244] S. G. KABALKINA and L. F. VERESCHAGIN, *Dok. Akad. Nauk. SSSR* **131**, 300 (1960).
- [245] LANDOLT-BÖRNSTEIN, *Numerical data and Functional Relationships in Science and Technology*, Springer Verlag, Berlin, 1982, edited by O. Madelung, M. Schulz, H. Weiss Vol. 17, Subvol. a: "Semiconductors: Physics of Group IV Elements and III-V Compounds".
- [246] A. AZIZ, A. RAFIZADEH, and H. A. RAFIZADEH, *Phys. Rev. B* **7**, 4527 (1973).
- [247] J. BERNHOLC, A. ANTONELLI, T. M. D. SOLE, Y. BAR-YAM, and S. T. PANTELIDES, *Phys. Rev. Lett.* **61**, 2689 (1988).

-
- [248] E. KAXIRAS and K. C. PANDEY, *Phys. Rev. Lett.* **61**, 2693 (1988).
- [249] A. J. STONE and D. J. WALES, *Chem. Phys. Lett.* **128**, 501 (1986).
- [250] W. S. Y. B. C. PAN and J. YANG, *Phys. Rev. B* **62**, 12652 (2000).
- [251] F. LORANT, F. BEHAR, W. A. GODDARD III, and Y. C. TANG, *J. Phys. Chem. A* **105**, 7896 (2001).
- [252] A. HARADA, F. SHIMOJO, and K. HOSHINO, *J. of non Crystalline Solids* (2005), to be published.
- [253] J. KŌGA, H. OKUMURA, K. NISHIO, T. YAMAGUCHI, and F. YONEZAWA, *Phys. Rev. B* **66**, 064211 (2002).

Acknowledgements

I acknowledge all those people, for they are many, that in several respects made this work possible.

At the beginning is Roberto Piazza, my master thesis promotor at the Politecnico di Milano, who had the totally crazy idea to send me in the Netherlands for a PhD with Daan Frenkel. I will never thank him enough for this crazy idea of him.

At the other beginning is Daan Frenkel, who accepted me as a PhD student in a molecular simulation group, despite my candid admission of the lack of even a minimal expertise in the field.

Evert Jan Meijer did his supervising job exactly in the way I would have suggested, if asked: pushing me restlessly a step further than the place I had just arrived. Hartelijk bedankt, Evert Jan.

Jan Los was the driving force, supported by a hard to believe freshness and a far fetching sight I can only admire, that conducted the carbon potential through its flavours, LCBOP1, LCBOP1+, LCBOP2, per aspera ad astra, but I know he's just got a good idea for the next improvement... tot LCBOP3, Jan!

Annalisa Fasolino had the initial idea on making a *really* reactive empirical potential for carbon. That's how we met, but not why I acknowledge her: it has been a lesson sitting next to her and see how ideas, that were clear in my mind but definitely not on the paper, could become well-formed English sentences, that connected to give a (actually, more than one) well-written scientific article. Whoever had been a trainee researcher would agree on how fortunate and enviable was this opportunity.

Chantal Valeriani was a precious collaborator during the demanding period of diamond nucleation ... well ... she *is* a precious collaborator, since diamond nucleation is everything but a closed chapter. I thank also Eduardo Sanz for a couple of seminal discussions about *his* nucleation method that was used, with few changes, for chapter 10. Thanks to Daniele Moroni for sharing some of his tough background on statistical mechanics and rare events methods.

Gooitzen Zwanenburg took care of the pc cluster, that should be rather baptized Argo than Jaipur, where I ran most of the calculations that made this thesis writable. Gooitzen himself, Ranieri Argenti, Jasper Heuft, Rene Pool, and Bastiaan Huisman took care, too many times to count them all, of my poor abilities in computer stuff. Thanks to them. Bas, it has been a pleasure chatting with you about life, the universe, and everything, but thanks also for figure 12.3! Elske Leenders made a necessary step towards the conclusion of this written work, translating into a "Samenvatting" the summary: something I would have never been able to do myself. I acknowledge Peter Bolhuis for his critic listening and fruitful discussion at all my group meeting talks. I acknowledge all my colleagues of the "Molsim" group for any interesting exchange of (scientific) opinions: when mentioning "Molsim" at the Universiteit van Amsterdam, I intrinsically acknowledge its leader, who made it possible: Berend Smit.

A coloro che sanno (l'italiano)

Redatta in vernacolo a me assai più confacente e caro, apro questa conclusiva pagina della mia dissertazione di dottorato, dedicandola a coloro che, sovr'a tutti, questa tesi han resa possibile. Risalgo senz'indugio ad altro inizio, ben più lontano di questo inquieto ed inquietante scorcio di terzo millennio: *ai miei genitori*. E non tanto per avermi reso ontologicamente possibile, quanto per aver sempre creduto in me. Locuzione che spesso s'usa di circostanza ma cui penso e spero di saper conferire il senso pieno. Ma a voi, mamma, babbo, non devo certo specificarlo, voi che sapete leggere dietro questi manierismi. A proposito di persone che hanno sempre creduto in me, credo che *mio fratello, Andrea*, non abbia rivali (che la tua avventura transatlantica veleggi sempre con il vento che ti soffia dalle spalle!). Genitori e fratello che con lettere, telefonate e visite regolari, han fatto sì che potessi sentirmi sempre a casa, a discapito dei mille chilometri che secondo la mappa separano Caravate da Amsterdam.

Miei cari paraninfi!

Matteo! ...

(e qui l'autore si disperse, una cum, in un decennio di ricordi e non seppe più cosa scrivere)
(*Sh'nn'n-daah: nicht pe-pem!*).

Valeria! Conoscerti, raggio di balsamica luce mediterranea, è stato certo l'evento più fortunato occorsomi durante la permanenza tra le brume nordiche.

Ancora grazie *Roberto* per avermi suggerito questa via, quando ancora confusamente pensavo a che avrei fatto della mia allora imminente laurea in ingegneria nucleare. Per quanto venire ad Amsterdam abbia implicato perderti come prezioso interlocutore - nel tuo essere aggressivo iconoclasta avevo trovato una voce davvero amica - l'eccezionale avventura ha, con un po' di difficoltà, remunerato la perdita.

Ancora grazie *Jan*, per essermi stato insostituibile Virgilio in una terra a me straniera.

Sara (quam pulchra es, amica mea): se delle gioie e dolori della ricerca che ha preceduto questo scritto ti è riverberata solo pallida eco, di queste duecentoquaranta pagine hai tutto il diritto di sentirti autrice quanto me, avendone condiviso ogni sospiro, ogni malumore, ogni scintilla per una frase ben tornita, avendo promosso ad ogni tramonto la macellazione del maledetto animale grufolante che poi risorgeva sornione ad ogni alba, avendo riletto ad nauseam bozze che mutavano senza posa di tra le tue dita, avendone caparbiamente discusso ogni formula, ogni concetto, ogni certezza. Con l'intima convinzione che questo libello non sarà il meglio tra quanto scaturirà dal lungo cammino che vorremo insieme percorrere.

Non è detto che Kublai Kan creda a tutto quello che dice Marco Polo quando gli descrive le città visitate nelle sue ambascerie, ma certo l'imperatore dei tartari continua ad ascoltare il giovane veneziano con più curiosità e attenzione che ogni altro suo messo o esploratore. Nella vita degli imperatori c'è un momento, che segue all'orgoglio per l'ampiezza sterminata dei territori che abbiamo conquistato, alla malinconia e al sollievo di sapere che presto rinunceremo a conoscerli e a comprenderli; un senso come di vuoto che ci prende una sera con l'odore degli elefanti dopo la pioggia e della cenere di sandalo che si raffredda nei bracieri; una vertigine che fa tremare i fiumi e le montagne istoriati sulla fulva groppa dei planisferi, arrotola uno sull'altro i dispacci che annunciano il franare degli ultimi eserciti di sconfitta in sconfitta, e scrosta la ceralacca di sigilli di re mai sentiti nominare che implorano la protezione delle nostre armate avanzanti in cambio di tributi annuali in metalli preziosi, pelli conciate e gusci di testuggine: è il momento disperato in cui si scopre che quest'impero che ci era sembrato la somma di tutte le meraviglie è uno sfacelo senza fine né forma, che la sua corruzione è troppo incancrenita perché il nostro scettro possa mettervi riparo, che il trionfo sui sovrani avversari ci ha fatto eredi della loro lunga rovina. Solo nei resoconti di Marco Polo, Kublai Kan riesce a discernere, attraverso le muraglie e le torri destinate a crollare, la filigrana d'un disegno così sottile da sfuggire al morso delle termiti.

It is not certain that Kublai Kan trusts everything Marco Polo says when he describes the cities he visited during his expeditions, but the emperor of Tartars clearly keep on listening to the young Venetian with more curiosity and attention than he shows for any other messenger or explorer of his. In the life of emperors there is a moment that follows pride in the boundless extension of the territories we have conquered, the melancholy and relief of knowing we shall soon give up any thought of knowing and understanding them. There is a sense of emptiness that frames us at evening, with the odor of the elephants after the rain and the sandalwood ashes cooling in the braziers, a dizziness the makes tremble rivers and mountains that are engraved on the fallow curves of the planispheres, and rolls up, one after the other, the despatches announcing to us the collapse of the last enemy troops, from defeat to defeat, and scrapes off the wax of the seals of kings never heard before that beseech our armies' protection, offering in exchange annual tributes of precious metals, tanned hides, and tortoise shells. It is the desperate moment when we discover that this empire, that had seemed to us the sum of all wonders, is an endless, formless ruin, that his corruption's gangrene has spread too far to be healed by our scepter, that the triumph over enemy sovereigns has made us heirs of their long fall. Only in Marco Polo's accounts was Kublai Kan able to discern, through the walls and towers doomed to crumble, the tracery of a pattern so subtle it could escape the termites' gnawing.